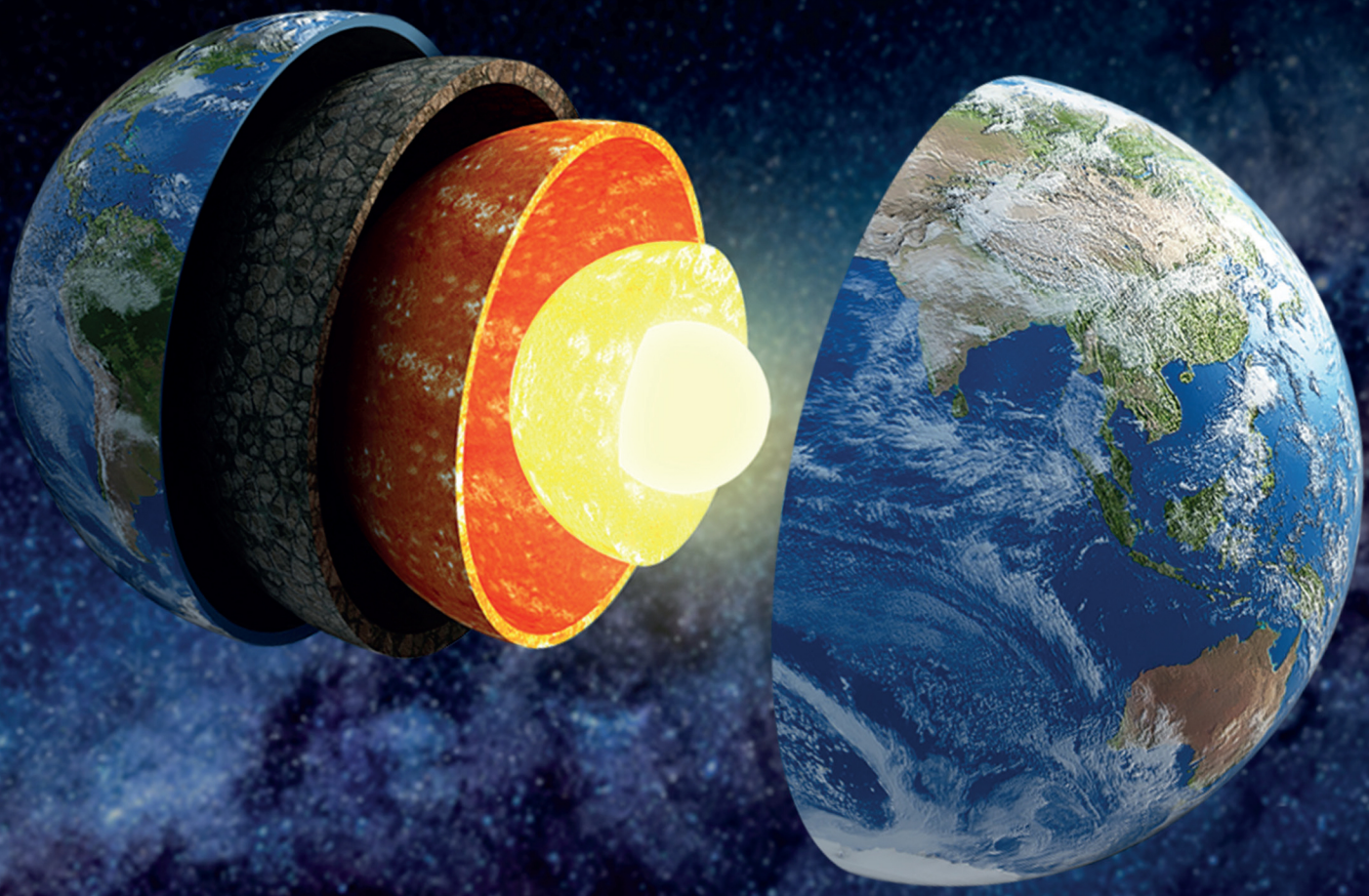

PROCEEDINGS OF THE 19TH ANNUAL MEETING OF THE ASIA OCEANIA GEOSCIENCES SOCIETY (AOGS 2022)

01 – 05 AUGUST 2022

Asia Oceania Geosciences Society
www.asiaoceania.org

World Scientific
Connecting Great Minds

Proceedings of the 19th Annual Meeting of the Asia Oceania Geosciences Society (AOGS 2022)

Singapore, 01 – 05 August 2022

This page intentionally left blank

Proceedings of the 19th Annual Meeting of the Asia Oceania Geosciences Society (AOGS 2022)

Singapore, 01 – 05 August 2022

Editors

Van-Thanh-Van Nguyen
McGill University, Canada

Edited by

Shie-Yui Liong
Consultant
Previously, Tropical Marine Science Institute, National University of Singapore.

Masaki Satoh
The University of Tokyo, Japan

World Scientific

NEW JERSEY • LONDON • SINGAPORE • BEIJING • SHANGHAI • HONG KONG • TAIPEI • CHENNAI • TOKYO

Published by

World Scientific Publishing Co. Pte. Ltd.

5 Toh Tuck Link, Singapore 596224

USA office: 27 Warren Street, Suite 401-402, Hackensack, NJ 07601

UK office: 57 Shelton Street, Covent Garden, London WC2H 9HE

British Library Cataloguing-in-Publication Data
A catalogue record for this book is available from the British Library.

Proceedings of the 19th Annual Meeting of the Asia Oceania Geosciences Society (AOGS 2022)

ISBN 978-981-127-543-2 (hardcover)
ISBN 978-981-127-544-9 (ebook for institutions)
ISBN 978-981-127-545-6 (ebook for individuals)

For any available supplementary material, please visit
https://www.worldscientific.com/worldscibooks/10.1142/13385#t=suppl

PREFACE

On behalf of the Editorial team, we are excited to offer the proceedings of the 19th Annual Meeting of the Asia Oceania Geosciences Society (AOGS 2022) which was held from 1 to 5 August 2022. The proceedings include selected extended abstracts from a challenging array of presentations at this conference. The AOGS Annual Meeting is a leading venue for professional interaction among researchers and practitioners, covering diverse disciplines of geosciences.

This page intentionally left blank

EDITORIAL BOARD

LIST OF REVIEWERS

This page intentionally left blank

TABLE OF CONTENTS

This page intentionally left blank

ADDRESSING ABRUPT GLOBAL WARMING, WARMING TREND SLOWDOWN AND RELATED INDIAN SUMMER MONSOON FEATURES IN RECENT DECADES

Indrani Roy[1]

ABSTRACT: This study addresses abrupt global warming and a slowdown thereafter that happened in recent decades. It separated the role of anthropogenic CO2 led linear trend to that from natural factors (volcano and the sun). It segregates a period 1976–1996 where two explosive volcanic eruptions occurred in active phases of strong solar cycles and also the period covers two whole solar cycles. That same period coincided with abrupt global warming. This study suggests that domination of a particular type of ENSO, the Central Pacific (CP) type ENSO and related feedback from water vapour played a crucial role. A plausible mechanism was proposed that could be triggered by explosive volcanos via a preferential North Atlantic Oscillation (NAO) phase. It modulates the CP ENSO via extratropical Rossby wave and affects the Aleutian Low. From that angle, it is possible to explain the disruption of ENSO and Indian Summer Monsoon teleconnection during the abrupt warming period and how it recovered subsequently afterward. Interestingly, individual models and also the CMIP5 model ensemble fails to agree with the observation. This study further explores important contributions due to natural drivers those are missed by models.

Keywords: ENSO, ISM, NAO, Hiatus, volcano, Sunspot Number

INTRODUCTION

The role of natural factors on climate is identified in various research (Roy and Kriplani, 2019a,b) though models miss many important contributions from natural drivers. The sun is one of the main drivers of natural factors, and solar influence on climate is discussed, in detail addressing various controversies (Roy, (2010, 2020b, 2021, 2018b). Model biases are another area that deserve attention too (Roy, Gagnon and Siingh, 2019). This study discussed mechanisms based on observed data and gave directions where models can improve.

RESULTS

Two decades of the last century were segregated where two explosive volcanic eruptions (El Chichon in 1982 and Pinatubo in 1991) occurred in active phases of strong solar cycles (Fig.1). Global temperature had risen .13ºC/decade during that period; whereas, the rise for overall period is 0.07ºC/decade. There was a slowdown of the rise in global temperature afterwards.

The influence of strong volcanic eruptions is shown using Sea Level Pressure (SLP) data for Dec-Jan-Feb (DJF) in Fig. 2 [Roy (2018a)]. Signals of SLP using Multiple Linear Regression (MLR) and anomaly technique are presented. Aerosol Optical Depth (AOD) represents volcano in the top plot. Both techniques identify strong positive North Atlantic Oscillation (NAO)

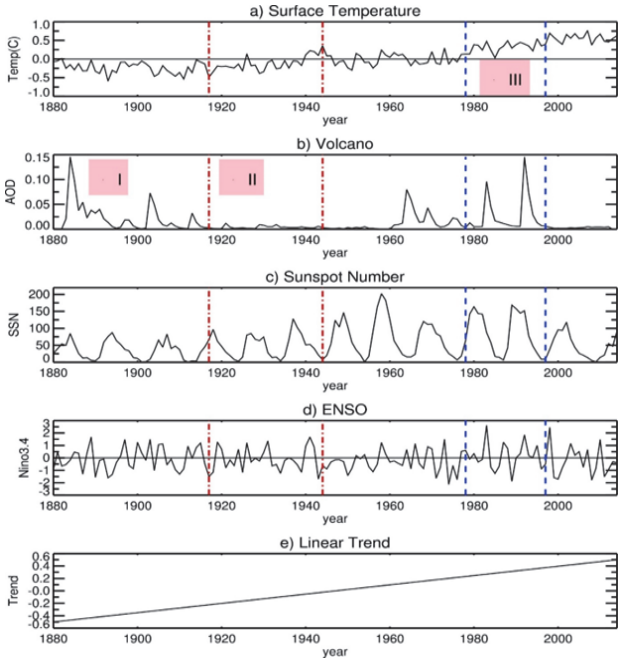

Fig. 1 Timeseries of various parameters. a) shows surface temperature from GISS data which is influenced by various parameters b) volcano, c) solar cyclic variability represented by Sunspot number (SSN), d) ENSO and e) Linear Trend. Main interest is period III and after. In period III two major volcanos erupted in active phases of strong solar cycles. ENSO in period III was strongest in terms of amplitude and variability. Global temperature had risen abruptly. [Roy (2020a)]

[1] University College London (UCL), Gower Street, LONDON, WC1E 6BT
Indrani.roy@ucl.ac.uk; Indrani_r@hotmail.com

 https://doi.org/10.1142/9789811275449_0001

pattern for strong volcanos. Signals in North Atlantic region are even extended high up in the stratosphere (Roy 2018a, not shown here).

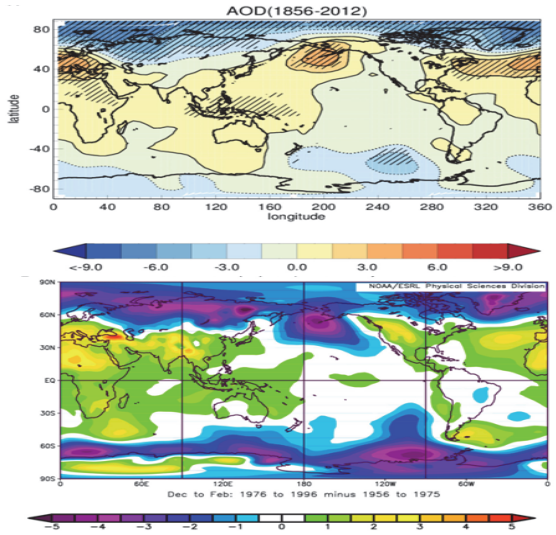

Fig. 2. The influence of strong volcanic eruptions are shown using SLP data, for DJF. The top plot shows signals for HadSLP2 data of Volcano using Multiple Linear Regression (MLR), where ENSO, SSN and trend removed. Significant regions at 95% levels are marked by hatching. Bottom plot shows SLP anomaly for the period 1976-1996 w.r.t. two previous decades (1956-1975). For both cases, strong positive NAO pattern is identified for strong volcanos.

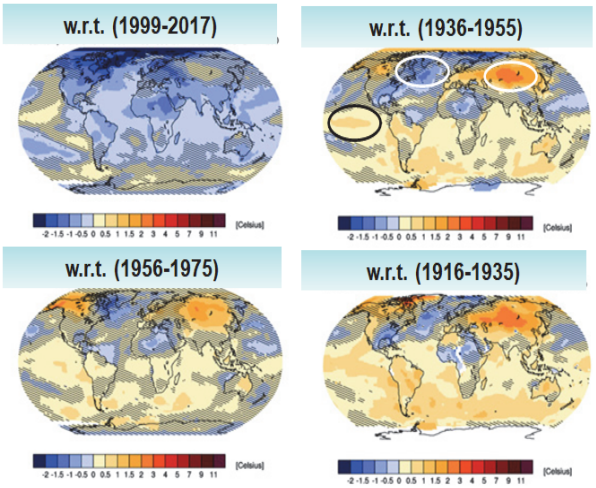

Fig. 3. The anomaly of surface temperature (ºC) in observation (DJF), using GISTEMP data [after, Roy (2018a)]. Anomaly during (1976-1996) is presented w.r.t. three other periods (covering two decades each). The first plot is an anomaly w.r.t. recent two decades. Significant regions (95% level) are shown without hatching. Central Pacific warming and cooling in the north Atlantic, while warming in Eurasian sectors are very distinct.

Fig. 3 detects significant warming in the Central Pacific, cooling in north Atlantic, while warming in Eurasian sector during DJF for '1976-1996'. Signals are similar using other data sources too (either GISTEMP or NOAA, ERSST, [Roy, 2018a]). Models however, do not capture those observed signals. Some models capture signature say, in Eurasian Sector, but not in N. Atlantic or Central Pacific and vice versa. It is true for all individual model as well as CMIP5 model ensemble [Roy (2018a)].

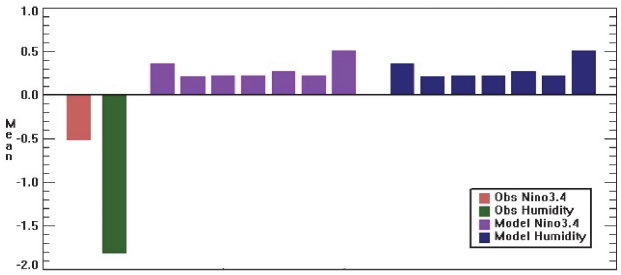

Fig. 4. Mean difference between '1999-2017' to '1976-1996' for Nino3.4 and specific humidity. The first two bar plots are for Niño3.4 and specific humidity using observed or reanalyses products. Seven arbitrary models are also presented; purple for Niño3.4 and blue for sp. humidity. Interestingly signs are different in models from observation. Though only a few models are presented, all models suggest similarly [Roy (2018a)].

Time Series (DJF) of various meteorological parameters indicate that though there is a steady rise in various parameters (e.g., Specific humidity, Nino 3.4 temperature etc. in CMIP5 models, that is not the case for observation and reanalyses (Roy 2018a, not shown here). The mean difference between '1999-2017' to '1976-1996' for Nino 3.4 and specific humidity suggest that signs of change are even different in models to that from observation (Fig. 4).

Studies indicated ENSO, Indian Summer Monsoon (ISM) usual teleconnection weakened in later two decades of the last century, which reverted back again in recent decades. In period of disruption, teleconnection of ISM via north Atlantic and Eurasian sector was strengthened. That feature of ISM disruption was identified using correlation between ISM (JJAS) and different regional temperature fields (Roy, 2018a, not shown here).

Figure 5 shows solar Max or peak years for high solar cycles (SSN>120) are biased towards cold event side of ENSO. Moreover, we find that the sun and ENSO (DJF) have different connections (which is cold event type) after 1998 and before 1957 in all active solar years (SSN >120) and not only to solar maximum or peak years. Such feature is however missed by all models (Roy, 2018a, not shown here). Thus, the solar contribution to warming as

observed via ENSO in later decades of the 20th century is missing in all models.

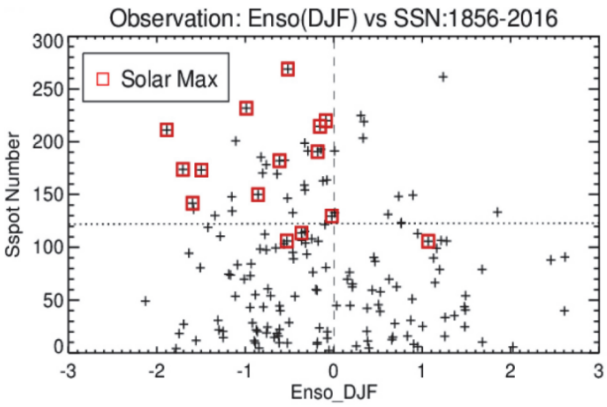

Fig. 5. Solar Max or peak years (marked by red) for high solar cycles (SSN>120) are biased towards the cold event side of ENSO. Interestingly, all points of the top right quarters are for the period 1958-1997.

CONCLUSIONS

Very strong influence from volcanoes was observed around the north Atlantic during 1976-1996, DJF by MLR as well as anomaly technique. The signal is also extended high up in the stratosphere. Temperature anomaly during '1976-1996' detected warming in the central Pacific, cooling in the north Atlantic, while warming in the Eurasian sector. Such pattern is noticed using different anomaly periods of two decades, earlier or later and various observed data sources. Performance of individual CMIP5 models and AR5 CMIP5 subsets were analysed but those fail to match with observation. No Consistency is found among those models too. Analyses on specific humidity and Nino 3.4 show observation and models even show different sign of change in recent period to that from previous two decades. ISM and ENSO teleconnection was shown weakened in those two decades. A series of mechanisms are proposed which are initiated by explosive volcanos that erupted during 1976-'96 and coincided with active phases of strong solar cycles. It modulates NAO, Aleutian Low (AL), Eurasian Snow, Central Pacific (CP) ENSO and ISM. Those also caused abrupt warming and disruption of ISM-ENSO teleconnections (Fig.6).

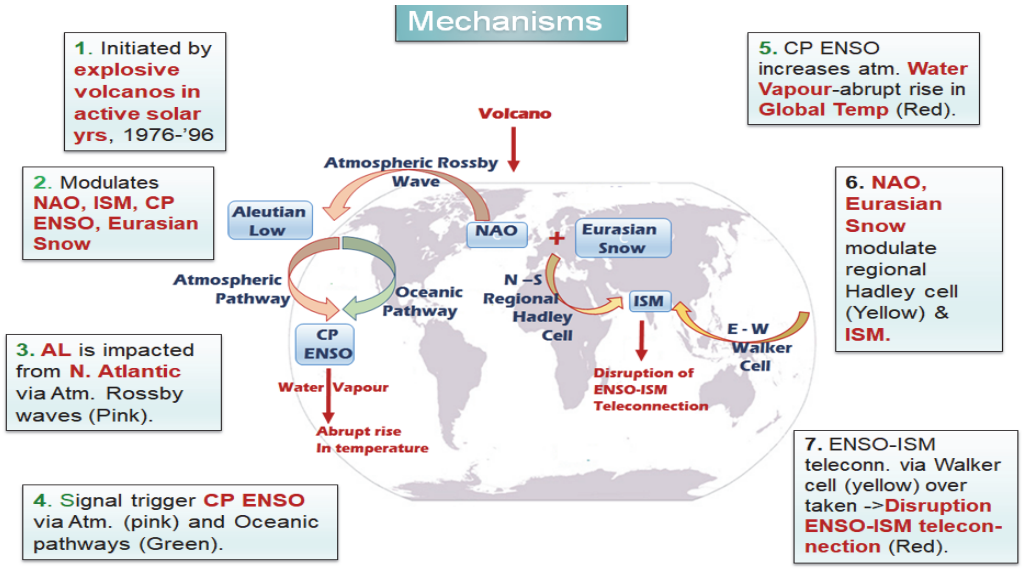

Fig. 6. Mechanisms are proposed following discussions earlier. Those are initiated by explosive volcanos in active phases of strong solar cycles. That modulated various features e.g, NAO, AL, ISM [after, Roy (2018a); Roy and Kriplani (2021)].

References

Roy I , 2010,, PhD Thesis, Imperial College, London, Doi: 10.25560/6038.

Roy, I, 2018a,. Front. Earth Sci. 6:136. doi: 10.3389/feart.2018.00136.

Roy, I, 2018b, Springer Nature, DOI: 10.1007/978-3-319-77107-6.

Roy, I. and Kriplani R, 2019a, Theor. and Appl. Clim., 137, 469–480. Doi: 10.1007/s00704-018-2597-z.

Roy I., and Kriplani R., 2019b, Theoretical and Appl. Clim., doi: 10.1007/s00704-019-02864-2.

Roy, I., Gagnon, A. and Siingh, D., 2019, Theo. and Appl. Clim., https://doi.org/10.1007/s00704-018-2536-z.

Roy I., 2020a, Pure and Appl. Geophy., Springer Nature, https://doi.org/10.1007/s00024-020-02522-z.

Roy, I. 2020b, Pure Appl. Geophys, Springer Nature. Doi: 10.1007/s00024-020-02564-3.

Roy, I and Kriplani R, 2021. Elsevier, DOI 10.1016/C2019-0-04482-2.

Roy, I , 2021, Natural Hazards, Springer Nature, https://doi.org/10.1007/s11069-021-04653-5.

EFFECTS OF URBANIZATION ON EXTREME PRECIPITATION IN A METROPOLITAN AREA USING THE WRF-UCM

H. S. Jung[1] and S. K. Park[1,2,3]

ABSTRACT: Cities are one of the major contributors to climate change and suffer potentially high health and environmental risks and great damages by natural disasters under a changing climate. Extreme rainfall events, often causing flash floods in urban areas, are one of the costliest natural disasters. In particular, rapid urbanization under local climate change often exerts strong impacts on extreme precipitation. Thus, understanding the characteristic changes in various aspects of extreme precipitation due to the urbanization processes is of utmost importance to properly plan and manage potential urban disasters. In numerical models, an urban region is usually represented by a land cover with low reflectivity, low heat capacity and water availability, and a large roughness length, whose characteristics can change according to the degree of urbanization. This study aims to quantify the effect of urbanization on various aspects of extreme precipitation, including its formation, development, location and amount, by conducting sensitivity experiments in terms of urban land cover/use for an extreme rainfall case in the Seoul metropolitan area, Korea, using the Weather Research and Forecast (WRF) model coupled with Urban Canopy Model (UCM) --- the WRF-UCM. Our results provide a basis for better quantitative precipitation forecasting and a reference for urban planning and design.

Keywords: WRF-UCM, Extreme precipitation, Urbanization, Land-use change.

INTRODUCTION

Extreme precipitation is very influential phenomenon because it has strong potential to causing massive property damage. Particularly, highly concentrated human resources of urban area suggests that the stronger damage potential exists. Furthermore, impermeable surface, which typically characterize urban areas, is vulnerable to the heavy rainfall due to limitation of water capacity.

Urbanization includes both an extension and advancement of an urban area, not only a non-urban area becoming a city but also growing population and buildings. Urban characteristics are categorized in two components, strong heating process including anthropogenic heat emission and strong heat absorption of the architectures and weak cooling process by deficient plant and soil. Heating processes of urban area induce the formation of heat dome covering a city, which is termed by the Urban Heat Island (UHI).

Urbanization affects on extreme precipitation while it varies in each city. Pathirana, et al. (2014) indicated that the UHI can induce the increase in rainfall. Further, An increase in extreme precipitation, which is appears to be effected by urbanization, is observed in East Asian megacities including Seoul, Republic of Korea (Oh et al., 2021).

Therefore, this study intents to feature the impact of urbanization through land use change experiments on extreme precipitation. Precipitation events are very sensitive hence they are difficult to represent, especially when developing rapidly. Thus, the urbanization effect is examined on a rapidly developed extreme case.

DATA AND METHOD

Case Overview

The selected case is extreme precipitation event during 13 00 KST 19 Jul 2021 - 18 00 KST 19 Jul 2021 in Seoul Metropolitan area, South Korea. In this study, the threshold of extreme precipitation was hourly cumulative precipitation higher than 30 mm. During the case time, hourly precipitation was observed up to 60 mm or more.

Model Framework

Coupled model, the WRF-UCM, which is compounding of the Weather Research and Forecasting (WRF) model with the single-layer Urban Canopy Model (UCM) conducted the experiments. The WRF model

[1] Department of Climate and Energy System Engineering, Ewha Womans University, 52, Ewhayeodae-gil, Seodaemun-gu, Seoul, 03760, REPUBLIC OF KOREA.
[2] Center for Climate/Environment Change Prediction Research, Ewha Womans University, 52, Ewhayeodae-gil, Seodaemun-gu, Seoul, 03760, REPUBLIC OF KOREA.
[3] Severe Storm Research Center, Ewha Womans University, 52, Ewhayeodae-gil, Seodaemun-gu, Seoul, 03760, REPUBLIC OF KOREA.

 https://doi.org/10.1142/9789811275449_0002

numerically describes a mesoscale weather. In addition, the UCM produces detailed urban circumstance considering thermodynamically and dynamically effecting components of civil structures, such as the width, height, conductivity, reflectivity, width and height of walls, roads and buildings in urban area. Further, Noah Land-Surface Model represents land-atmosphere interaction process.

The high-resolution simulation up to 1 km conducted using three-nested domain by the 4.2 version of WRF over 18 hours from 18 00 UCT 18 July 2021 to 12 00 UCT 19 July 2021. Domains were designed from the coarsest domain 1 (D01) to the finer domain 2 (D02) and the finest domain 3 (D03) with one-way feedback. Horizontal resolutions of each domain were sequentially 25 km, 5km and 1 km from D01 to D03. Moreover, coarsest domain centered at N37 E125 and used 0.25-degree Global Data Assimilation System (GDAS) Final (FNL) as initial and boundary condition while D02 and D03 used their parent domain.

To represent radiation process, Rapid Radiative Transfer Model and Dudhia scheme were used for longwave and shortwave radiation, respectably. Further, Yonsei university planetary boundary Layer scheme and WRF single-moment 6-class microphysics scheme were selected and deep convection scheme of Kain-Fritsch was applied except D03. Especially, the model spin-up time was 12 hours.

Land Use and UCM Sensitivity Experiment Design

The sensitivity experiment was conducted through changing the land use data replacing urban grids to forest grids before the geogrid process in WRF Pre-Processing System (WPS). Furthermore, the sensitivity study on the UCM was also conducted.

Environmental Geographic Information Service (EGIS) was used to basic land cover to WRF simulation. Used EGIS is reclassified version according to U.S. Geological Survey (USGS) land use category. Following these 3 categories, required to run the UCM, are added. “Low (High) Intensity Residual” and “Industrial or Commercial”. EGIS is land use data provided by Ministry of Environment of Korea.

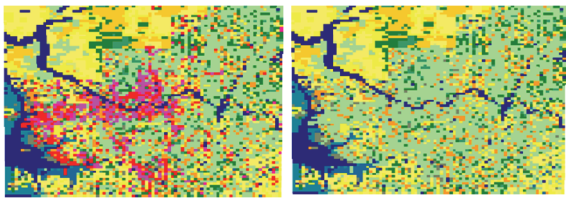

Fig. 1 (left) the land use of the urban case, (right) of the no urban case.

Table 1 Model and data setting for sensitivity experiments

EXP	UCM	LU
URB(CTRL)	Off	EGIS
UCURB	On	EGIS
NOURB	Off	Changed EGIS

RESULTS

Total precipitation (mm) 18:00 KST 19 Jul 2021 There were sequentially two precipitation events, preceding weaker case and the extreme case after 17 00 KST 19 Jul 2021. The analyze focused on the extreme case. Considering the location and air flow of precipitation, it is highly likely that it is precipitation caused by orographic lifting. In Fig. 2, 30 min cumulative precipitation (mm) at maximum, the amounts of precipitations varied by the experiments.

The UHI is one of the typical phenomena in the urban area and its intensity is defined by the temperature difference between urban and rural area. In this study, 2m temperature was used to identify the UHI. The UHI was growing up until 16:30 KST, which is described in Fig. 3, after which it declined. The thermal concentration in the center appear in common at every experiments.

As shown in the Fig. 4, the moist northwesteries penetrates into the urban area before the extreme precipitation begin near the precipitated region. Further, significantly higher humidity is shown in NOURB at center of Seoul.

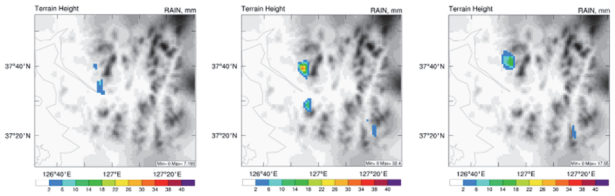

Fig. 2 Contours of 30 min cumulative precipitation (mm) at 17:45 KST 19 Jul 2021 of (left) UCURB, (center) URB, and (right) NOURB, on gray scale contour of terrain height (m).

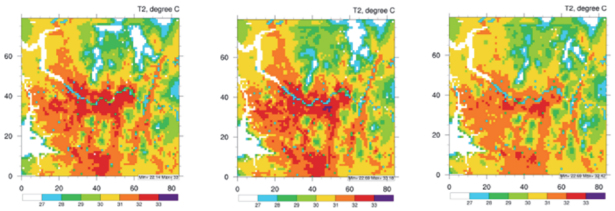

Fig. 3 Contours of two meters temperature (˚C) at 16:30 KST 19 Jul 2021 of (left) UCURB, (center) URB, and (right) NOURB.

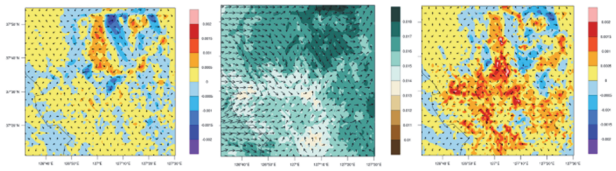

Fig. 4 Contours of 2m moisture flux ($\mathrm{kg\,kg^{-1}}\ m\ s^{-1}$) with 2m water vapor mixing ratio ($\mathrm{kg\,kg^{-1}}$) CTRL and differences of EXP to CTRL(EXP - CTRL) at 16:45 KST 19 Jul 2021

CONCLUSION AND DISCUSSION

Enhanced orographic precipitation by urbanization

Although the overall moisture content was higher in "nonURB", the precipitation was twice as high in "URB", and strong heating was taking place in the area due to the urban topography. In addition, the direct cause of precipitation is considered to be orographic lifting.

This suggests that even when urban areas are not directly responsible for the occurrence of precipitation, they can be affected in a way that intensifies precipitation. Thus, we have to concern various causes in urban-precipitation.

Basin topography – Natural source intensifying UHI

The “nonURB” experiment can show the natural dynamics of the region. Since the thermal concentration in the Seoul metropolitan area is also shown in “nonURB”, it suggests that there is not only an artificial cause but also a topographical cause of the thermal concentration in urban areas. The overall distribution and the location of the maximum temperature were also consistent. It also shows urban and topographical effects are compounded.

Extreme precipitation modelling in urban areas with the UCM

The base of UCM is to subdivide urban land use into three categories and set appropriate urban parameters, such as heat emission, building height and road width, to enable physical calculation of the building unit accordingly. Although it is generally known that using UCM is effective to high-resolution urban weather modeling, Using UCM does not always improve results. More precise parameters are need to be considered.

ACKNOWLEDGEMENTS

This research is supported under the grant of Basic Science Research Program through the National Research Foundation of Korea (NRF) funded by the Ministry of Education 2018R1A6A1A08025520). It is partly supported by the NRF grant funded by the Korea government (MSIT) (NRF-2021R1A2C1095535).

References

Oh, S. G., Son, S. W., & Min, S. K. (2021). Possible impact of urbanization on extreme precipitation–temperature relationship in East Asian megacities. Weather and Climate Extremes, 34, 100401.

Pathirana, A., Denekew, H. B., Veerbeek, W., Zevenbergen, C., & Banda, A. T. (2014). Impact of urban growth-driven landuse change on microclimate and extreme precipitation—A sensitivity study. Atmospheric Research, 138, 59-72.

Zheng, Z., Xu, G., & Gao, H. (2021). Characteristics of Summer hourly extreme precipitation events and its local environmental influencing factors in Beijing under urbanization background. Atmosphere, 12(5), 632.

APPLICATION OF K_{DP} EVOLUTION ON THE VERY-SHORT-RANGE RAINFALL FORECAST

Chi-June Jung [1], Yu-Cheng Kao [2] and Ben Jong-Dao Jou [1,3]*

ABSTRACT: On 16 October 2021, localized torrential rainfall (> 70 mm h^{-1}) occurred in the slope area of northern Taiwan during an approaching surface front. Flash floods downstream of the catchment area resulted in a severe drowning accident without warning. In this observational study, the newly-established C-band disaster prevention rainfall radar in northern Taiwan is used for analysis and comparison. At 15-18 local time (LST), extreme values of the specific differential phase K_{DP} (> 2° km^{-1}) can be used to identify the heavy rainfall region's location, intensity, and movement. For flash floods downstream of the catchment area, potentially, there is a priori warning capability. In this event, tracking intense and concentrated K_{DP} on complex terrain has an advantage over radar reflectivity. The direct application of K_{DP} on quantitative precipitation estimates can effectively complement the transmission-delay problem of ground rain gauges.

Keywords: specific differential phase K_{DP}, polarimetric radar, heavy rain

INTRODUCTION

The specific differential phase K_{DP} is a dual-polarization radar parameter, defined as the slope of range profiles of the differential propagation phase shift Φ_{DP} between horizontal and vertical polarization states. The K_{DP} is not affected by propagation attenuation and is closely related to rain intensity. The application of K_{DP} improved the accuracy of quantitative rainfall estimation (QPE) (Jou et al. 2015; Chang et al. 2021; Kao et al. 2021).

Kuster et al. (2021) defined the K_{DP} core as $K_{DP} \geq 1.0°$ km^{-1} near or within 3 km below the environmental melting layer observed by S-band radar. The K_{DP} core likely indicates a significant amount of precipitation descending, melting, and may lead to the formation of a downburst. K_{DP} core was first seen below the melting layer, enhance within minutes, and can develop above the melting layer. Within 20 minutes, the K_{DP} core gradually approached the ground, accompanied by a significant rainfall process

This study uses a C-band polarimetric radar, Shulin radar (RCSL), to discuss the evolution of K_{DP} and related rainfall. The application of K_{DP} to QPE is also illustrated. We take the heavy rain event in Hubaotan, New Taipei City, on the afternoon of 16 October 2021, as an example. The application of real-time radar data is expected to improve the accuracy and efficiency of disaster prevention warning information.

OVERVIEW OF THE HEAVY RAIN EVENT

On 16 October 2021, the environment was mainly affected by the strengthening of the northeasterly wind. The rainfall echo had moved into the land of northeastern Taiwan at 15 LST; the northwest-southeast belt-shaped rainfall echo gradually moved southwest through northern Taiwan. The hourly K_{DP} observations were consistent with the reflectivity distribution but highlighted the distribution of extreme rainfall (Fig. 1). The main rainfall areas were distributed on the northwest side and the ridge of Snow Mountain (Fig. 2). The Taiping rainfall station marked No. 2 on the map is adjacent to the location of the Hubaotan. The gauge measured maximum hourly rainfall at 17 LST was 74 mm, and then the precipitation area gradually moved westward along the terrain.

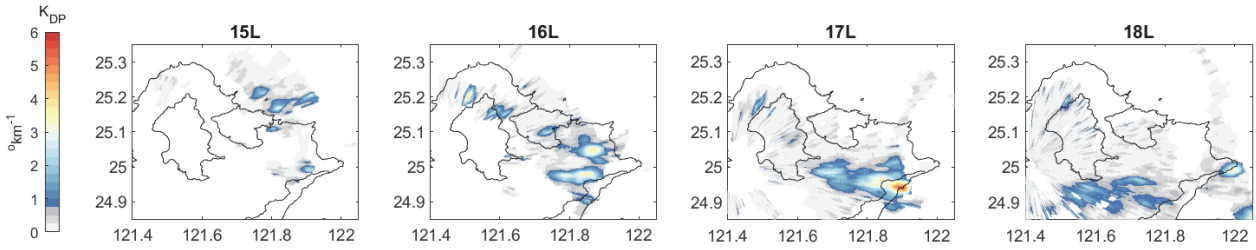

Fig. 1. The observed K_{DP} at the 1-degree elevation angle of RCSL between 15 to 18 LST on 16 October 2021.

[1] Department of Atmospheric Sciences, National Taiwan University, Taipei 10617, TAIWAN
[2] Environmental Simulation Co. Ltd., Taipei 10663, TAIWAN
[3] Center for Weather Climate and Disaster Research, National Taiwan University, Taipei 10617, TAIWAN
* Corresponding author: Dr. Ben Jong-Dao Jou, jouben@ntu.edu.tw

 https://doi.org/10.1142/9789811275449_0003

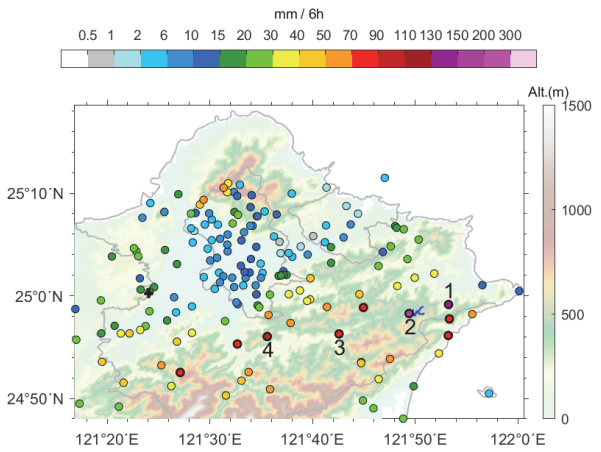

Fig. 2. Topography of northern Taiwan and the accumulated rainfall between 15 to 21 LST on 16 October 2021. The colored dots show the rain amount and location of each gauge station.

OBSERVATIONAL FEATURES OF K_{DP}

Fig. 3 indicates the locations of maximum K_{DP} value observed by radar at the 1-degree elevation angle from 15 to 18 LST and the frequency of occurrence of K_{DP} greater than 2° km^{-1} (rain rate approximately 60 mm h^{-1}).

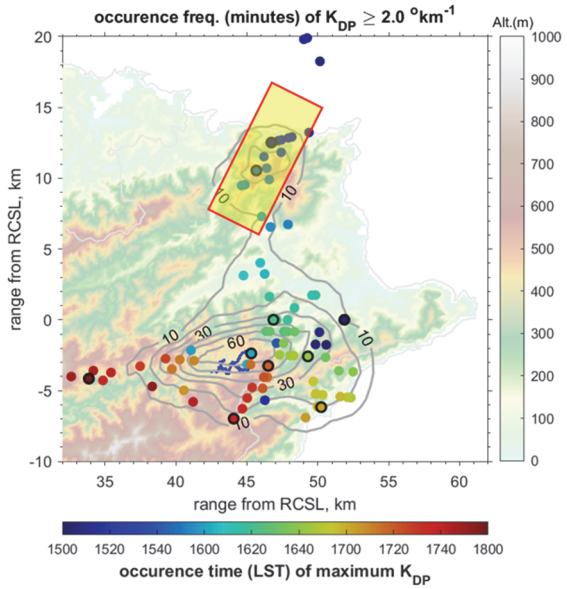

Fig. 3. The locations of maximum K_{DP} value (colored dots) and the frequency of occurrence of K_{DP} ≧2° km^{-1} (contours in the unit of minutes) between 15 to 18 LST on 16 October 2021. The water system in the upper watershed of Hubaotan is drawn with blue lines. The rectangle on the northeast indicates the region for the analysis of the vertical cross-section in Fig. 3.

After 15 LST, the convection system moved in from the sea with the northeasterly wind. Around 1530 LST, the K_{DP} strengthened over terrain, and the K_{DP} of the melting layer reached 1.5° km^{-1}. At 1535 LST (Fig. 4a), the precipitating core with K_{DP} > 4° km^{-1} can be identified below 4 km altitude, and the corresponding rainfall intensity is over 100 mm per hour. At 1543 LST (Fig. 4b), the following full volume scans show that the precipitating core moves downstream of the prevailing wind and descends toward the ground; at this time, there was the most significant rainfall on the ground (Fig. 4d), and the 10-minute accumulated rainfall was 13.5 mm (converted to a rainfall intensity of 81 mm/h).

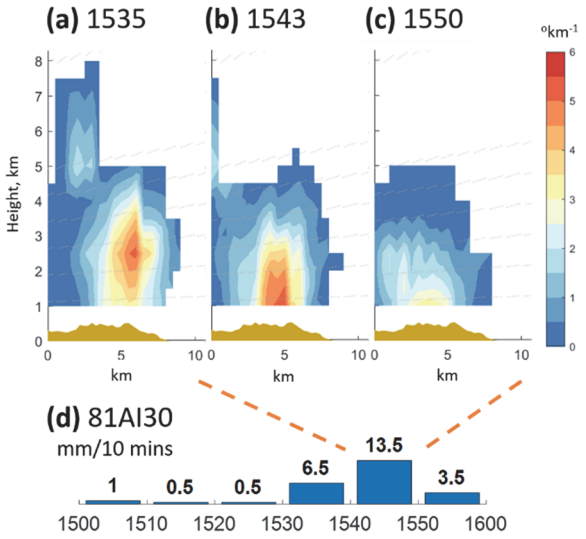

Fig. 4. The evolution of vertical K_{DP} structure over terrain and the corresponding rain gauge measurements. The local time is labeled in the subfigures.

The maximum K_{DP} was often found on the terrain (Fig. 3), and it had occurred upstream of Hubaotan as early as 16 LST. After that, the convection develops again. The precipitating outflow may spread downhill to the northeast or southeast side and converge with the environmental easterly wind component to initiate new convection. K_{DP}≧2° km^{-1} remained for 50 to 60 minutes nearby Hubaotan; in other words, there is persistent high-intensity rainfall in the watershed, consistent with the observed rainfall at the adjacent rainfall stations.

QUANTITATIVE RAINFALL ESTIMATION

For the gauge stations with the most significant hourly rainfall, the evolution of the vertical K_{DP} structure and its relationship with rain were analyzed as in Fig. 5. On the windward side of Jilin (marked No. 1 in Fig. 2), the rainfall started earlier (Fig. 5b), and the enhanced convection occurred before 1630 LST (Fig. 5a). K_{DP}≧1.5° km^{-1} reached 5 km height. In Taiping (marked No. 2 in Fig. 2) on the leeward side, the K_{DP} is weak, the development height is low (Fig. 5c), and the rainfall time is later (Fig. 5d), suggesting that the precipitation particles are advected here after the lifting of the windward side.

The relationship between K_{DP} and rain rate is listed below (Chang et al. 2021).

$$R(K_{DP}) = 35.4|K_{DP}|^{0.799}$$

The radar estimated rainfall time series corresponding to the two gauges are also quite close to the observed rainfall amount (Fig. 5b and d). The red circle in Fig. 5d indicates that the real-time data from the Taiping gauge station was delayed. By analyzing the hourly rainfall data every 10 minutes, the black circle in Fig. 5d is the revision of the observed rainfall to a correct time, which is also consistent with the radar estimated rainfall. In other words, radar data can effectively assist in identifying abnormal gauge observations.

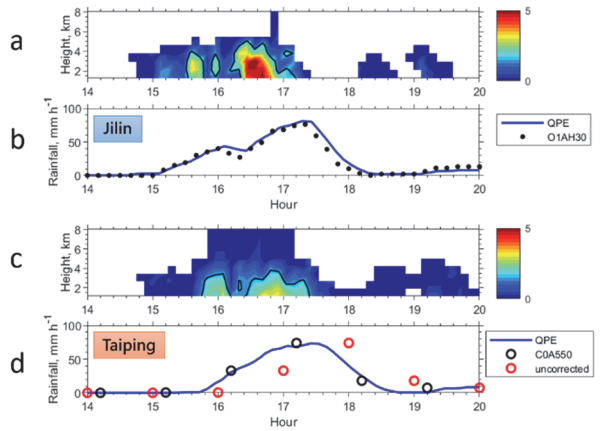

Fig. 5. The evolution of the vertical K_{DP} structure (a and c) and its relationship with rainfall (b and d). The blue line represents the radar QPE, and the black dots show the gauge measurements. The red circle in (d) is the data uncorrected time delay.

CONCLUDING REMARKS

The C-band polarimetric radar (RCSL) in northern Taiwan is used to study the flash flood case on 16 October 2021 and suggests the potential for early warning.

1. The extreme values of the specific differential phase K_{DP} (> 2° km^{-1}) can be used to identify the heavy rainfall (>60 mm h^{-1}) region's location, intensity, and movement.
2. The K_{DP} over land develops (> 1° km^{-1} above the melting layer) and causes localized heavy rainfall over the next 10 to 20 minutes.
3. The direct application of K_{DP} on quantitative precipitation estimates can effectively complement the transmission-delay problem of ground rain gauges.

The current work focuses on the analysis of low-level data below 3 km altitude. However, the enhanced K_{DP} above the melting layer appeared in summer deep convection over northern Taiwan (Jou et al. 2021). We will continue to investigate the applicability of signals above the melting level to improve early warning.

ACKNOWLEDGMENTS

The authors thank the Central Weather Bureau for providing data and ensuring data quality. National Science and Technology Council (Ministry of Science and Technology) grants 110-2625-M-002-006, 111-2625-M-002-005, and 110-2923-M-002-006 supported this research.

References

Chang, P., J. Zhang, Y. Tang, L. Tang, P. Lin, C. Langston, B. Kaney, C. Chen, and K. Howard, 2021: An Operational Multi-Radar Multi-Sensor QPE System in Taiwan. Bull. Am. Meteorol. Soc. 102(3), E555-E577.

Jou, B. J.-D., H. Uyeda, U. C.-J. Jung, R. R.-K. Hsiu, and K. S.-L. Yu, 2021: Warm Season Convective Variability in Snow Mountain Range and Heavy Rains in Taipei. The Multiscale Global Monsoon System, Ed. C P Chang et al., World Scientific Publishing, Singapore, 193–208.

Jou, B. J.-D., U. C.-J. Jung, and R. R.-G. Hsiu, 2015: Quantitative Precipitation Estimation Using S-Band Polarimetric Radars in Taiwan Meiyu Season. *Atmos. Sci.*, **43(2)**, 91–113.

Kao, Y.-C., C.-J. Jung, and B. J.-D. Jou, 2021: Application of Shulin rainfall radar real-time data in disaster prevention 2021 Conference on Weather Analysis and Forecasting, Taipei, Taiwan.

Kuster, C.M., B.R. Bowers, J.T. Carlin, T.J. Schuur, J.W. Brogden, R. Toomey, and A. Dean, 2021: Using KDP Cores as a Downburst Precursor Signature. Weather and Forecasting, 36(4), 1183–1198

SYSTEMATIC REVIEW AND ASSESSMENT OF THE IMPACT OF RAPID URBANIZATION AND URBAN HEAT ISLAND ON VULNERABLE POPULATION

D. Banerjee[1], P. Bhiwapurkar [1]

ABSTRACT: This paper reviews recent literature to synthesize the impact of rapid urbanization and the Urban Heat Island (UHI) effect on vulnerable populations in the US. Rapid urbanization characterized by expanding urban boundaries, replacement of vegetated surfaces with impervious surfaces, low tree canopy cover, and infrastructure development such as freeways complemented by former development-zoning policies have been well documented as a derivative of resource and energy inequality (or energy justice) in low-income communities who are underprepared and under-resourced while living in an aging and dilapidated housing stock. However, literature on UHI is primarily driven by energy and mitigation studies whereas vulnerability studies are driven by demographic data; thus, largely remain isolated due to the lack of an integrated interdisciplinary framework to capture the impact of UHI in vulnerable populations. Through a systematic literature review, we are enquiring, what are UHI impacts on the energy needs and overheating of the population living in aging and dilapidated housing. What resiliency frameworks exist and how does it relate to the UHI, overheating, and housing? We use ScienceDirect, Web-of-Science, Google-Scholar, and Scopus databases and limit our search to the first 200 literature written in English to do a systematic bibliometric analysis to synthesize and compare evidence from literature by using keywords "Urban Heat Island", "Energy-Burden", "Energy-Justice", "Overheating", "Vulnerability", "Resilience". Our study suggests that UHI disproportionately impacts the energy need and indoor overheating of the low-income population, and the discriminatory spatial pattern of intra-urban heat exposure strongly correlates with the built environment characteristics and historical housing policies. The impact further extends to heat-related mortality and cardiovascular diseases. The outcome of this study suggests that future investigation into UHI and its relation to the energy consumption needs to consider demographic data to synthesize the energy burden.

Keywords: Urban Heat Island, Vulnerable Population, Bibliometric Analysis, Energy Demand

INTRODUCTION

The urban heat island (UHI) effect is one of the most significant demonstrations of urban climate change due to human activities that have been well-documented in various climate literature for decades (Leal et al. 2018; Parker et al. 2021). UHI causes health, environmental, and built environment vulnerability that possesses a great threat to low-income communities that are underprepared and under-resourced during heatwaves due to lack of access to health care and dilapidated housing conditions (Lee et al. 2022). As demonstrated by existing vulnerability studies, children and the older population are most vulnerable (Park et al. 2021; Sanchez-Guevara et al. 2019). Such populations residing in poor-quality houses exacerbate heat and air pollution-related health issues (Macintyre et al. 2018). With rapid urbanization and urban sprawl, some neighborhoods experience a higher percentage of replacement of vegetated surfaces with impervious materials, low tree canopy cover, industrial land use, and proximity to the highway as a derivative of former development-zoning policies that are still evident in our built environment which further amplify racial inequalities (Tayebi et al. 2019; Barron et al. 2018). Thus, excess heat due UHI effect impacts the low-income communities that are underprepared and under-resourced while living in aging and dilapidated housing stock (Johnson et al. 2012; Diaz-Sarachaga et al. 2020).

DATA AND METHOD

We use ScienceDirect, Web-of-Science, Google-Scholar, and Scopus databases and limit our search to the first 200 literature written in English to do a systematic bibliometric analysis to synthesize and compare evidence from both primary sources (i.e., original research reports) and secondary sources (review articles) by using keywords "Urban Heat Island", "Energy-Burden", "Energy-Justice", "Overheating", "Vulnerability", "Resilience". Literature that does not focus on built environmental vulnerability or on the urban heat island effect was removed. Through Structured Query Language we have extracted information from existing literature to summarize the findings as a set of logical entities.

STUDY AREA

Through a systematic literature review study, we are enquiring about the impact of UHI on the energy needs

[1] School of Architecture and Interior Design, University of Cincinnati, Cincinnati, Ohio 45220, USA

 https://doi.org/10.1142/9789811275449_0004

and overheating of the population living in aging and dilapidated housing and what resiliency frameworks exist, and how it relates to the UHI, overheating, and housing.

RESULTS

Literature on UHI is primarily driven by energy and mitigation studies whereas vulnerability studies are driven by demographic data; thus, largely remain isolated due to the lack of an integrated interdisciplinary framework to capture the impact of UHI in vulnerable populations (Gonzalez-Trevizo et al. 2021).

Our study suggests, that UHI disproportionately impacts the energy need and indoor overheating of the low-income population (Synnefa et al., 2020; Shu et al. 2022). A study by Hoffman et al. (2020) suggests that discriminatory spatial pattern of intra-urban heat exposure has a significantly strong correlation with present-day built environment characteristics such as tree canopy cover, pervious-impervious material, and greenspace, etc., which overlaps with historical housing policies in the US, also known as redlining. Thus, present-day higher temperatures in certain neighborhoods considerably overlapped with the historically redlined group "D" neighborhoods where the demographics are often people of color or socially isolated populations with low annual income and a lack of health care service. In the United States, northern cities with higher heating degree days will experience a 2-10% heating reduction whereas southern cities with more cooling degree days will experience a 2-15% increase in cooling energy demand; thus, an approximate 10% increase in total energy demand for 4.5F of global mean surface temperature (GMST) raise (Ortiz et al. 2022; Mavrogianni et al. 2009; Li et al. 2019). Additionally, with increasing energy demand additional grid capacity will be needed in future cities (Santamouris et al. 2015). Reportedly due to a lack of income-based targeting of energy assistance programs; low-income and minority populations keep their home at a much higher temperature due to lack of access or the functional cost of operating an air conditioning system which leads to heat-related health hazards and in an extreme situation may lead to heat-related death (Samuelson et al., 2020; Williams et al. 2020). In the US heat cause more death than all other meteorological events combined (Sheridan et al. 2009).

Mitigation methods suggested by UHI studies often neglect the neighborhood-specific financial ability to implement strategies. Heat vulnerability research ignores indoor housing conditions and thus fails to account for indoor exposure and its health consequences. On a city scale, various resiliency has been studied such as increasing vegetation, adding green roofs, conservation strategies, cool pavements, building optimization, and shading structures (Alvizuri et al. 2017; Santamouris et al, 2021); however, most of these solutions are often not infeasible to implement in a developed city. Building specific resilience often neglects existing building structural stability to adapt to the proposed mitigation.

CONCLUSION

Most of the existing studies discuss energy injustice or UHI impact at a macro level but failed to capture the interrelation between indoor overheating, energy cost, and the impact of the urban heat island effect on a more granular neighborhood level. Thus, neighborhood-specific urban and building fabric impact on UHI is still not widely studied. Most of the heat resilient strategies primarily rely upon urban microclimate simulations by considering weather data, whereas very limited studies consider onsite fixed or traverse station data or do comparisons to validate simulations outcome. Thus, neighborhoods or local scale engagement in UHI mitigation or adaptation for future predicted climate models remains challenging.

References

Alvizuri, J, J Cataldo, L A Smalls-Mantey, and F A Montalto. 2017. "Green Roof Thermal Buffering: Insights Derived from Fixed and Portable Monitoring Equipment." ENERGY AND BUILDINGS 151 (September): 455–68.

Barron, Laura, Dominique Ruggieri, and Charles Branas. 2018. "Assessing Vulnerability to Heat: A Geospatial Analysis for the City of Philadelphia." URBAN SCIENCE 2 (2).

Diaz-Sarachaga, Jose Manuel, and Daniel Jato-Espino. 2020. "Analysis of Vulnerability Assessment Frameworks and Methodologies in Urban Areas." NATURAL HAZARDS 100 (1): 437–57.

Gonzalez-Trevizo, M E, K E Martinez-Torres, J F Armendariz-Lopez, M Santamouris, G Bojorquez-Morales, and A Luna-Leon. 2021. "Research Trends on Environmental, Energy and Vulnerability Impacts of Urban Heat Islands: An Overview." ENERGY AND BUILDINGS 246 (September).

Hoffman, Jeremy S., Vivek Shandas, and Nicholas Pendleton. 2020. "The Effects of Historical Housing Policies on Resident Exposure to Intra-Urban Heat: A Study of 108 US Urban Areas." Climate 8 (12): 1–15.

Johnson, Daniel P, Austin Stanforth, Vijay Lulla, and George Luber. 2012. "Developing an Applied Extreme Heat Vulnerability Index Utilizing Socioeconomic and Environmental Data." APPLIED GEOGRAPHY 35 (1–2): 23–31.

Leal Filho, Walter, Leyre Echevarria Icaza, Alice Neht, Maris Klavins, and Edward A Morgan. 2018. "Coping

with the Impacts of Urban Heat Islands. A Literature Based Study on Understanding Urban Heat Vulnerability and the Need for Resilience in Cities in a Global Climate Change Context." JOURNAL OF CLEANER PRODUCTION 171 (January): 1140–49.

Lee, Kanghyun, and Robert D Brown. 2022. "Effects of Urban Landscape and Sociodemographic Characteristics on Heat-Related Health Using Emergency Medical Service Incidents." INTERNATIONAL JOURNAL OF ENVIRONMENTAL RESEARCH AND PUBLIC HEALTH 19 (3).

Li, Xiaoma, Yuyu Zhou, Sha Yu, Gensuo Jia, Huidong Li, and Wenliang Li. 2019. "Urban Heat Island Impacts on Building Energy Consumption: A Review of Approaches and Findings." ENERGY 174 (May): 407–19.

Macintyre, H L, C Heaviside, J Taylor, R Picetti, P Symonds, X -M. Cai, and S Vardoulakis. 2018. "Assessing Urban Population Vulnerability and Environmental Risks across an Urban Area during Heatwaves - Implications for Health Protection." SCIENCE OF THE TOTAL ENVIRONMENT 610 (January): 678–90.

Mavrogianni, A, M Davies, Z Chalabi, P Wilkinson, M Kolokotroni, and J Milner. 2009. "Space Heating Demand and Heatwave Vulnerability: London Domestic Stock." BUILDING RESEARCH AND INFORMATION 37 (5–6): 583–97.

Ortiz, L, H Gamarro, J E Gonzalez, and T McPhearson. 2022. "Energy Burden and Air Conditioning Adoption in New York City under a Warming Climate." SUSTAINABLE CITIES AND SOCIETY 76 (January).

Park, Chae Yeon, James H Thorne, Shizuka Hashimoto, Dong Kun Lee, and Kiyoshi Takahashi. 2021. "Differing Spatial Patterns of the Urban Heat Exposure of Elderly Populations in Two Megacities Identifies Alternate Adaptation Strategies." SCIENCE OF THE TOTAL ENVIRONMENT 781 (August).

Parker, James. 2021. "The Leeds Urban Heat Island and Its Implications for Energy Use and Thermal Comfort." ENERGY AND BUILDINGS 235 (March).

Samuelson, H, A Baniassadi, A Lin, P Izaga González, T Brawley, and T Narula. 2020. "Housing as a Critical Determinant of Heat Vulnerability and Health." Science of the Total Environment 720.

Sanchez-Guevara, Carmen, Miguel Nunez Peiro, Jonathon Taylor, Anna Mavrogianni, and Javier Neila Gonzalez. 2019. "Assessing Population Vulnerability towards Summer Energy Poverty: Case Studies of Madrid and London." ENERGY AND BUILDINGS 190 (May): 132–43.

Santamouris, M, C Cartalis, A Synnefa, and D Kolokotsa. 2015. "On the Impact of Urban Heat Island and Global Warming on the Power Demand and Electricity Consumption of Buildings-A Review." ENERGY AND BUILDINGS 98 (SI): 119–24.

Santamouris, M, and F Fiorito. 2021. "On the Impact of Modified Urban Albedo on Ambient Temperature and Heat Related Mortality." SOLAR ENERGY 216 (March): 493–507.

Sheridan, Scott C, Adam J Kalkstein, and Laurence S Kalkstein. 2009. "Trends in Heat-Related Mortality in the United States, 1975-2004." NATURAL HAZARDS 50 (1): 145–60.

Shu, Chang, Abhishek Gaur, Liangzhu (Leon) Wang, Michal Bartko, Abdelaziz Laouadi, Lili Ji, and Michael Lacasse. 2022. "Added Value of Convection Permitting Climate Modelling in Urban Overheating Assessments." BUILDING AND ENVIRONMENT 207 (A).

Synnefa, Afroditi, Shamila Haddad, Priyadarsini Rajagopalan, and Mattheos Santamouris. 2020. "SI: Survivability under Overheating: The Impact of Regional and Global Climate Change on the Vulnerable and Low-Income Population." CLIMATE 8 (11).

Tayebi, S, H Mohammadi, A Shamsipoor, S Tayebi, S A Alavi, and S Hoseinioun. 2019. "Analysis of Land Surface Temperature Trend and Climate Resilience Challenges in Tehran." INTERNATIONAL JOURNAL OF ENVIRONMENTAL SCIENCE AND TECHNOLOGY 16 (12): 8585–94.

Williams, Augusta A, Joseph G Allen, Paul J Catalano, and John D Spengler. 2020. "The Role of Individual and Small-Area Social and Environmental Factors on Heat Vulnerability to Mortality Within and Outside of the Home in Boston, MA." CLIMATE 8 (2).

SPATIAL AND TEMPORAL DISTRIBUTION AND ANALYSIS OF HCHO CONCENTRATION BASED ON SENTINEL-5P REMOTE SENSING PRODUCTS

K. Li[1], C. Jia[1] and Y.F. Ming[1]

ABSTRACT: Recently, Volatile organic compounds (VOCs) pollution has become one of the main problems of global air pollution. HCHO is the main intermediate product of VOCs photolysis, so it is beneficial for us to better understand VOCs by mastering the distribution characteristics of HCHO and the influencing factors of its generation and attenuation. With the development of space remote sensing technology, monitoring atmospheric HCHO by satellite remote sensing has become an important detection method. Therefore, based on sentinel-5P HCHO product, this paper analyzed the spatial and temporal distribution characteristics of tropospheric HCHO concentration and its influencing factors in Shandong Province, China. The results show that the average HCHO concentration in Shandong province in 2019 and 2020 is 10.98×10^{15}molec/cm^2. In terms of time, the average HCHO concentration from large to small is as follows: Summer> Autumn> Spring> Winter, the maximum and minimum values appeared in June and December, respectively. In space, it shows a decreasing trend from west to east, and the concentration in the eastern coastal area is lower than that in the western inland area. It is found that natural sources such as temperature, and anthropogenic sources such as industrial production all affect the change of tropospheric HCHO concentration. In terms of temperature, the higher the temperature, the higher the concentration of HCHO. VOCs released by vegetation in the growth stage will cause the increase of atmospheric HCHO concentration. In terms of industrial production, incomplete combustion of biomass such as coal, and industrial waste gas released after processing and utilization of HCHO as raw materials also affect the change of tropospheric HCHO concentration to a certain extent. COVID-19 had a certain impact on HCHO concentration, and the shutdown during COVID-19 led to a downward trend in HCHO concentration in industrial intensive areas.

Keywords: Sentinel-5p satellite, Volatile organic compounds (VOCs), Formaldehyde (HCHO) column concentration, Analysis of time and space, COVID-19.

INTRODUCTION

In recent years, volatile organic compounds (VOCs) pollution has become one of the main problems of global air pollution. VOCs is a kind of organic matter with a low boiling point and relatively active chemical properties. Not only will it generate secondary organic aerosols and ozone in the process of photochemical reaction but also threaten human health and life safety. (Houweling et al. 1998). At present, as many as hundreds of VOCs have been identified, mainly from natural sources such as vegetation release and anthropogenic sources such as vehicle exhaust, industrial production, and biomass combustion, among which natural sources account for the principal part. (Zou 2013). However, direct and continuous monitoring of VOCs is challenging due to the complex composition and different physical and chemical properties of currently known VOCs species. HCHO is the main intermediate product of VOCs photolysis and has a linear relationship with the total amount of VOCs, so it is an important indicator of VOCs. Therefore, the use of remote sensing satellite data to grasp the distribution characteristics of formaldehyde and the influencing factors of its production and attenuation will help us to better understand VOCs and their spatial and temporal distribution and related characteristics, and formulate reasonable prevention and control measures for air pollutants. (Palmer 2003).

DATA SOURCES AND METHODS

Formaldehyde column concentration data

Sentinel-5p is a global air pollution monitoring satellite launched by the European Space Agency (ESA) on October 13, 2017. The satellite is fitted with TROPOMI and has an imaging width of 2600km with a temporal resolution of 7km × 3.5km on a daily scale.The data product uses Differential Optical Absorption Spectroscopy (DOAS) to fit the standard differential spectrum of formaldehyde with the measured solar irradiance and earth irradiance to get the concentration of the whole layer of the oblique column.Then through the simulated air quality factor (AMF) and combined with the atmospheric model, the concentration of the inclined

[1] School of Geomatics and Spatial Geoinformation, Shandong University of Science and Technology, 579 Huangdao District, Qingdao City, Shandong Province, CHINA

 https://doi.org/10.1142/9789811275449_0005

column was converted into the concentration of the vertical column in the troposphere. (Volkamer et al. 2005).

This paper is selected from the global tropospheric formaldehyde daily data from December 1, 2018, to April 30, 2021. The product storage format is NETCDF-4, and the overall deviation of the data is within 30%.

Data processing methods

In order to ensure the reliability of the data as much as possible, the required concentration data were screened from the HCHO concentration products. It is mainly to eliminate data outliers, such as cloud cover (RCF)>0.2. Solar zenith Angle (SZA) >70° data, as well as scan the edge of the orbit abnormal pixel values, etc. In order to facilitate analysis, use of the adjacent interpolation, the interpolation data for the spatial resolution of 0.01 ° , the monthly, seasonal and annual mean values of HCHO concentrations were calculated, to analyze the spatio-temporal distribution characteristics of HCHO in Shandong, China, and to analyze the relationship between HCHO and natural influencing factors such as temperature and human influencing factors such as industrial activities and COVID-19. The specific technical route is shown in Figure 1, which mainly includes data product acquisition, data format conversion, data reprojection, data clipping and spatio-temporal change characteristics analysis, etc. The unit of the data product is molec/m^2. For the convenience of statistics, the unit of HCHO concentration is defined as 10^{15}molec/cm^2.

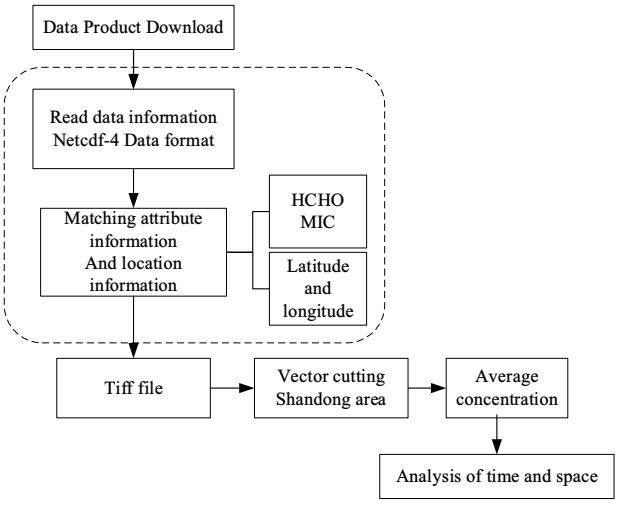

Fig. 1 HCHO concentration extraction technology

CONCLUSION AND ANALYSIS

Figure 2 shows the average HCHO concentration data distribution in Shandong, China. The results show that the average HCHO concentration in Shandong province is 10.98 × 10^{15}molec/cm^2. By analyzing its spatial distribution characteristics, it can be seen that the high concentration of HCHO in Shandong is mainly concentrated in the western region of Shandong, and the overall trend is decreasing from west to east.According to the existing data, the concentration of HCHO is related to the emission rate of isoprene, and the main source of isoprene is the release of surface vegetation. The more lush the vegetation, the faster the generation rate of HCHO. The spatial distribution of vegetation coverage and HCHO concentration in Shandong Province was consistent, that is, vegetation and crops in the west were more lush, and these organisms would release more volatile organic compounds during the growth stage, resulting in the increase of atmospheric HCHO concentration. Rapid air circulation in coastal cities, seawater can adsorb impurities, purify the air and other reasons are also one of the reasons for the low concentration of formaldehyde in the eastern region

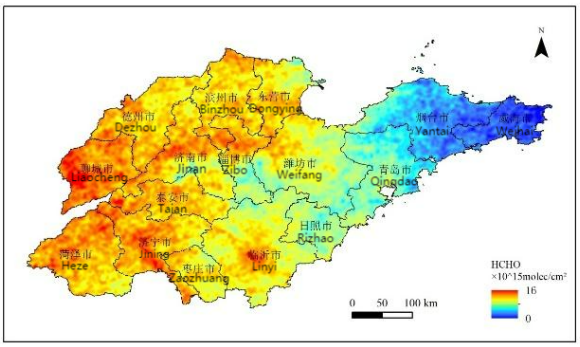

Fig. 2 Spatial distribution of mean tropospheric HCHO concentration in Shandong

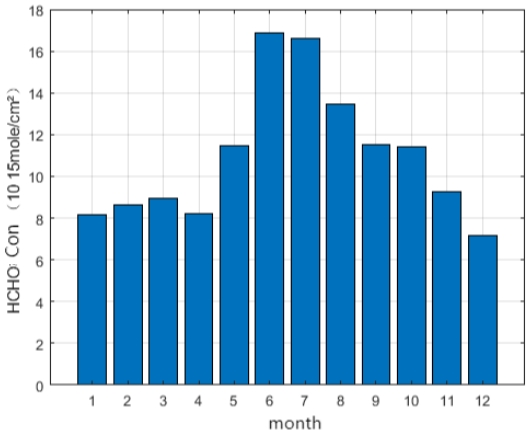

Fig. 3 Seasonal mean change of HCHO concentration

According to the monthly HCHO concentration data, the average concentration of each season was calculated (Figure 3), which was shown as: summer (15.64 × 1015molec/cm2)> Autumn (10.73 × 10^{15} molec/cm^2) > Spring (9.59 × 10^{15} molec/cm^2) > Winter (7.94 × 10^{15}molec/cm^2), with obvious seasonal characteristics. There was no significant difference between spring and

autumn, the highest concentration in summer and the lowest concentration in winter. In summer, the solar radiation is strong, the temperature and humidity are high, the photochemical reaction is strong, and HCHO has a strong emission force.

The epidemic in China emerged in early December 2019. According to the Shandong Provincial Bureau of Statistics, affected by the epidemic, most enterprises in Shandong Province stopped production from January to February, and the added value of industrial enterprises above designated size in the province decreased by 10.6%. With the basic control of the epidemic in China, the gradual lifting of prevention and control measures, and the acceleration of the resumption of work and production, a number of data have recovered compared with the previous period. In March, the year-on-year decline of added value of industrial enterprises above designated size narrowed by 12.4 percent compared with that in January and February, and industrial enterprises above designated size basically resumed work and production. As of April 21, the average operating rate and the rate of returning to work had reached 99.1 percent and 95.1 percent, respectively. The changes of HCHO concentration in Shandong Province before the epidemic (October 2019 to January 2020), during the epidemic (February to March 2020) and after the basic control of the epidemic (April to May 2020) were statistically analyzed. The mean values of HCHO concentration in the three stages were as follows: 8.41×10^{15}molec/cm^2, 7.46×10^{15}molec/cm^2, 9.85×10^{15}molec/cm^2, decreased by 11% and 24% respectively during the epidemic period compared with before and after the epidemic. Therefore, the waste gas produced by industrial activities is also one of the reasons for the increase of formaldehyde concentration.

References

Houweling, S., Dentener, F. and Lelieveld, J. (1998). The impact of nonmethane hydrocarbon compounds on tropospheric photochemistry. Journal of Geophysical Research: Atmospheres, 103(D9):10673-10696.

Zou, Y.(2013). Study on the effect of volatile organic compounds on EKMA characterizations in Guangzhou. Guangzhou, Jinan University.

Palmer, P.I.(2003). Mapping isoprene emissions over North America using formaldehyde column observations from space. Journal of Geophysical Research, 108(D6). DOI:10. 1029/ 2002JD002153.

Volkamer, R., Molina, L.T., Molina, M.J., Shirley, T., Brune, W.H. (2005). DOAS measurement of glyoxal as an indicator for fast VOC chemistry in urban air. Geophysical Research Letters, 32(8):93-114.

CHANGES IN CLIMATE EXTREMES IN HISSAR-ALLAY MOUNTAINOUS REGION, TAJIKISTAN

E.S. Brhane [1] and K. Dairaku [2]

ABSTRACT: This study attempted to examine spatio-temporal features of the present and future climate of Hissar-Allay Mountainous Region, Tajikistan. In addition, the characteristics of droughts were evaluated. For this purpose, historical data (1960-2018) from seven stations and bias-corrected future (2018-2100) projected precipitation and temperature data from RegCM4-3 based on two climate scenarios (RCP4.5 and RCP8.5) were used. Various statistical and geospatial tools, and indices were used to analyze changes, variability, and trends in precipitation and temperature. The Mann-Kendall (M-K) test and Sen's slope estimator were applied to analyze the direction and magnitude of trends. We also used the Standard Precipitation Index (SPI), to characterize drought in the basin. The results suggest a marked climate variability (moderate to high), strongly forced by the topographic feature of the area. Time-series analyses over the past 59 years show that temperatures have constantly increased at an average rate of 0.2°C-0.25°C/decade. However, only weak signals of past changes were detected for precipitation. For the future, the two climate scenarios (RCP4.5 and RCP8.5) show precipitation increasing annually, both increasing and decreasing seasonally, and temperature increasing consistently at all stations. Moreover, droughts have been intensified and frequently occurred in most parts of the region.

Keywords: M-K test, Sen's slope estimator, RCP, standard precipitation Index, Hissar-Allay Mountainous Region

INTRODUCTION

Over the past decades, climate change and variability studies have gained great attention worldwide. A better understanding of the change and variability in climate parameter is essential, especially in regions most vulnerable to climate change. As reported by the World Bank, Tajikistan is one of the Central Asian countries most vulnerable to climate change and variability (Fay et al., 2010). This study attempted to examine spatial and temporal features of historical and future climate of Hissar-Allay mountainous region, Tajikistan.

The main aim of this study was to analyze the historical and future climate conditions of Hissar-Allay mountainous region, Tajikistan. Basically, the study has the following specific objectives: assessment of the variability of climate variables (precipitation and temperature); conduct trend analysis of the climate parameter over historical and future period and evaluation of spatiotemporal characteristic of drought.

RESEARCH SITE

The study explored climate change and variability in Hissar-Allay mountainous region, Tajikistan. The geographic location of the Hissar-Allay Mountain region (Fig. 1) extends from 38°30'2"N to 40°11'48"N latitude and 67°23'53"E to 69°56'54"E longitude. The elevation of the region above mean sea level varies from 346 up to 5000+m, which causes the wide contrast of soil-climatic conditions.

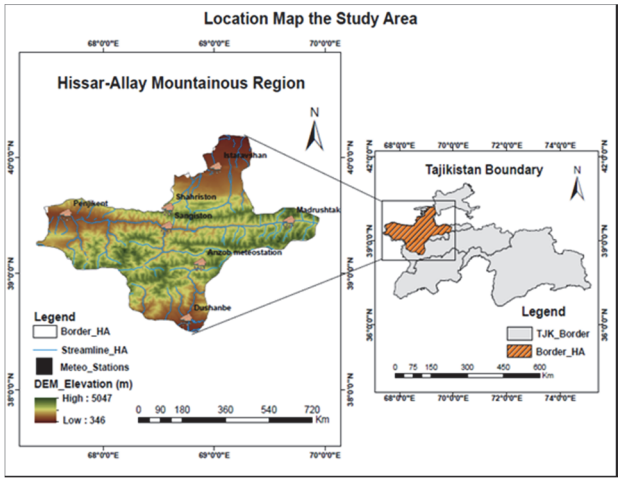

Fig. 1. Location map of the Research site

DATA AND METHODOLOGY

Data

Table 1. Summary of temporal and spatial data, including data type and their sources that are needed to implement this study.

Data Type	Period/scale	Data Sources
Observed Rainfall and temperature	1960-2018	NMSA
CORDEX-RCP climate	2015-2100	ESGF
DEM	30m by 30m	USGS

NMSA: National Meteorology Agency
ESGF: Earth System Grid Federation

[1] Degree program in System and Information Engineering, University of Tsukuba, 1-1-1 Tennodai, Tsukuba, Ibaraki 305-8577, JAPAN
[2] Graduate School of Systems and Information Engineering, University of Tsukuba, 1-1-1 Tennodai, Tsukuba, Ibaraki 305-8577, JAPAN

 https://doi.org/10.1142/9789811275449_0006

Methods

Various statistical and spatial tools, and indices (PCI and SPI) were used to display and analyze climate variability and trends in temperature and precipitation data and drought condition.

Climate variability

Climate variability analysis involves the use of descriptive statistics (i.e., Coefficient of Variation), and the Precipitation Concentration Index (PCI).

The coefficient of variation (CV) is used to categorize the degree of variability of rainfall and temperature events. Table 2 shows the categories of degree of variability according to (Hare, 2003).

$$CV = \frac{\sigma}{\mu} * 100 \quad (1)$$

Where: σ is standard deviation and μ is the mean precipitation.

Table 2. Degree of variability based on CV value

CV Value	Degree of Variability
CV<20	Less variation
20 < CV < 30	Moderate variation
CV >30	High variation
CV>40	Very high variation
CV>70	Extremely high variation

PCI, defined by (Oliver, 1980), is a powerful indicator of temporal precipitation distribution (Table 3) used to study the variability (heterogeneity pattern) of precipitation at different scales (annual or seasonal). PCI values were, calculated as given by (Oliver, 1980) and later modified by (De Luis et al., 2011) as follows:

$$PCI_{annual} = \frac{\sum_{i=1}^{12} P_i^2}{\left(\sum_{i=1}^{12} P_i\right)^2} \quad (2)$$

Where: P_i the rainfall amount of the i^{th} month.

Table 3. Temporal distribution of precipitation based on PCI value (Oliver, 1980)

PCI Value	Temporal Distribution
PCI ≤ 10	Uniform distribution
11 ≤ PCI ≤ 15	Moderate distribution
16 ≤ PCI ≤ 20	Irregular distribution
PCI > 20	Strong irregularity of distribution

Spatial distribution

Spatial variation in annual temperature and rainfall were determined using the Inverse Distance Weighted (IDW) interpolation technique using ArcGIS software.

Trend of climate change

Trend analysis of precipitation and temperature is performed using a non-parametric Mann-Kendall (M-K) test and Sen's slope estimator to determine the direction and magnitude of trend, respectively.

Drought analysis

The Standardized Precipitation Index (SPI) (McKee et al., 1993), was used to characterize the drought events. The drought indices for 6- and 12-month time scales (SPI-6 and SPI-12) were selected for examining the drought characteristics. A drought event occurred when the drought index (SPI) values were less than -1.0 (Table 4).

Table 4. Classification of drought based on SPI value (McKee et al., 1993)

SPI Value	Drought Category
2,0+	Extremely wet
1.5 to 1.99	Very wet
1.0 to 1.49	Moderately wet
−0.99 to 0.99	Near normal
−1.0 to −1.49	Moderately dry
−1.5 to −1.99	Severely dry
−2 and less	Extremely dry

Climate projection

The future climate projections were obtained from RCM model output (RegCM4-3) derived from MPI-M-MPI-ESM-LR (GCM) based on Coupled Model Intercomparison Project (CMIP5) driven by RCP scenarios RCP4.5 (medium) and RCP8.5 (high) emission scenario. The bias-correction of simulated RCM data of precipitation and temperature was carried out using linear-scaling approach.

RESULT AND DISCUSSION

The results from precipitation concentration index (PCI) reveals that about 79.8% and 20.2% of annual precipitation had moderate concentration and high irregularity of precipitation distribution respectively (Fig. 2). The results indicate that a pronounced variability (moderate to very high) strongly forced by the topographic feature of the area.

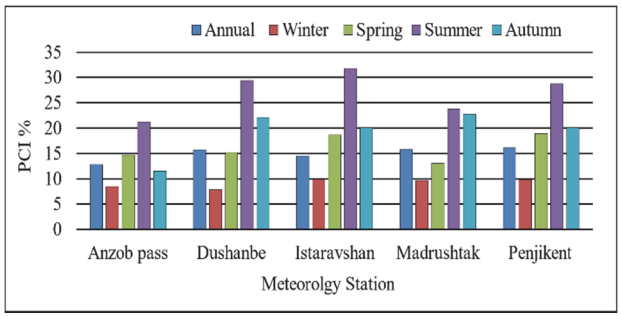

Fig. 2. Mean PCI % value of annual and seasonal rainfall for each station in study area (1960-2018)

The analysis of spatial distribution (Fig. 3) shows the strong influence of topography on Tajikistan's climate with mean annual air temperatures to vary from -3.5^{0}C (mountain regions) to 20.5^{0}C (lowlands). Similarly, mean annual precipitation varies from less than 200mm to over 700 mm, with spring being the wettest seasons

Time-series analyses over the past 59 years indicate that temperatures have constantly increased with an average rate of 0.2°C-0.25°C/decade (Fig. 4). However, precipitation, only weak signals of past changes could be noticed (Fig. 4).

In the future, the two climate scenarios (RCP4.5 and RCP8.5) showed that precipitation projection will increases annually, and both increasing and decreasing trends seasonally, similarly projected temperature consistently increases at all station.

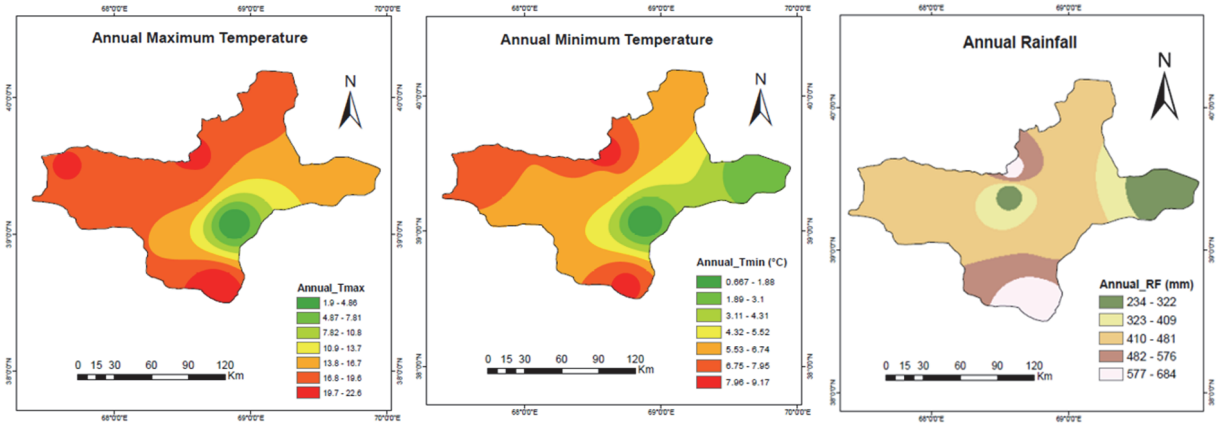

Fig. 3. Spatial distribution of annual precipitation and temperature (minimum and maximum)

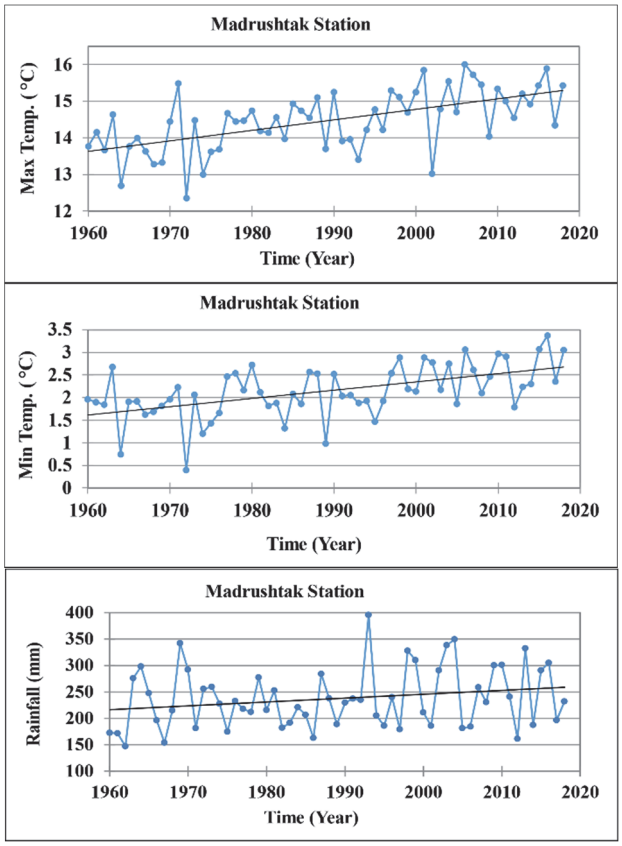

Fig. 4. Trend analysis of rainfall and temperature (maximum and minimum)

Based on the result of the analysis, droughts have been intensifying and frequently occurred in most parts of the basin in different years (Fig. 5).

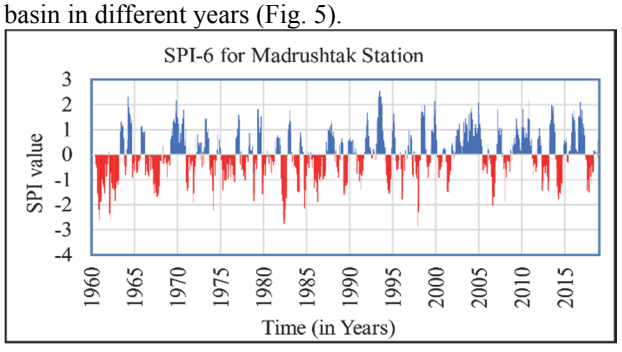

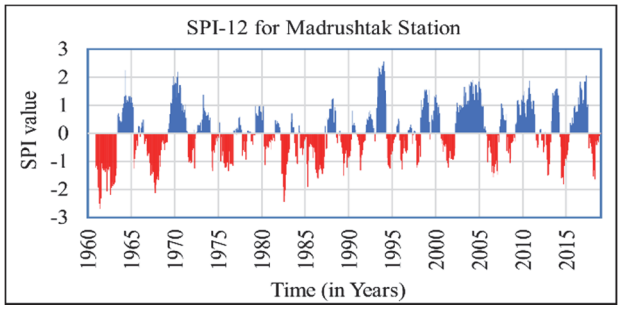

Fig. 5. Six-monthly and 12-monthly SPI values for the period 1960–2018 in selected weather stations.

CONCLUSION

In this study, an attempt was made to investigate the spatio-temporal characteristics of the present and future climate in our study site. In addition, the characteristics of drought were evaluated. The study confirmed that the climate model used in the study indicate that there will be radical/drastic changes, especially in temperature conditions due to climate change. In addition, precipitation in the future shows both an increasing and decreasing trend and shows moderate to high variability and irregularity in the study area. This change in climatic conditions will strongly affect the different sectors of the region/study area and at the country level in general.

References

De Luis, M., Gonzalez-Hidalgo, J.C., Brunetti, M. and Longares, L.A. (2011). Precipitation concentration changes in Spain 1946–2005. Nat. Hazards Earth Syst. Sci. 11,1259–1265.

Fay, M., Block, R.I. and Ebinger, J. (2010). Adapting to Climate Change in Eastern Europe and Central Asia, Vol. 52862. World Bank Group,180.

Hare, W. (2003). Assessment of Knowledge on Impacts of Climate Change, Contribution to the Specification of Art, 2 of the UNFCCC. WBGU.

McKee, T.B., Doesken, N.J. and Kleist, J. (1993). The relationship of drought frequency and duration to time scales. AMS 8th Conference on Applied Climatology, (January), 179–184.

Oliver, J.E. (1980). Monthly precipitation distribution: a comparative index. The Professional Geographer. 1980; 32(3):300–309.

IMPACT OF CLIMATE CHANGE ON STREAMFLOW USING A REGIONAL CLIMATE MODEL (CASE STUDY IN RIBB WATERSHED, LAKE TANA SUB-BASIN, ETHIOPIA)

E.S. Brhane[1] and K. Dairaku[2]

ABSTRACT: This study investigates the impacts of climate change on streamflow of the Ribb River watershed using the SWAT model and a Regional Climate Model (RCM). Regional climate scenario projected by the CORDEX RCM (RCA4) with the horizontal grid spacings of ~50km was used to estimate historical (1979-2015) and future (2020-2100) climate under RCP4.5 and RCP8.5 scenarios. The projected climate variables were bias-corrected using a linear-scaling approach. Trends of the projected climate variables were checked by the M-K trend analysis. The variables showed an increasing trend for monthly maximum and minimum temperatures compared to the reference period for both RCP scenarios. However, there was no systematic increasing and decreasing trend of precipitation over the century. Annual precipitation, long rainy and dry seasons showed an increasing trend, while short rainy seasons showed a decreasing trend under both RCPs. The SWAT model was applied to evaluate the impacts of future climate change on hydrology and water resources. The performance of the model was evaluated through calibration and validation process using observed streamflow data over the period (1979-2012). The SWAT model performed well with reasonable accuracy (R2>0.7). The projected streamflow showed an increasing trend except for the 2080s in the RCP8.5 scenario, and its magnitude varied up to 58-66% in dry and 21-55% in rainy season for each RCP scenario compared to the reference period. Increases in seasonal and annual streamflow were mainly associated with increases in the projected precipitation.

Keywords: Mann-Kendal test, Regional Climate Model (RCM), CORDEX, Ribb watershed, RCA4

INTRODUCTION

The planet earth is undergoing global climate change. This change in climate causes significant impacts on water resource by disturbing the normal hydrological processes. The IPCC findings indicate that developing countries, like Ethiopia, will be more vulnerable to climate change and variability due to their over-reliance on agriculture, which is highly sensitive to climate change (IPCC, 2007). The Blue Nile Basin is one of the largest and most water-rich basins in the country, with high population pressure, and heavy dependence on the agricultural economy. UNEP (2013) has designated the basin as a climatic and hydrological disaster hotspot. Our study area (i.e., Ribb watershed) is a part of Blue Nile basin, where multi-purpose water resources development projects are currently being proposed and constructed. Therefore, it is critical to determine hydrological responses to climate change for sustainability of projects and looking for possible mitigation measures.

This study investigates the impacts of climate change on streamflow of the Ribb River watershed using hydrological model SWAT and a Regional Climate Model (RCM). The specific question addressed in this study is how future climate change scenarios will affect the hydrologic components (streamflow and evapotranspiration) and consequently the magnitude and variability of river flows. Answering this question is of direct relevance to the ongoing debate on the concept of stationarity in the context of water infrastructure design. Moreover, it is extremely relevant to the improvement of water resources management and development plan in the watershed.

DESCRIPTION OF RESEARCH SITE

Ribb watershed is the part of the Lake Tana sub-basin in Blue Nile Basin, Ethiopia (Fig. 1). The geographical location of the watershed is 11°40' to 12°20' N latitude and 37°30' to 38°20' E longitude. It covers the total area of 1,975 km^2 including ungauged areas. However, the present study was carried out in the gauged area of the watershed, which covers an area of 1,539.1 km^2.

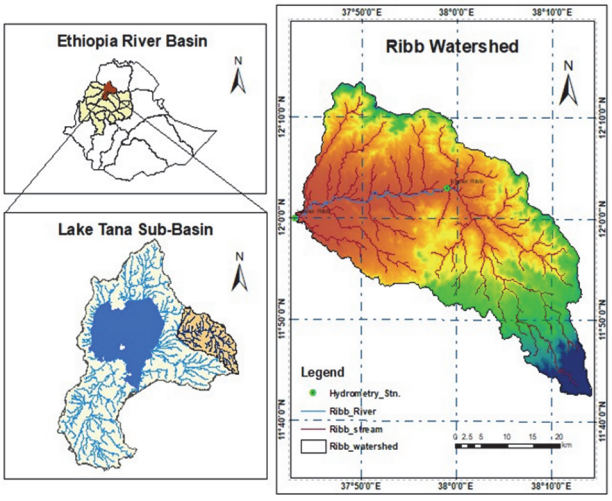

Fig. 1. Location map of the study area (Ribb watershed)

[1] Degree program in System and Information Engineering, University of Tsukuba, 1-1-1 Tennodai, Tsukuba, Ibaraki 305-8577, JAPAN
[2] Graduate School of Systems and Information Engineering, University of Tsukuba, 1-1-1 Tennodai, Tsukuba, Ibaraki 305-8577, JAPAN

 https://doi.org/10.1142/9789811275449_0007

DATA AND METHODOLOGY

Methodology: This study is organized into four categories:

1. Projection of climate variables by RCM based on the two representative concentration pathways (RCP) scenarios (RCP4.5 and RCP8.5).
2. Bias correction of the climate variables to local scale meteorological variables using a linear scaling approach.
3. Hydrologic modelling using the SWAT model (Arnold et al., 2012)
4. Analyze of the impact of climate change on hydrological components (streamflow and evapotranspiration)

The methodological framework of the study is schematically illustrated in Fig. 2.

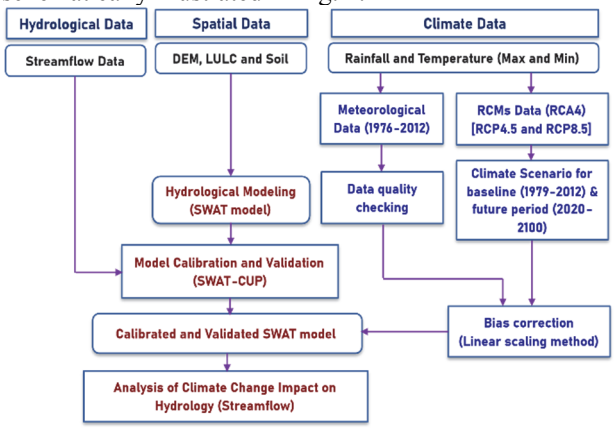

Fig. 2. Study framework for assessment of climate change impacts on future streamflow

Hydrological Model Using SWAT Model

For hydrological modeling, we used ArcSWAT 2012, a GIS-based version that is freely available on the SWAT website (https://swat.tamu.edu/). The SWAT model is a process-based continuous hydrological model that can be used to assess the impacts of climate change on streamflow (Arnold et al., 2012).

The spatial and temporal data (Table 1) required to simulate the SWAT model includes DEM data, LULC data, soil data, and climate data (measured and simulated). In addition, streamflow (river discharge) data were used for calibration and validation.

Table 1. Summary of SWAT model input data, including source, and description of data.

Data Type	Sources	Scale/Period
DEM	SRTM	30m*30m
LULC	Landsat-8 image	30m*30m
Soil Data	FAO soil map	1/25000
Climate data (observed)	ENMA (from six meteorology stations)	1976-2012
Climate data (simulated)	CORDEX-RCM	1979-2100
Streamflow data	MoWIE (from lower Ribb gauged station)	1979-2012

ENMA: Ethiopia national Meteorology Agency
MoWIE: Minister of Water, Irrigation and Energy

Climate Modelling and Bias Correction

In this study, simulated outputs from the regional climate model (RCA4) from CORDEX-Africa for baseline (1979-2012) and future (2011-2100) periods were used. The Rossby Center Regional Climate Models version-4 (RCA4) was originally developed by the Swedish Meteorological and Hydrological Institute (SMHI) as a part of the CORDEX initiative (Samuelsson et al., 2015). Representative Concentration Pathways: RCP4.5 mid-range and RCP8.5 high-level were adopted. Climate scenarios were used for three future periods: 2020s (2011-2039), 2050s (2040-2069) and 2080s (2070-2099).

Although the RCM data (daily precipitation and temperature) has finer horizontal grid spacing but it is still required further bias correction by specific nearest meteorological stations data. The linear-scaling approach (Teutschbein and Seibert, 2012) was adopted for its suitability and simplicity.

RESULT AND DISCUSSION

The performance of the SWAT model was evaluated through a calibration and validation process using observed streamflow data over a period of 1979-2012 (Sisay et al., 2017). The SWAT model performed well for our study area with reasonable accuracy as shown in Table 2 both Nash-Sutcliffe Efficiency (NSE) and coefficient of determination (R^2) > 0.7 and the Percent Bias (PBIAS) within the specified range ±15 (Moriasi et al., 2007) for both the calibration and validation periods (1979-2012 and 2002-2012).

Table 2. Summary of model performance criteria for calibration and validation

Period	Year	Evaluation of statistics of parameters		
		R2	NSE	PBIAS
Calibration	1979-2001	0.75	0.8	4.5
Validation	2002-2012	0.79	0.73	5.3

For two future periods (2020s and 2050s), both climate scenarios resulted in a moderate increase in mean annual streamflow, which is due to projected increased in precipitation (Fig. 3). However, the RCP8.5 climate scenario showed a slight decrease in streamflow in the 2080s due to larger increase in projected temperature which leads to an increase in evapotranspiration (Fig. 4) in Belg (short rainy season) rather than an increase in precipitation.

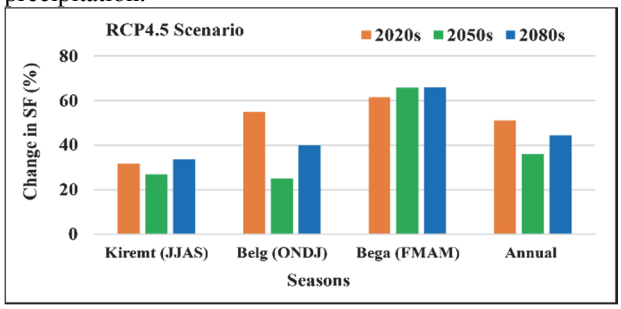

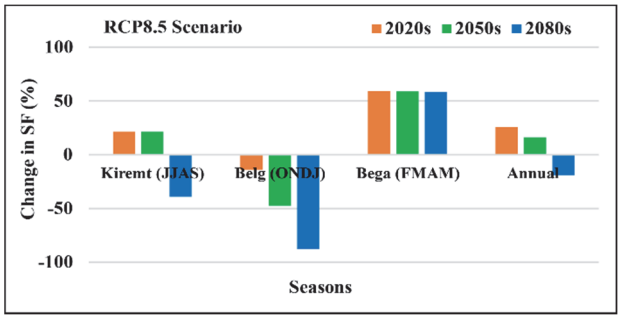

Fig. 3. Projected percentage change in seasonal and annual streamflow (SF) over the Ribb watershed

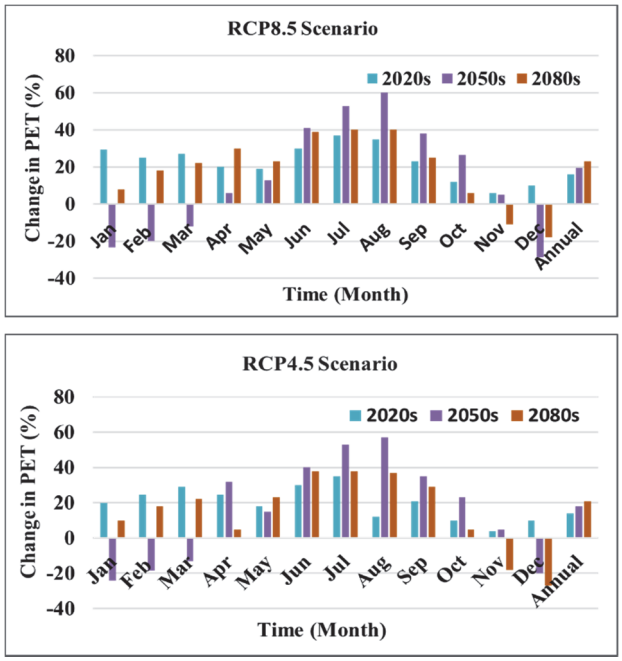

Fig. 4. Percentage change in monthly and annual potential evapotranspiration (PET) with respect to the baseline period.

CONCLUSION

This study aimed to evaluate the impact of climate change on hydrology and water resources of the Ribb River watershed. The SWAT model was well able to simulate the hydrological processes in the Ribb watershed. The future annual discharge, surface runoff and evapotranspiration in the watershed were projected to increase in both RCP4.5 and RCP8.5 scenarios except for the 2080s RCP8.5 scenario. To meet with water resource development and investigate the robustness of the results, further research on future water stress is required by considering multi-model ensemble climate scenarios and socio-economic changes (land use/land cover change).

References

Arnold, J.G., Kiniry, J.R., Srinivasan, R., Williams, J.R., Haney, E.B. and Neitsch, S.L. (2012). SWAT input/output documentation version 2012 at http://swat.tamu.edu/media/69296/SWATIO-Documentation-2012.pdf

IPCC (2007). Climate Change 2007: Synthesis Report. Contribution of Working Groups I, II and III to the Fourth Assessment Report of the Intergovernmental Panel on Climate Change [Core Writing Team, Pachauri, R.K and Reisinger, A. (eds.)]. IPCC, Geneva, Switzerland, 104 pp.

Moriasi, D.N., Arnold, J.G., Van Liew, M.W., Binger, R.L., Harmel, R.D. and Veith, T.L. (2007). Model evaluation guidelines for systematic quantification of accuracy in watershed simulations. *Transactions of ASABE 50:885-900.*

Samuelsson, P., Gollvik, S., Kupiainen, M., Kourzeneva, E. and Van de Berg, W.J. (2015). The Surface Processes of the Rossby Centre Regional Atmospheric Climate Model (RCA4); SMHI: Norrköping, Sweden, 2015.

Sisay, E., Halefom, A., Khare, D., Singh, L. and Worku, T. (2017). Hydrological modelling of ungauged urban watershed using SWAT model. *Modeling Earth Systems and Environment*, *3*(2), pp.693-702.

Teutschbein, C.A. and J. Seibert (2012). Bias correction of regional climate model simulations for hydrological climate-change impact studies: Review and evaluation of different methods. *Journal of Hydrology (456-457): 12-29.*

IDENTIFYING THE MAIN VARIABLES TO CLASSIFYING THE SYNOPTIC PATTERNS OF ASIAN DUST STORM OVER SOUTH KOREA BY PRINCIPAL COMPONENT ANALYSIS (PCA)

Seungyeon Lee[1,3], Xiaohao Qin[2], Jiwon Yoon[3,4], Sujung Lim[3,4], Ebony Lee[1,3], and Seon Ki Park[1,3,4]

ABSTRACT: In air quality prediction, it is essential to find the upstream areas from which a small initial error can grow into large forecast errors in the region of interest. The conditional nonlinear optimal perturbation for initial conditions (CNOP-I) is a suitable tool for targeted (adaptive) observations. To calculate the CNOP-I several variables are included; those are used from the multiple energy equations (eg. kinetic energy, dry energy, moist energy, etc). In particular, the previous studies on improving the Asian dust storms (ADSs) prediction mainly considered the kinetic energy calculation, which included only two variables (u-wind and v-wind). However, variables affecting the actual ADS's development and movement also include the other variables. This study aims to identify the main variables and classify the synoptic patterns for given ADS cases using the principal component analysis (PCA). We focus on the ADS events that occurred during the last 32 years (1990—2021) over South Korea. Through the PCA, we identified the top five variables — temperature, specific humidity, divergence, ozone mass mixing ratio, and eastward wind — which affect origination and translocation of the ADSs. Furthermore, the ADSs are significantly affected by vertical velocity, divergence, relative humidity, eastward wind, and potential vorticity; for example, strong downdraft and divergence make ADSs finally land on the Korean Peninsula. For a further study, we plan to identify the sensitive areas in targeted observations for air quality prediction via CNOP-I. We expect to improve air quality forecasts by classifying the synoptic situations that bring about severe Asian dust storm outbreaks in South Korea and by identifying the upstream areas for targeted observations to which we can enhance observations, potentially through international collaborations.

Keywords: Asian dust storms, South Korea, Principal component analysis, Classification.

INTRODUCTION

In air quality prediction, initial conditions, based on both atmospheric and aerosol/chemistry observations, are essentially required for a coupled atmosphere-chemistry model (Sukhodolov et al., 2020). In general, we have more accurate model results with a higher amount and quality of observations; however, forecast errors in a region of interest may grow from an initial error in a specific upstream region, mostly due to the lack of observations therein (Tastu et al., 2011). Therefore, to improve air quality prediction, finding the upstream areas from which a small initial error can grow into large forecast errors in the region of interest is essential. The conditional nonlinear optimal perturbation for initial conditions (CNOP-I) represents the initial error that can lead to the largest error at the forecast time, which enables us to identify the sensitive regions as an enormous initial error value (Mu et al., 2003). Thus, CNOP-I is a suitable tool for targeted (adaptive) observations (Park and Zupanski, 2022).

To calculate the CNOP-I, several variables are included: those are used from the multiple energy equations (eg. kinetic energy, dry energy, moist energy, etc). In particular, the previous studies on improving the Asian dust storms (ADSs) prediction mainly considered the kinetic energy calculation, which included two variables (u-wind and v-wind) (Mu et al., 2009). However, variables affecting the actual ADS's development and movement also include the other variables.

This study aims to identify the main variables and classify the synoptic patterns for given ADS cases using the principal component analysis (PCA).

METHODOLOGY AND DATA

Methodology

A PCA is beneficial for reducing the dimensions of nonlinear meteorological variables and classifying meteorological phenomena. We use the T-mode PCA, which is time series orthogonal in the temporal domain; in this case, the covariance, correlation, or cross-product matrix is computed relating the series of data recorded in the N observations. The eigenvectors are orthonormal time series, and the principal components are the projection of the time series recorded at the M stations on the eigenvectors, which transforms the variables into new variables (new coordinates) using a linear combination that includes the existing variables. Among all the eigenvector values, the eigenvalue having the enormous eigenvector value is the main component that forms a

[1] Department of Climate and Energy System Engineering, Ewha Womans University, 52, Ewhayeodae-gil, Seodaemun-gu, Seoul, 03760, REPUBLIC OF KOREA
[2] Institute of Atmospheric Physics, Chinese Academy of Sciences, CHINA
[3] Severe Storm Research Center, Ewha Womans University, Seoul, REPUBLIC OF KOREA
[4] Center for Climate/Environment Change Prediction Research, Ewha Womans University, REPUBLIC OF KOREA

 https://doi.org/10.1142/9789811275449_0008

linear combination. Selecting only these principal components (PCs) implies a dimensional reduction.

Each PC axes has a score, which means the explanation ability for each place and represents an orthogonal pattern in the spatial domain

Data

We selected some ADS cases from the report provided by the Korean Meteorological Administration (KMA) from 1990 to 2021 (a total of 32 years) (Kim et al., 2020).

After the events collection, we used the fifth generation ECMWF atmospheric reanalysis of the global climate (ERA5) hourly grid data on pressure levels (Hersbach 2018) to find the main variables by PCA. The horizontal resolution of the data is 0.25°×0.25°, and the vertical resolution is 37 pressure levels from 1000 hPa to 1 hPa. This reanalysis data set has 16 variables: divergence (d), fraction of cloud cover (cc), geopotential height (z), ozone mass mixing ratio (O_3), potential vorticity (pv), relative humidity (r), specific cloud ice water content (ciwc), specific cloud liquid water content (clwc), specific humidity (q), specific cloud rain water content (crwc), specific cloud snow water content (cswc), temperature (T), U-component of wind (u), V-component of wind (v), vertical velocity (w) and relative vorticity (vo).

Among these variables, we select the principal components (main variables) by using PCA.

RESULTS

Through the PCA, the percentage of explained variances using 16 PC axes explains almost 80% of the ADS cases in South Korea.

The main variables rank from 1 to 16. The first time step is 48 hours before ADSs happened; the top five variables are temperature, specific humidity, divergence, Ozone mass mixing ratio, and eastward wind (Table 1). Surface heating and convergence (d) make strong updraft and eastward wind makes ADSs start above the Gobi desert.

The five variables 24 hours before are temperature, specific humidity, divergence, ozone mass mixing ratio, and eastward wind, which affect the ADSs' carrying (moving) (Table 1). And is the variables are almost the same as thoses 48 hours before. Continuous surface heating makes strong convergence (d), keeping the sand dust particles floating; the eastward wind makes ADS move to the Korean Peninsula.

Table 2 represents the main variables for the first ADSs observed in South Korea. The top 5 variables, affecting the ADS over the Korean Peninsula, are vertical velocity, divergence, relative humidity, eastward wind, and potential vorticity. Especially, strong downdraft and divergence make ADS land on the Korean peninsula.

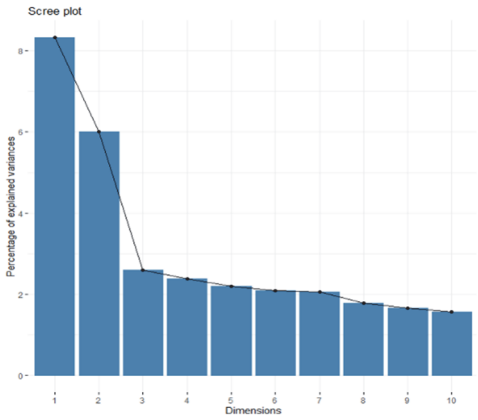

Fig. 1 The percentage of explained variances for each principal component dimension (PC axes).

Table 1 The main variables affecting the ADS cases for 48 hours and 24 hours before ADSs happened.

Variables for affecting cluster the ADS cases: 48 hours & 24 hours before		
#	Variables	Coefficient
1	**Temperature (T)**	10.13
2	**Specific humidity (q)**	9.59
3	**Divergence (d)**	7.95
4	**Ozone mass mixing ratio (O_3)**	7.83
5	**U-component (eastward) wind (u)**	7.44
6	Vertical velocity (w)	7.38
7	Relative vorticity (vo)	6.71
8	Relative humidity (r)	6.46
9	Potential vorticity (pv)	6.07
10	Geopotential (z)	5.93
⋮	⋮	⋮

Table 2 The main variables affecting the ADS cases' cluster for the first observed ADSs.

Variables for affecting cluster the ADS cases: The first observed time		
#	Variables	Coefficient
1	**Vertical velocity (w)**	10.56
2	**Divergence (d)**	10.19
3	**Relative humidity (r)**	9.90
4	**Eastward wind (u)**	9.67
5	**Potential vorticity (pv)**	9.51
6	Relative vorticity (vo)	9.27
7	Geopotential (z)	8.47
8	Specific cloud liquid water content (clwc)	7.12
9	Specific cloud ice water content (ciwc)	6.94
10	Fraction of cloud cover (cc)	6.78
⋮	⋮	⋮

CONCLUSION

We investigated the main variables, which affect the development and translocation of the ADSs that happened in South Korea using the PCA method. For the development and movement stages, the leading five variables are temperature, specific humidity, divergence, ozone mass mixing ratio, and eastward wind. Surface heating and convergence (divergence) make strong updraft and eastward wind which develop the ADS above the Gobi Desert and keep the dust particles floating. In addition, at the first observed moments over the Korean Peninsula, the leading five variables are vertical velocity, divergence, relative humidity, eastward wind, and potential vorticity. Primarily, strong downdraft (vertical velocity) and divergence make ADS finally land on South Korea.

For a further study, we plan to identify the sensitive areas in targeted observations for air quality prediction via CNOP-I. We expect to improve air quality forecasts by classifying the synoptic situations that bring about severe Asian dust storm outbreaks in South Korea and by identifying the upstream areas for targeted observations to which we can enhance observations, potentially through international collaborations.

ACKNOWLEDGEMENTS

This research is supported by the NRF grant funded by the Korea government (MSIT) (NRF-2021R1A2C1095535). It is partly supported under the grant of Basic Science Research Program through the National Research Foundation of Korea (NRF) funded by the Ministry of Education (2018R1A6A1A08025520).

References

Hersbach, H., Bell, B., Berrisford, P., Biavati, G., Horányi, A., Muñoz Sabater, J., Nicolas, J., Peubey, C., Radu, R., Rozum, I., Schepers, D., Simmons, A., Soci, C., Dee, D., and Thépaut, J.-N (2018). ERA5 hourly data on single levels from 1979 to present. Copernicus Climate Change Service (C3S) Climate Data Store (CDS). Available from https://cds.climate.copernicus.eu/cdsapp#!/dataset/reanalysis-era5-single-levels.

Kim, Y. H., Jeong, J. Y., Kim, J. E., Yoo, H. J., Ko, H. J., Ko, M. Y., Jeong, J. Y. and Ahn, H. G. (2020). Report of Asian dust storms in 2020: Jeju, South Korea. National Institute of Meteorological Sciences. (in Korean)

Mu M., Duan W. S., and Wang B. (2003). Conditional nonlinear optimal perturbation and its applications. Nonlin. Processes Geophys., 10, 493-501.

Mu M., Zhou F., and Wang H. (2009). A method for identifying the sensitive areas in targeted observations for tropical cyclone prediction: Conditional nonlinear optimal perturbation. Mon. Wea. Rev., 137, 1623-1639.

Park, S. K., and Zupanski, M. (2022) *Principles of Data Assimilation*. Cambridge University Press, New York, 400 pp.

Sukhodolov, T., Egorova, T., Stenke, A., Ball, W. T., Brodowsky, C., Chiodo, G., and Rozanov, E. (2021). Atmosphere–ocean–aerosol–chemistry–climate model SOCOLv4. 0: description and evaluation. Geosci. Model Develop., 14(9), 5525-5560.

Tastu, J., Pinson, P., Kotwa, E., Madsen, H., and Nielsen, H. A. (2011). Spatio-temporal analysis and modeling of short-term wind power forecast errors. Wind Energy, 14(1), 43-60.

PROBABILISTIC EXTREME TEMPERATURE FORECASTS USING THE BAYESIAN PROCESSOR OF ENSEMBLE OVER TAIWAN

Hsin-Yu Chu[1], Yun-Jing Chen[1], Zoltan Toth[2] and Hui-Ling Chang[1]

ABSTRACT: A statistical post-processing (SPP) system called Bayesian Processor of Ensemble (BPE) is demonstrated in this study for the generation of extended-range probabilistic extreme temperature forecasts at selected weather stations in Taiwan. BPE is based on the Bayes' Theorem, and comprises three main components: (1) the estimation of the prior, the climatic distribution of the predictand; (2) the generation of the likelihood distribution, capturing the relationship between the predictors and predictand, and (3) the fusion of the prior and likelihood distributions for the generation of the predictive (or posterior) distribution, given the latest operational ensemble forecasts. The Bayesian use of the prior distribution allows BPE to optimally calibrate, with a maximum level of informativeness, the predictive distribution, even under operational constraints such as limitations in the size of the reforecast data sample, and low skill in raw extended-range ensemble forecasts.

Keywords: Probabilistic Forecasts, Statistical Post-processing, Bayesian Processor of Ensemble, Extreme Temperature, Climatic Prior.

INTRODUCTION

In recent years, demand for detailed, site specific extended range forecasts in agricultural, energy, and hydrological sector out to sub-seasonal time scales has increased. Current operational practices, however, cannot meet such demands. First, the generation and storage of large reforecast data used to calibrate forecasts are time and resource intensive. Typical annual updates cycle to operational numerical weather prediction model would require retraining the SPP system every time the NWP model is updated. Unfortunately, often only a short joint sample of model-observation pairs are available at the time, negatively affecting forecast quality with conventional SPP methods. Second, by using only a small set of forecast-observation pairs, most regression methods leave much of the observational data (i.e., observational climatology) unused. And third, the skill of raw ensemble output interpolated to observation sites is often lower than that of climatology at extended lead-times. To ameliorate these limitations, a fully Bayesian method, the Bayesian Processor of Ensemble (BPE, Krzysztofowicz and Evans, 2008) is tested for the generation of probabilistic forecasts.

METHODOLOGY

In this study, two statistical post-processing methods, Ensemble Kernel Density Model Output Statistics (EKDMOS) and Bayesian Processor of Ensemble (BPE) are used to post-process raw ensemble forecasts to be valid at 29 manned meteorological stations in Taiwan, generating probability forecasts for weekly extreme temperature up to 4 weeks. The performance of these forecasts from these two systems are then compared using various probabilistic verification metrics.

Ensemble Kernel Density Model Output Statistics (EKDMOS)

Bias from the raw ensemble mean (predictor) is first removed by regressing against the predictand. Next, the distribution of error in the calibrated ensemble mean forecast is estimated using a validation set. The forecast error distribution is then used as a 'Kernel' to dress the bias-corrected ensemble members, after which post-processed probabilistic distributions are formed using equal weights on each forecast member (Fig. 1).

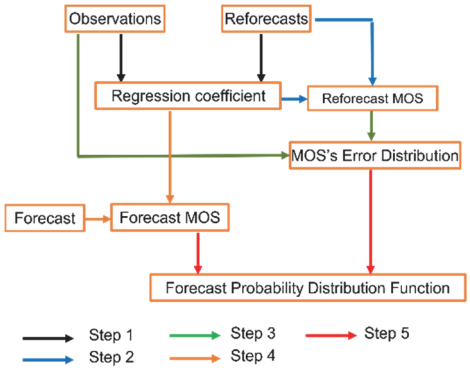

Fig. 1. The algorithm of EKDMOS as currently used at Central Weather Bureau(CWB).

[1] Central Weather Bureau, Taipei, TAIWAN
[2] Global Systems Laboratory, National Oceanic and Atmospheric Administration, Boulder, CO, USA

 https://doi.org/10.1142/9789811275449_0009

Bayesian Processor of Ensemble (BPE)

BPE is a theoretically based, fully Bayesian algorithm for the generation of calibrated, most informative posterior probabilistic guidance. Starting with the latest operational forecast, BPE fuses the likelihood function and prior distribution to generate a posterior predictive distribution. The moments of the likelihood distribution are inferred from a smaller set of predictor-predictand pairs, while the prior distribution is constructed using each location's longer climatological predictand data. For further details, see Fig. 2.

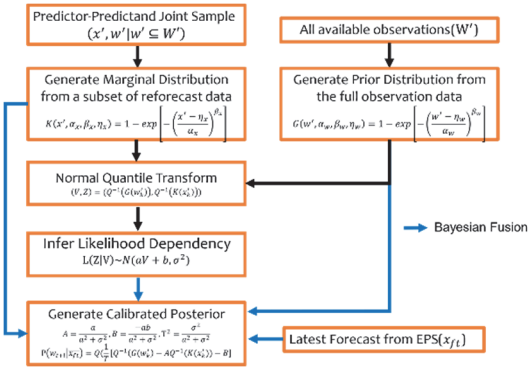

Fig. 2. The algorithm of BPE currently used at CWB. Arrow in blue indicate steps that involves Bayesian Fusion.

Data and Experiments

We use the reforecast of NCEP-GEFSv12 as the raw model to generate the post-processed forecasts. The data cover 20 years, with forecasts available once a week, at a 6-hourly interval. For each member, the 6-hourly data between 354-516 and 522-684 hours lead times (accounting for time zone) are used to find the coldest and warmest temperature in week 3 and week 4, respectively. Next, the mean of the ensemble members are calculated and used as the predictor. The predictand is the ground truth collected from the 29 manned observation stations in Taiwan.

From the available 20 years of reforecast, we use longer/shorter training samples to simulate the effect of operational limitations in the size of the data. A total of four experiments are conducted, each with a certain length of training sample. The description of the experiments are shown in Table 1.

RESULTS

Continuous Ranked Probability Skill Score (CRPSS)

Continuous Ranked Probability Score (CRPS) is a mean absolute error type measure of the error in the continuous probability distribution relative to the ground truth:

$$\mathrm{CRPS} \equiv \int_{-\infty}^{\infty} [F(y) - F_o(y)]^2 dy$$

Where $F(y)$ is the cumulative distribution function and $F_o(y)$ is the unit step function from observations, with a binary switch set at the value of ground truth.

CRPSS is a probabilistic verification skill metric that evaluates one system's CRPS relative to a baseline, in this study the climatology, ranging between $(-\infty, 1]$:

$$CRPSS \equiv 1 - \frac{\overline{CRPS_{forecast}}}{\overline{CRPS_{baseline}}},$$

Where unity indicates perfect skill.

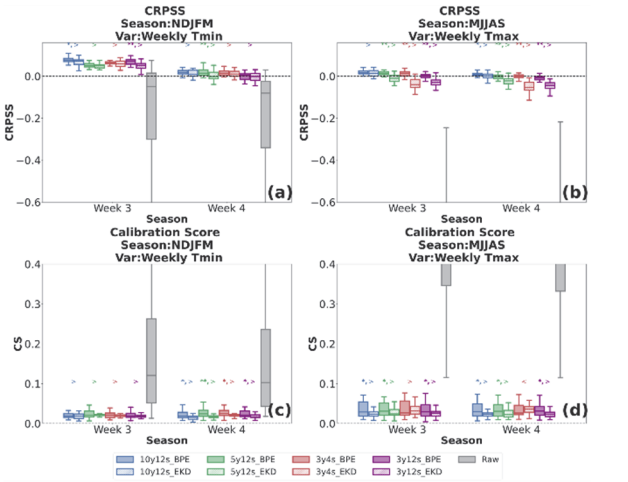

Fig. 3. Boxplot of CRPSS of (a)Weekly Minimum Temperature and (b)Weekly Maximum Temperature and CS of (c)Weekly Minimum Temperature and (d) Weekly Maximum Temperature, grouped by lead time. The experiments are indicated by the legend. * and ** at the top indicates statistically significant differences in the performance of the two methods compared at the 0.05 and 0.01 level using Welch's t-test, with > or < indicating higher CRPS or CS values.

Table 1. Designation and description of experiments

Designation	Description
3y12s	For each year of validation, 3 years(3y) of training set is randomly selected from the rest of the reforecasts. BPE parameters are trained every month, therefore 12 sets(12s) of parameters are trained for every validating year.
3y4s	For each year of validation, 3 years(3y) of training set is randomly selected from the rest of the reforecasts. BPE parameters are trained by pooling data every 3 month, therefore 4 sets(4s) of parameters are trained for every validating year.
5y12s	For each year of validation, 5 years(5y) of training set is randomly selected from the rest of the reforecasts. The abbreviation "12s" follows the same naming rule as experiment 3y12s.
10y12s	For each year of validation, 10 years(10y) of training set is randomly selected from the rest of the reforecasts. The abbreviation "12s" follows the same naming rule as experiment 3y12s.

For weekly minimum temperature (Fig. 3-(a)), the CRPSS of BPE is higher than EKDMOS, passing Welch's t-test at a significance level of 0.05 in 50% of the experiments for week 3, and 25% of the experiments for

week 4. For weekly maximum temperature (Fig. 3-(b)), BPE surpasses EKDMOS at the same statistical significance level for 75% and 100% of all cases for weeks 3 and 4, respectively. These results indicate an overall better accuracy for BPE.

Calibration Score (CS)

The Calibration score (Krzysztofowicz and Sigrest, 1999) is the root mean square error in forecast probabilities from 0 to 1, with interval of 0.1, against corresponding ideal observed frequencies:

$$CS \equiv \sqrt{\frac{1}{11}\left\{\sum_{i=0}^{10}(r_{0.1i} - 0.1i)^2\right\}}$$

Where $0.1i$ is the probability of ith percentile. $r_{0.1i}$ is the frequency of ground truth that happen to exceed ith percentile given the forecast. Ideally, a perfect calibrated forecast should have $r_{0.1i}$ identical to $0.1i$ Consequentially, lower(zero) CS values indicate better(perfect) calibration.

Both methods result in near-perfect calibration, with CS indistinguishable from a value of 0.02. This is a major improvement over the raw ensemble. A more detailed comparison finds that for week 3 weekly minimum temperature(Fig. 3-(c)), there are no statistically significant differences between the methods. For week 4, the CS for EKDMOS is slightly lower than for BPE, passing Welch's t-test at a significance level of 0.05 in 100% of the experiments in week 4. For weekly maximum (Fig. 3-(d)), the CS of EKDMOS is again slightly lower than BPE, passing Welch's t-test at a significance level of 0.05 in 75% of the experiments in week 3 and 100% of the experiments in week 4. The reason for these minor differences is currently under investigation.

Brier Skill Score (BSS)

BSS measures the forecast skill of Brier Score(BS) in a dichotomous event by a forecast system relative to another baseline, in our case, the climatological forecast. We use it to evaluate the forecast performance at warm/cold tercile and extreme climatological percentiles for both EKDMOS and BPE.

Except for the 5y12s configuration, BPE cold tercile/extreme probabilistic forecasts excel over EKDMOS, see Fig. 4-(a). The advantage of BPE increases as the reforecast sample size is reduced. BPE probabilistic forecasts for the 33th, 15th, and 10th climatic percentiles are skillful under most scenarios for week 3. For week 4, neither methods show consistent skill. BSS indicates a major advantage for most BPE configurations over EKDMOS for warm tercile/extreme probabilistic forecasts(Fig. 4-(b)). For week 3, BPE probabilistic forecasts for the 67th, 85th and 90th climatic percentiles are marginally skillful for some scenarios. For week 4, albeit forecasts with neither of the post-processing methods are skillful, probabilistic forecasts produced by BPE are closer to climatology, indicating a slightly more reliable forecast than EKDMOS.

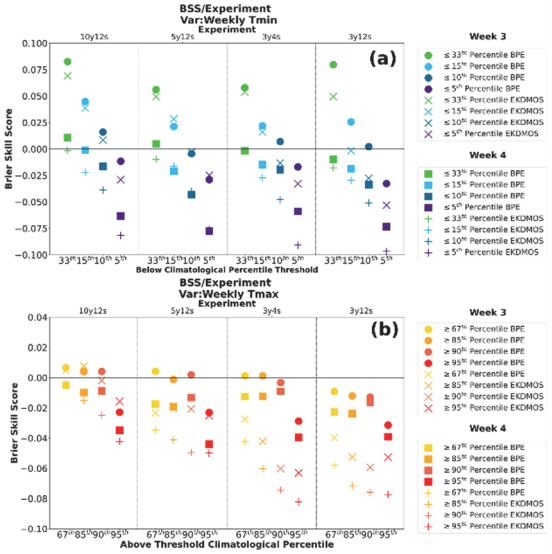

Fig. 4. Brier Skill Score (BSS) of: (a) forecast probability of weekly minimum temperature under 33th, 15th ,10th and 5th climatological percentile and (b) weekly maximum temperature above 67th, 85th, 90th and 95th climatological percentile(marked on the principal abscissa), grouped by experiment(marked on the secondary abscissa) . The result of week 3 and week 4 are represented by different markers as indicated in the legend.

KEY TAKEAWAYS

1. Probabilistic forecasts for extreme temperature events post-processed with BPE generally exhibit higher CRPS and BSS than those post-processed with the frequentist EKDMOS.
2. Due to its Bayesian framework, the advantage of BPE is larger when only smaller hind-cast datasets are available.

ACKNOWLEDGEMENTS

The authors thank Central Weather Bureau for providing the required datasets, and the computing resources in order to conduct the experiments presented in this study.

References

Krzysztofowicz, R., and Sigrest, A. A. (1999). Calibration of probabilistic quantitative precipitation forecasts. Weather and Forecasting, 14(3), 427-442.

Krzysztofowicz, R., and Evans, W. B. (2008). Probabilistic Forecasts from the National Digital Forecast Database. Weather and Forecasting, 23(2), 270-289. doi:10.1175/2007waf2007029.1.

HEAVY RAIN MICROPHYSICS IN TROPICAL AND SUBTROPICAL NORTHEAST ASIA, SOUTHEAST ASIA, AND OCEANIA–VIDEOSONDE OBSERVATIONS

T. Takahashi[1,2], T. Kawano[2], K. Suzuki[3], and K. Muangkote[4]

ABSTRACT: Rain was studied using 236 videosondes launched from 14 locations across tropical and subtropical Northeast Asia, Southeast Asia, and Oceania in 1988-2009. Particle distribution and sounding/radar data were used to determine precipitation mechanism. Over the tropical ocean, the major mechanism of raindrop growth was found to be the Freezing Process (based on frozen drops) and not the Cool Rain Process (based on graupel). Among heavy rain clouds, frozen drop and graupel particle concentrations were very high in some, fully accounting for their rainfall, but only moderate in others, too low to account for their very heavy rainfall. New analysis suggests the following mechanism for Mixed Process heavy rain formation: Falling graupel particles collect supercooled drops and become frozen drops which accumulate near the melting level, where they grow further by collecting drizzle drops from a merging cell. Melted drops grow further by coalescence. We also extend our analysis of mesoscale system, summer rain clouds at Ubon Ratchathani, observed with videosondes and C-band radar. We report that graupel-dominant clouds produced longer duration rainfall than frozen-drop-dominant clouds. Finally, we review our data showing that lightning frequency correlates with both graupel particle concentration and ice crystal concentration, consistent with the riming electrification mechanism of thunderstorm electrification. Our 2010-2012 Hokuriku winter cloud observations provide evidence in naturally-occurring clouds that space charge increases with the product of graupel particle and ice crystal peak concentrations. Graupel/ice crystal paucity explains the low lightning activity observed over the tropical ocean. All of these observations involve the videosonde, which we developed to observe precipitation particles in clouds.

Keywords: Precipitation mechanisms and microphysics in Asian tropics and subtropics, Heavy rain mechanism, Videosonde observations of precipitation particles, Asian tropical MCS precipitation, Lightning mechanism

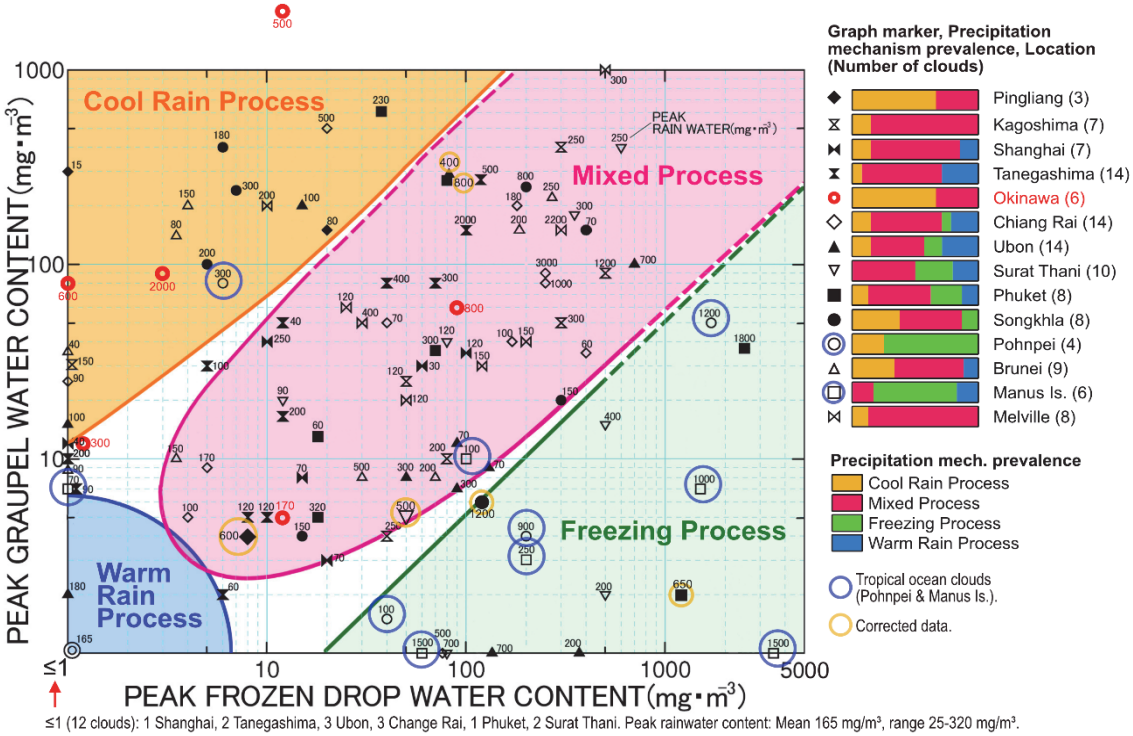

≤1 (12 clouds): 1 Shanghai, 2 Tanegashima, 3 Ubon, 3 Change Rai, 1 Phuket, 2 Surat Thani. Peak rainwater content: Mean 165 mg/m³, range 25-320 mg/m³.

Fig. 1. Heavy and light rain clouds. Modified from Takahashi (2006). Okinawa data (2007-2009) added to the data in the original figure (1988-1999). Particle statistics are calculated in 500 m bins throughout this report. The videosonde was first described in Takahashi (1990).

[1] Emeritus Professor
[2] Department of Earth and Planetary Sciences, Kyushu University, Fukuoka, JAPAN
[3] Department of Biological & Environmental Sciences, Yamaguchi University, Yamaguchi, JAPAN
[4] Retired, Thai Meteorological Department, THAILAND

 https://doi.org/10.1142/9789811275449_0010

ALL-REGION ANALYSIS OF RAINFALL

Fig. 1 plots the 118 clouds (out of 236 total videosonde flights) in which the convective area was transected with successful data transmission through the main growth area of the cloud. The videosonde-derived precipitation particle distribution could be used to determine precipitation mechanism, of which there were four main types: (1) Cool Rain Process: numerous graupel particles (and sometimes also snowflakes), few frozen drops; (2) Freezing Process: numerous frozen drops, few graupel particles; (3) Mixed Process: graupel particles and frozen drops both numerous; and (4) Warm Rain Process: graupel particles and frozen drops both scarce.

In some clouds, peak rainwater content was similar to the sum of peak graupel and frozen drop water contents; while in other clouds, peak rainwater content was over an order of magnitude greater. Of the clouds in the tropical ocean locations (Pohnpei and Manus Island), 7 were Frozen Drop Process clouds, but only 1 was a Cool Rain Process cloud.

At the tropical ocean locations (Pohnpei and Manus Island), the Freezing Process was the most prevalent precipitation mechanism by far. In Pingliang, in the northwest corner of the study region, the Cool Rain Process dominated. Between them was a wide band in which the Mixed Process was most prevalent.

To study heavy rain clouds, Fig. 2 plots only those clouds from Fig. 1 with peak rainwater content ≥500 mg/m^3. There are clusters of heavy-rain clouds in the Cool Rain, Freezing, and Mixed Process domains, but none in the Warm Rain domain, demonstrating the importance of having an active ice phase.

Many clouds had only moderate levels of graupel and frozen drops that failed to account for their very heavy rainfall (e.g. CV7 and A13, the two highest). A high proportion of the clouds in the Mixed Process group produced remarkably high precipitation relative to their moderate graupel and frozen drop mass contents.

A clue to the precipitation mechanism in Mixed Process clouds can be found in the particle distribution plot of the cloud marked with a green circle in Fig. 2 (Kagoshima 1), which is reproduced in Fig. 3. Note the accumulation of frozen drops near the melting level and the graupel particles just above it. This suggests the possibility that the graupel particles collect supercooled droplets and develop into the frozen drops below them.

In Fig. 2, there is a heavy-rain cluster in the Cool Rain Process domain at ~100 mg/m^3 peak graupel particle concentration and another heavy rain cluster in the Freezing Process domain at ~100 mg/m^3 peak frozen drop concentration. This suggests that heavy rain generation requires 100 mg/m^3 of graupel particles or frozen drops. However, in the Mixed Process domain, there is no heavy rain cluster where the sum of the peak graupel particle and frozen drop concentrations equals ~100 mg/m^3 (e.g. at 50 mg/m^3 of each), but the cluster is instead at a little over 100 mg/m^3 of each. This is consistent with the idea that in Mixed process clouds, graupel particles and frozen drops do not contribute independently to rain production, but rather, graupel particles contribute indirectly by developing into frozen drops, and then the frozen drops

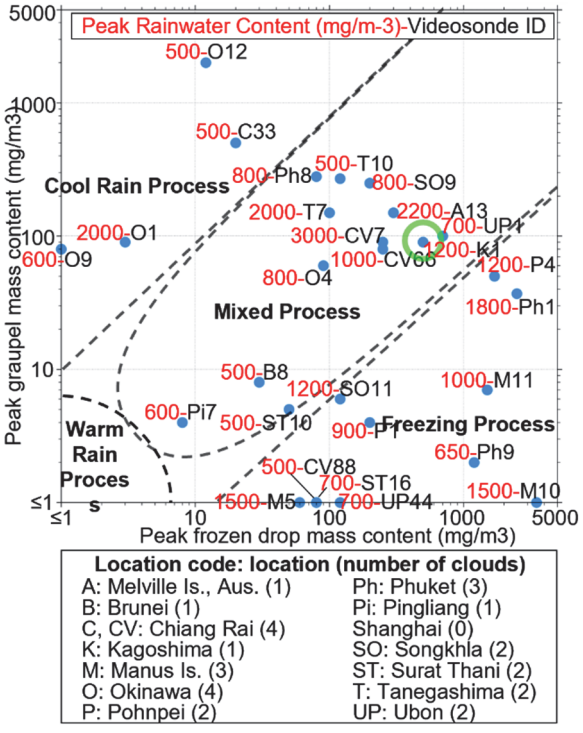

Fig. 2. Clouds from Fig. 1 with peak rainwater content ≥500 mg/m^3.

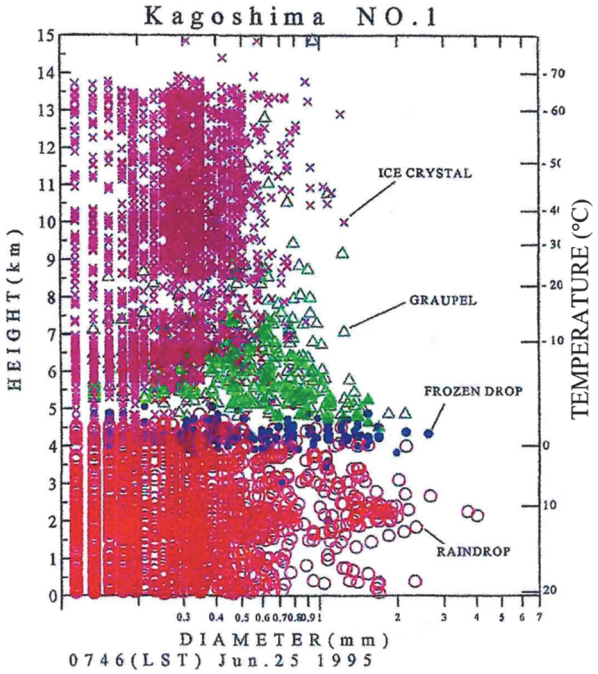

Fig. 3. Videosonde-derived particle distribution plot.

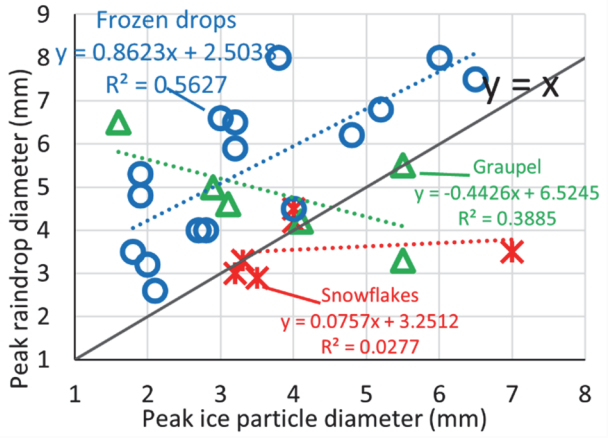

Fig. 4. Peak raindrop diameter vs. peak frozen particle diameter for the heavy-rain clouds in Fig. 2. Marker type indicates whether the largest ice particle in the cloud was a frozen drop, graupel particle, or snowflake.

develop into raindrops, as suggested by the particle distribution in Fig. 3.

More clues to the precipitation mechanism can be found in Fig. 4, which plots peak ice particle diameter vs peak raindrop diameter for each of the heavy-rain clouds in Fig. 2. For the clouds in which a frozen drop was the largest ice particle (blue circles): (1) there is a fairly strong, positive correlation between peak frozen drop diameter and peak raindrop diameter, and (2) all of the markers are above the y=x line, showing that peak raindrop diameter was always larger than peak frozen drop diameter, which suggests that frozen drops melt into raindrops that then continue to grow.

We propose the following mechanism for Mixed Process clouds (Fig. 5): Falling graupel particles collide with supercooled drops and form frozen drops which accumulate in a band near the melting level. The graupel layer continuously replenishes the frozen drop layer. The frozen drops grow, fall, and melt into raindrops which

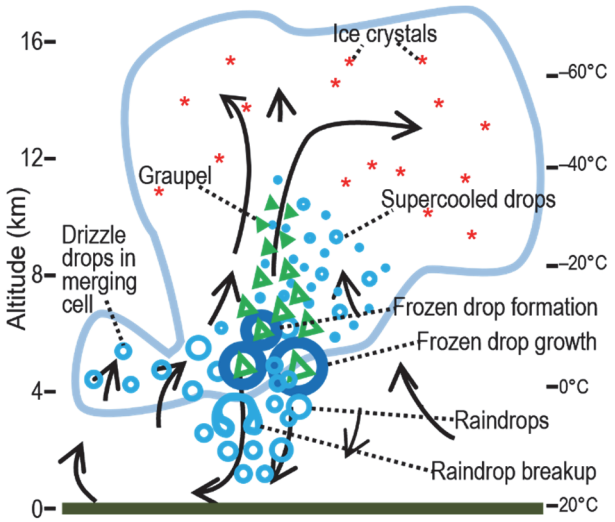

Fig. 5. Proposed mechanism for heavy rain formation in Mixed Process clouds.

continue to grow by coalescence. Merging cells, when present, contribute large amounts of supercooled drizzle, which greatly accelerates drop growth.

We previously saw frozen drops near the melting level in a 3D microphysics cloud model (Takahashi and Shimura 2004).

UBON OBSERVATIONS

In Ubon Ratchathani in 1998, we conducted observations of summer, mesoscale system, rain clouds using both videosondes and the Thai Meteorological Department C-band radar. We investigated the relationship between particle type and distribution, precipitation mechanism, rain area, and rain duration.

Tropical cyclones developed frequently over the tropics and moved from east to west. Those that migrated over the center of the Indochinese peninsula developed into circular, mesoscale, cloud systems there (Fig. 6A). We often observed new cells developing at the front of the mesoscale cloud system, extending its lifespan (Takahashi 2006).

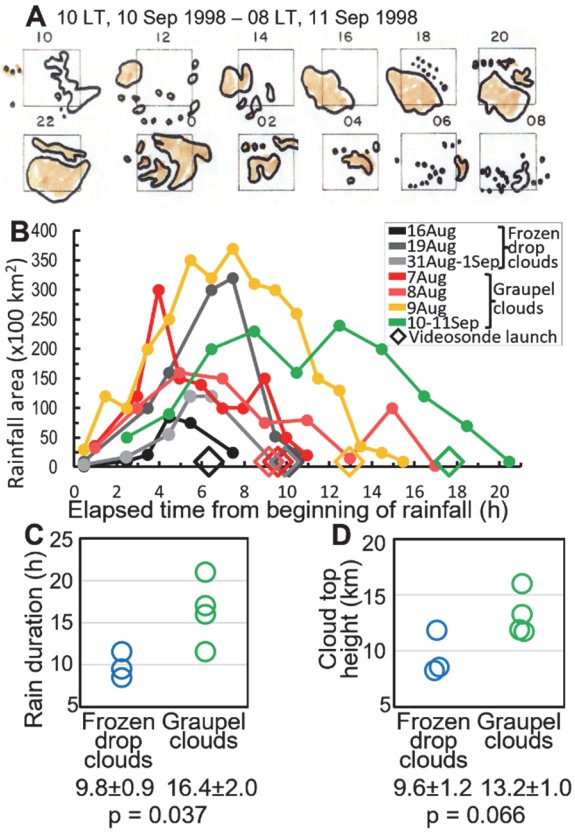

Fig. 6. Ubon Ratchathani observations. A: Coloring of radar traces marks a single cloud system from beginning to end (10-11Sep1998). Squares are 200 km/side, centered on Ubon. B-D: Graupel clouds and frozen drop clouds compared with respect to rain duration and cloud top height, with mean ± SEM and p values (2-tailed, heteroscedastic T-test).

We limited analysis to cloud clusters that met the following requirements: a single, distinct rainfall system; a complete radar record from the beginning to the end of rainfall; and surveyed by videosonde. 7 cloud clusters met these criteria. They fell into two categories: graupel clouds and frozen drop clouds. Graupel clouds contained numerous graupel particles, and even more numerous ice crystals, but far fewer frozen drops. Frozen drop clouds contained numerous frozen drops, but far fewer graupel particles. The approximate proportion of frozen drops relative to the sum of frozen drops and graupel particles was >80% for each frozen drop cloud and <25% for each graupel cloud. The frozen drops were mostly distributed below the graupel particles and ice crystals.

We analyzed the clouds for rainfall duration, defined here as the period during which an area ≥100 km^2 displays C-band radar echo intensity ≥5 dBZ. The graupel clouds produced significantly longer-lasting rainfall (Fig. 6B-C). The graupel clouds also trended taller (Fig. 6D), though the difference was not statistically significant, perhaps because of the small sample size.

RIMING ELECTRIFICATION

It is now well-recognized that riming electrification is a major, thunderstorm-charge-separation mechanism (Takahashi 1978). In this process, a high amount of charge is separated when graupel particles and ice crystals collide under riming conditions.

From 2010 to 2012, we launched 77 videosondes and conjoined HYVIS-videosondes into winter clouds at Kashiwazaki, part of the Hokuriku "snow country" region of Japan (Takahashi et al. 2019). The videosondes measured both space charge and ice particle concentrations during ascent. Fig. 7 plots peak space charge vs. the product of peak ice crystal concentration and peak graupel particle concentration for each cloud. There is clear correlation, consistent with riming electrification. This might explain, at least in part, why lightning frequency is so low over the tropical ocean, even compared to other tropical locations with high rainfall as in the maritime continent (Christian et al. 2003, Takahashi 2006). It is likely that local lightning frequency is largely a function of the extent and duration of high graupel particle × ice crystal concentrations. We found graupel particle and ice crystal concentrations and their product to be relatively low over our tropical ocean launch sites (Pohnpei and Manus Is., Fig. 1). Listed here are the means for each location of the following particle values for all of the heavy rain clouds in Fig. 2 [Location, peak graupel particle concentration (m^{-3}), peak ice crystal concentration (m^{-3}), the product of peak graupel particle and peak ice crystal concentrations in the same cloud (m^{-6})]: Ubon 70, 40, 4300; Manus Is. 23, 110, 4500; Pohnpei 70, 600, 5.4×10^4; Brunei 80, 1200, 9.6×10^4; Surat Thani 230, 810, 3.4×10^5; Pingliang 300, 1500, 4.5×10^5; Okinawa 260, 2300, 8.4×10^5; Kagoshima 1500, 8000, 1.2×10^7; Chiang Rai 1400, 2900, 1.3×10^7; Melville Is. 2000, 3.0×10^4, 6.0×10^7; Tanegashima 1900, 1.1×10^4, 3.1×10^7; Songkhla 2000, 2.5×10^4, 1.0×10^8; Phuket 4200, 2.6×10^4, 2.6×10^8.

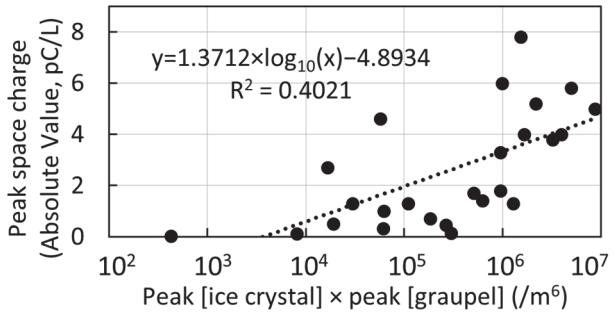

Fig. 7. Peak space charge in Hokuriku winter clouds correlates with peak [ice crystal] × peak [graupel particle], consistent with riming electrification.

ACKNOWLEDGEMENTS

We would like to thank the meteorological agencies of the many countries in which we conducted field observations for their critically important support, and also the Central Research Institute of Electric Power Industry in Japan. We are very grateful for the essential contributions of the many students, postdocs, and technicians of our labs who contributed to this work. Kanji Takahashi helped to edit this report.

References

Christian, H.J. et al. (2003). Global frequency and distribution of lightning as observed from space by the Optical Transient Detector. J. Geophys. Res., 108(D1): 4005–4020.

Takahashi, T. (1978). Riming electrification as a charge generation mechanism in thunderstorms. J. Atmos. Sci. 35(8):1536–1548.

Takahashi, T. (1990). Near absence of lightning in torrential rainfall producing Micronesian thunderstorms. Geophys. Res. Lett. 17(13):2381–2384.

Takahashi, T. (2006). Precipitation mechanisms in east Asian monsoon: Videosonde study. J. Geophys. Res. Atmos. 111(D9):D09202.

Takahashi, T. and Shimura, K. (2004). Tropical rain characteristics and microphysics in a three-dimensional cloud model. J. Atmos. Sci. 61(23):2817–2845.

Takahashi, T., Sugimoto, S., Kawano, T. and Suzuki, K. (2019). Microphysical structure and lightning initiation in Hokuriku winter clouds. J. Geophys. Res. Atmos. 124(23):13,156–13,181.

STATISTICAL POSTPROCESSING OF 1-14-DAY PROBABILISTIC FORECASTS FOR COLD EXTREMES OVER TAIWAN

Hui-Ling Chang[1], Yun-Jing Chen[1], Zoltan Toth[2], Pay-Liam Lin[3]

ABSTRACT: Two statistical post-processing methods, ensemble Model Output Statistics (EMOS) and Ensemble Kernel Density MOS (EKDMOS), are applied in 20-year reforecasts of the National Centers for Environmental Prediction (NCEP) global ensemble forecast system version 12 (GEFS v12) to produce calibrated and downscaled 1-14-day probabilistic forecasts of cold extremes at specific stations over Taiwan. To generate an EMOS forecast, the MOS equation is built using the ensemble mean, and applied to each ensemble member. The EKDMOS uses a kernel density estimation (KDE) to create a probability density function (PDF) from the EMOS forecasts.

Calibration is performed using a leave-one-out cross-validation procedure, where one winter is used for validation, and the remaining 19 winters are used for training. Forecast evaluation shows that the EMOS is under-dispersive, just like the raw ensemble (RawEns) forecasts, with some bias removed. In contrast, the EKDMOS well represents the forecast uncertainty with most of the bias removed. Compared to the RawEns or EMOS, the EKDMOS obviously improves the reliability and discrimination of probabilistic forecasts. The EKDMOS increases the Brier skill score (BrSS) of the RawEns and EMOS by decreasing its reliability, and increasing its resolution components. For any threshold and any lead time, users with a wider spectrum of cost/loss ratio can obtain more benefit from the EKDMOS as compared to the RawEns or EMOS. The EKDMOS distribution, as expected from a reliable forecast system, necessarily approaches the climatology of the training sample when forecast informativeness is lost beyond 10 days.

Keywords: Ensemble Model Output Statistics (EMOS), Ensemble Kernel Density MOS (EKDMOS), cold extremes, leave-one-out cross validation, reliability, discrimination, economic value.

INTRODUCTION

The goal of this research is to generate 1-14-day calibrated and downscaled probabilistic forecasts for cold extreme weather over Taiwan. Unfortunately, most ensemble forecast systems suffer from problems with systematic bias and spread deficiency (Veenhuis, 2013). This limits the utility of predictions for extreme events but can be potentially corrected by statistical post-processing. In this study, the Model Output Statistics (MOS) equation was built using ensemble mean forecasts, and applied to each member to generate ensemble MOS (EMOS) forecasts. The spread and probability distribution of the bias-corrected members are then adjusted using a kernel density estimation (KDE) method.

FORECAST AND OBSERVATIONAL DATA

This study used 20 winters of reforecast data (2000-2019) from the National Centers for Environmental Prediction (NCEP) global ensemble forecast system version 12 (GEFS v12) for lead times up to 14 days. The reforecast data updates daily with 5 members out to 16 days, except for Wednesday, when 11 members out to 35 days are available. The horizontal resolution of the data is .5 by .5 degree in latitude and longitude. For training and validation, we used the daily minimum temperature from 25 manned stations over Taiwan.

STATISTICAL POST-PROCESSING AND VALIDATION PROCEDURE

The generation of calibrated probabilistic forecasts for cold extremes follows three main steps (Fig. 1): (1) The gridded raw ensemble forecasts are bilinearly interpolated to stations over Taiwan. This will be called RawEns hereafter, which is an uncalibrated multi-value ensemble forecast. (2) MOS equations are built using ensemble mean forecasts, and applied to each member to generate ensemble MOS forecasts (EMOS). This is a multi-value ensemble forecast with bias-corrected members. (3) We apply a Kernel Density Estimation (KDE) method to EMOS to produce a forecast probability distribution with calibrated spread, called EKDMOS (see next section). Finally, probabilistic forecasts are derived by counting the empirical frequency for RawEns and EMOS, and a

[1] Central Weather Bureau, Taipei, TAIWAN
[2] Global Systems Laboratory, National Oceanic and Atmospheric Administration, Boulder, Colorado, USA
[3] National Central University, TAIWAN

 https://doi.org/10.1142/9789811275449_0011

calculation of the area under the density curve for EKDMOS.

For the forecast calibration in this study, leave-one-out cross validation was used for EMOS and EKDMOS. That is, the forecasts in each year were trained using the data of the remaining years. For the production of calibrated forecasts in a given month, the training data used that month and the surrounding two half months. For example, February forecasts were trained with data from Jan 16 to March 15.

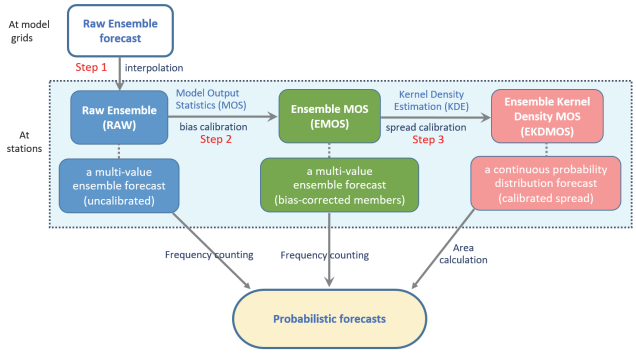

Fig. 1 The generation of calibrated probabilistic temperature forecasts.

Methodology - Ensemble Kernel Density Model Output Statistics (EKDMOS)

Figure 2 illustrates how probabilistic forecasts of daily minimum temperature below a given threshold are generated with EKDMOS. First, a kernel is defined as a normal distribution with a variance equal to that in the ensemble mean forecasts (Fig. 2a). Next, 1/N fraction of this kernel is applied to each of an N-member ensemble. Finally, the "dressed" members are summed up into a single probability density distribution (pdf). The forecast probability of cold extremes equals the area under the pdf curve. As an example, the probability of temperature less than 10 degree Celsius is given by the pink area in Fig. 2b.

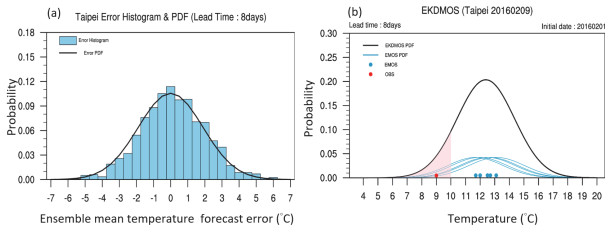

Fig. 2 Schematic diagram of EKDMOS.

RESULTS FROM FORECAST EVALUATION

Distribution of ensembles

The analysis rank histogram (ARH), also called Talagrand diagram, evaluates whether the spread of an ensemble adequately represents forecast uncertainty. The Probability Integral Transform (PIT) Histogram (Gneiting et al. 2005) is visually similar to ARH, and is used to assess the reliability of probability distribution forecasts, like EKDMOS. The assessments of ARH for RawEns and EMOS, and the PIT histogram for the EKDMOS (not shown) indicate that both the RawEns and EMOS are under-dispersive, while the EKDMOS is well calibrated with most of the bias in the spread removed.

Reliability and discrimination

Reliability diagrams (Fig. 3) indicate that probabilistic forecasts for cold extremes from EKDMOS are (much) better calibrated than EMOS (RawEns). Relative Operating Characteristic (ROC) analysis shows that EKDMOS extreme cold forecasts for the 10th climatic percentile (not shown) also has much better discrimination compared to the EMOS and RawEns.

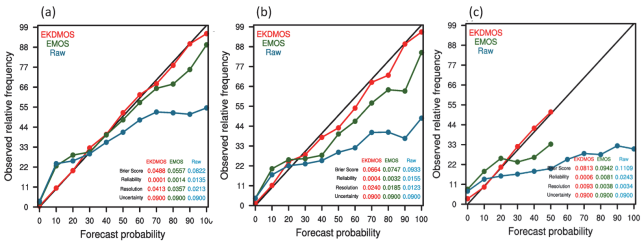

Fig. 3 Reliability diagrams for (a) 1-day, (b) 8-day, and (c) 15-day lead time cold extreme EKDMOS (red), EMOS (green), and RawEns (blue) forecasts for the 10th climatic percentile.

Brier skill score (BrSS)

An evaluation of the Brier skill score (BrSS) and its reliability and resolution components (Fig. 4) indicates that EKDMOS extreme cold forecasts have higher skill compared to EMOS and RawEns. This is accomplished by higher resolution and lower reliability error compared to the other two methods.

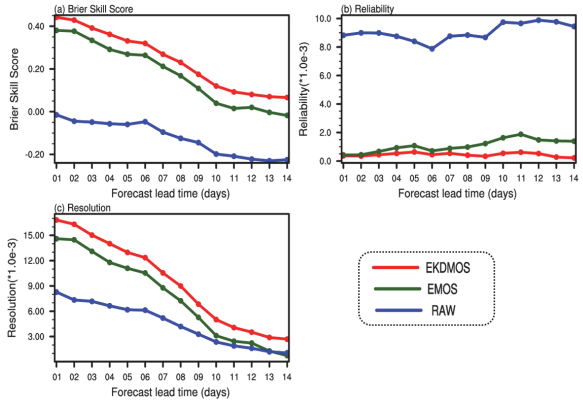

Fig. 4 (a) Brier skill score (BrSS) and its (b) reliability and (c) resolution terms for different lead time cold extreme forecasts. The red, green, and blue curves are for EKDMOS, EMOS, and RawEns.

Relative economic value

An Economic Value analysis for different extreme thresholds and different lead times (Fig. 5) indicates that users with a wider spectrum of cost/loss ratio can obtain more benefit from the EKDMOS as compared to EMOS or RawEns.

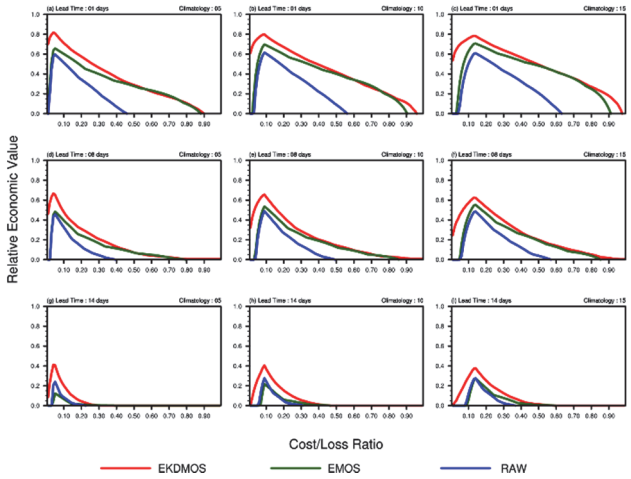

Fig. 5 Distribution of maximum economic value as a function of a user's cost/loss ratio at 1-day (top row), 8-day (middle row), and 15-day (bottom row) lead time for the 5th (left column), 10th (middle column), and 15th (right column) cold extreme climatic percentiles, for EKDMOS (red), EMOS (green), and RawEns (blue).

Verification of the EKDMOS probabilistic forecasts for cold events

A verifying date versus lead time display of EKDMOS probabilistic forecasts for the daily minimum temperature at Taipei station falling below 10 °C (Fig. 6) shows that the forecast probability values beyond 10 days tend to fall in the range of 5 to 15 %. Note that the observed frequency of the training sample is 5% for Taipei station. In other words, the EKDMOS distribution, as expected from a reliable forecast system, necessarily approaches the climatic frequency value as forecast skill is lost at extended lead times. The range of forecast probabilities around the expected value may be due to fluctuations in ensemble variance, due either to sampling fluctuations in a finite ensemble, or genuine case dependent variations in atmospheric predictability.

CONCLUSIONS

In this study, calibrated and downscaled 1-14-day probabilistic forecasts for cold extremes were generated using EKDMOS. An evaluation of ARH and PIT histograms shows that unlike RawEns and EMOS, which are under-dispersive, the EKDMOS is well calibrated, with most of the bias in the spread removed. Compared to RawEns or EMOS, EKDMOS probabilistic forecasts exhibit better reliability and discrimination, as well as higher economic value for a wider range of users. Even though EKDMOS displays significantly improved forecast quality and value, when forecast skill is lost at extended lead times, its forecast distribution still approaches the climatological distribution of the training sample.

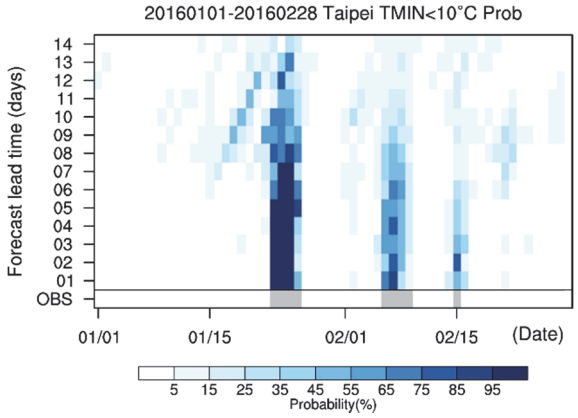

Fig. 6 Observed daily minimum temperature below 10 C at Taipei station for Jan-Feb 2016 (verifying date, horizontal axis) is indicated with dark blue shading at the bottom. EKDMOS 1-14-day lead time (vertical axis) probabilistic forecasts for such events are marked by shades of color.

ACKNOWLEDGEMENTS

H.-L. Chang is sponsored by the Ministry of Science and Technology, R.O.C. (110-2111-M-008-021).

References

Gneiting, T., A. E. Raftery, A. H. Westveld III, and T. Goldman, 2005: Calibrated probabilistic forecasting using ensemble model output statistics and minimum CRPS estimation. *Mon. Wea. Rev.*, **133**, 1098–1118.

Glahn, H. R., and D. A. Lowry, 1972: The use of Model Output Statistics (MOS) in objective weather forecasting. *J. Appl. Meteorol.*, **11**, 1203–1211.

Glahn, H. R., Peroutka, M., Weidenfeld, J., Wagner, J., Zylstra, G. and Schuknecht, B., 2009: MOS uncertainty estimates in an ensemble framework. *Monthly Weather Review*, **137**, 246–268.

Veenhuis, A. B., 2013: Spread Calibration of Ensemble MOS Forecasts. *Monthly Weather Review*, **141**, 2467–2482.

EVALUATION OF PROBABILISTIC FORECASTS OF CONSECUTIVE DAYS WITHOUT MEASURABLE RAINFALL OVER TAIWAN

Shih-Chun Chou[1], Hui-Ling Chang[1], Chih-Yung Feng[2], Han-Fang Lin[2] and Pay-Liam Lin[3]

ABSTRACT: Demand for probabilistic forecasts of consecutive days without measurable rainfall has grown significantly by users in different sectors of society, especially in agriculture, livestock, and water resource management. The purpose of this study is to provide users with reliable and skillful forecasts, which help users obtain more economic benefits in decision making. In this study, Analog post-processing (AP) is applied in 20-year reforecasts of the National Centers for Environmental Prediction (NCEP) Global Ensemble Forecast System version 12 (GEFS v12) to produce calibrated and downscaled probabilistic forecasts of consecutive days without measurable rainfall over Taiwan land area. Long-term forecast evaluation indicates that: (1) the problem of under-dispersion of the raw forecasts is effectively mitigated through the AP. (2) The probabilistic forecasts of consecutive days without measurable rainfall have good reliability and discrimination (potential usefulness) within next four weeks. (3) The calibrated forecasts provide higher economic benefits for users with a much wider spectrum of cost-to-loss ratio compared to the raw forecasts.

Keywords: ensemble prediction system, potential usefulness, economic value.

INTRODUCTION

To address the severe impact of climate change, international governments are committed to comprehensive and inclusive planning and change to achieve a climate-resilient future through cross-sectoral collaboration. In Taiwan, the Central Weather Bureau (CWB) has been actively communicating with other agencies to provide customized forecast products to enhance the value of weather forecast information.

Since the need for consecutive daylight for pasture exposure for cattle breeding in Taiwan, CWB has attempted to produce well-calibrated forecasts of 7-day and 14-day without rainfall through statistical post-processing (SPP). Therefore, in this study, we compared the raw and the calibrated ensemble probabilistic forecast from the same ensemble prediction system (EPS) through a series of the verification evaluation, including the forecast quality, the reliability of the probability, the potential usefulness, and the relative economic value (EV). The purpose of this study is to evaluate the long-term forecasting performance of probabilistic forecasts of consecutive days without rainfall, and the calibration of the SPP technique.

FORECAST AND OBSERVATION DATA

The forecast data were obtained from National Oceanic and Atmospheric Administration/National Weather Service/Environmental Forecast System version 12 (GEFSv12), including both reforecast and forecast data. The horizontal resolution is $0.5 \times 0.5^{\circ}$ in latitude and longitude. The reforecast was integrated once per day out to 16 days except on Wednesday when the forecast was extended to 35 days. The reforecast has a smaller ensemble size (5 (11) members for the 16-day (35-day) run) than the real-time forecast (31 members). For longer verification period required to ensure adequate statistical representativeness, we used the reforecasts on Wednesday and real-time forecast in 10 members without control run.

Regarding the observation data used for training and validation, we used all rain gauge data to produce 1 kilometer (km) gridded rainfall analysis through Graphic Forecast Editor (GFE) during the period from January 2000 to December 2019 for the same period as the forecast. Since the calibrated forecasts can be directly downscaled to the observation-based resolution in the Analog Post-processing (AP) procedure, and the grid-to-grid verification is necessary, the resolution of the forecast data is downscaled to 1 km by simple linear interpolation in this study.

METHODOLOGY

For the assumption of the consistence in EPS forecast performance, we attempted to use the relationship between historical and observation to obtain that the latest forecast is likely to correspond to the closet real situation. This is the concept of statistical analogy. Therefore, the technique of statistical calibration for ensemble forecast is called analogs post-processing (AP; Hamill and Whitaker, 2006) in this study.

[1] Central Weather Bureau, Taipei, TAIWAN (R. O. C.)
[2] Manysplended Infotech Ltd, Taipei, TAIWAN (R. O. C.)
[3] National Central University, Zhongli District, Taoyuan City, TAIWAN (R. O. C.)

 https://doi.org/10.1142/9789811275449_0012

Analog Post-processing (AP)

Referring to the definition of the similarity function (Chang et al., 2022) including ensemble mean and ensemble spread, pattern matching is conducted between the current ensemble forecasts and all historical forecasts to search a set of the most resemble historical observations. Note that it is free to decide how many of the most similar historical observations. In this study, after our sensitive test for ensemble size, the most 20 similar historical observations were used to be the set of calibrated ensemble forecasts.

RESULTS FROM FORECAST EVALUATION

Considering seasonal differences in the rainfall characteristics of Taiwan, July to September was defined as summer, October to April as winter, and May to June as mei-yu season. In evaluation of probabilistic forecast, we defined the threshold of consecutive days without rainfall as 7-day (14-day) cumulative rainfall < 5 (10) mm.

Evaluation of ensemble quality

The rank histogram (RH) is a commonly used diagnostic for forecast quality of an EPS. The results of the 7-day cumulative rainfall forecast in week-1 (Fig. 1) show that the RAW ensembles are over-forecasting and under-dispersive due to the L-shaped and U-shaped behaviors of the RHs. Conversely, the RHs of the AP ensemble shows relatively flat shape.

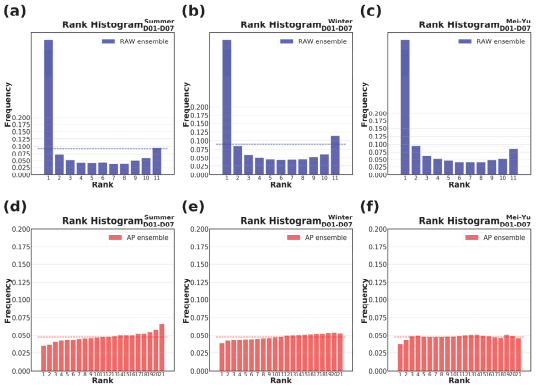

Fig. 1 The rank histograms of 7-day rainfall forecasts at lead time week-1; the upper and bottom sides are the results of RAW and AP ensemble, respectively; the left to right sides are the results of summer, winter and mei-yu, respectively; the dashed line represents the frequency of the sequence evenly distributed.

To assess the ensemble qualities from lead time week-1 to week-4, we defined a rank bias which sums up the difference between the actual frequency and the ideal frequency of each order. The closer the rank bias is to 0, the closer the ensemble quality is to the ideal. The results (Fig. 2) show the rank bias of the AP ensemble is significantly smaller than that of the RAW ensemble in all seasons. It also indicates that the AP method can significantly improve the ensemble quality of GEFSv12.

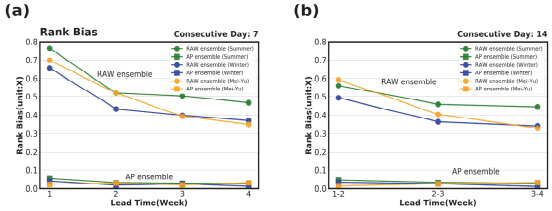

Fig. 2 The line charts of rank bias for (a) 7-day (b) 14-day rainfall forecasts within lead time 4 weeks; color representations are seasons: Summer (green), Winter (blue), and Mei-Yu (orange); shape representations are RAW ensemble (circle) and AP ensemble (square).

Evaluation of ensemble probabilistic forecast

To evaluate the reliability of a probabilistic forecast, we commonly used a reliability diagram. According to Fig. 3, the red lines are closer to the diagonal line of the reliability diagram than blue lines, regardless of the consecutive days or how long the lead time is. It means that the AP calibrated probabilistic forecast has much better reliability than raw forecasts.

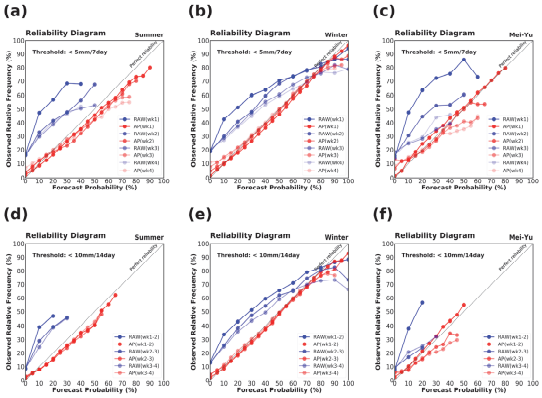

Fig. 3 The reliability diagrams for (a) to (c) 7-day (d) to (f) 14-day without rainfall within lead time 4weeks; colors distinguish the results for the RAW (blue line) and AP (red line) probabilistic forecasts; the right to left sides representation are the same as in Fig. 1.

To quantify the performance of probability forecast, we calculated the brier skill score (BSS). The results (Fig.4) clearly show that (1) the BSS values of the AP ensemble are larger than those of the RAW ensemble; (2) the BSS values of AP ensemble are all larger than 0. It represents that the AP ensemble not only performs better than the RAW ensemble, but also has a more significant forecast skill compared to the climate frequency forecast.

Using observations as conditional judgments, we evaluate ROC area to access the discrimination and potential usefulness in the NWP. Fig. 5 illustrates that the ROC area of the AP ensemble is larger than that of the RAW ensemble. In addition, it was found that the ROC area for 14-days is larger than that for 7-day when the lead time is longer, e.g., 2-3 weeks or 3-4 weeks. It may reduce the high uncertainty in rainfall forecast by increasing the number of accumulated days.

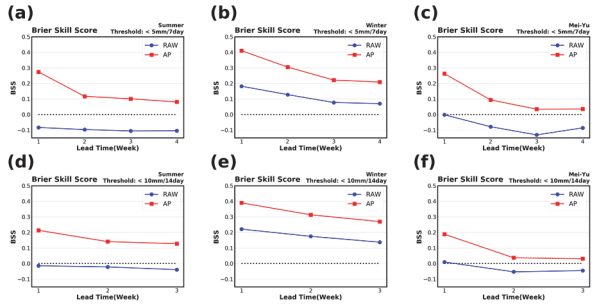

Fig. 4 The line charts of BSS for (a, b, c) 7-day (d, e, f) 14-day without rainfall within lead time 4weeks; color and the right to left sides representation are the same as in Fig. 3.

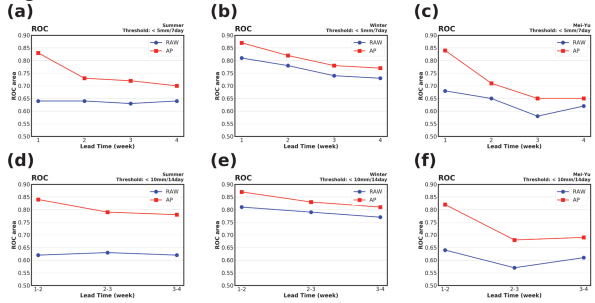

Fig. 5 The line charts of ROC area for (a, b, c) 7-day (d, e, f) 14-day without rainfall within lead time 4weeks; color and the right to left sides representation are the same as in Fig. 3.

Evaluation of forecast value

The EV analysis is commonly used to evaluate the potential forecast value by combining the information of both the forecast performance and the cost-loss ratio of each user. According to the result (Fig. 6), the EVs on the red line are usually higher than those on the blue line. It represents that the EV for using AP calibrated forecasts is higher than that with RAW forecast.

However, some users in a few range of cost-loss ratios are not suggested using the AP ensemble to obtain the highest EV (Fig. 6). Therefore, we defined a "user breadth" to compare what percentage of users refer to the forecast to get the highest EV under the weather condition. Although most of the red lines have higher EV than the blue lines, some ranges of users, such as those with cost-loss ratios around 0.9, have higher EVs by referring to the RAW forecasts. When both the red and blue lines are less than 0, it means that users with this cost-lost ratio should refer to climate frequency as the threshold for taking disaster prevention actions as comparing with the RAW and AP forecasts. Therefore, we can obtain user breadths of the RAW, AP and climate frequency forecasts. Fig. 7 shows that (1) AP calibrated forecast can provide wider spectrum of cost-to-loss ratio in all seasons and lead times within 4 weeks; (2) when the lead time is longer, the percentage of users who should choose climate frequency forecast to obtain the highest EV will increase.

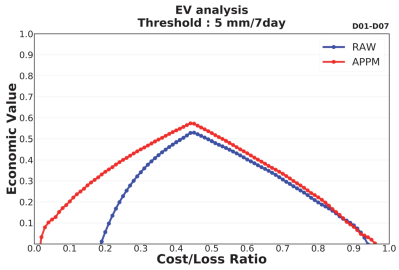

Fig. 6 EV distribution of 7-day without rainfall at lead time week-1; color representation is the same as in Fig.3.

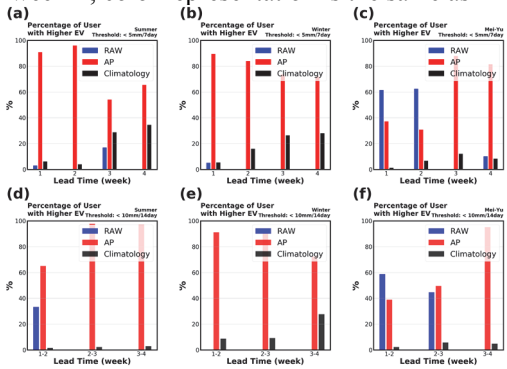

Fig. 7 The bar plots of percentage of user with the highest EV using RAW (blue), AP (red) and climatology (black) forecasts within lead time 4 weeks; the right to left sides representation are the same as in Fig. 3.

CONCLUSION

The study concluded that (1) compared with RAW ensemble, AP calibrated ensemble forecast has significantly improvement of the ensemble dispersion; (2) AP calibrated ensemble probabilistic forecast has good reliability, discrimination and potential usefulness up to lead time within 4 weeks; (3) the AP calibrated forecast can provide the highest economic benefits for users with a much wider spectrum of cost-to-loss ratio compared to the RAW forecasts.

ACKNOWLEDGEMENTS

Thanks to the CWB for providing datasets and computing resources. We also thank Dr. Chih-Yung Feng, Han-Fan Ling for technical support at Manysplendid Infotech Ltd, and Prof. Pay-Liam Lin at National Central University for valuable discussions.

References

Chang, H. L., Z. Toth, S. C. Chou, C. Y. Feng, H. F. Lin and P. L. Lin, 2022: Statistical Post-Processing of 1-14 Day Precipitation Forecasts for Taiwan. 18th Annual Meeting of the Asia Oceania Geosciences Society, pp. 25-27, https://doi.org/10.1142/9789811260100_0009.

Hamill, T. M., and J. S. Whitaker (2006). Probabilistic quantitative precipitation forecasts based on reforecast analogs: Theory and application. *Mon. Wea. Rev.*, **134**, 3209–3229.

EXTENDED-RANGE RESERVOIR INFLOW FORECASTING BASED ON CALIBRATED AND DOWNSCALED RAINFALL FORECASTS

Hui-Ling Chang[1], Tao-Chang Yang[2] and Jing-Shan Hong[1]

ABSTRACT: Reservoir inflow forecasts, which can be used to estimate the future storage of reservoirs, are essential for water resources management. This work develops a framework for reservoir inflow forecasting for the coming 2 weeks based on the rainfall forecasts from the National Centers for Environmental Prediction (NCEP) global ensemble forecast system version 12 (GEFS v12).

Analog Post-processing (AP) and Probability-Matched mean (PM) are applied to obtain a quantitative precipitation forecast (QPF) as the input of a hydrological model for reservoir inflow forecasting. AP searches for the best analogs to the current forecast in a historical set of predictions. The AP ensemble forecasts are derived from the observed high-resolution rainfall patterns corresponding to the historical forecast analogs that most resemble the current ensemble rainfall forecast. Then PM is applied on the AP ensemble mean to get a QPF with a more realistic range of rainfall amounts. Evaluation shows that the QPF not only corrects the rainfall pattern and amount of the raw forecasts, but also displays the fine scale details of rainfall. The calibrated and downscaled QPF is then ingested into the Hydrologiska Byråns Vattenbalansavdelning-based (HBV-based) hydrological model for reservoir inflow forecasting. Shih-Men reservoir in northern Taiwan is chosen as the study area, which is a multifunction reservoir for water supply, agriculture, hydropower generation, and flood control. The HBV-based hydrological model is optimally calibrated by using the historical rainfalls, temperature and runoffs in the reservoir catchment. By coupling the calibrated and downscaled QPF with the HBV-based hydrological model, the 1-14 days ahead reservoir inflow forecasting can be carried out and shows a satisfactory forecasting performance.

Keywords: Reservoir inflow forecasts, Analog Post-processing (AP), Probability-Matched mean (PM), calibrated and downscaled rainfall forecasts, HBV-based hydrological model.

INTRODUCTION

Reservoir inflow forecasts can be used to estimate the future storage of reservoirs, which is essential for water resource management, such as drought warning and decision support of drought-disaster prevention. This study aims to develop a framework for reservoir inflow forecasting for the coming 2 weeks based on calibrated and downscaled rainfall forecasts. The purpose is to improve the accuracy of reservoir inflow forecasts to make a better decision for water resource management.

FORECAST AND OBSERVATION DATA

This study used 20 years of rainfall reforecasts from the National Centers for Environmental Prediction (NCEP) global ensemble forecast system version 12 (GEFS v12) for lead times up to 14 days. The update frequency of reforecast data is once per week with 11 members, and the horizontal resolution is .5 by .5 degree in latitude and longitude. Regarding the rainfall observation used for training and validation, we adopted the Simple Kriging method to produce gridded rainfall analysis based on rain gauge data for the same period as the rainfall reforecast. In order to optimize the simulation performance of the hydrological model, the observed rainfall, temperature, and inflow data over Shih-Men reservoir catchment were used to calibrate the model parameters. The validation for rainfall and reservoir inflow forecasts was performed using leave-one-out cross validation procedure. That is, the forecasts in each year were trained using the data of the remaining years between 2000 and 2019.

PROCEDURES OF RESERVOIR INFLOW FORECASTS BASED ON POST-PROCESSED RAINFALL FORECASTS

Figure 1 shows the flowchart of reservoir inflow forecasts based on post-processed rainfall forecasts. First, the analog post-processing (AP) is used to produce calibrated and downscaled ensemble rainfall forecasts, which will be called AP ensemble forecasts hereafter. Then the probability-matched mean (PM) is applied to convert the AP ensemble forecasts into a single deterministic forecast, which will be called APPM hereafter. An example of the forecast product APPM is

[1] Central Weather Bureau, Taipei, TAIWAN
[2] National Central University, Taiwan, National Cheng Kung University, TAIWAN

 https://doi.org/10.1142/9789811275449_0013

shown on the bottom right of the flowchart in Fig. 1, which is a week-2 rainfall forecast from a Mei-yu front case in 2013. From left to right are the observation, raw forecast, and APPM. This case shows that the APPM not only corrects the rainfall pattern and amount of the raw forecasts, but also displays the fine scale details of rainfall. In the final step, the calibrated and downscaled rainfall forecast (APPM) is ingested into the HBV-based hydrological model for reservoir inflow forecasting.

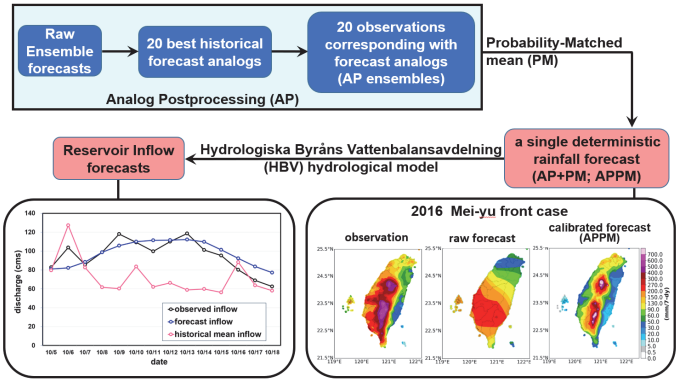

Fig. 1 Flowchart of reservoir inflow forecasting based on post-processed rainfall forecasts.

CALIBRATION AND DOWNSCALING OF RAINFALL FORECASTS

Analog Post-processing (AP)

Figure 2 illustrates the analog post-processing (AP; Hamill and Whitaker 2006; Hamill et al. 2015) for rainfall forecasts. First, we search for the 20 past dates on which the forecasts are most similar to today's forecast. Then the 20 observations corresponding to the forecast analogs are used as the calibrated ensemble forecasts, that is the AP ensemble forecasts mentioned above.

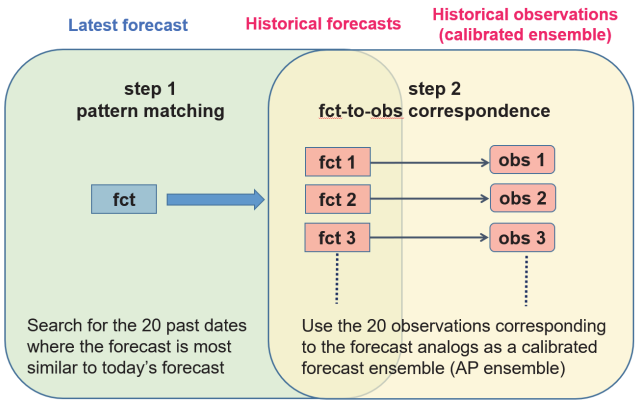

Fig. 2 Schematic diagram of analog post-processing.

Probability-Matched mean (PM)

After obtaining the AP ensemble forecasts, the Probability Matching was applied to the ensemble mean to convert the AP ensemble forecasts into a single deterministic forecast. The purpose is to obtain a single rainfall map, which has the pattern of the ensemble mean with reduced noise compared to the control, but with more realistic rainfall amounts compared to the ensemble mean (Fig. 3).

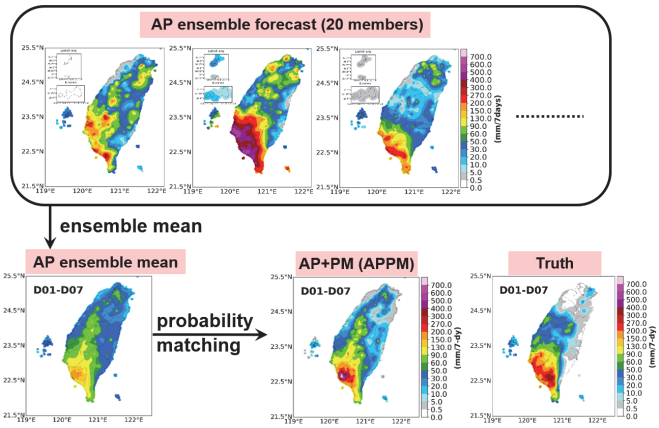

Fig. 3 Illustration of converting the AP ensemble into the APPM, which is used as an input of the HBV-based hydrological model.

RESERVOIR INFLOW FORECASTING

HBV-based Hydrological Model

In order to forecast the reservoir inflow, we need to construct a horological model for simulating the hydrological processes in the reservoir catchment. Then the post-processed rainfall forecasts are used as the input of the hydrological model to forecast the reservoir inflow. This study used a lumped and continuous rainfall-runoff model based on the structure of the Hydrologiska Byråns Vattenbalansavdelning (HBV) hydrological model (Bergström, 1972), which will be called "HBV-based hydrological model" herein. To optimize the model simulation performance, the shuffled complex evolution method (Duan et al. 1992) and fuzzy multi-objective function (Yu and Yang 2000) were used for the calibration of model parameters.

Model Calibration and Validation

The rainfall, temperature, and inflow observation in the Shih-Men reservoir catchment between 2000 and 2019 were used for the model calibration and validation. For being consistent with the rainfall validation, we also used the leave-one-out cross validation procedure. The simulation result shows good correspondence with the observation in inflow amount and tendency (Fig. 4).

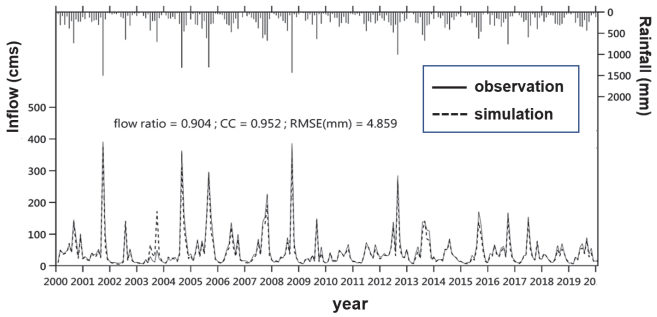

Fig. 4 Validation results from inflow simulation for each year between 2000 and 2019. The solid and dashed curves represent the simulated and observed reservoir inflow in the bottom of the figure, respectively. The thin bar represents the rainfall in the Shih-Men reservoir catchment.

Preprocessing of rainfall data ingestion

Before the reservoir inflow forecasting, a preprocessing of rainfall data ingestion is needed. First, 7-day accumulated rainfall was transformed into daily rainfall because the HBV-based horological model in this work adopted daily rainfall as input. Figure 5 illustrates how to distribute the 7-day accumulated rainfall into each day through averaging, and compute the mean rainfall for different lead times. After obtaining the high-resolution daily rainfall forecast over Taiwan, the mean forecast rainfall of all the grid points over the Shih-Men reservoir catchment was calculated and used as the input of the HBV-based hydrological model to forecast the 1-14 days ahead inflow.

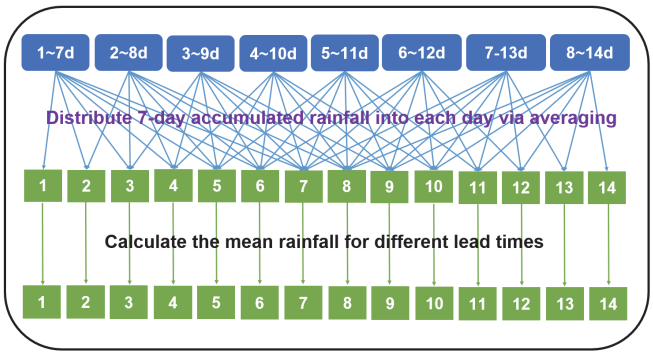

Fig. 5 Illustration of preprocessing of rainfall data ingestion.

Evaluation of reservoir inflow forecasts

The 1-14 days-ahead forecast hydrograph from the case of Typhoon Aere (Fig. 6) shows that the inflow forecasts for the Shih-Men reservoir catchment using the post-processed rainfall forecasts coupling the HBV-based hydrological model performs better than that using the historical mean inflow.

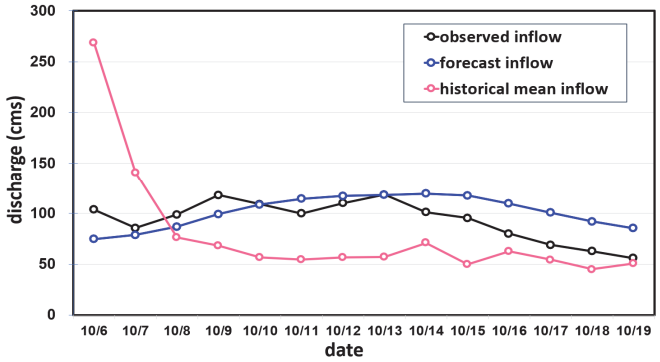

Fig. 6 Forecast hydrograph for the coming 14 days from the case of Typhoon Aere. The black, blue, and red curves display the inflow of the observation, forecast from the HBV-based hydrological model, and historical mean inflow, respectively.

CONCLUSION

The purpose of this study is to produce accurate extended-range reservoir inflow forecasting based on post-processed rainfall forecasts. The 1-14 days post-processed rainfall forecast shows corrected rainfall pattern and amount, and also displays fine scale details of rainfall. The reservoir inflow forecasting using the post-processed rainfall forecasts coupling the HBV-based hydrological model performs better than that using the historical mean inflow.

ACKNOWLEDGEMENTS

This research is sponsored by the Council of Agriculture, Executive Yuan, R.O.C. (111AS-18.2.2-ST-a1).

References

Bergström, S., "Development and application of a digital runoff model," SMHI Notiser och preliminära rapporter, serie HYDROLOGI, No. 22, Norrköping, Sweden (1972).

Duan, Q., Sorooshian, S., and Gupta, V. K., 1992 : Effective and efficient global optimization for conceptual rainfall-runoff models. *Water Resources Research*, **28(4)**, 1015-1031.

Hamill, T. M., and J. S. Whitaker, 2006 : Probabilistic quantitative precipitation forecasts based on reforecast analogs: Theory and application. *Mon. Wea. Rev.*, **134**, 3209 –3229.

––, M. Scheuerer, and G. T. Bates, 2015 : Analog probabilistic precipitation forecasts using GEFS reforecasts and climatology-calibrated precipitation analyses. *Mon. Wea. Rev.*, **143**, 3300–3309.

Yu, P.-S., and T.-C., Yang, 2000 : Fuzzy Multi-Objective Function for Rainfall-Runoff Model Calibration. *Journal of Hydrology*, **238**, 1-14.

CLOUD-CLEARED RADIANCE OF GEOSTATIONARY HYPER-SPECTRAL INFRARED SOUNDER BASED ON COLLOCATED IMAGE

X. Gong[1,2], J. Li[1,2], Z. Li[3], R. Yin[4] and W. Han[4]

ABSTRACT: Geostationary Interferometric Infrared Sounder (GIIRS) onboard Fengyun-4A (FY-4A) satellite provides high-spectral-resolution infrared observations with high temporal resolution of the targeted observing areas. It provides useful information of the atmospheric thermodynamics like temperature and humidity profiles. Due to uncertainties in modeling cloudy radiances, only clear radiances of GIIRS are assimilated in the operational numerical weather prediction (NWP) model. Advanced Geostationary Radiation Imager (AGRI) onboard the FY-4A provides a variety of cloud products with high spatial resolution. Synergistic use of GIIRS and AGRI not only provides sub-pixel cloud information of GIIRS single field-of-view (FOV), but also helps retrieve the cloud-cleared radiances (CCRs) in some cloud regions. The inter-comparisons between GIIRS and AGRI radiance measurements show good agreements; the mean biases of (AGRI - GIIRS) are less than 0.2 K for B12 (10.8 um) and B13 (12.0 um) for clear sky only. The convolved GIIRS CCRs are compared to the mean radiances of AGRI clear pixels (AGRI CLRs); and the GIIRS CCRs are reasonably close to the AGRI CLRs. Furthermore, preliminary results show that 32% more of CCRs than clear sky are added for radiance assimilation in NWP model without consideration of cloud impact for Typhoon Maria (2018) case.

Keywords: GIIRS, AGRI, cloud-cleared radiance, FY-4A

INTRODUCTION

Geostationary Interferometric Infrared Sounder (GIIRS) onboard FengYun-4A (FY-4A) provides infrared (IR) observations of 1650 channels covering 700 ~ 1130 cm−1 and 1650 ~ 2250 cm−1 spectrums with spectral resolution of 0.625 cm-1, and spatial resolution of 16 km for the targeted observing areas. Advanced Geostationary Radiation Imager (AGRI) on FY-4A provides a variety of cloud products with spatial resolution of 2 ~ 4 km for IR bands (Yang et al. 2017). Because of coarse spatial resolution of geostationary (GEO) sounder, up to 80% of IR observations are affected by clouds. Due to difficulties and deficiency in modeling cloudy radiances, usually only clear radiances, clear field-of-views (FOVs) or clear channels that are not affected by clouds, are assimilated in the operational numerical weather prediction (NWP) models (Li et al., 2022). The GIIRS clear observations based on the collocated AGRI cloud masks have been applied to CMA GRAPES 4D_var model and show positive impact on forecasts (Yin et al. 2021).

As an alternative way to utilize cloudy radiances, the cloud-clearing (CC) technique derives the clear equivalent radiances by combining the advanced IR sounder with microwave (MW) sounder or imager (Smith et al. 2004; Li et al. 2005). This allows the sounding information in some cloud regions been assimilated into NWP model, which potentially improves the cloud simulations. The CC technique has been applied to IR sounders (AIRS and CrIS) onboard polar orbiting weather satellites, which show positive impacts on improving hurricane forecasts (Wang et al. 2017). This investigation is focus on applying the CC approach for GEO hyperspectral infrared (IR) sounder using imager onboard the same platform and evaluating the impact of assimilating cloud-cleared radiances (CCRs) on NWP forecasts.

The methodologies and technical approaches for the GIIRS CCRs based on AGRI are developed. The inter-comparisons between GIIRS and AGRI radiance measurements show good agreements for clear sky; and the GIIRS CCRs are compared to the AGRI clear radiances. Besides, preliminary results show that GIIRS CCRs have increased the data yields for radiance assimilation into NWP model without consideration of cloud impact.

COLLOCATION

Since GIIRS and AGRI instruments fly on the same platform FY-4A, they have very different observation modes. The reprocessed GIIRS L1 data for July 10 to 11, 2018, for Typhoon Maria (2018) case (Han et al. 2021) is used in this study. Both the full disk and regional AGRI

[1] Key Laboratory of Radiometric Calibration and Validation for Environmental Satellites, National Satellite Meteorological Center (National Center for Space Weather), CMA, Beijing, 100081, P. R. CHINA
[2] Innovation Center for FengYun Meteorological Satellite, Beijing, 100081, P. R. CHINA
[3] Cooperative Institute for Meteorological Satellite Studies, University of Wisconsin-Madison, Madison, WI, USA
[4] Center for Earth System Modeling and Prediction of CMA, Beijing, 100081, P. R. CHINA

 https://doi.org/10.1142/9789811275449_0014

L1b radiance observations and cloud mask product (CLM) are matched-up with GIIRS observations. Each GIIRS FOV is matched-up with 5×5 AGRI pixels.

INTER-COMPARISON

Only three bands of AGRI (B12 10.8 μm, B13 12.0 μm, and B14 13.3 μm) that have full spectral coverages over GIIRS spectrums are used. For each GIIRS FOV, the GIIRS radiances are spectrally convolved with respect to the spectral respond functions (SRFs) of AGRI bands; the AGRI radiances are spatially averaged with respect to the point distribution function (PDF) of GIIRS FOV; the cloud fraction and mean radiance of AGRI clear pixels (AGRI CLR) are calculated as well. Fig. 1 shows the brightness temperatures (BTs) of a randomly selected GIIRS FOV overlapped with the SRFs of AGRI bands. Fig. 2 shows the AGRI 10.8 μm BT (K) and CLM before and after collocation with GIIRS.

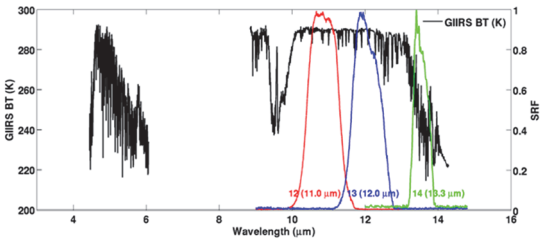

Fig. 1 The brightness temperatures (BTs) of a GIIRS FOV overlapped with the spectral respond functions (SRFs) of AGRI band B12, B13 and B14.

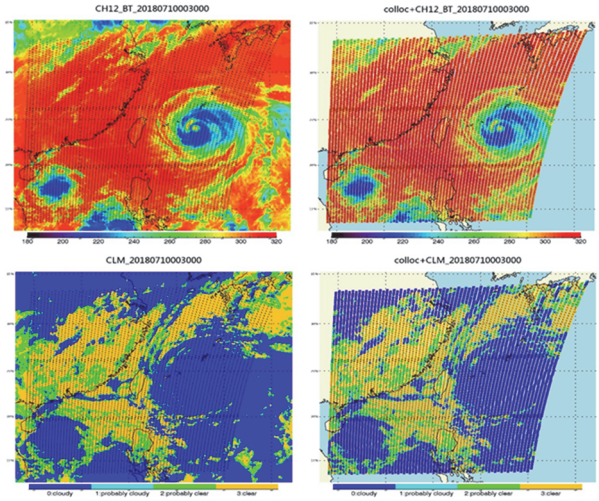

Fig. 2 The AGRI 10.8 μm BT (K) (top) and cloud masks (CLM) (bottom) before and after collocation with GIIRS

Fig. 3 shows the mean biases of (AGRI – GIIRS) versus cloudiness of GIIRS FOVs for band B12, B13 and B14. Overall, the inter-comparisons between GIIRS and AGRI show good agreements. For B12 and B13, the mean biases are less than 0.2 K for clear sky; the more clouds, the larger the mean biases. For B14, the CO2 absorption band, the mean biases are around 0.6 ~ 0.9 K for clear sky and partially cloudy. For all three bands, the mean biases are less than -1.0 K for overcasts.

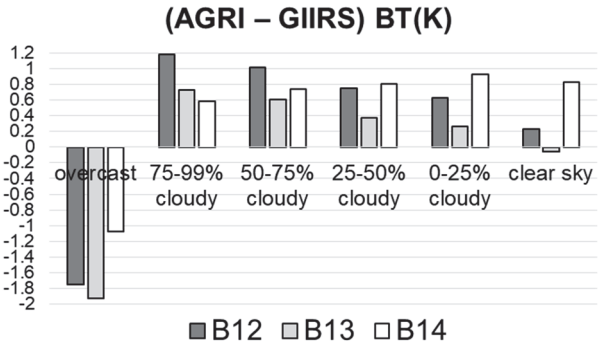

Fig. 3 The mean biases of (AGRI – GIIRS) versus cloudiness for AGRI band B12, B13 and B14.

CLOUD-CLEARING

In order to remove the cloud effect, homogeneousness is assumed in both clear and cloudy portions. Therefore, the radiance differences between the two adjacent GIIRS FOVs are solely caused by the cloud coverages. Li et al. (2005) introduces the optimal CC approach for AIRS based on 9 IR (four CO2 and two H2O) bands of MODIS. As for CrIS/VIIRS, due to lack of absorption bands, additional quality controls (QCs) are needed to remove those prone to amplified noises or violating homogeneous assumption (Wang et al., 2017).

AGRI has only 3 IR (two window and one CO2) bands overlapped with GIIRS temperature sounding channels between 700 ~ 1130 cm^{-1}. The convolved GIIRS CCRs are compared to the AGRI CLR radiances. Due to large instrument errors of band B14, further QC is required to make sure that GIIRS CCRs are close enough to AGRI CLR radiances for absorption channels. The absolute bias of (AGRI CLR – GIIRS CCR) should be less than 2×NEdT for each band. Fig. 4 shows the mean biases of (AGRI CLR – GIIRS CCR) for cloudiness of 0-25%, 25-50%, 50-75%, as well as the mean biases of (AGRI - GIIRS) for clear sky. Results show that the GIIRS CCRs are reasonably close to the AGRI CLR radiances for partially cloudy.

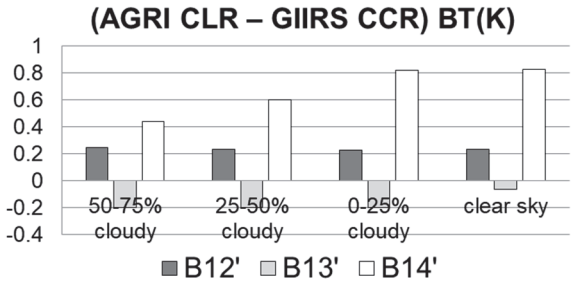

Fig.4 The mean biases of (AGRI CLR – GIIRS CCR) for cloudiness of 50-75%, 25-50%, 0-25%, as well as the mean biases of (AGRI - GIIRS) for clear sky, for AGRI band B12, B13 and B14.

Fig. 5 shows AGRI 10.8 μm BT (K) and CLM with the round spot (or diamond) represents for clear sky (or CC successful FOVs). The CCRs fills in the blocks between clear skies and overcasts. Fig. 6 shows the GIIRS L1 original and CCR BTs (K) of a GIIRS FOV with 68% cloudiness. The cloud effect is removed by the CC approach.

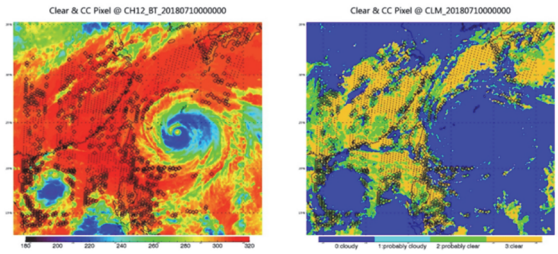

Fig. 5 The AGRI 10.8 μm BT (K) (left) and CLM (right) with the round spot (or diamond) represents for GIIRS clear sky (or CCR successful FOVs).

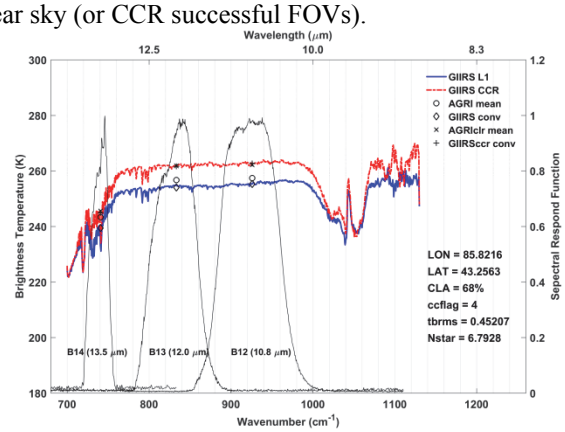

Fig. 6 The GIIRS L1 original and CCR BTs (K) of a GIIRS FOV with 68% cloud fraction.

In this study, for Typhoon Maria (2018) case, around 22% FOVs are clear skies, while 41% FOVs are overcasts. The CC approach is applied to all partially cloudy FOVs. Around 12% of all sky (32% of partially cloudy) is cloud-cleared with additional QCs, which significantly increases the data yields for radiance assimilation in NWP model without consideration of cloud impact. Preliminary results show that assimilation of GIIRS clear radiances has positive impacts on the hurricane track forecasts (Yin et al., 2021); and assimilation of CCR further improves that.

SUMMARY

Synergistic use of GIIRS and AGRI onboard FY-4A not only provides sub-pixel cloud information of GIIRS FOV, but also helps retrieve CCRs in some cloud regions. The methodologies and technical approaches for inter-comparison and retrieval of CCRs are developed. Results show that GIIRS and AGRI have good agreements for clear sky; and GIIRS CCRs are reasonably close to AGRI CLR radiances. Around 32% more CCR data than clear sky are added for radiance assimilation in NWP model.

ACKNOWLEDGEMENTS

This work is supported by the National Natural Science Foundation of China (41909058). The data used in this study is obtained from NSMC.

References

Han, W., and Yin, R. (2021). FY-4A GIIRS targeted observations for Typhoon Maria (2018) with high temporal resolution of 15 minutes (Version 1.0) [Dataset]. Zenodo. Doi:10.5281/zenodo.4656877.

Li, J., Geer, A. J., Okamoto, K., Otkin, J. A., Liu, Z., Han, W. and Wang, P. (2022). Satellite all-sky infrared radiance assimilation: Recent progress and future perspectives. Advances in Atmospheric Sciences, 39(1), 9–21.

Li, J., Liu, C. Y., Huang, H. - L., Schmit, T. J., Menzel, W. P. and Gurka, J. (2005). Optimal cloud - clearing for AIRS radiances using MODIS. IEEE Transactions on Geoscience and Remote Sensing, 43(6), 1266–1278.

Smith, W. L., Zhou, D. K., Huang, H.-L., Li, J., Liu, X., and Larar, A. M., (2004) Extraction of profile information from cloud contaminated radiances, in Proc. ECMWF Workshop on Assimilation of High Spectral Resolution Sounders in NWP, Jun. 28–Jul. 1 2004, pp. 145–154.

Wang, P., Li, J., Li, Z., Lim, A. H., Li, J., Schmit, T. J., and Goldberg, M. D. (2017). The impact of Cross-track Infrared Sounder (CrIS) cloud-cleared radiances on Hurricane Joaquin (2015) and Matthew (2016) forecasts. Journal of Geophysical Research: Atmospheres, 122(24), 13201–13218.

Yang, J., Zhang, Z., Wei, C., Lu, F., and Guo, Q. (2017). Introducing the new generation of Chinese geostationary weather satellites, Fengyun-4. Bulletin of the American Meteorological Society, 98(8), 1637–1658.

Yin, R., Han, W., Gao, Z., and Li, J. (2021). Impact of high temporal resolution FY-4A geostationary interferometric infrared sounder (GIIRS) radiance measurements on typhoon forecasts: Maria (2018) case with GRAPES global 4D-Var assimilation system. Geophysical Research Letters, 48(15), e2021GL093672.

IMPACTS OF ASSIMILATION FY2G AND FY4A ATMOSPHERIC MOTION VECTORS ON TYPHOON PREDICTION

Peigen Guan[1] and Keyi Chen[1]

ABSTRACT: Atmospheric motion vectors (AMVs) have produced positive impacts on global weather forecasts, but few studies have evaluated the impacts of AMVs data from Fengyun (FY) geostationary satellite series, especially from FY-2G and FY-4A, on typhoon forecasts in a regional model. In this study, the AMVs data of FY-2G and FY-4A were compared and evaluated by pre-processing methods such as height assignment, quality control, channel combination and thinning. Typhoon Haishen (No.10 super typhoon in 2020) was taken as an example. The AMVs data of the two satellites were assimilated by using 3DVAR provided by WRFDA and simulated by the WRF model to evaluate the forecast results of the two satellites, respectively. The results show that the AMV data from FY-4A are better overall than those from FY-2G, with smaller RMSEs and biases for full wind speeds. On the other hand, assimilation of AMVs data improves the forecasts of environmental fields, resulting in the simulated track closer to the best track. Another experiment shows that the assimilation of AMVs data has a good impact on precipitation prediction In general, the assimilation of FY-2G and FY-4A AMV data has a relatively positive impact on typhoon prediction, and the AMVs data combined with multiple channels can provide better prediction.

Keywords: Assimilation, Atmospheric Motion Vectors, Typhoon

INTRODUCTION

As early as the 1970s, China began to research and develop meteorological satellites. FY-4 is China's second-generation geostationary meteorological satellite.

Atmospheric motion vector (AMV) is one of the inversion products of Fengyun series satellites. Wan Xiaomin et al. (Wan et al, 2017) used GRAPES numerical model to assimilate AMVs data before and after the improvement of inversion algorithm of FY-2E meteorological satellite cloud guide product in 2014, and compared and analyzed their observation distribution and deviation characteristics, and found that the FY-2E infrared channel cloud track wind product after the improved algorithm improved the GRAPES numerical model assimilation and prediction to some extent. Liu Rui et al. (Liu et al., 2012) used WRF-3DVAR assimilation system to assimilate AMVs data products retrieved from FY-2C infrared and water vapor channels, and found that reasonable selection of AMVs data to be added to the model was beneficial to supplement the mesoscale information not included in the initial field of the model, so as to improve the prediction ability of the model. As indirect satellite observation data, AMVs products can help us make full use of satellite observation and inversion products by studying their effects on assimilation and forecast. Therefore, this paper will study the assimilation and forecast influence of the AMVs products of FY-4 series satellites.

DATA AND MODEL

In order to study the influence of assimilating atmospheric motion vector product of FY-4 on typhoon prediction, and to compare the differences between the old and new generations of FY-4 series satellites, the AMVs data used in this study are atmospheric motion vector products derived from infrared and water vapor channel inversion of FY-4A and FY-2G geostationary satellites provided by The National Satellite Meteorological Center of China (NSMC).

The analytical data used in this paper are FNL global reanalysis data provided by NCEP/NCAR. The temporal resolution of the data is 6h (0000 UTC, 0600 UTC, 1200 UTC, 1800UTC), and the spatial resolution is 0.25°x 0.25°. The vertical direction is 1000hPa to 10hPa, a total of 26 layers.

The WRF (Weather Research and Forecasting Model) model and WRFDA (Weather Research and Forecasting Model Data Assimilation) are used in this paper Assimilation system for this study. WRF model and WRFDA assimilation system are mesoscale prediction models and data assimilation systems jointly developed by the Center for Environmental Prediction (NCEP) and the National Center for Atmospheric Research (NCAR).

ASSIMILATION EXPERIMENT

The first typhoon case we selected was the 10th typhoon "Haishen" in the Pacific Ocean in 2020. A total of 9 groups of experiments were set up for typhoon "Haishen", including 1 group of control tests and 8 groups

[1] Chendu University of Information Technology, Chengdu, CHINA

 https://doi.org/10.1142/9789811275449_0015

of cyclic assimilation tests. The control experiment will not assimilate any AMVs data and will serve as a control for all assimilation experiments. Eight groups of cyclic assimilation experiments were performed to assimilate FY-2G infrared channel AMVs data, FY-2G water vapor channel AMVs data, FY-2G combined AMVs data, FY-4A infrared channel AMVs data, FY-4A water vapor channel AMVs data, FY-4A three channels combined AMVs data and FY-2G+FY-4A five channels combined AMVs data. (see Table 1 for specific experimental Settings).

Table 1 Assimilation experiment Settings

Experiments	ID	Settings
control	CONT	Without data assimilation
cyclic assimilation	FY2G-IR	FY-2G AMVs data from infrared channel
	FY2G-WV	FY-2G AMVs data from water vapor channel
	FY2G-IR+WV	FY-2G AMVs data from combined channel
	FY4A-IR	FY-4A AMVs data from infrared channel
	FY4A-WV1	FY-4A AMVs data from lower water vapor channel
	FY4A-WV2	FY-4A AMVs data from higher water vapor channel
	FY4A-IR+WV	FY-4A AMVs data from combined channel
	FY2G+FY4A	FY-2G+FY-4A five channels combined AMVs data

The region shown in FIG. 1 is selected as the simulation region of this experiment. The selection center is (30°N, 130°E), the grid number is 300×300, the horizontal resolution of the mode is 15km, and the vertical direction is 40 eta layers with unequal distances. The drive field data are FNL0.25°x0.25° reanalysis data from NCEP. The assimilated data came from the AMVs data after the quality control of IR1 and IR3 channels of FY-2G and the AMVs data (within the region) after the quality control of C009, C010 and C012 channels of FY-4A. The parameterized scheme is shown in Table 2.

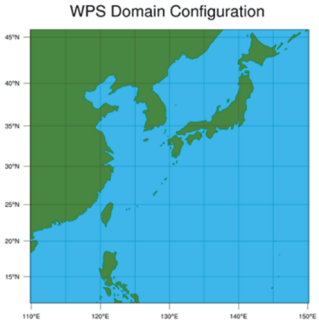

Figure 1 Numerical experiment of Typhoon "Haishen"

Table 2 Parameterization scheme of typhoon Poseidon numerical experiment(Liang et al., 2018)

parameterization schemes	settings
Microphysics scheme	Lin
Cumulus convection scheme	Kain-Fritsch scheme
radiation scheme	RRTMG /RRTMG
Planetary boundary layer scheme	Yonsei University scheme
Land-surface scheme	MM5 similarity

In the experiment of "Haishen", we use CMA optimal path data to verify the simulated path and intensity of typhoon "Haishen". FIG. 2a-c shows the typhoon track simulation of this assimilation experiment. From the perspective of typhoon path prediction, the assimilation of AMVs data can significantly improve the deviation of typhoon path simulation in the control experiment, effectively correct the typhoon path and make the forecast path closer to the real situation of typhoon movement.

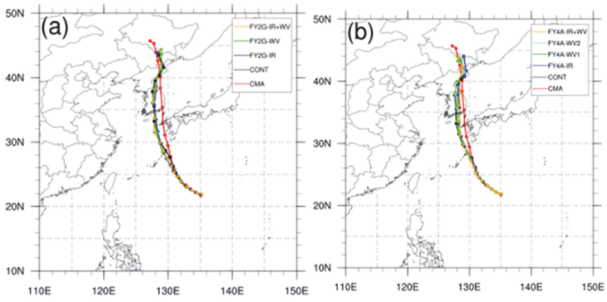

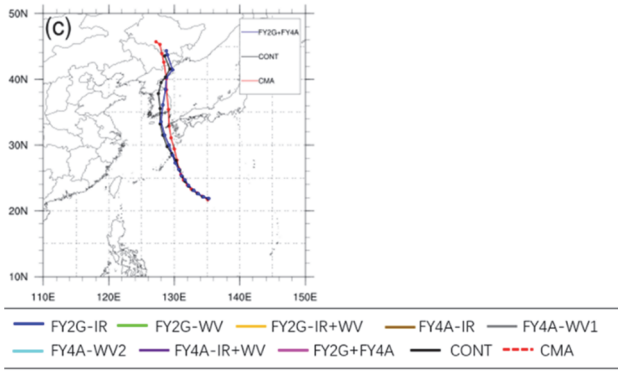

Figure 2 a. Assimilation FY-2G AMVs typhoon "Haishen" path forecast b. assimilation FY-4A AMVs typhoon "Haishen" path forecast c. assimilation FY-2G+FY4A AMVs typhoon "Haishen" path forecast

In the experiment of Typhoon "In-Fa", 9 groups of experiments were still set, and the experimental Settings were consistent with those of Typhoon "Haishen" (see Table 2 for specific Settings). FIG. 3-a shows the actual 24-hour UTC precipitation from 2020.7.27.00 to 2020.7.28.00. The precipitation data comes from 2421 national meteorological observation stations in China. FIG. 3 (b-j) shows the precipitation simulation results of the control experiment and eight groups of cyclic assimilation experiments.

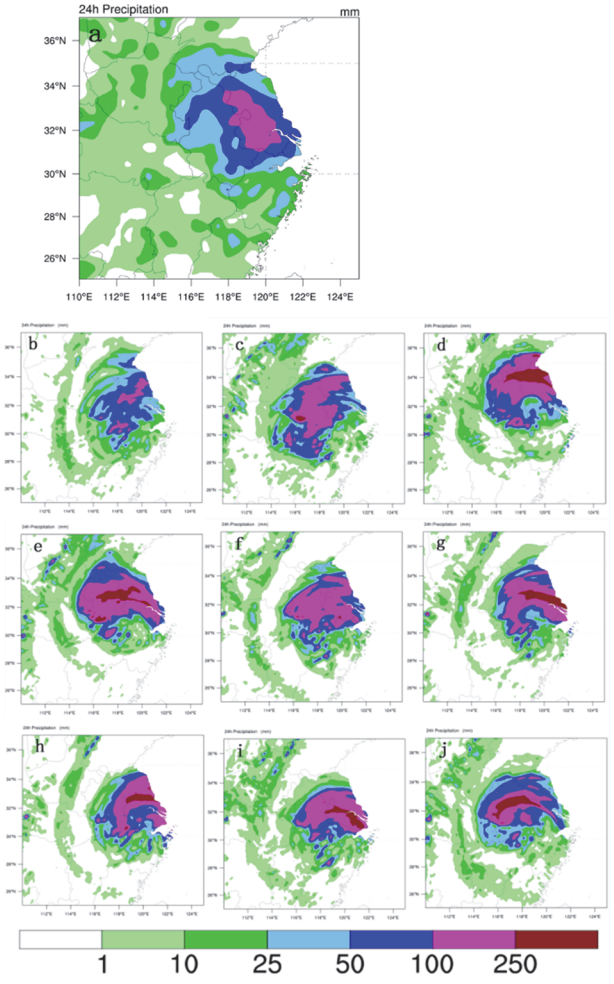

Figure 3 Comparison of 24-hour precipitation (a. Actual precipitation b. Control experiment c. Assimilation FY2G-IR d. Assimilation FY2G-WV e. Assimilation FY2G-IR+WV f. Assimilation FY4A-IR g. Assimilation FY4A-WV1 h. Assimilation FY4A-WV2 i. Assimilation FY4A-IR +WV j. Assimilation FY2G+FY4A)

According to the experimental results of Typhoon "In-Fa", the AMVs data from FY-4A satellite perform better in precipitation prediction.

SUMMARY

Eight sets of cyclic assimilation experiments and one set of control experiments were used to study the influence of AMVs data of assimilation Fengyun satellite on Typhoon "Haishen" and "In-Fa". The experimental results showed that assimilation Fengyun satellite AMVs could effectively correct the path deviation of control experiment and improve the typhoon path prediction effect. Assimilation of FY-4A AMVs could obtain typhoon path prediction closer to observation.

Assimilation of AMVs may lead to larger precipitation simulation, in which AMVs assimilating water vapor channel are more likely to have higher precipitation simulation than AMVs assimilating infrared channel. Channel consolidation can improve the situation of high precipitation simulation to a certain extent. Assimilation Fengyun-4 satellite AMVs data can simulate the location of precipitation center better.

References

Wan Xiaomin, Tian Weihong, Han Wei, et al (2017). Improvement of FY-2E Cloud Track Wind Algorithm and Its Assimilation Application in GRAPES [J]. Meteorological Monthly, 2017 (01, 2017): 1-10.

Liu Rui, Zhai Guoqing, Wang Zhanggui, et al (2012). Experimental study on the influence of FY-2C Cloud Track Wind Data Assimilation on typhoon forecast [J]. Chinese Journal of Atmospheric Sciences, 2012, 36(2): 350-360.

Liang Jiahao, Chen Keyi (2018). Effects of FY-2G Cloud AMVs data assimilation on typhoon numerical forecast [C]// The 35th Annual Meeting of Chinese Meteorological Society S9 satellite data assimilation.

ASSIMILATION OF SOIL MOISTURE IN THE STRONGLY COUPLED ATMOSPHERE-LAND SURFACE DATA ASSIMILATION SYSTEM

S. Lim[1,2], S. K. Park[1,2,3] and M. Zupanski[4]

ABSTRACT: Soil moisture is essential in numerical weather prediction using a coupled atmosphere-land surface model because it affects the latent and sensible fluxes, emission from the land surface, and eventually the atmospheric variables, especially temperature, water vapor mixing ratio, and precipitation. Therefore, soil moisture observations in a coupled atmosphere-land surface data assimilation system can provide useful information for both land surface and atmosphere. The National Aeronautics and Space Administration's Soil Moisture Active Passive (SMAP) mission provides space-borne observations of soil moisture and freeze/thaw state: the L-band microwave radiometer aboard SMAP observes soil moisture at the top 5 cm of the land surface, having nearly global coverage every 2-3 days with a 1000 km swath. In this study, we employ the Maximum Likelihood Ensemble Filter (MLEF) to assimilate the SMAP 9-km enhanced soil moisture retrievals into the Noah land surface model (Noah LSM or simply Noah) coupled with the Weather Research and Forecasting (WRF) model. As a strongly coupled atmosphere-land data assimilation system, MLEF simultaneously corrects atmospheric and land surface variables. For the soil moisture assimilation, the observation processing includes quality control, thinning, statistical bias correction, and horizontal and vertical covariance localization. To investigate the soil moisture impacts on the coupled data assimilation, we assimilate both soil moisture and atmospheric observations — the SMAP soil moisture retrievals and the National Centre for Environmental Prediction (NCEP) Prepared Binary Universal Form for the Representation of meteorological data (PrepBUFR), respectively. Our results indicate that the WRF-Noah-MLEF system generates analysis increments of soil moisture that provide additional information to atmospheric variables, especially in the lower atmospheric layers, through cross-covariance between land and atmosphere.

Keywords: Soil Moisture, Satellite Observation, Coupled Data Assimilation, Maximum Likelihood Ensemble Filter

INTRODUCTION

Soil moisture is important in numerical weather prediction (NWP) because it affects the latent and sensible fluxes, emission from the land surface, and eventually the atmospheric variables (e.g., temperature and moisture, etc.). Thus, the soil moisture observations in a coupled data assimilation system can provide useful information on both the land surface and the atmosphere through the cross-variable components of a coupled error covariance (Park et al., 2015).

In this study, we have developed the soil moisture assimilation system within a strongly coupled atmosphere-land data assimilation system. Compared with atmospheric data assimilation systems, we investigate how the coupled data assimilation system produces analysis increments of atmospheric variables, especially in the lower atmospheric layers, as well as land surface variables.

DATA AND MODEL

Soil Moisture Active Passive (SMAP)

We use the National Aeronautics and Space Administration's Soil Moisture Active Passive (SMAP) enhanced L2 radiometer half-orbit 9 km EASE-grid soil moisture, which provides space-borne observations of soil moisture and freeze/thaw state derived from brightness temperatures (TBs). The L-band microwave radiometer aboard SMAP observes soil moisture (in $m^3\ m^{-3}$) at the top 5 cm of the land surface, having nearly global coverage every 2-3 days with a 1000 km swath.

Strongly Coupled Data Assimilation System

The Weather Research and Forecasting (WRF) version 4.3.3 coupled with the Noah Land Surface Model (Noah LSM or Noah) describes interactions between short-term weather changes and land surface changes. In particular, Noah LSM simulates the soil variables,

[1] Center for Climate/Environment Change Prediction Research, Ewha Womans University, 52 Ewhayeodae-gil, Seodaemun-gu, Seoul 03760, REPUBLIC OF KOREA
[2] Severe Storm Research Center, Ewha Womans University, 52, Ewhayeodae-gil, Seodaemun-gu, Seoul, 03760, REPUBLIC OF KOREA
[3] Department of Climate and Energy System Engineering, Ewha Womans University, 52, Ewhayeodae-gil, Seodaemun-gu, Seoul, 03760, REPUBLIC OF KOREA
[4] Cooperative Institute for Research in the Atmosphere, Colorado State University, Fort Collins, Colorado, 80524, USA

 https://doi.org/10.1142/9789811275449_0016

including soil temperature or soil moisture, and provides the radiative and heat fluxes between the ground and the atmosphere using four soil layers (e.g., 10, 30, 60, and 100 cm thickness). As a data assimilation system, we use the Maximum Likelihood Ensemble Filter (MLEF) — a hybrid ensemble-variational data assimilation system (e.g., Zupanski, 2005; Lim et al., 2015). It updates the control variables through the iterative minimization of a cost function and uses information on the flow-dependent error covariance.

SOIL MOISTURE ASSIMILATION

To assimilate the soil moisture observation within a strongly coupled data assimilation system, we have developed the observation operator to assimilate the soil moisture and included the land surface variables such as soil moisture and temperature in the control variables. As a result, MLEF simultaneously corrects the atmospheric and land surface variables through the cross-components of the coupled error covariance.

We obtain all observations passing over our study domain within a 6-hour assimilation window (Fig. 1). Then, it should satisfy the following quality control conditions: i) observation should be larger than zero; ii) we use only recommended retrieval quality flag; iii) the observation have to pass over the study domain; iv) observation innovation (i.e, observation minus model) must be smaller than 3. The observation operator conducts horizontal interpolation when grid points are located on land. We apply an observation error (0.06 m^3 m^{-3}) and a statistical bias correction. The horizontal localization length scale is set to be 250 km while the vertical localization sets propagate the observation information to the land by 5 % and the atmosphere by 95 %.

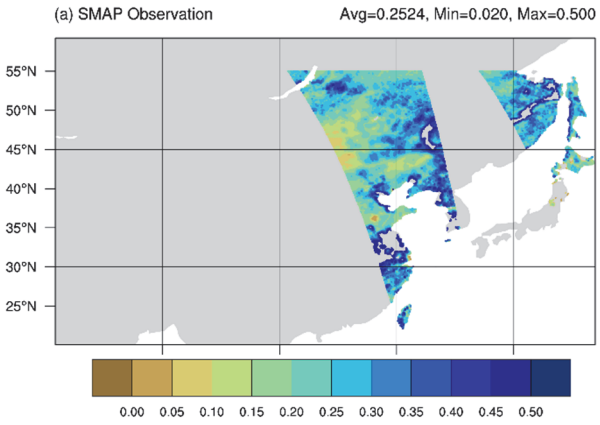

Fig. 1 (a) The SMAP soil moisture observation at 07:12 UTC and 08:51 UTC 06 July 2021.

EXPERIMENTAL DESIGN

To investigate the soil moisture impacts on the coupled data assimilation system, we designed our experiments as follows: i) Experiment PREP assimilates only the conventional atmospheric observation, which is PrepBUFR, ii) Experiment SMAP assimilates only the SMAP L2 soil moisture retrievals, iii) Experiment PREP+SMAP assimilates the above two observations at once. The experimental period is from 00 UTC on 2 July 2021 to 18 UTC on 6 July 2021. Forty ensembles are used with a 30 km horizontal resolution and 34 vertical layers up to 50 hPa.

As for the verification, we selected the model result on 06 UTC 6 July 2021 and compared it with reanalysis data (e.g., MERRA2 or ERA5) through spatial interpolation and regridding. Although the reanalysis data contain uncertainty, they can be easily compared with our model results as they are global and gridded. Soil moisture is additionally verified with the ERA5-Land and in-situ observations, the Automated Agriculture Observing System (AAOS), at the top soil layer.

RESULTS

The coupled data assimilation system successfully reduces the root mean square error (RMSE; Table 1) from the background to the analysis. It turns out that assimilating both the atmospheric and soil moisture data (i.e., PREP+SMAP) exerts less impact on atmospheric variables than assimilating the atmospheric data only (i.e., PREP); however, the former exerts stronger impact on soil moisture than the latter.

Table 1 Reduction of RMSE (%) from the background to the analysis during the experimental periods with respect to atmospheric variables (e.g., temperature, specific humidity, zonal wind, and meridional wind) and soil moisture.

Experiments	PREP	SMAP	PREP+SMAP
Temperature	5.82	-	2.20
Specific humidity	2.50	-	0.56
Zonal wind	12.34	-	4.46
Meridional wind	13.25	-	5.37
Soil moisture	-	3.47	3.93

We also investigated the analysis increment (i.e., analysis minus background) to correct the background error (Fig. 2). Note that, when the soil moisture is not assimilated (i.e., PREP), the analysis increment of soil moisture is small; however, when the soil moisture is assimilated (i.e., SMAP or PREP+SMAP), additional

analysis increments for soil moisture are created on the observation path. As a result, it reduces the RMSE of soil moisture against MERRA2 reanalysis data. It also affects the atmospheric variables through the cross-components of the coupled error covariance. For example, the positive analysis increment of soil moisture generates a positive (negative) correlation to the analysis increment of specific humidity (temperature) in the lower atmospheric layers. As a preliminary result, the impact of soil moisture observation is much stronger than that of atmospheric observation. Thus, we need further study to balance both observations to improve soil moisture and atmospheric variables simultaneously.

CONCLUSION

The strongly coupled atmosphere-land surface data assimilation system (e.g., WRF-Noah-MLEF system) successfully reduces the RMSE from the background to the analysis of the land surface and atmospheric variables. The WRF-Noah-MLEF system provides the analysis increments for soil moisture in the land surface model and temperature with negative correlation and specific humidity with positive correlation in the atmosphere model. As a further study, we will adjust the coupled data assimilation system (e.g., observation error, localization lengths, inflation methods, etc.) to improve temperature and specific humidity in the lower atmosphere, and precipitation as well as soil moisture.

ACKNOWLEDGEMENTS

This research is supported under the grant of Basic Science Research Program through the National Research Foundation of Korea (NRF) funded by the Ministry of Education (2018R1A6A1A08025520). It is partly supported by the NRF grant funded by the Korea government (MSIT) (NRF-2021R1A2C1095535).

References

Lim, S. J., Park, S. K., Zupanski, M.: Ensemble data assimilation of total column ozone using a coupled meteorology– chemistry model and its impact on the structure of Typhoon Nabi (2005). Atmos. Chem. Phys., 15, 10019-10031. doi:10.5194/acp-15-10019-2015, 2015.

Park, S. K., Lim, S., Zupanski, M.: Structure of forecast error covariance in coupled atmosphere–chemistry data assimilation. Geosci. Model Dev., 8, 1315-1320. doi: 10.5194/gmd-8-1315-2015, 2015.

Zupanski, M.: Maximum Likelihood Ensemble Filter: Theoretical Aspects, Mon. Wea. Rev., 133, 1710–1726, 2005.

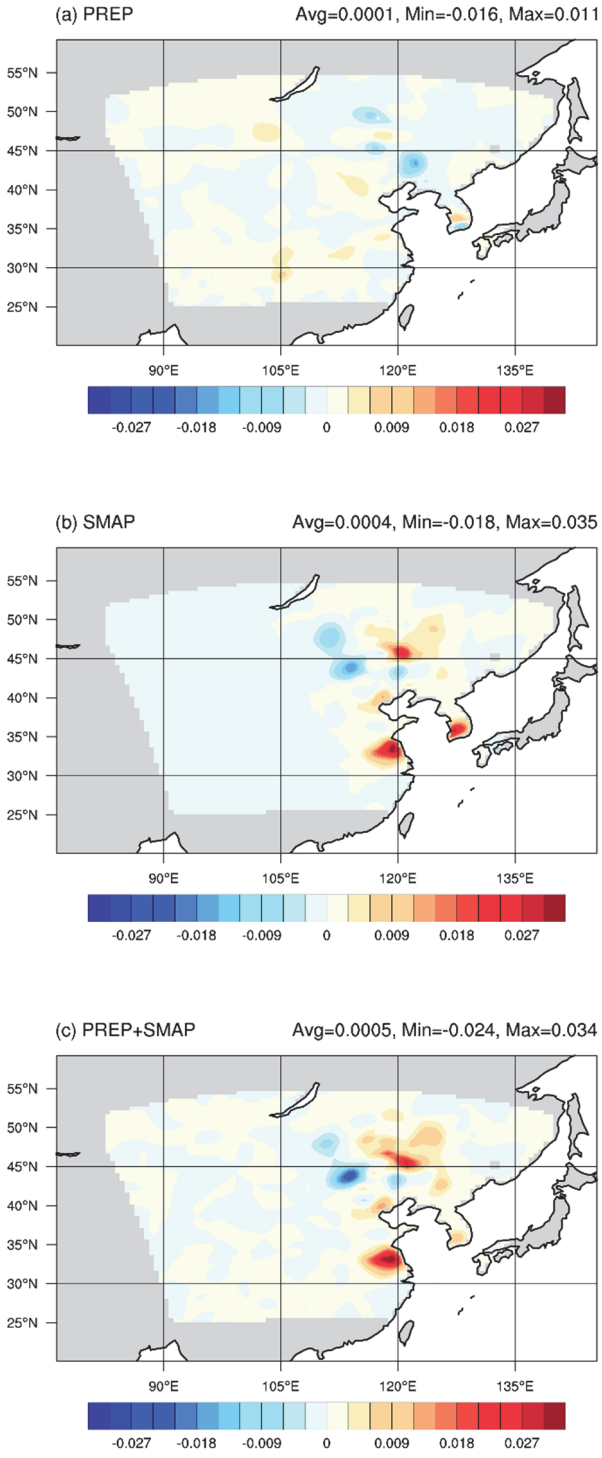

Fig. 2 Analysis increments of soil moisture at the topsoil layer on 06 UTC 6 July 2021 for (a) PREP, (b) SMAP, and (c) PREP+SMAP.

IMPROVING AIR QUALITY PREDICTIONS THROUGH OPTIMIZATION OF OPTIONAL PHYSICAL PARAMETERIZATION SCHEMES IN WRF-CHEM USING MICRO-GENETIC ALGORITHM

Ji Won Yoon[1,2], Ebony Lee[2,3], Sujeong Lim[1,2], Seungyeon Lee[2,3] and Seon Ki Park[1,2,3]

ABSTRACT: This study aims to improve the air quality forecasting skill in East Asia by employing the Weather Research and Forecasting model coupled with Chemistry (WRF-Chem) and by selecting its optimal set of physical parameterization schemes, especially in the planetary boundary layer (PBL) and land surface (LS) processes, via the micro-genetic algorithm (μGA). Among a bunch of available options (8 PBL schemes and 4 LS schemes), the selected optimal schemes are the Asymmetric Convective Model, version 2 (ACM2) for PBL and the Noah land surface model with multiple parameterization options (Noah-MP) for LS, respectively. For the given Asian dust storms cases, the WRF-Chem, using the optimized schemes, resulted in higher correlation coefficients with observations in all variables, including aerosol optical depth, PBL height, temperature and relative humidity at 2 m, and wind speed and direction at 10 m, than using the other sets of parameterization schemes.

Keywords: WRF-Chem, Micro-Genetic Algorithm, Asian dust storms, Parameterization scheme, optimization.

INTRODUCTION

In these days, the problems of air pollution through human economic activity and high energy consumption are rising in East Asia due to the rapid economic growth. Therefore, in order to alleviate the air quality-related problems, it is necessary not only to improve the national and local air pollution control measures but also to predict the air quality more accurately through a numerical modeling system. In particular, the air quality prediction is highly dependent on the land surface and the planetary boundary layer (PBL) parameterization schemes in a coupled meteorology-chemistry model, such as the Weather Research and Forecasting model coupled with Chemistry (WRF-Chem; Banks & Baldasano, 2016; Rizza et al., 2018). Therefore, in this study, to improve the air quality forecasting skill in East Asia, we designed an optimization system by applying the micro-genetic algorithm (μGA) coupled with the WRF-Chem model (i.e., the WRF-Chem-μGA system) and found an optimal set of the physical parameterization schemes for the air quality forecasting.

METHODOLOGY AND DATA

Cases of Asian Dust Storms

The Asian dust storm (ADS) cases that affected South Korea from 2002 to 2020 were classified into five types: A, B, C, D, and E, by considering the source regions and the transport routes of the ADSs (Kim et al., 2020). In Type A, the ADSs originate from the Gobi Desert, pass through Bohai Bay, and then affect South Korea: it accounted for 52 % of all the cases. We selected six cases from Type A: 4-8 May 2016, 21-24, May 2018, and 4-7 April 2018 for optimization; and 7-10 April 2016, 4-7 May 2017, and 9-11 May 2020 for validation that are expressed as CASE1, CASE2, and CASE3, respectively.

Micro-Genetic Algorithm

The GA is a global optimization algorithm based on Charles Darwin's theory of natural evolution (Holland, 1973; Holland, 1975). The three critical operators in the optimization processes of GA are selection, crossover, and mutation. The selection operator selects individuals from a population to inherit their genes to the next generation based on the fitness function. The crossover operator generates new offspring from the chromosomes of two parents. The mutation operator alters some of the offspring's genes to keep up genetic diversity in the next generation. The generations produced through these operators continue to evolve until the best solution is found or the maximum generation is satisfied. However, it requires excessive computing resources to search for optimal solutions. The μGA used in this study effectively reduces the computing resources by applying

[1]Severe Storm Research Center, Ewha Womans University, 52, Ewhayeodae-gil, Seodaemun-gu, Seoul, REPUBLIC OF KOREA.
[2]Center for Climate/Environment Change Prediction Research, Ewha Womans University, 52, Ewhayeodae-gil, Seodaemun-gu, Seoul, 03760, REPUBLIC OF KOREA.
[3]Department of Climate and Energy System Engineering, Ewha Womans University, 52, Ewhayeodae-gil, Seodaemun-gu, Seoul, 03760, REPUBLIC OF KOREA.

 https://doi.org/10.1142/9789811275449_0017

reinitialization instead of the mutation operator and requiring a smaller population than GA (Krishna-kumar, 1990).

We designed the WRF-Chem-μGA optimization system to find an optimal combination of the physical parameterization schemes for the air quality and weather prediction.

Experimental Design

We used the WRF-Chem version 4.2.2, which is a fully coupled meteorology-chemistry model (Grell et al., 2005). The horizontal grid spacing is 30 km with 50 vertical levels. The meteorological initial and boundary conditions are provided from the Global FNL (Final) generated by the National Centers for Environmental Prediction's Global Forecast System. The chemical initial and boundary conditions are derived from the Community Atmosphere Model with Chemistry generated by the National Center for Atmospheric Research's Community Earth System Model. The default physics schemes are the Morrison microphysics scheme, the Grell 3D ensemble convective parameterization scheme, and the RRTMG short- and long-wave radiation schemes, except for the PBL and land surface schemes. For chemistry, the Model for Ozone and Related Chemical Tracers (MOZART-4) gas-phase chemical mechanism coupled with the Goddard Chemistry aerosol Radiation and Transport (GOCART) aerosol scheme (MOZART-GOCART) is selected. The anthropogenic emissions are based on the EDGAR-HTAP global emission inventory.

As an experimental study to find the optimal set of physical parameterization schemes using a testbed system, we selected a total of 12 parameterization schemes out of two categories of physical processes in WRF-Chem: eight schemes in the PBL process and four schemes in land surface physics. The PBL schemes include the non-local closure schemes (i.e., the YonSei University; YSU, Asymmetric Convective Model, version 2; ACM2, and Total Energy-Mass Flux; TEMF) and the local closure schemes (i.e., Mellor–Yamada–Janjic; MYJ, Quasi-Normal Scale Elimination; QNSE, Mellor–Yamada–Nakanishi–Niino level-2.5; MYNN2, Bougeault–Lacarrere; BouLac, and University of Washington; UW). The LS schemes (i.e., land surface models; LSMs) include Noah, Rapid Update Cycle (RUC), Noah land surface model with multiple parameterization options (Noah-MP), and Community Land Model version 4.0 (CLM4).

The fitness function is used to evaluate the performance of the individual corresponding to the scheme combinations in the optimization process. Therefore, the fitness function should be defined clearly and implemented efficiently, considering the study's objective. In this study, we defined the fitness function using the correlation coefficient to obtain an appropriate assessment for model variables. In addition, we used the MERRA2 (Molod et al., 2015) reanalysis data for optimization and verification.

$$Fitness\ function = \sum_{i=1}^{3}(r_{AOD} + r_{PBLH} + r_{T2m} + r_{RH2m} + r_{WS10m} + r_{WD10m}) \quad (1)$$

where subscripts AOD, PBLH, T2m, RH2m, WS10m, and WD10m indicate aerosol optical depth, PBL height, 2 m temperature, 2 m relative humidity, 10 m wind speed, and 10 m wind direction, respectively.

The population size and evolutionary generation were set to 5 and 100, respectively, referring to the values generally used for micro-GA. The optimization was performed simultaneously for three cases.

RESULTS

The fitness function converged to the maximum in the 13th generation and the optimal set of the physical parameterization schemes consisted of the ACM2 for PBL and Noah-MP for land surface.

We compared the optimal combination of the physical parameterization schemes with the combination of physical parameterization schemes mainly used in numerical simulations using WRF-Chem. Table 1 is the list of the experiments for verification.

Table 1. List of the experiments for verification.

EXP.	PBL	LSM
OPTM	ACM2	Noah-MP
EXP1	YSU	Noah
EXP2	MYJ	Noah
EXP3	MYJ	RUC
EXP4	MYNN2	RUC

We used fitness function to evaluate the prediction performance in terms of all variables for different combinations of the physical parameterization schemes. The best performances were obtained by OPTM in terms of all variables, such as the AOD, PBLH, T2m, RH2m, WS10m, and WD10m. For the AOD, all experiments showed a moderate correlation. In CASE2, OPTM showed the highest correlation. For the PBLH, OPTM showed a high correlation with the most significant improvement in all cases (Fig. 1). The spatial comparison with the MERRA2 reanalysis data showed that OPTM experiments best simulated the AOD and PBL Height (Fig. 2).

Overall, the optimized set of the physical parameterization schemes out of the optimization system, the ACM2 for PBL and Noah-MP for land surface, produced better simulation results than others.

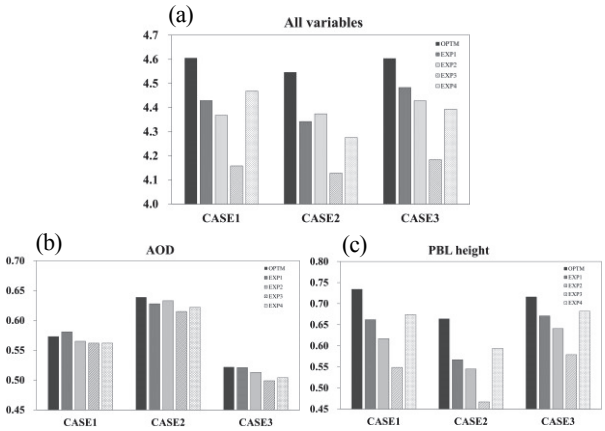

Fig. 1. Comparison of the optimized vs. non-optimized experiments using the correlation coefficients for (a) all variables, (b) AOD, and (c) PBLH.

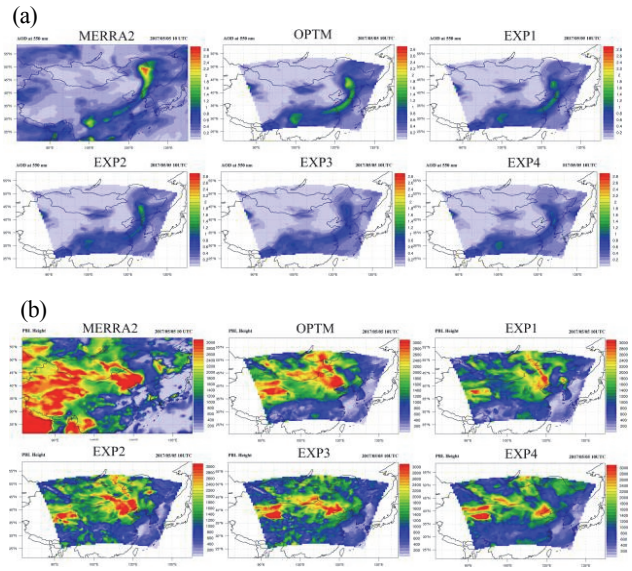

Fig. 2. Spatial comparison of (a) AOD and (b) PBLH for MERRA2 and experiments, in CASE2.

CONCLUSIONS

This study aims to find the optimized combination of the PBL scheme and LSM in the WRF-Chem model for improving the air quality forecasting skill in East Asia. For the objective of this study, we designed the optimization system by applying the micro-genetic algorithm coupled with the WRF-Chem model. The fitness function was composed of the correlation coefficients by considering various variables related to air quality. We simultaneously optimized three ADS cases using the optimization system and found that the optimal combination consists of the ACM2 (PBL) and Noah-MP (land surface). We then compared the optimal to non-optimal parameterization scheme set and found that the overall performance of WRF-Chem using the optimal scheme set was excellent in simulations of the air quality and meteorological variables. The results of this study will be helpful for the simulation studies of ADSs using WRF-Chem.

ACKNOWLEDGEMENTS

This research is supported under the grant of Basic Science Research Program through the National Research Foundation of Korea (NRF) funded by the Ministry of Education (2018R1A6A1A08025520). It is partly supported by the NRF grant funded by the Korea government (MSIT) (NRF-2021R1A2C1095535).

References

Banks, R. F., Tiana-Alsina, J., Baldasano, J. M., Rocadenbosch, F., Papayannis, A., Solomos, S. and Tzanis, C. G. (2016). Sensitivity of boundary-layer variables to PBL schemes in the WRF model based on surface meteorological observations, lidar, and radiosondes during the HygrA-CD campaign. Atmos. Res. 176: 185-201.

Grell, G. A., Peckham, S. E., Schmitz, R., McKeen, S. A., G. Frost, Skamarock, W. C. and Eder, B. (2005). Fully coupled 'online' chemistry in the WRF model. Atmos. Environ. 39: 6957–6976.

Holland, J. H. (1973). Genetic algorithms and the optimal allocation of trials. SIAM J. Comput. 2(2): 88-105.

Holland, J. H. (1975). Adaptation in natural and artificial system: An introductory analysis with applications to biology, control, and artificial intelligence. Ann Arbor, MI, USA: University of Michigan Press.

Kim, Y. H., Jeong, J. Y., Kim, J. E., Yoo, H. J., Ko, H. J., Ko, M. Y., Jeong, J. Y. and Ahn, H. G. (2020). Report of Asian dust storms in 2020: Jeju, South Korea. National Institute of Meteorological Sciences. (in Korean)

Krishnakumar, K. (1990). Micro-genetic algorithms for stationary and non-stationary function optimization. Paper presented at SPIE 1196, Symposium on Visual Communications, Image Processing, and Intelligent Robotics Systems, International Society for Optics and Photonics, International Society for Optical Engineering, Philadelphia, PA, USA.

Molod, A., Takacs, L., Suarez, M. and Bacmeister, J. (2015). Development of the GEOS-5 atmospheric general circulation model: Evolution from MERRA to MERRA2. Geosci. Model Dev. 8(5): 1339-1356.

Rizza, U., Miglietta, M. M., Mangia, C., Ielpo, P., Morichetti, M., Iachini, C., Virgili, S. and Passerini, G. (2018). Sensitivity of WRF-Chem model to land surface schemes: assessment in a severe dust outbreak episode in the Central Mediterranean (Apulia Region). Atmos. Res. 201: 168–180.

ISOLATION AND CHARACTERISATION OF PLANT GROWTH PROMOTING BACTERIA FROM AERIAL ROOTS OF HONG KONG PLANTS

M. Lam[1], G. K. K. Lai[1], S. D. J. Griffin[1], F. C. C. Leung[1]

ABSTRACT: In Hong Kong (as in much of SE Asia), rainfall surpasses 2200 millimetres per year. In addition, local granite-derived soils are poorly retentive of nutrients, creating oligotrophic conditions with < 0.47% nitrogen in surface soil levels and negligible concentrations below. Despite such challenges, numerous non-leguminous (and often lithophytic) plants, such as *Ficus microcarpa* and *Glochidion hongkongense*, are not only abundant but also grow rapidly to great size. These very high levels of carbon sequestration imply correspondingly large rates of nitrogen uptake that can only be explained by microbial nitrogen fixation. In this project, samples of aerial roots were recovered from a number of common Hong Kong plant species. nitrogen free (NF) media was used to identify potentially nitrogen fixing bacteria, which were then streaked to purity before DNA extraction and sequencing. Complete genomes of three isolates, 9ba2, *Kosakonia radicincitans* JS2a2 and *Gluconobacter thailandicus* ISBL3, were generated by hybrid assembly, using both Illumina MiSeq and Oxford Nanopore MinION platforms. Genomic analysis revealed numerous highly-conserved nitrogenase related (*nif*) genes across the different genera. Mineral transport systems, particularly for iron and molybdate, were also strongly represented. For example, in *K. variicola* 9bα-2, a 166 kbp plasmid not only encodes the *fec*(RABCDE) operon for ferric citrate uptake, but also the molybdate-responsive ModE transcription factor. The probiotic use of nitrogen fixing bacteria such as these has been proposed as a more sustainable measure for plant growth promotion that could reduce requirements for chemical fertilisers. Significantly, the extent of microbial nitrogen fixation that we estimate in Hong Kong suggests that the contribution to the nitrogen cycle of non-legume-associated microbes may be greatly underestimated.

Keywords: oligotrophic soil, nitrogen fixation, plant growth promoting bacteria

INTRODUCTION

Nitrogen is a limiting essential nutrient for plant growth. Although abundant in the atmosphere, N_2 is inaccessible to plants. Instead, plants typically acquire nitrogen through inorganic, water-soluble forms such as ammonium and nitrates in soil.

In the humid, sub-tropical climate of Hong Kong, rainfall surpasses 2200 millimetres per year (Hong Kong Observatory 2021). Local granite soils found in this region are also poorly retentive of nutrients and prone to leaching from rainfall. With soil total nitrogen concentrations < 0.04% in topsoil and negligible concentrations below (Jim 1998), local plants would be expected to display the common signs of nutrient deficiency such as yellowed leaves and stunted growth. In contrast, 75% of the land mass is woodland, shrubland or grassland, with high plant diversity including at least 20 unique species (Hong Kong Herbarium 2021). Furthermore, there is an abundance of numerous non-leguminous (and often lithophytic) plant species such as *Ficus microcarpa* and *Glochidion hongkongense* which grow to great size.

While symbiotic nitrogen-fixing bacteria are well-known to support the growth of legumes, they are traditionally not associated with non-leguminous plants due to the absence of similar root nodules. Nevertheless, it seems hard to reconcile the often vigorous growth of certain Hong Kong species in poor (or even very little) soil without invoking a role for nitrogen-fixing, and likely other plant growth promoting bacteria.

This investigation therefore aims to isolate and characterise plant growth promoting bacteria from non-leguminous plants in Hong Kong. As plant probiotics they may even provide a more sustainable source of nutrients that traditional (and very soluble) chemical fertilisers.

MATERIALS AND METHODS

Study Area

The study area of Telegraph Bay in Pokfulam next to the Pokfulam Country Park comprises mature woodland spanning roughly 48.7 acres, where most samples were collected. Topographically, this area is low in elevation, roughly 48 m to 158 m above sea level. It is a hilly terrain with commercial and residential areas nearby.

Sample Collection and Isolation

Aerial root tip samples, measuring ~20mm in length were collected from several plant species and incubated in nitrogen free (NF) broth for 7 days at 32 °C after surface sterilisation using 1% *w/w* 8-hydroxyquinoline sulphate. The surface layer was picked and transferred to a new NF

[1] The ISF Academy, 1 Kong Sin Wan Road, Pokfulam, HONG KONG
*Correspondence: sgriffin@isf.edu.hk

 https://doi.org/10.1142/9789811275449_0018

broth medium to incubate for an additional 7 days at 32 °C. Next, the top layer was picked and transferred to NF, M710 (Jensen's Medium) and Pikovskaya's agar. Isolates growing on M710 agar and producing a clear zone on Pikovskaya's agar were picked and passaged to purity on both M710 and Luria agar.

DNA Extraction and Genomic Analysis

Genomes were analysed using BLAST and TYGS for phylogeny, as well as Uniprot, Clustal Omega, and PATRIC and Phyre2 for genomic analysis. The *nif* operon (Fig.1) encodes the molybdenum–iron nitrogenase enzyme complex (Kessler 1998), has been used as the primary discriminator for potential nitrogen fixing bacteria in this investigation.

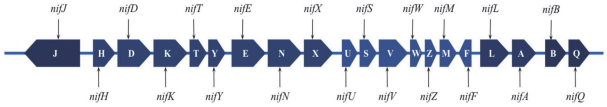

Fig. 1 The *nif* operon is required for iron-molybdenum nitrogen fixation

RESULTS AND DISCUSSION

Adaptable *nif* Genes

Two isolates, *Klebsiella variicola* 9ba2 (from *Philodendron erubescens*) and *Kosakonia radicincitans* JS2a2 (from *Ficus microcarpa*) were found to possess the *nif* operon. These Gram-negative isolates demonstrated rapid growth on NF medium producing large, mucoid colonies. Together with *Klebsiella sp.* CTHL.F3a isolated from kimchi (Lee 2022), all isolates possessed highly conserved N-fixation genes, with the exception of *nifX* and *nifQ*, which showed greater differences across genera.

Subsequent predictive modelling using Phyre2 revealed differences in both the structure and pocket site of *nifX* and *nifQ* (Fig. 2, Fig. 3).

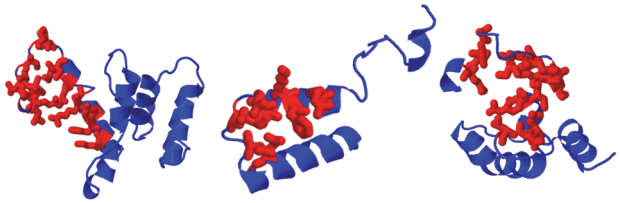

Fig. 2 (*left to right*) NifQ protein of 9ba2, JS2a2 and CTHL.F3a

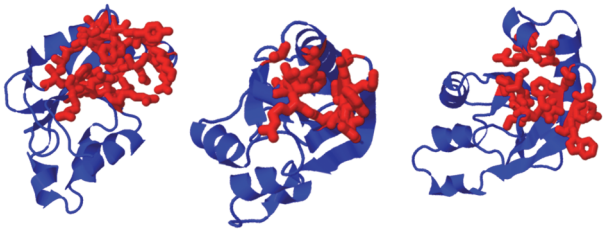

Fig. 3 (*left to right*) NifX protein of 9ba2, JS2a2 and CTHL.F3a

Differences between *nifQ* and *nifX* may suggest host and/or environmental adaptation: *nifQ* is associated with molybdenum storage and transfer (Hernandez 2008), while *nifX* is associated with active site NifB-cofactor (Nonaka 2019) and FeMoco transfer (Lahiri 2009).

Endophytic, Plant Growth Promoting Genes

For all three samples: 9ba2, JS2a2 and ISBL3, genomic analysis revealed numerous genes suggesting an endophytic life cycle (Fig. 4).

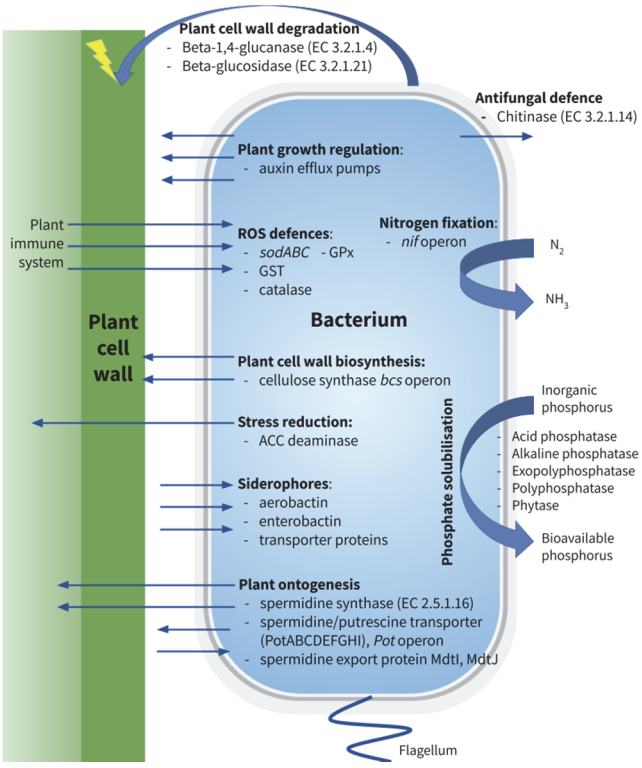

Fig. 4 Schematic of endophytism-associated genes found in isolates (*after* Pinski 2019)

Plant cell wall-degrading enzymes such as beta-1,4-glucanase and biosynthesis enzymes like cellulose synthase are linked to endophytism as they allow modification of the host intracellular environment.

Nitrogen-fixing and phosphate-solubilising capabilities in endophytes are also significant since they can provide key nutrients for plant growth (Krouk 2020).

In addition, the presence of polyamine synthases and transporters, as well as spermidine and putrescine exporters (Chen 2019) and auxin efflux carrier proteins (Zwiewka 2019), strongly suggest the ability for the isolates to manipulate plant structure and ontogenesis – all traits consistent with endophytism (Afzal 2019).

Sample ID	9ba2	JS2a2	ISBL3
Taxonomy	*Klebsiella variicola*	*Kosakonia radicincitans*	*Gluconobacter thailandicus*
Plant Source	*Philodendron erubescens*	*Ficus microcarpa*	*Syngonium podophyllum*
Genome Mbp	5.68	~5.26	3.31
%G+C	57.29	54.55	56.30
Genes			
Plant ontogenesis	25	21	12
Cell wall modification	3	4	2
Siderophore	10	16	2

Tab. 1 High numbers of genes linked to endophytism are found in the likely plant growth-promoting isolates.

CONCLUSION

This study has identified three likely endophytes, possessing genes such as the *nif* operon for nitrogen fixation, *pho* operon for phosphate solubilisation and polyamine transporters for plant ontogenesis. The presence of these endophytes may help to explain the ability for non-leguminous plant species in Hong Kong to grow well under oligotrophic conditions.

Further sampling will be required to establish whether these (and similar) bacteria are typical and widespread in Hong Kong. Furthermore, *nif*-targeted fluorescent primers for *in situ* hybridisation (FISH probes) may help to elucidate their localisation on plant roots.

Nitrogen-fixing microbes may present a sustainable method for plant growth promotion when used *in situ* for crop species. However, because endophytes are highly adapted to the internal environments of their hosts, it will be necessary to determine which crop plants could most easily benefit from this approach.

ACKNOWLEDGEMENTS

This work is funded under the *ISF Shuyuan Research Program*.

References

Afzal, I., Shinwari, Z. K., Sikandar, S., Shahzad, S. (2019). Plant beneficial endophytic bacteria: Mechanisms, diversity, host range and genetic determinants. Microbiol. Res., 221, 36–49.

Chen, D., Shao, Q., Yin, L., Younis, A., Zheng, B. (2019). Polyamine function in plants: Metabolism, regulation on development, and roles in abiotic stress responses. Frontiers in Plant Science, 9: 1945 Hernandez, J. A., Curatti, L., Aznar, C. P., Perova, Z., Britt, R. D., Rubio, L. M. (2008). Metal trafficking for Nitrogen Fixation: NifQ donates molybdenum to Nifen/NifH for the biosynthesis of the nitrogenase femo-cofactor. PNAS, 105(33), 11679–11684.

Hong Kong Herbarium. (2021). The Vegetation of Hong Kong. Hong Kong Herbarium. From https://www.herbarium.gov.hk/en/special-topics/hong-kong-plants/hong-kong-plants-detail/index-id-11.html (Retrieved May 19, 2022)

Hong Kong Observatory. (2021). Climate of Hong Kong. Climate. Retrieved May 31, 2022, from https://www.hko.gov.hk/en/cis/climahk.htm

Jim, C.Y. (1998) Physical and chemical properties of a Hong Kong roadside soil in relation to urban tree growth. Urban Ecosyst., *2*, 171–181.

Kelley, L. A., Mezulis, S., Yates, C. M., Wass, M. N., Sternberg, M. J. (2015). The Phyre2 web portal for protein modeling, prediction and analysis. Nature Protocols, 10(6), 845–858. Kessler, P. S., Blank, C., Leigh, J. A. (1998). The *nif* gene operon of the methanogenic archaeon *Methanococcus maripaludis*. J. Bacteriol., 180(6), 1504–1511.

Krouk, G., Kiba, T. (2020). Nitrogen and phosphorus interactions in plants: From agronomic to physiological and molecular insights. Curr. Opin. Plant Biol., 57, 104–109.

Lahiri, S., Cole, B., Pulakat, L. Gavini, N. (2007). The NifX Protein is Involved in the Final Stages of FeMo-cofactor Transport to the MoFe Protein. Am. J. Biochem. Biotechnol., 3(2), 92-102.

Lee, C. T., Lai, G. K., Griffin, S. D. and Leung, F. C. (2022). Complete genome sequence of *Klebsiella* sp.. CTHL.F3a, a cellulolytic strain isolated from Korean kimchi. Microbiol. Resour. Announc., 11(8).

Nonaka, A., Yamamoto, H., Kamiya, N., Kotani, H., Yamakawa, H., Tsujimoto, R., Fujita, Y. (2019). Accessory Proteins of the Nitrogenase Assembly, NifW, NifX/NafY, and NifZ, Are Essential for Diazotrophic Growth in the Nonheterocystous Cyanobacterium *Leptolyngbya boryana*. Front. Microbiol., 10: 495.

Pikovskaya, R.I. (1948) Mobilization of Phosphorus in Soil Connection with the Vital Activity of Some Microbial Species. Microbiol., 17, 362-370

Pinski, A., Betekhtin, A., Hupert-Kocurek, K., Mur, L., Hasterok, R. (2019). Defining the Genetic Basis of Plant-Endophytic Bacteria Interactions. Int. J. Mol. Sci., 20(8): 1947.

Sievers, F., Wilm, A., Dineen, D., Gibson, T. J., Karplus, K., Li, W., Lopez, R., McWilliam, H., Remmert, M., Söding, J., Thompson, J. D., Higgins, D. G. (2011). Fast, scalable generation of high-quality protein multiple sequence alignments using Clustal Omega. Mol. Syst. Biol., 7(1), 539.

Zwiewka, M., Bilanovičová, V., Seifu, Y. W., Nodzyński, T. (2019). The nuts and bolts of pin auxin efflux carriers. Front. Plant Sci., 10: 985.

IDENTIFICATION OF MICROBES FOR THE BIOREMEDIATION OF POLYESTER (PET) MICROFIBRE

L. Siu[1], G. K. K. Lai[1], S. D. J. Griffin[1] and F. C. C. Leung[1]

* Corresponding author: sgriffin@isf.edu.hk

ABSTRACT: Plastic waste pollution is an environmentally threatening issue that especially harms the marine population. Target 14.1 of the UN Sustainability Goals seeks to "prevent and significantly reduce marine pollution of all kinds" by 2025. Plastics constitute up to 80% of marine debris but, of this, microplastics may be the most damaging to marine ecosystems. In their recent study of microplastics recovered from the South China Sea, Yu et al. (2020) found that over 80% were microfibres, with the greatest proportion (30.8%) composed of the polyester, polyethylene terephthalate (PET) (Yu et al. 2020). The purpose of this investigation is to discover microbes with PET-degrading activity that might then be used in water/waste treatment to reduce polyester microfibre pollution in marine environments. Working with bacteria recovered from samples of polyester fabric that had been buried in soil/leaf litter for three months before recovery, we have used a progressive series of aromatic substrates (toluene, sodium benzoate, benzyl benzoate and finally a suspension of PET microfibres) as a screen, since the repeat unit of PET includes benzene carboxylate ester bonds.

Keywords: marine microfibre remediation; PET degradation; PET pollution

INTRODUCTION

Target 14.1 of the UN Sustainability Goals seeks to "prevent and significantly reduce marine pollution of all kinds" by 2025, an ambitious target that will almost certainly be missed by a very wide margin (Bai et al. 2020). The UN Environment Programme itself, in its October 2021 report, predicts plastic pollution in oceans will instead more than double by 2030. Tiny PET fibers disposed of in the ocean constitute up to 80% of marine debris, ingested by marine animals and severely damaging their health, being the most damaging to marine ecosystems of the total plastic pollution (Barnes et al. 2009).

With its high tensile strength, PET (Fig. 1) is now the main ingredient for 60% of plastic for plastic bottles and is also spun into fabric for polyester-based clothing worldwide, contributing at least 42 million metric tons of microplastic waste per year (Geyer et al. 2017). As seen in Fig. 1, the benzene ring of the polyester structure connects to carbon and oxygen, forming a strong aromatic bond similar to that of sodium benzoate that is hard to degrade. In this investigation, aromatic substrates (toluene, sodium benzoate, benzyl benzoate and a suspension of PET microfibres in hexafluoro-2-propanol) were used as carbon sources to screen for polyester-degrading microbes.

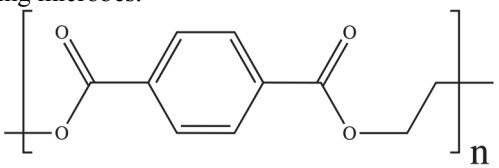

Fig. 1: Chemical structure of PET

Established bacterias with PET degrading functions includes the enzyme arylesterase (Fig. 2) that was reported by Haernvall et al. in 2017 found within *Pseudomonas pseudoalcaligenes* which hydrolyzes ionic phthalic polyesters, where increase water solubility and hydrophobicity of the polyester can enhance arylesterase hydrolysis (Haernvall et al. 2017), as well as the MHETase (Fig. 3) reported by Yoshida et al. in 2016 within *Ideonella sakaiensis* that hydrolyzes PET through converting the sophisticated polymer into harmless monomers, terephthalic acid and ethylene glycol (Yoshida et al. 2016).

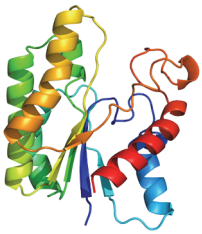

Fig. 2: structure of arylesterase found in *Pseudomonas pseudoalcaligenes*

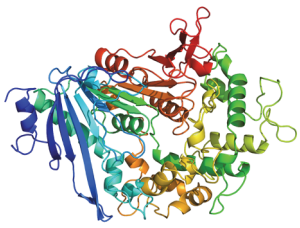

Fig. 3: structure of MHETase found in *Ideonella sakaiensis*

METHODS

Sample collection process

PET fabric was collected from the school's uniform recycling site. The uniform was cut into rectangular sheets and placed inside laundry meshes. The samples of PET fabric were then buried in soil and leaf litter for three months. After recovery, the fabric was rinsed with 0.9%

[1] Shuyuan Department, The ISF Academy, 1 Kong Sin Wan Road, Pokfulam, HONG KONG

 https://doi.org/10.1142/9789811275449_0019

w:v saline and an aliquot of each extract incubated in minimal salts medium (Schmidt-Emrich et al. 2016) at 27 °C with shaking containing 10% v:v toluene as the sole carbon source.

Sample isolation process

After 7-10 days, viable bacteria (determined by streaking on Luria agar) were transferred to a minimal salts medium containing 5% w:v sodium benzoate. Isolates with greatest turbidity were passed to purity on Luria agar. PET-degrading activity was tested by growth on agar made with Zhang's medium (Zhang 2012) to which a thin layer of PET fibers dissolved in hexafluoro-2-propanol had been applied.

DNA extraction and analysis

DNA was extracted from two selected isolates using a DNeasy PowerSoil Kit (Qiagen) and sequenced via both Illumina MiSeq and Oxford Nanopore MinIon platforms to generate complete genomes by hybrid assembly (Unicycler v0.4.3). PATRIC, NCBI BLAST, Phyre2 and Clustal Omega were used for comparative genomic analysis.

RESULTS AND DISCUSSION

Identification of two *Pseudomonads* with potential PET degradation activities

Genomic analysis isolated two *Pseudomonads*, LS_1a and LS_2c, which showed activity towards all of the carbon sources tested. Table 1 below identifies the detailed characteristics of the two isolates.

Sample ID	LS_1a	LS_2c
Estimated genome size	5.75 Mbp	6.35 Mbp
% G+C	63.08%	66.46%
Source	soil/leaf litter	soil/leaf litter
GenBank accession	Pseudomonas sp. LS.1a CP092827	Pseudomonas aeruginosa LS.2c CP092634
Closest genome Source	- Pseudomonas sp. 43(2021) - Oryza sativa ssp. japonica rhizosphere (Italy) - ANI 99.41%	- Pseudomonas aeruginosa AZPAE15026 clinical UTI (Colombia) - ANI 99.99%

Through DNA analysis, functions and key genes for aromatic degradation of PET fibers were found, as shown in table 2 below.

Sample ID	LS_1a	LS_2c
Function	- Xylene and sodium benzoate degradation	- Xylene and sodium benzoate degradation
Key genes	- Toluene tolerance proteins - benzoate transport proteins - benABC operon - dmpK-P operon - Five copies of catechol-1,2-dioxygenase	- Toluene tolerance proteins - Benzoate transport proteins - benABC operon

Similarities of known PET degradation enzymes with isolates LS_1a and LS_2c

Both isolates possess an arylesterase similar to the PET-degrading arylesterase found in *Pseudomonas pseudoalcaligenes* reported by Haernvall et al. (2017). Protein structures found by Phyre2 (Fig. 4, 5) revealed similarities in their tertiary structures.

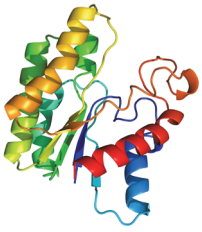

Fig. 4: structure of arylesterase found in LS_1a

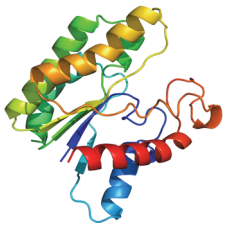

Fig. 5: structure of arylesterase found in LS_2c

Comparison of LS_1a with *Ideonella sakaiensis* ISF6_4831

Enzymes of the well-known PET-degrading pathway of *Ideonella sakaiensis* ISF6_4831 through the enzyme MHETase share some homology with proteins in LS_1a as shown in table 2:

ISF6_4831	LS_1a
PETase (Serine hydrolase)	Dienelactone hydrolase (Cysteine hydrolase)
MHETasE	Arylesterase
Teraphthalate dioxygenase	Benzoate 3,4 dioxygenase
Teraphthalate transporter	Benzoate transporter

Similarities of enzymes shown in table 3 above and the existence of xylene and benzoate degradation function supports the idea that LS_1a and LS_2c might be able to hydrolyse PET through a pathway similar to Fig. 6.

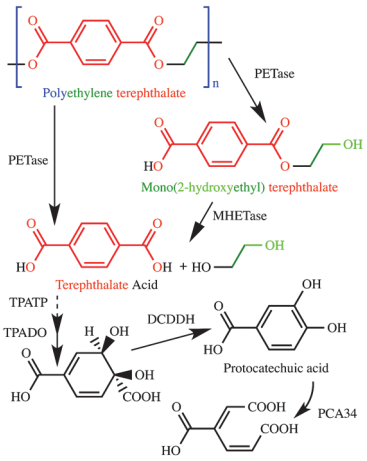

Fig. 6: Enzymatic hydrolysis of PET using MHETase from *Ideonella sakaiensis* ISF6_4831

CONCLUSION

Although LS_1a and LS_2c can make use of PET to survive, its rate of PET degradation is very slow. Similarities in the enzymes (table 2) of LS_1a and ISF6_4831, as well as similarities in the tertiary structure of the enzyme arylesterase of LS_1a, LS_2c, and *Pseudomonas pseudoalcaligenes* (Fig. 2, 4, 5) however, support the idea that a range of microbes might be actively evolving to make use of the increasingly abundant sources of environmental PET (Austin et al. 2018).

FURTHER INVESTIGATION

It is significant that LS_1a seems to be more effective than the other isolates in functional tests. Therefore, the next step in investigating the potential of PET degradation in LS_1a is to clone the relevant genes into E. coli to verify their activities. Additionally, a later step would be to look further at site-directed mutagenesis and/or by directed evolution particularly within the LS_1a cysteine hydrolase to see if PET-degrading activities can be enhanced.

ACKNOWLEDGEMENTS

This work is funded under the *ISF Shuyuan Research Program.*

References

Altschul, S. F., Gish, W., Miller, W., Myers, E. W., Lipman, D. J. (1990). Basic local alignment search tool. *Journal of Molecular Biology*, 215(3), 403–410. doi: 10.1016/S0022-2836(05)80360-2

Austin, H. P., Allen, M. D., Donohoe, B. S., Rorrer, N. A., Kearns, F. L., Silveira, R. L., Pollard, B. C., Dominick, G., Duman, R., El Omari, K., Mykhaylyk, V., Wagner, A., Michener, W. E., Amore, A., Skaf, M. S., Crowley, M. F., Thorne, A. W., Johnson, C. W., Woodcock, H. L., … Beckham, G. T. (2018). Characterization and engineering of a plastic-degrading aromatic polyesterase. *Proceedings of the National Academy of Sciences*, 115(19). doi: 10.1073/pnas.1718804115

Bai, C., & Guo, H. (2020). Big earth data in support of the Sustainable Development Goals. *Chinese Academy of Sciences.*

Barnes, D. K., Galgani, F., Thompson, R. C., & Barlaz, M. (2009). Accumulation and fragmentation of plastic debris in global environments. *Philosophical transactions of the Royal Society of London.* Series B, Biological sciences, 364(1526), 1985–1998. doi: 10.1098/rstb.2008.0205

Geyer, R., Jambeck, J. R., Law, K. L. (2017). Production, use, and fate of all plastics ever made. *Science Advances*, 3(7). doi: 10.1126/sciadv.1700782

Haernvall, K., Zitzenbacher, S., Yamamoto, M., Schick, M. B., Ribitsch, D., Guebitz, G. M. (2017). A new arylesterase from Pseudomonas pseudoalcaligenes can hydrolyze ionic phthalic polyesters. *Journal of Biotechnology,* 257, 70–77. doi: 10.1016/j.jbiotec.2017.01.012

Schmidt-Emrich, S., Stiefel, P., Rupper, P., Katzenmeier, H., Amberg, C., Maniura-Weber, K., & Ren, Q. (2016). Rapid assay to assess bacterial adhesion on textiles. *Materials*, 9(4), 249. doi: 10.3390/ma9040249

Yoshida, S., Hiraga, K., Takehana, T., Taniguchi, I., Yamaji, H., Maeda, Y., Toyohara, K., Miyamoto, K., Kimura, Y., Oda, K. (2016). A bacterium that degrades and assimilates poly(ethylene terephthalate). *Science*, 351(6278), 1196–1199. doi: 10.1126/science.aad6359

Yu J, Tang D, Wang S, He L and Pathira Arachchilage KRL (2022) Spatial Distribution and Composition of Surface Microplastics in the Southwestern South China Sea. Front. Mar. Sci. 9:830318. doi: 10.3389/fmars.2022.830318.

Zhang, C. (2012). Isolation and characterization of a benzoic acid degrading pseudomonas putida from a pharmaceutical wastewater treatment plant. *African Journal of Microbiology Research*, 6(21), 4608-4613. doi: 10.5897/AJMR12.548

CELLULOLYTIC ISOLATE *KLUYVERA* SP. CRP FROM RED PANDA FAECES (*AILURUS FULGENS*) FOR SECOND-GENERATION BIOFUEL PRODUCTION

A. C. H. Wai[1], G. K. K. Lai[1], S. D. J. Griffin[1*], F. C. C. Leung[1]

ABSTRACT: Second-generation biofuels derive energy from lignocellulosic waste, a considerably more sustainable feedstock than food commodities. Lignocellulose, however, requires pre-treatment to release fermentable sugars, a process that may be bacterial. In this work, *Kluyvera* sp. CRP, isolated from faeces of a Chinese red panda (*Ailurus fulgens*), demonstrated significant cellulolytic activity *in vitro*. Its complete genomic sequence (5,157,963 bp, 54.80% GC content), which was established through hybrid assembly, found similarity to an endophytic strain of *Kluyvera* and genomic analysis revealed an extensive carbohydrate metabolism with multiple isoforms of degradative enzymes. Hence, *Kluyvera* sp. CRP, or its isolated enzymes, may provide a useful tool for the valorisation of agricultural waste.

Keywords: second-generation biofuels, cellulose degradation, *Kluyvera*.

INTRODUCTION

The 7th UN Sustainability Goal strives for affordable and clean energy; and, in its target 7.1, looks to "increase substantially the share of renewable energy in the global energy mix" by 2030. Second-generation biofuels, from the valorisation of cellulosic waste, are sustainable and carbon-neutral alternatives that offer more effective land-use to minimise the food market effects of biofuels generated from sources such as maize and sugarcane. Lignocellulosic biomass, such as industrial, agricultural, and municipal waste, however, requires pre-treatment in order to release fermentable sugars and this presents an obstacle to efficient production (Acheampong et al., 2017).

Common methods of pre-treatment include physical methods such as microwave heating and ultrasonic disruption; chemical treatments, such as with acids, alkalis, ionic liquids and organic solvents; and, physio-chemical treatment aimed at opening up fibrous structures, for instance with steam, ammonia or CO_2 (Haghighi Mood et al., 2013; Wu et al., 2022). Biological methods using microbes or their isolated enzymes require less energy and do not produce chemical waste or by-products that will impede subsequent fermentation.

Whilst a variety of fungi and even mixtures of microbes have been found effective for lignocellulose degradation, growth may be slow and a significant proportion of the released carbon sources may be consumed during the process. In contrast, bacteria exhibit faster growth and do not utilise released products like cellulose as extensively (Wu et al., 2022).

Lignocellulose-degrading bacteria has been isolated from sewage treatment facilities (Cai et al., 2018); from soil (Brown et al., 2012); in mollusc gut degrading microalgae (Muñoz et al., 2014); and, from termite gut and wood boring beetles (Bugg et al., 2011).

This project has looked for strongly cellulolytic bacteria in faeces of the Chinese red panda (*Ailurus fulgens*). This species uses bamboo as its major food source, so that previous characterisation of its gut microbiota has indicated the presence of extensive carbohydrate metabolism, especially cellulose-degrading pathways (Kong et al., 2014). Isolates were also screened for the degradation of chitin (the N-acetyl-glucosamine analogue of cellulose), since mutations in the associated *chb* operon can enable involvement in cellulose metabolism (Kachroo at al., 2007).

METHODS

Bacterial Isolation and Genomic Sequencing

Cellulolytic bacteria was isolated using CMC (carboxymethylcellulose) agar as previously described (Wai et al., 2022), from faeces of a healthy, adult Chinese red panda (*Ailurus fulgens*) housed at Ocean Park, Hong Kong (22.245682 N, 114.176321 E).

Cellulolytic activity was compared on CMC agar stained with Gram's iodine according to the method of Kasana et al. (2008). In addition, chitinolytic activity was determined on agar containing colloidal chitin according to the method of Souza et al. (2009).

[1] The ISF Academy, 1 Kong Sin Wan Road, Pokfulam, HONG KONG
* Correspondence: sgriffin@isf.edu.hk

 https://doi.org/10.1142/9789811275449_0020

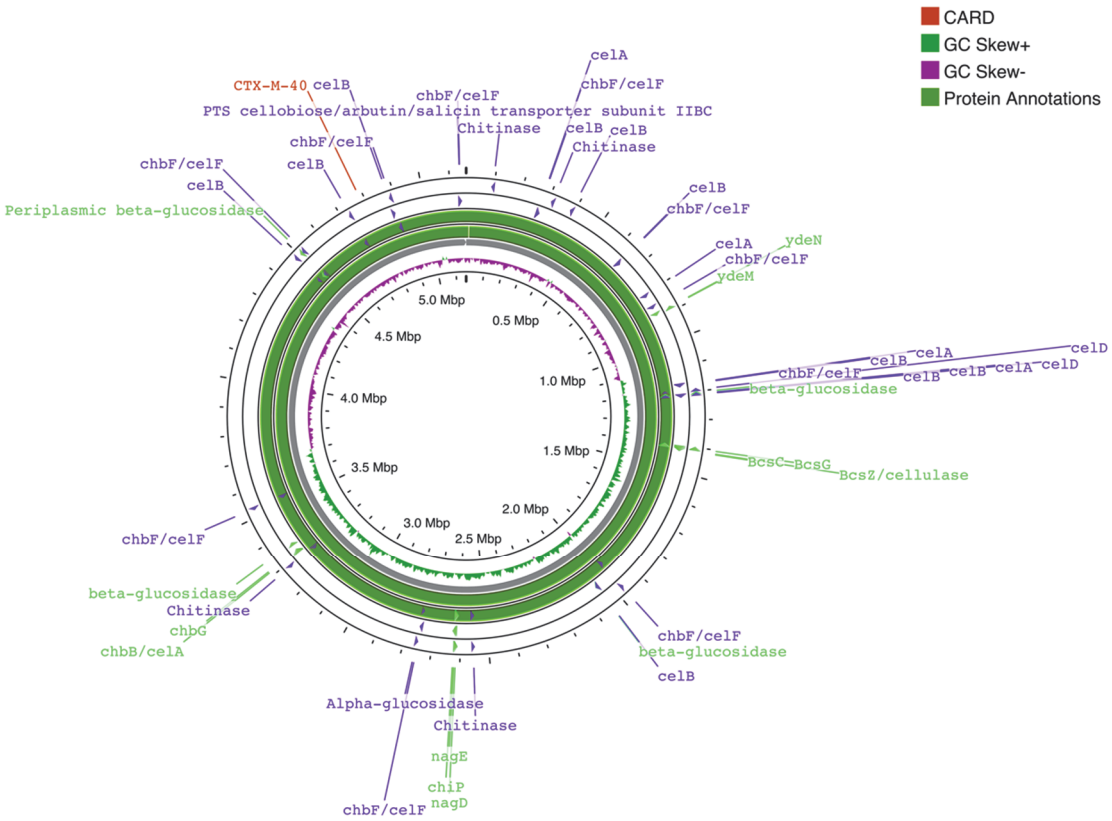

Fig. 1 Circular representation of the CRP genome, highlighting the genes of cellulose and chitin metabolism.

CRP, which showed the strongest cellulolytic and chitinolytic activity, was sequenced via both Illumina MiSeq and Oxford Nanopore MinION platforms and its complete genome obtained by hybrid assembly using Unicycler v0.4.3 (Wick et al., 2017).

Genomic Analysis

Genomic sequences were annotated using PATRIC-BRC (Davis et al., 2020) and NCBI PGAP v5.0 (Haft et al., 2018). Predicted proteins were characterised using Uniprot (The UniProt Consortium, 2021), with alignments by Clustal Omega (Sievers et al., 2011). 3-D structures generated by Phyre2 (Kelley et al., 2015).

RESULTS AND DISCUSSION

The complete genomic sequence of CRP totals 5.16 Mbp and Mash/MinHash using PATRIC found it closest to *Kluyvera* genomosp. 3 strain PO2S7 (CP050321) – an endophyte previously isolated from *Oryza sativa* (Singha et al., 2021) – with an average nucleotide identity of 98.83%.

Cellulolytic pathways are strongly represented, with four genes encoding beta-glucosidase (EC 3.2.1.21), ten genes encoding of 6-phospho-beta-glucosidase (*chbF/celF*) (EC 3.2.1.86), together with multiple copies of cellobiose phosphotransferase, the *bcs* operon (Fig. 1), and the 12 gene *chb* operon.

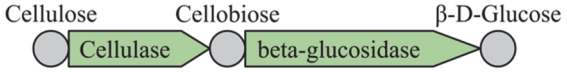

Fig. 2 Cellulose degradation pathway as identified in CRP.

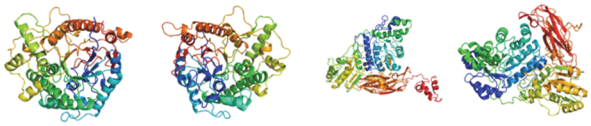

Fig. 3 The four beta-glucosidase isoforms (EC 3.2.1.21) in CRP at NCBI loci (K7B04_) 09595, 15785, 21375, and 05550 respectively.

Cellulose Degradation Pathway

A complete cellulose degradation pathway (Fig. 2) was identified in CRP. A cellulase (*bcsZ*) in CRP sequence is nested within the *bcs* operon. This is consistent with the observed activity on CMC agar.

Four isoforms of beta-glucosidase are found in CRP and structural modelling by Phyre2 shows different structures for each (Fig. 3) suggesting different evolutionary origins and specialisations.

Cellulose biosynthesis operon

The nine gene *bcs* operon (Römling & Galperin, 2015) is present in the sequence (Fig. 4), which is consistent with the cellulolytic activity observed. Protein sequence alignment of the *bcs* operon with that of *Kluyvera* strain PO2S7 showed a 99% identity (4534/4560 aligned) between the two, with a gap of 10 residues in *bcsB* of CRP

the most significant discrepancy (see Fig. 5). Protein Structures modelled by Phyre2 shows no significant difference in structure between the two proteins (Fig. 6).

CONCLUSION

Kluyvera sp. CRP shows strong activity with both chitin and cellulose. Genomic analysis shows prominent chitin and cellulolytic pathways. These could give CRP an advantage in breaking down lignocellulosic waste.

Our next steps will include the cloning of the individual cellulase/beta-glucosidase isoforms identified in CRP and characterisation of their activities under different conditions.

Data Availability

R Raw and processed sequence data for *Kluyvera* sp. CRP (CP082841) is available through NCBI under BioProject PRJNA758164.

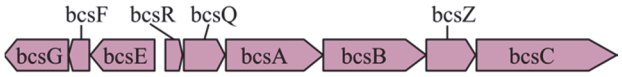

Fig. 4 The *bcs* operon as identified in CRP.

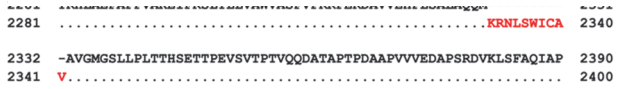

Fig. 5 Sequence alignment of CRP and *Kluyvera* strain PO2S7 between *bcsA* and *bcsB* by Clustal Omega: a 10-residue gap is present at the start of *bcsB* in CRP.

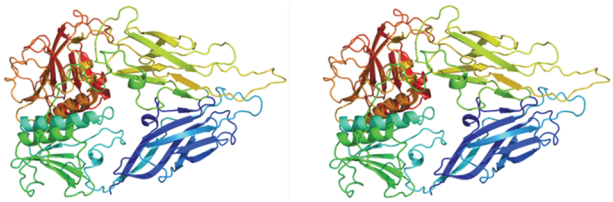

Fig. 6 Phyre2-modelled structures of the *bcsB* proteins in CRP (*left*) and in genomosp. 3 strain PO2S7 (*right*) show striking similarity.

References

Acheampong, M., Ertem, F. C., Kappler, B., Neubauer, P. (2017). In pursuit of Sustainable Development Goal (SDG) number 7: Will biofuels be reliable? *Renewable and Sustainable Energy Reviews*, *75*, 927–937.

Davis, J. J., Wattam, A. R., Aziz, R. K., Brettin, T., Butler, R., Butler, R. M., Chlenski, P., … Stevens, R. (2020) The PATRIC Bioinformatics Resource Center: expanding data and analysis capabilities. *Nucleic Acids Research*, 48(D1): D606-D612.

Haft, D. H., DiCuccio, M., Badretdin, A., Brover, V., Chetvernin, V., O'Neill, K., Li, W., … Pruitt, K. D. (2018). RefSeq: an update on prokaryotic genome annotation and curation. *Nucleic Acids Research*, 46: D851–D860.

Haghighi Mood, S., Hossein Golfeshan, A., Tabatabaei, M., Salehi Jouzani, G., Najafi, G. H., … Ardjmand, M. (2013). Lignocellulosic biomass to bioethanol, a comprehensive review with a focus on pretreatment. *Renewable and Sustainable Energy Reviews*, *27*, 77–93.

Kachroo, A. H., Kancherla, A. K., Singh, N. S., Varshney, U., Mahadevan, S. (2007). Mutations that alter the regulation of the chb operon of Escherichia coli allow utilization of cellobiose. Molecular Microbiology, 66(6), 1382–1395.

Kasana, R. C., Salwan, R., Dhar, H., Dutt, S., Gulati, A. (2008). A rapid and easy method for the detection of microbial cellulases on agar plates using Gram's iodine. *Current Microbiology*, *57*(5), 503–507.

Kelley, L. A., Mezulis, S., Yates, C. M., Wass, M. N., Sternberg, M. J. (2015). The Phyre2 web portal for protein modeling, prediction and analysis. *Nature Protocols*, *10*(6), 845–858.

Kong, F., Zhao, J., Han, S., Zeng, B., Yang, J., Si, X., Yang, B., Yang, M., Xu, H., Li, Y. (2014). Characterization of the Gut Microbiota in the Red Panda (*Ailurus fulgens*). *PLOS ONE*, *9*(2), e87885.

Römling, U., Galperin, M. Y. (2015). Bacterial cellulose biosynthesis: Diversity of operons, subunits, products, and functions. *Trends in Microbiology*, *23*(9), 545–557.

Sievers, F., Wilm, A., Dineen, D., Gibson, T. J., Karplus, K., Li, W., Lopez, R., … Higgins, D. G. (2011) Fast, scalable generation of high-quality protein multiple sequence alignments using Clustal Omega. *Molecular Systems Biology*, 7: 539.

Souza, C. P., Burbano-Rosero, E. M., Almeida, B. C., Martins, G. G., Albertini, L. S., Rivera, I. N. G. (2009). Culture medium for isolating chitinolytic bacteria from seawater and plankton. *World Journal of Microbiology and Biotechnology*, *25*(11), 2079–2082.

The UniProt Consortium (2021) UniProt: the universal protein knowledgebase in 2021, *Nucleic Acids Research*, 49(D1), D480–D489.

Wick, R. R., Judd, L. M., Gorrie, C. L., Holt, K. E. (2017). Unicycler: Resolving bacterial genome assemblies from short and long sequencing reads. *PLoS Computational Biology*, 13(6): 97 e1005595.

Wu, Z., Peng, K., Zhang, Y., Wang, M., Yong, C., Chen, L., Qu, P., Huang, H., Sun, E., Pan, M. (2022). Lignocellulose dissociation with biological pretreatment towards the biochemical platform: A review. *Materials Today. Bio*, *16*: 100445.

IMPACT OF CLIMATE CHANGE ON FLOODS IN GIN RIVER BASIN, SRI LANKA

J.M.M.U. Jayapadma[1], K.Souma[2], H. Ishidaira[2], J. Magome[2] and T.N. Wickramaarachchi[3]

ABSTRACT: Flooding has been detrimental to economies, globally causing severe damage to human lives and property. Developing countries, including Sri Lanka, are highly vulnerable to heavy floods mainly due to the lack of infrastructure and expertise on efficient flood risk management. Gin River basin in Sri Lanka, having a catchment area of 932 km^2, is one such river basin that has been affected by heavy floods in the past. Therefore, bias-corrected General Circulation Model (GCM) outputs from Coupled Model Inter-comparison Project Phase 5 (CMIP5) were used as inputs for the Rainfall-Runoff Inundation (RRI) model to simulate the impact of climate change on flood peak discharge, maximum inundation depths of the Gin River basin. Future climate projections of five GCMs that performed well in the target area, corresponding to the RCP4.5 emission scenario, were used to simulate the future flood flow using the validated RRI model. GCM averaged projections indicated a 10% increase in southwest monsoon rainfall from May to September compared with the past (1980-2000). Projected changes in the precipitation have declined the mean annual discharge by 34% while aggravating the flow exceeding 5% of the time by 5% on average at the Baddegama river gauging station (downstream) of the basin. Furthermore, the RRI model simulations corresponding to the RCP4.5 emission scenario for 2040-2060 revealed critical information, including expansion of peak inundation extent, which will aid efficient flood risk planning and management in the basin.

Keywords: Climate change, Flood modelling, RRI, Gin River

INTRODUCTION

Human-induced climate change intensifies the global water cycle and its variability, posing severe threats to human livelihood, especially regarding water supply, energy production, ecosystem integrity, and disaster preparedness. Both frequency and extremes of heatwaves, heavy precipitation, droughts, floods, and tropical cyclones are expected to change all over the world, under all the emission scenarios until at least the mid of 21st century (IPCC, 2021). Specifically, the average and heavy precipitation will be further intensified over Asia with high to medium confidence (IPCC, 2021). Therefore, it is a timely requirement to study and understand the processes underlying climate change and its impact on floods, one of the costliest climate-driven disasters, to seek effective adaptation measures at both regional and basin scales.

MATERIALS AND METHODS

Study Area

The location map of the Gin River basin and the location of river gauges and rainfall gauging stations are shown in Fig 1. The Gin River is approximately 113km long and is frequently subjected to flooding. Its climate is mainly governed by the monsoon rains.

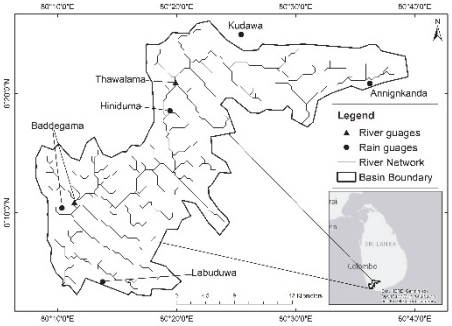

Fig 1. Basin overview

Climate model data

General Circulation Model (GCM) projections of the Coupled Model Inter-comparison Project Phase 5 (CMIP5) were obtained from the Data Integration and Analysis System (DIAS) developed by the Japan Agency for Marine-Earth Science and Technology (JAMSTEC) and partner universities (Kawasaki *et al.*, 2017). The performance of GCMs were evaluated based on the monthly mean spatial correlation and the root mean square error (RMSE) of the key climate variables including precipitation, outgoing longwave radiation

[1] Special Educational Program on River Basin Environmental Science, Integrated Graduate School of Medicine, Engineering, and Agricultural Sciences, University of Yamanashi, 4-3-11 Takeda, Kofu, Yamanashi, 400-8511, JAPAN
[2] Interdisciplinary Centre for River Basin Environment, University of Yamanashi, 4-3-11 Takeda, Kofu, Yamanashi 400-8511, JAPAN
[3] Department of Civil and Environmental Engineering, Faculty of Engineering, University of Ruhuna, Hapugala, Galle, SRI LANKA

 https://doi.org/10.1142/9789811275449_0021

(OLR), sea level pressure, sea surface temperature (SST), air temperature, specific humidity, zonal wind and meridional wind using the online tools available in the DIAS. Five GCMs that performed well in the basin were selected according to the performance assessment and the three-step statistical bias-correction method adopted by Nyunt *et al.*, 2013 which is available in DIAS. In this study, biases inherent in GCM projections addressing the underestimation of extremes, poor seasonal simulation, and high-frequency wet day error in relation to observations are corrected. The bias correction was carried out with reference to observed rainfall obtained from the Asian Precipitation—Highly Resolved Observational Data Integration Towards Evaluation of Water Resources (APHRODITE) project (Yatagai *et al.*, 2012). The bias-corrected future rainfall projections for 2040-2060 under the RCP4.5 emission scenario were input to the validated flood model to evaluate the impact of future climate on flood discharge and inundation in the basin.

Flood modelling using RRI

The rainfall-runoff inundation model (RRI), capable of simulating rainfall-runoff and inundation simultaneously, was employed in this study to simulate the river flow and inundation. The governing equations of the model are derived based on the mass balance and momentum equations elaborated in Sayama *et al.*, 2012. First, the model's ability to simulate major flood events that occurred in the basin was tested based on an event-based calibration (Jayapadma *et al.*, 2022). Then it was verified further using APHRODITE rainfall data for the historical period 1980-2000. The model was calibrated and validated through a trial and error approach using the observed river flow records obtained from the Department of Irrigation, Sri Lanka. The hydrological map including Digital Elevation Model (DEM), flow accumulation, and flow direction data, based on Shuttle Elevation Derivatives at multiple Scales (HydroSHEDS) with 15-sec (around 500 m) resolution (Lehner, Verdin and Jarvis, 2008) were obtained from the U.S. Geological Survey. Daily evapotranspiration data at 0.25° resolution were obtained from the Global Land Data Assimilation System (GLDAS) (Rodell *et al.*, 2004). Land-use maps were obtained from the Land cover project by the European Space Agency's Climate Change Initiative (ESA, 2017). The model performance was evaluated based on the Nash Sutcliffe Efficiency (NSE) and Critical Success Index (CSI), as shown in Equations (1) and (2). Q_{obs} is the observed discharge, Q_{sim} is the simulated discharge, $\overline{Q_{obs}}$ is the mean observed discharge, and N is the number of outputs. *NSE* varies from 0 to 1 where the *NSE* of 1 suggests a perfect agreement between observed and the simulated hydrographs. The *CSI* value varies from 0 to 1, where the *CSI* value of 1 indicates a perfect agreement between the simulated inundated area and the observed inundated area. Grid cells with an inundation depth over 0.5 m where the depth exceeds the soil depth were considered inundated (height of the water from the local surface).

$$NSE = 1 - \frac{\sum_{i=1}^{N} (Q_{obs,i} - Q_{sim,i})^2}{\sum_{i=1}^{N} (Q_{obs,i} - \overline{Q_{obs}})^2} \quad (1)$$

$$CSI = \frac{A_{sim} \cap A_{obs}}{A_{sim} \cup A_{obs}} \quad (2)$$

RESULTS AND DISCUSSION

Bias Correction for Climate Change Projection

The three-step bias correction method effectively corrected the biases that existed in raw GCM rainfall projections in relation to APHRODITE rainfall data, as shown in Fig.2.

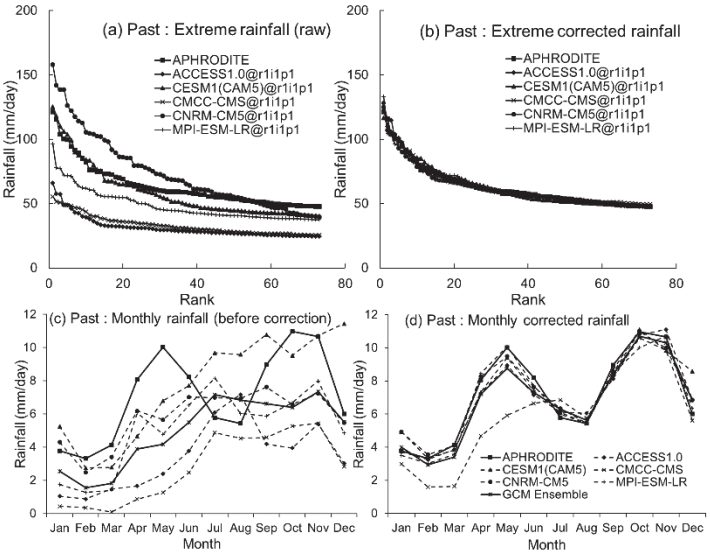

Fig 2. Extreme and monthly rainfall projections before and after bias correction

Changes in seasonal rainfall

The GCM ensemble projected an increase in seasonal rainfall in the future except for the 1st inter-monsoon rainy season from March to April under the RCP 4.5 emission scenario, as shown in Fig.3. A very small increment (0.85%) of rainfall was predicted in the Northeast monsoon season while it was 9.7% and 15.7% for the Southwest monsoon and the 2nd inter-monsoon seasons respectively. The intensified monsoon rainfall may affect

the frequency of extreme events altering the river flow in the basin.

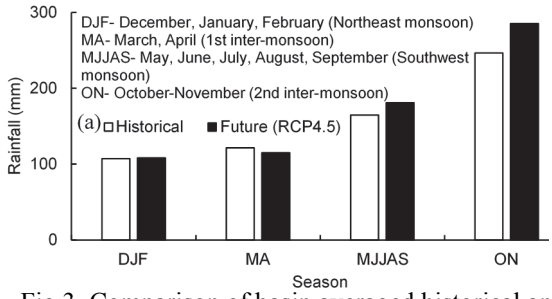

Fig 3. Comparison of basin averaged historical and future seasonal rainfall

Validation of RRI under historical climate

Model performance indices during model validation (NSE>0.7) indicated a good agreement between simulated and observed river discharge measured at the Baddegama gauging station (Fig.4). Although some peak events were underestimated, the model simulations were reasonably accurate to be used in the climate-impact assessment.

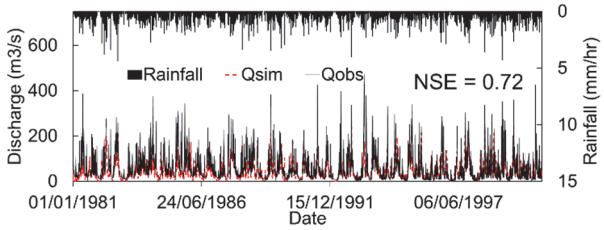

Fig 4. Comparison of observed and simulated river flow corresponding to historical climate

Impact of climate change on river flow and inundation

High flows exceeding 5% of the time in the basin are expected to increase by 5% while the mean annual discharge of the river is projected to decline by 34% at the downstream gauging station (Fig.5 (a)). Fig.5 (b) shows the comparison of the 20-year average of the annual maximum inundated area projected by the GCM ensemble for the future (185.71 km^2) and the past (180.16 km^2), indicating an expansion of 3.5%.

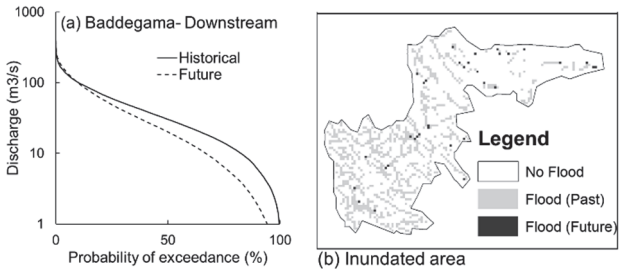

Fig 5. (a) Comparison of flow duration curves at the downstream gauging station and (b) comparison of the 20-year average of annual maximum inundated area

CONCLUSION AND FUTURE DIRECTIONS

The monsoon rainfall received by the basin is expected to intensify if the climate changes under the RCP4.5 emission scenario. The mean river flow is expected to decrease significantly while the higher flows are to increase significantly. Therefore, adaptation measures should be implemented to cope with the predicted expansion of the inundated area. In addition, this study could be extended by incorporating possible land-use projections and climate simulations under different emission scenarios to generate useful information that could be used to tackle the potential impacts of climate change on the basin hydrology.

ACKNOWLEDGEMENTS

The authors would like to thank Dr. Takahiro Sayama of Kyoto University and Dr. Anil Aryal of University of Yamanashi for their helpful comments. This study was supported by JSPS KAKENHI Grant Number JP19H02246 and JP19H01378.

References

ESA (2017) 'Land Cover CCI: Product User Guide', pp. 1–91.

IPCC (2021) Climate Change 2021: The Physical Science Basis. Contribution of Working Group I to the Sixth Assessment Report of the Intergovernmental Panel on Climate Change. Cambridge University Press.

Jayapadma, J. M. M. U. et al. (2022) 'The Effect of Incorporation of Embankment Information for Flood Simulation of the Gin River, Sri Lanka', Journal of Disaster Research, 17(3), pp. 475–486. doi: 10.20965/jdr.2022.p0475.

Kawasaki, A. et al. (2017) 'Data Integration and Analysis System (DIAS) Contributing to Climate Change Analysis and Disaster Risk Reduction', Data Science Journal, 16(0). doi: 10.5334/dsj-2017-041.

Lehner, B., Verdin, K. and Jarvis, A. (2008) 'New global hydrography derived from spaceborne elevation data', Eos, Transactions, American Geophysical Union, 89(10), pp. 93–94. doi: 10.1029/2008EO100001.

Nyunt, C. et al. (2013) 'Bias Correction Method for', Annual Journal of Hydraulic Engineering, JSCE., 69(4), p. I_19-I_24.

Rodell, M. et al. (2004) 'The Global Land Data Assimilation System', Bulletin of the American Meteorological Society, 85(3), pp. 381–394. doi: 10.1175/BAMS-85-3-381.

Sayama, T. et al. (2012) 'Analyse pluie-débit-inondation de la crue de 2010 au Pakistan dans le bassin de la rivière Kaboul', Hydrological Sciences Journal, 57(2), pp. 298–312. doi: 10.1080/02626667.2011.644245.

Yatagai, A. et al. (2012) 'APHRODITE: Constructing a Long-Term Daily Gridded Precipitation Dataset for Asia Based on a Dense Network of Rain Gauges', Bulletin of the American Meteorological Society, 93(9), pp. 1401–1415. doi: 10.1175/BAMS-D-11-00122.1.

RECENT ADVANCES AND SHORTCOMINGS IN DOWNSCALING APPROACHES FOR CLIMATE CHANGE IMPACT AND ADAPTATION STUDIES

V-T-V. Nguyen[1]

ABSTRACT: The present paper provides an overview of some recent advances and shortcomings of downscaling methods for assessing the potential impacts of climate change on hydrological regime. In general, three broad categories of these downscaling procedures currently exist: (i) dynamical downscaling (DD) methods based on Regional Climate Models; (ii) statistical downscaling (SD) procedures that relied on the empirical relationships between large-scale atmospheric variables (predictors) and surface hydrologic parameters (predictands); and downscaling approaches based on machine learning (ML) methods. More specifically, it has been widely known that DD methods could provide reasonable description of the large regional climate conditions, but they could not accurately capture observed characteristics of hydrologic processes at a local or station scale. SD procedures could describe accurately the observed properties of various local hydrologic processes and could be adapted to the local climatic conditions for a given site. ML-based downscaling methods were found to be more efficient and more robust for describing the linkages between large-scale climate predictors and local hydrologic variables, but they could not provide significant improvements over SD procedures. However, since DD, SD, and ML methods have different associated skills, it is recommended that the best approach to developing climate change scenario for impact and adaptation studies should be based on the combination of these three procedures.

Keywords: Downscaling methods, Climate modeling, Climate change impact and adaptation, Hydrologic modeling.

INTRODUCTION

Climate change will have important impacts on the hydrologic cycle at different temporal and spatial scales. The temporal scales could vary from a short sub-hourly time interval (for urban water cycle) to a long yearly time scale (for annual water balance computation). The spatial resolutions could be from a few square kilometers (for small urban watersheds) to several thousand square kilometers (for large river basins). General Circulation or Global Climate Models (GCMs) have been recognized to be able to represent reasonably well the main features of the global distribution of basic climate parameters, but these models so far could not reproduce well details of regional climate conditions at temporal and spatial scales of relevance to hydrological impact studies (Nguyen and Nguyen, 2008; Maraun et al., 2010). In other words, outputs from GCMs are usually at resolution that is too coarse (generally greater than 200km) for many climate-related impact studies. Hence, there is a great need to develop tools for downscaling GCM predictions of climate change to regional and local or station scales. In recent years, different downscaling methods have been proposed in several studies around the world. Of particular importance for the management of water resources systems are those procedures dealing with the linkage of the large-scale climate variability to the historical observations of the surface parameters of interest (e.g., precipitation and temperature). If this linkage could be established, then the projected change of climate conditions given by a GCM could be used to predict the resulting change of the selected surface parameters for hydrological impact studies. The required linkage can be developed using a wide range of downscaling methods (Willems et al., 2012).

Therefore, the main objective of the present study is to provide a critical review of the feasibility and adequacy of various existing downscaling techniques to identify the most suitable procedure for evaluating the impacts of global climate changes on the hydrologic processes at a given location or over a given watershed of interest. Of particular interest is the ability of downscaling approaches for describing accurately the linkages between large-scale climate variables and the physical and statistical characteristics of precipitation and temperature processes since these two processes are the main components of the runoff generating mechanism. This state-of-the-art review work has provided an overview of the adequacy of each downscaling approach in terms of their ability to simulate adequately surface parameters critical for assessment of climate change impacts on hydrological regime.

OVERVIEW OF DOWNSCALING APPROACHES

Global atmospheric general circulation models or Global Climate Models (GCMs) have been developed for

[1] Department of Civil Engineering, McGill University, Montreal, Quebec, CANADA H3A 0C3

 https://doi.org/10.1142/9789811275449_0022

simulating the present climate and for predicting future climatic change. In recent years, the reliability of these models has been significantly improved as compared with those in the early 1990s. Recent GCMs could describe reasonably well the climate system at the continental and hemispheric spatial scales (IPCC, 2021). Despite this significant progress, these models are still unable to provide reliable results at the temporal and spatial scales that are relevant for many impact studies. One reason for this problem is that GCMs were not primarily developed for climate change impact studies, and hence are not well suited for simulating regional hydrologic variability at the catchment scale or at a given location. A second reason is that the refining of GCM results for the high regional (or local) resolutions of interest would incur extremely heavy computational costs because of the high complexity in the modeling of the atmospheric processes. Moreover, results from different GCMs are not fully consistent with each other at the regional scale (Willems et al., 2012). This inconsistency would put their reliability into question (Maraun et al., 2010; IPCC, 2021).

To circumvent the above-mentioned issues, tools for generating the high-resolution meteorological inputs required for modelling hydrological processes are needed. "Downscaling" approaches have subsequently emerged as an efficient means of relating large-scale atmospheric predictor variables to local- or station-scale hydrologic processes. In general, downscaling methods could be grouped into three broad categories (Figure 1): (i) Dynamical Downscaling (DD) methods, involving the explicit solving of the process-based physical dynamics of the system (Mearns et al., 2003); (ii) Statistical (or empirical) Downscaling (SD) procedures that were based on the relationships between coarse-scale predictor climate variables (e.g., atmospheric circulation indices) and at-site predictand surface parameters (e.g., precipitation) (Wilby et al., 2004); and (iii) downscaling approaches based on Machine Learning (ML) methods (Vandal et al., 2019).

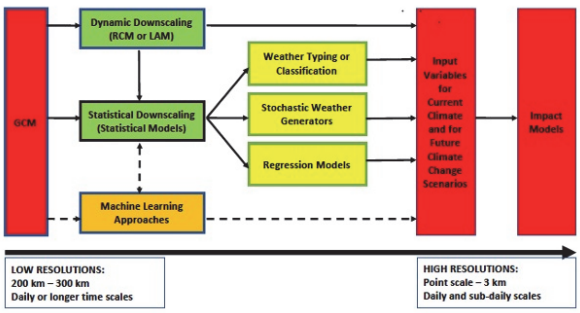

Fig. 1 Downscaling methods

Dynamic Downscaling Methods

The main objective of DD is to extract the local information from the large-scale GCM data using limited-area models or Regional Climate Models (RCMs). In general, three different DD approaches have been used for climate change impact studies (Mearns et al., 2003): (i) running a regional-scale limited-area model with the coarse GCM data as boundary conditions (the so-called "one-way nesting" method); (ii) performing global-scale experiments with high resolution atmosphere GCMs using coarse GCM data as initial (and partially as boundary) conditions; and (iii) using a variable-resolution global model with the highest resolution over the area of interest. Of these three methods, the most popular procedure could be the nesting of a higher resolution RCM with the coarse GCM data as boundary conditions.

Compared with GCMs, RCMs could model the physical dynamics of the atmosphere using horizontal resolution in the order of 20-50 km. The resolution of these RCMs is thus more suitable for coupling RCMs and hydrologic models for evaluating the impacts of climate change on hydrologic regime. Hence, the main advantage of RCMs is that they can describe the smaller-scale atmospheric features (e.g., orographic precipitation better than the host GCM). In addition, RCMs could be used to evaluate the relative significance of different external forcings such as terrestrial-ecosystem or atmospheric chemistry changes. However, there are several acknowledged limitations of the DD using RCMs (Mearns et al., 2003). The main limitation is that RCMs require considerable computing resources as GCMs (which restricted the number of experiments and the duration of climate simulations). Furthermore, the climate scenarios produced by RCMs are sensitive to the choice of boundary conditions used to initiate the experiments. DD methods cannot correct the large-scale GCM model inaccuracies. Finally, for many hydrologic applications, it is still necessary to downscale the spatially average results from RCMs to smaller spatial scales or individual sites for local hydrological impact studies.

Statistical Downscaling Methods

Statistical (or empirical) downscaling (SD) methodologies can be classified into three categories according to the computational techniques used (Wilby et al., 2004): weather typing approaches; stochastic weather generators; and regression methods. In general, these SD methods require three common assumptions: (i) the surface local-scale parameters are a function of synoptic forcing; (ii) the GCM used for deriving downscaled relationships is valid at the scale considered; and (iii) the derived relationships remain valid under changing climate conditions.

Among these three procedures, the regression and stochastic weather generator methods are the most popular because the weather classification schemes are somewhat subjective (Nguyen and Nguyen, 2008). Furthermore, several features distinguish DD and SD methods. DD methods contain more complete physics than SD techniques. However, the more complete physics significantly increases computational cost, which limits the simulation of a climate by these models to typically a single realization. On the other hand, SD approaches are relatively fast and less expensive than computationally intensive DD methods. These convenient features of the SD allow the users to develop a large number of different climate realizations and thus to be able to quantify the confidence interval of simulated climate variables. In addition, SD methods can directly account for the observed climate and weather data available at the local study site. The results are thus consistent with the local climate conditions as described by the observations. Finally, many downscaling approaches are based on the mixture of more than one of the above-mentioned downscaling methods (Nguyen and Nguyen, 2008).

Machine Learning-Based Downscaling Methods

These more recent downscaling approaches are based on machine learning (ML) methods such as Artificial Neural Network (ANN) and Support Vector Machine (SVM). So far it has been found that the direct application of these state-of-the-art ML methods to statistical downscaling did not provide a direct significant improvement over the traditional regression-based SD procedures (Vandal et al., 2019). The key challenge remains in this statistical downscaling work is how to be able to identify the climate predictors given by climate models that could significantly affect the temperature and precipitation characteristics at a given local site. The use of ML methods could provide hence a more efficient and more robust procedure for selecting these significant climate predictors.

CONCLUSIONS

In summary, the present review has indicated that, while significant advances have been made regarding the accuracy and reliability of global/regional climate modeling, outputs from these GCMs/RCMs are still not appropriate for the assessment of climate change impacts on hydrologic regime at small spatial and short time scales. To circumvent this difficulty, several downscaling methods have been proposed in the scientific and technical literature. Despite of some shortcomings, these methodologies have been found to be able to provide some useful tools for the assessment of the potential impacts of climate change in practice. However, downscaling methods are still relied on the accurate and reliable outputs of GCMs/RCMs to be able to develop realistic scenarios for describing possible changes of hydrologic processes under changing climate conditions.

Furthermore, due to their different nature and different associated skills, it is recommended that the best approach for developing physically plausible climate scenarios for impact and adaptation studies at a local site or area should be based on the combination of these three DD, SD, and ML methods.

ACKNOWLEDGEMENTS

This research work was supported by the Natural Science and Engineering Research Council of Canada (NSERC Discovery Grant).

References

IPCC (Intergovernmental Panel on Climate Change) 2021. Climate Change (2021): The Physical Science Basis. Sixth Assessment Report, Geneva, 3949 pages.

Maraun, D., Wetterhall, F., Ireson, A.M., Chandler, R.E., Kendon, E.J., Widmann, M., Brienen, S., Rust, H.W., Sauter, T., Themebl, M., Venema, V.K.C., Chun, K.P., Goodess, C.M., Jones, R.G., Onof, C., Vrac, M., and Thiele-Eich, I. (2010). Precipitation Downscaling under Climate Change: Recent Developments to Bridge the Gap between Dynamical Models and the End User, *Review of Geophysics*, 48: RG3003.

Mearns, L.O., Giorgi, F., Whetton, P., Pabon, D., Hulme, M., Lal, M. (2003). Guidelines for Use of Climate Scenarios Developed from Regional Climate Model Experiments, IPCC, 38 pages.

Nguyen, V-T-V., and Nguyen, T.D. (2008). Statistical Downscaling of Daily Precipitation Process for Climate-Related Impact Studies, Chapter 16 in "Hydrology and Hydraulics", V.P. Singh (Ed.), Water Resources Publications, pp. 587-604.

Vandal, T., Kodra, E., and Ganguly, A.R. 2019. Intercomparison of Machine Learning Methods for Statistical Downscaling: The Case of Daily Extreme Precipitation, Theoretical and Applied Climatology, 137: 557-570.

Wilby, R.L., Charles, S.P., Zorita, E., Timbal, B., Whetton, P., and Mearns, L.O., (2004). Guidelines for use of climate scenarios developed from statistical downscaling methods, IPCC, 27 pages.

Willems, P., Olsson, J., Arnbjerg-Nielsen, K., Beecham, S., Pathirana, A., Gregersen, I.B., Madsen, H., and Nguyen, V-T-V. (2012). Impacts of climate change on rainfall extremes and urban drainage systems. IWA Publishing, London, UK, 226 pages.

ASSESSMENT OF WATER QUALITY PARAMETERS BY USING MULTIVARIATE ANALYSIS AND WATER QUALITY INDICES OF AN INDUSTRIAL SEAPORT RIVERBANK AREA IN BANGLADESH

M.S. Islam[1,2], K. Nakagawa[3], M.A.A. Mamun[2], A.S. Khan[4], M.A. Goni[5], R. Berndtsson[6]

ABSTRACT: The present study investigated the physicochemical and metal concentrations in water samples collected from Pasur River, Bangladesh. Mongla seaport stands on the bank of this river. Many industries and other commercial sectors situated in this port area are discharging their wastes into the river without proper treatment. The concentration range of TSS, chloride, iron (Fe), and manganese (Mn) were from 363.2 to 1482.7, 108.2 to 708.93, 1.13 to 2.75, and 0.19 to 1.41 mg/L, significantly exceeding the health-based guideline of WHO and Bangladesh (DoE) standards. The average pH value was 8.73, higher than the WHO and DoE standard limit. The water quality evaluation indices such as Metal Index (*MI*), Comprehensive Pollution Index (*CPI*), and Water Quality Index (*WQI*) were used to determine the pollution levels of the Pasur River. *WQI* (ranging from 391.3 to 1336.1), *CPI* (6.71 to 23.13), and *MI* (7.23 to 23.27) were very high and greatly exceeded standard limits indicating that the Pasur River water is highly polluted. The results of Pearson correlation analysis, principal component analysis (PCA), and cluster analysis (CA) indicated that the sources of pollutants were both geogenic and anthropogenic. The spatial distribution of quality indices and cluster groups indicates that the studied river's urban and seaport areas were more contaminated. The primary anthropogenic sources are municipal wastewater, industrial effluents, runoff from an agricultural area, local bazar, car garage wastes, highway, and stormwater runoff.

Keywords: Surface water, Industrial riverbank, Pollution level, Quality indices, Multivariate analysis.

INTRODUCTION

The present study was conducted on the Pasur River in the Mongla port area (**Figure 1**). A significant site of oil refinery (petroleum and vegetable oil), cement, dye and paint, leather, and shipbreaking industries is established near the Pasur River. Poorly or untreated toxic effluent were directly discharges by the industry in to the Pasur River that becomes increasingly polluted. The river water is used for different functions such as industrial purposes, household activities, bathing, irrigation of fields, and cooking foods by the adjacent rural populations. In the dry season, when the drinking water is at crisis level, local rural people use the river water for drinking purposes after boiling. The river was once an important freshwater source for drinking and domestic uses, fisheries, and agricultural irrigation. The river is still used for fishing, and fishermen use smaller or larger boats for fishing. Polluted fish is another crucial reason to assess and monitor the surface water of this river. Given the above, this study focused on assessing the Pasur River water quality by using water quality evaluation indices such as Water Quality Index (*WQI*) (Tabrex et al. 2022), Comprehensive Pollution Index (*CPI*) (Xiong et al. 2021), and the Metal Index (*MI*) (Bakan et al. 2010). Though some research has been conducted for this river, but there are still no systematic studies focusing on both physicochemical parameters and toxic metal pollution and pollution source determination in this selected area.

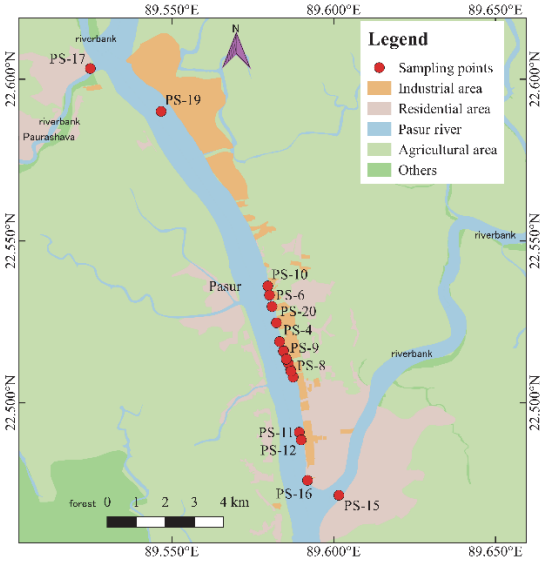

Figure 1. Location showing the study area and sampling points

[1] Graduate School of Fisheries and Environmental Sciences, Nagasaki University, 1-14 Bunkyo-machi, Nagasaki 852-8521, JAPAN
[2] Department of Chemistry, Jashore University of Science and Technology, Jashore-7408, BANGLADESH
[3] Institute of Integrated Science and Technology, Nagasaki University, 1-14 Bunkyo-machi, Nagasaki 852-8521, JAPAN
[4] Environmental Laboratory, Asia Arsenic Network, Arsenic Center, Benapole Road, Krishnobati, Pulerhat, Jashore-7400, BANGLADESH
[5] Department of Chemistry, Bangladesh University of Engineering and Technology, Dhaka-1000, BANGLADESH
[6] Division of Water Resources Engineering & Centre for Advanced Middle Eastern Studies, Lund University, Box 118, SE-221 00 Lund, SWEDEN

 https://doi.org/10.1142/9789811275449_0023

Thus, assessment of pollution status is insufficient in this area. It is also essential to identify the pollution sources. For this purpose, we used multivariate analysis to indicate sources of water pollutants, including metals (Algul et al. 2020; Krishna et al. 2009). Therefore, the main goal of this study was (i) to determine the water quality parameters of the Pasur River based on physicochemical and toxicological parameters, (ii) to use water quality indices such as *WQI*, *CPI*, and *MI* for assessing the water quality parameters with spatial distribution for the Pasur River, and (iii) to identify the source of pollutants including metal contamination in water by using multivariate analysis methods.

METHODS AND MATERIALS

The pH, temperature, and total dissolved solids (TDS) were measured on site by a calibrated apparatus. A portable calibrated pH Meter (HI 2211, HANNA Romania, Romania) was used for measuring pH. TDS was determined by calibrated multimeter (CT-676, BOECO Germany, Hamburg, Germany). Total alkalinity, chloride, total suspended solids (TSS), total hardness, iron, and manganese were measured by acid-base titration, Mohr's titration, filtration, EDTA complexometric titration, and flame-AAS method, respectively. All laboratory equipment was immersed in 10% nitric acid for 48 h, rinsed with distilled water, and dried in an oven before the analyses. Analytical grade chemicals and reagents were used during the experimental analysis.

RESULTS AND DISCUSSION

This study revealed that pH, iron, manganese, total suspended solids, and chloride at some locations had much higher concentrations in the river water than recommended by WHO and Bangladesh Environmental standards (DoE). The water quality index (*WQI*), Comprehensive Pollution Index (*CPI*), Metal Index (*MI*), and pollution level were shown by **Table 1**. It is revealed that the average value of *WQI*, *CPI*, and *MI* was higher than standard limit and pollution level were higher of all sampling stations.

The positively correlated parameters with one another included Mn with Fe ($r = 0.757$), $p < 0.01$); total hardness (TH) with alkalinity ($r = 0.739$, $p < 0.01$) and TDS ($r = 0.992$, $p < 0.01$), and TDS with alkalinity ($r = 0.735$, $p < 0.01$). Fe was moderately correlated with TSS ($r = 0.483$), and chloride was moderately related to Fe ($r = 0.641$, $p < 0.05$). Higher correlation between variables may indicate common sources, mutual dependence, and similar or nearly identical metal accumulation properties in surface water. The spatial variation of *WQI* is shown that southeast part of the study area had the highest values. The sampling points were close to the Mongla Seaport

Table 1. Water quality index (*WQI*), Comprehensive Pollution Index (*CPI*), Metal Index (*MI*), and pollution status

Sample ID	*WQI*	*CPI*	*MI*	Pollution Level
PS-1	466.4	10.80	8.93	High
PS-2	746.6	13.72	14.30	High
PS-3	638.8	23.13	11.23	High
PS-4	466.1	7.62	8.37	High
PS-5	744.8	12.73	14.00	High
PS-6	440.2	9.65	8.50	High
PS-7	826.5	16.58	14.77	High
PS-8	750.6	14.46	13.67	High
PS-9	391.3	9.64	7.23	High
PS-10	399.9	15.99	9.33	High
PS-11	1336.1	17.24	23.27	High
PS-12	875.6	12.09	16.33	High
PS-13	1008.1	13.96	18.40	High
PS-14	447.9	6.71	8.20	High
PS-15	706.1	11.82	13.00	High
PS-16	967.9	14.39	17.43	High
PS-17	807.5	10.82	15.20	High
PS-18	808.9	12.13	15.20	High
PS-19	582.9	10.05	10.90	High
PS-20	641.9	11.65	11.83	High
Average	702.7	12.76	13.0	High

responsible for increasing the pollution and hence WQI. High WQI is probably related to domestic waste, effluents from industry and nearby local markets, and agricultural runoff. The trend of *CPI* distribution is somewhat like the distribution for *WQI*. The *CPI* gradually decreases from south to north in the study area. Highest *CPI* was found in the south and south-eastern parts, whereas the north region is associated with low *CPI*. The sites with high pollution load are densely populated urban areas including a trunk road, bazaars, shops, car washing garages, and many small and heavy industries situated beside the bank of Pasur River.

The spatial distribution of *MI* indicates a trend with increasing concentrations from north to south. the southern study area thus indicates higher pollution pressure. The southern region is close to Mongla Seaport and urban areas with heavy industries. The highest value of *MI* was found in sampling location PS-11, which is closely associated with the Mongla seaport area. Many ships gather here for extensive loading and unloading activities. This may be the probable reason for higher metal pollution at this site.

Principal component 1 (PC1), had positive loadings for all parameters but especially high loading for total hardness, TDS, Mn, and chloride ($r = 0.63$–0.81), and moderately associated with pH, alkalinity,

temperature, and Fe, accounting for 36.6% of the total variance. PC2 was strongly associated with Fe, Mn, and TSS also confirmed from the correlation matrix. PC3 had high association with TSS. Again, the strong association between Fe and Mn indicates that similar sources are at hand. These pollutants have similar geogenic and anthropogenic sources such as untreated industrial effluents, agricultural runoff, municipal waste, and landfills from nearby urban areas.

The 20 samples were classified into four distinct groups, clusters A, B, C and D. The results shows that cluster A was not strongly related with any parameters. Cluster B was related to high TSS, Fe, and Mn. Cluster B contained higher indices values (*WQI*, *CPI*, and *MI*) than cluster A and D. High TSS, pH, chloride, Fe, and Mn were classified in cluster C. Cluster C was ranked as the most polluted area among the four clusters with respect to *WQI*, *CPI*, and *MI*. Cluster D was related to pH, TDS, and chloride. This cluster's *WQI*, *CPI* and *MI* values were lower than cluster B and C but higher than cluster A. The decreasing order of indices was cluster C > cluster B > cluster D > cluster A. Thus, cluster C was most polluted, and cluster A the least.

The scatter plot of the 20 samples described by principal components and classified into four clusters. PC 1 has smaller scores for cluster a indicating that it had less concentration of the quality parameters than cluster B, C, and D. Thus, it can be confirmed that samples of cluster A were less polluted than others. Both cluster C and cluster B showed positive scores for PCs 1 and 2, but cluster C was more affected than cluster B. PC 3 revealed that cluster B is significantly more influenced than cluster D. Thus, the sample of cluster B was more affected and polluted than cluster D. The spatial distribution of each cluster can be observed and shown that cluster C is the study area's most contaminated sampling point. the location of cluster C is associated with Mongla seaport and nearer the Sundarban mangrove forest in the west part of the study area. Cluster B is located south to north at different study area sites. The samples of this cluster contained high metal concentrations indicating a metal contamination area. The contamination of this area is higher than for cluster D and cluster A. Sample of cluster D is in the southeast region and near the residential area. It contains the highest value of total hardness and TDS. All cluster A samples are in the southeast area but far from cluster C. Samples of cluster A contain the lowest value of metals and other physicochemical parameters.

CONCLUSIONS

The present study concluded that pH, iron, manganese, total suspended solids and chloride at some locations had much higher concentrations in the river water than recommended by who and Bangladesh Environmental Standards (DoE) and thus are not safe for household use or aquatic ecosystems. The severe enrichment of pollutants in this area is primarily due to some geogenic and anthropogenic sources related to industrial, agricultural, urbanization, and fishing activities. Mongla seaport authority, municipal corporation, district administration, and the department of environment can take the initiative to protect the river water from pollution and untreated industrial and municipal waste. This study recommends that continuous monitoring of the pollution level of the Pasur river as well as adjoining agricultural areas should be assessed regarding the risk for human health and ecosystems in the vicinity of the river. Finally, public can play a key role in pollution reduction due to awareness of the impacts and remedies of pollution to them.

ACKNOWLEDGEMENTS

The authors wish to express their sincere thanks to Department of Chemistry at "Jashore University of Science and Technology" and the "Asian Arsenic Network" for the laboratory support to complete this research.

References

Algul, F.; Beyhan, M. (2020). Concentrations and sources of heavy metals in shallow sediments in Lake Bafa, Turkey. Sci. Rep. 10:11782.

Bakan, G.; Ozkoc, H.B.; Tulek, S.; Cuce, H. (2010). Integrated environmental quality assessment of Kızılırmak River and its coastal environment. Turk. J. Fish. Aquat. Sci. 10:453–462.

Goher, M.E.; Hassan, A.M.; Abdel-Moniem, I.A.; Fahmy, A.H.; El-sayed, S.M. (2014). Evaluation of surface water quality and heavy metal indices of Ismailia Canal, Nile River, Egypt. Egypt. J. Aquat. Res. 40:225–233.

Krishna, A.K.; Satyanarayanan, M.; Govil, P.K. (2009). Assessment of heavy metal pollution in water using multivariate statistical techniques in an industrial area: A case study from Patancheru, Medak District, Andhra Pradesh, India. J. Hazard. Mater. 167:366–373.

Tabrez, S.; Zughaibi, T.A.; Javed, M. (2022). Water quality index, Labeo rohita, and Eichhornia crassipes: Suitable bio-indicators of river water pollution. Saudi. J. Biol. Sci. 29:75–82.

Xiong, B.; Li, R.; Johnson, D.; Luo, Y.; Xi, Y.; Ren, D.; Huang, Y. (2021). Spatial distribution, risk assessment, and source identification of heavy metals in water from the Xiangxi River, Three Gorges Reservoir Region, China. Environ. Geochem. Health 43:915–930.

SENSITIVITY EXPERIMENTS OF LAND COVER IMPACT ON FLOOD EVENT (2015) IN PAKISTAN

H. Shahid[1], M. Toyoda [1] and S. Kato[1]

ABSTRACT: Among natural disasters in Pakistan, flooding is the most frequent and devastating. In Punjab, the flood-prone areas suffer heavy damage during the heaving rainfall of the monsoon. The population density of Punjab region is increasing every year. Conversely, the dependence of population on rivers and urbanization on agricultural land is increasing every year. Many researchers tried to investigate flood mechanism and predict flood disasters. Researchers have mainly focused on the upstream of the Indus River due to flash flood disaster risk. At the downstream of Indus river, the high population density area after the confluence of the Indus and Chenab rivers is also important due to the riverine. In this region, severe inundation by flooding occurred in 2015. In this study, Rainfall-Runoff-Inundation Model (RRI) and River model (iRIC) were used to evaluate the inundation. We aimed to comprehensively evaluate the inundation risks (inundation depth, peak inundation discharge, and inundation area) by considering extreme rainfall events over densely populated areas located downstream of the confluence point of the Indus and Chenab Rivers. In addition, sensitivity experiments for land cover were conducted to reveal the impact of land-cover change (urbanization and afforestation) on inundation. The Nash-Sutcliffe model efficiency coefficient for river discharge calculation at the Tounsa barrage and Trimmu headworks (on just before the confluence point of Indus and Chenab) was 0.83 and 0.67 respectively. Furthermore, the flooding at the confluence point of the Indus River was reproduced by iRIC with high accuracy. The results showed that planting and afforestation will mitigate flooding scale, but urbanization increases the risk of flooding especially after the confluence point of two rivers at the high population dense area. Planting between the Indus River and Chenab River could mitigate flood disasters downstream of the confluence point.

Keywords: Flooding, river confluence point, RRI, iRIC, Landcover change

INTRODUCTION

Among many natural disasters, flooding is frequent and most devastating in the province of Punjab Pakistan. Riverine flooding occurs especially in the province of Punjab because there is a confluence point of 5 rivers to the Indus River in this province. There are the highest risk areas that are prone to flood and suffer a lot of damage during the heaving rainfall of the monsoon (Rahman et al., 2017). Also, the population density of Punjab region is increasing every year, which increased the dependence of population density on rivers and urbanization on agricultural land. Sayama focused on the Kabul River basin and conducted simulation using the Rainfall-Runoff-Inundation model (RRI) for run-off and inundation (Sayama et al., 2012). They reported their model can apply to large-scale flooding and to provide supplemental information to agencies for relief operations. Researchers have focused on the northern parts of the Indus basin because of extreme rainfall in short period of time cause flash flooding which cause flood disaster in this region. The inundation risks in the southern parts of the Indus basin especially after the confluence of Chenab and Indus Rivers, including the impact of urbanization in this region, also require a further assessment. The area after the confluence points of Chenab and Indus Rivers (Rahim yar khan District) has the highest water discharge and 2.5 times more population density than the average population density.

The purpose of the study is to find out the inundation phenomena after the region of the confluence point of Indus River and Chenab River. Also, a sensitivity experiment of landcover change (Urbanization and planting) is conducted to evaluate the response of flooding in this area.

METHODOLOGY

The study methodology is finding flood inundation using the numerical model software Rainfall-Runoff Inundation (RRI) with rainfall data input during monsoon (00:00 UTC 1, Jul. 2015 - 00:00 UTC 1, Sep. 2015) in the southern region of Punjab. The RRI software simulation results outputted the flood inundation area with discharge time series values at different grid points. The discharge time series data is used in International River Interface Cooperative (iRIC) software to find the flood inundation with a horizontal resolution of less than 150m. After that run sensitive model experiments of landcover change by simulation, to find out the impact of urbanization and afforestation on the flood inundation area in the down region of the Indus River after the confluence point.

The area of the Indus River for the numerical simulation is quite large in RRI with the low-resolution of 1/60 degree horizontal topography in the simulation. To select the area of the Indus River for the simulation, the northern part of Pakistan is considered because heavy rainfall occurs in that region. The area covers the northern

[1] Department of Architecture and Civil Engineering, Toyohashi University of Technology, Toyohashi 441-8580, Aichi, JAPAN

 https://doi.org/10.1142/9789811275449_0024

part of mountainous areas Pakistan called Gilgit Baltistan, province KPK, and most of the province Punjab region (**Fig.1**). The observed rainfall data by the government of Pakistan's meteorological department has been inputted in the RRI simulation using the Thiessen method. There are 70 rainfall gauges in different observation sites all over the selected area of simulation (**Fig.1**; X mark). The river width parameters after the confluence point of Chenab and Indus rivers were obtained from Google Earth with the help of a known variable of the catchment area. The depth parameters were obtained from a previous study with a maximum limitation of 4.5 m.

$$W = 2.5A^{0.4} \quad (1)$$

$$D = 0.1A^{0.4} \quad (2)$$

iRIC model is used for simulation targeted confluence area. iRIC can consider water discharge from upstream as boundary conditions. Therefore, hourly river discharge from RRI is input to iRIC. The river discharge of the Indus River and Chenab River upstream of the confluence point is used for iRIC. The horizontal resolution of iRIC is 150 m, the time step is set 0.1 sec and output intervals are 3600 sec. The sensitivity experiments of landcover change are listed in the table (**Table.1**).

RESULTS AND DISCUSSION

Validation of Models

RRI simulation results of case 1 (original landcover) is obtained after running the simulation. RRI simulation results gave water inundation and water flow (discharge and water height). The calculated discharge curves at two points just before the confluence point of Indus and Chenab Rivers (Tounsa barrage and Trimmu headworks) are calibrated from the observation discharge curve (**Fig.2**). To validate the results of the simulation Nash coefficient is found out. Nash Sutcliffe model efficiency coefficient is calculated as one minus the ratio of the error variance of the modeled time series divided by the variance of the observed time-series. The value of the Nash coefficient is 0.83 at Tounsa and 0.67 at Trimmu which proves the simulation results are good from RRI.

$$NSE = 1 - \frac{\sum_{t=1}^{T}(Q_m^t - Q_o^t)^2}{\sum_{t=1}^{T}(Q_o^t - \bar{Q})^2} \quad (3)$$

To validate the results of iRIC simulation, the Moderate Resolution Image Spectroradiometer (MODIS) Near Real-Time Global Flood Mapping of 2015 has been used. For the comparison of the flooded area between observed and calculated area, FIT (%) value has been found out. The value of FIT is 0.62 which validates the results of iRIC simulation.

$$FIT = \frac{IA_{obs} \cap A_{sim}}{IA_{obs} \cup IA_{sim}} \quad (4)$$

Table.1: Sensitivity Experiment Cases

Case 1	Control case (original case)
Case 2	Six cities (Lahore, Islamabad, Peshawar, Faisalabad, D.G. Khan, and Multan) Urbanization
Case 3	All areas converted into a forest
Case 4	All land cover areas changed to urbanization
Case 5	Urban grids (No. 18) are expanded to eight surrounding grids
Case 6	Shrubs, herbaceous and vegetation, and bare areas (No. 6, 7, 8, 9, 10, 16, 17) were all converted into a forest
Case 7	Urbanization between the Chenab and Indus Rivers, combine with Case 6 area
Case 8	Cases 5 and 6 are combined (simultaneous planting and urbanization)

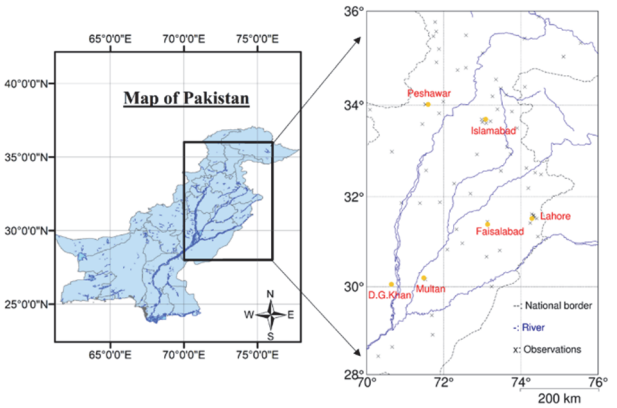

Fig.1: RRI inundation area and rainfall input points

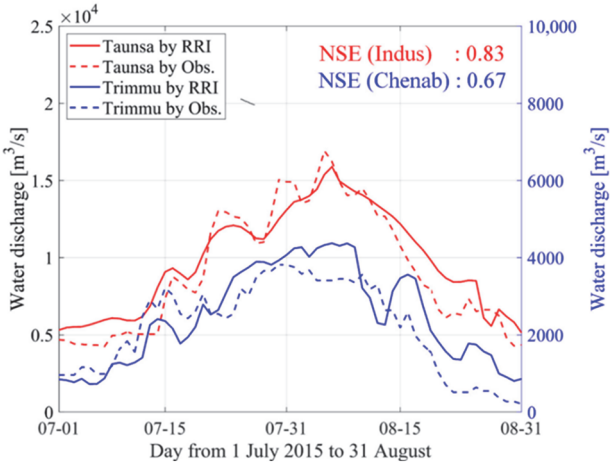

Fig.2: Comparison between observed and calculated discharge

Sensitivity Experiments

Case 1 (**Figs.3(a) and 4(a)**) shows the inundation on the upper Indus basin and lower Indus basin. On the upper Indus basin, the flooding occurs due to intensive rainfall and lower Indus basin the flooding occurs due accumulation of water flow from upstream area. Case 2 and 5 had an impact on the magnitude of flooding in the upstream area. however, the scale of flooding at the confluence point was almost similar to the one in Case 1. Case 3 of complete afforestation showed that the flooding was completely prevented which shows that the area is sensitive to planting to prevent flooding (**Figs.3(b) and 4(b)**). The inundation pattern in Case 4 showed severe flooding occurred in both the upper Indus basin and lower Indus basin. Also, urbanization increased the flooding along the bank of both Chenab and Indus Rivers (**Figs.3(c) and 4(c)**).

The results showed that Case 6 had the largest impact on the inundation area, the flow of the Indus River and the confluence point (**Figs.3(d) and 4(d)**). Planting vegetation, especially in the upper Indus basin, coincided with a high precipitation area and, therefore, reduced the impact of inundation on the upper Indus basin and the flow of the main river. The flow of the Chenab River is reduced due the planting at the bare area between the Chenab River and the Indus River. The results of Case 7 and 8 showed that the Indus River flow had less flow discharge than Case 1 due to planting on the upper Indus basin. However, the results showed that compared with Case 6, the development between the rivers could cause flooding near the confluence point areas.

Sensitivity Experiments in iRIC

Sensitivity experiments will also be conducted in iRIC to see the effect of landcover change on the inundation after the confluence point of Indus and Chenab river at the high population density area. The inundation pattern is the same in iRIC as in RRI. Case 2 and 5 had not significantly affected the inundation after the confluence point. Case 3 and Case 4 has highest impact on the inundation depth. Case 6 had also large impact on the inundation area, the flow of the Indus River and confluence point. The main Indus river flow decreased from 4.5m to 3m, and the surrounding inundation also decreased respectively. Case 7 results showed that development in the area between the Chenab and Indus Rivers would increase the risk of inundation after the confluence point of these rivers despite planting in the upper region. Case 8 results showed that major urbanization would also increase the risk of flooding after the confluence point.

CONCLUSION

Simulation results of the land cover change experiments showed that the inundation pattern was affected by land cover changes. Extreme urbanization increased the risk of inundation and extreme afforestation greatly affected inundation in the Indus basin. Case 6 (Planting) in the upper Indus basin significantly reduced inundation and the flow of the main Indus River and contributed to flood disaster prevention in the high-risk area of the upper Indus basin. Planting between the Indus and Chenab Rivers showed a major effect on inundation after the confluence point of both rivers. Urbanization with planting showed that there was an inundation area after the confluence point. Overall, a sustainable development is needed with afforestation to prevent flooding in the region.

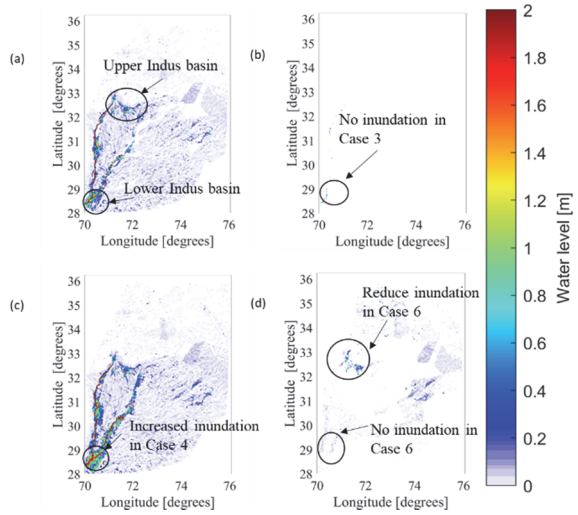

Fig.3: Simulation results of RRI (a) Case 1; (b) Case 3; (c) Case 4; (d) Case 6.

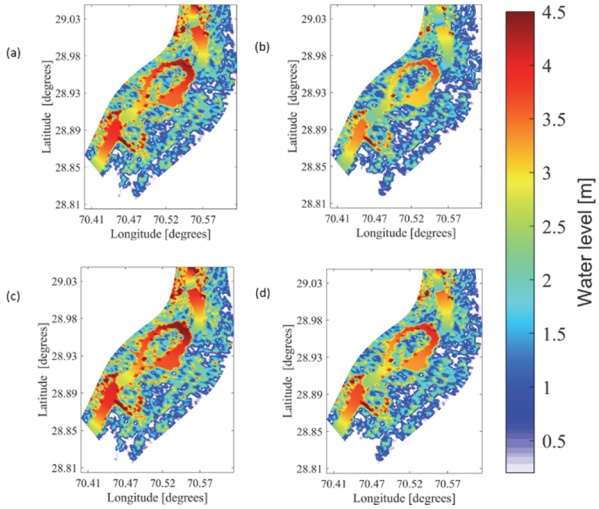

Fig.4: Simulation results of iRIC (a) Case 1; (b) Case 3; (c) Case 4; (d) Case 6.

References

Rahman, G., Atta-Ur-Rahman., Muhammad, M., Mehtab, A., Humayun, A. and Umayya, Z. (2017). Socio-economic Damages caused by the 2014 Flood in Punjab Province, Pakistan. *Proceedings of the Pakistan Academy of Sciences*, 54(4), 365-374.

Sayama, T., Ozawa, G. and Kawakami, T. (2012). Rainfall runoff inundation analysis of the 2010 Pakistan flood in the Kabul. *Hydrological Science Journal,*57(2), 298-312.

RAINFALL FORECAST BY IDENTIFICATION OF CHARACTERISTIC COMPONENTS OF RAINFALL USING SINGULAR SPECTRUM ANALYSIS

Priya Shejule[1] and Sreeja Pekkat [2]

ABSTRACT: Complete information on hydro climatology is necessary for developing water resource-based sectors. Rainfall forecast is one of the critical issues for the hydrologic community, which indirectly affects human beings, socio-economic status, climate change, and global well-being. Recent advances in science and technology have evolved and improved the rainfall forecast skill. Despite the advances, the challenge is identifying appropriate accurate techniques to forecast rainfall. Although there are many forecasting techniques, it is noted that considerable improvement is still needed for rainfall forecast at a smaller time scale. The difficulty in forecasting increases with the smaller time step of the rainfall series. In the present study, we have attempted rainfall forecast on a daily scale. The singular spectrum analysis (SSA) is found to be an efficient method that can handle the non-linear, non-stationary time series data. In the present study, SSA is applied to forecast the daily rainfall for the next one year based on daily rainfall data from NASA power. The observations from this study show that SSA successfully interprets the trend, periodicity, cyclic component, and noise of the time series. The method successfully displays the repetition pattern of rainfall, rise and fall in rainfall magnitude. Overall, rainfall at the daily time step for the whole year was forecasted with reasonable accuracy.

Keywords: Rainfall forecast; Singular spectrum analysis; Daily time step

INTRODUCTION AND MOTIVATION

Complete information on hydrology and climatology is required to frame the sustainable development of water resources based sectors. According to the fifth IPCC (Intergovernmental Panel on Climate Change) climate assessment report, climate change is responsible for extreme weather events (Pachauri et al. 2014), which leads to floods and droughts around the world.

The available climate change models predict long-term variations in rainfall process for various assumed scenarios. However, researchers over the globe are still in search of smaller time-step rainfall forecast model that can be effectively used in early planning and management of water resources based sector.

Forecasting rainfall at smaller time scale is a difficult task. Earlier studies proved that time series models failed to predict extreme rainfall events. Thus, it necessitates developing a better model, which will analyze the internal structure of the time series. The current study proposes the application of forecasting technique capable of identification of internal structure of time series. Here attempt has been made to obtain daily rainfall forecast for duration of one year.

STUDY AREA AND DATA COLLECTION

The daily rainfall data of the Guwahati city India for the period 1981-2017 is selected in the present analysis. The Guwahati city has longitude extent of 91° 4'25" to 91° 52'00" E and latitude extent of 26° 4'45" to 26° 13'25" N. The Fig. 1 shows the daily rainfall series plot for the given study area.

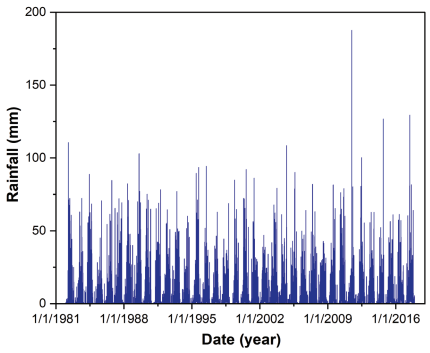

Fig. 1. Daily rainfall data series for Guwahati city

METHODOLOGY

In the present study, the singular spectrum analysis (SSA) is applied for the analysis and forecast of time series. SSA is a robust technique capable of interpreting the time series in different components such as trend, periodicity, cyclic component, and noise (Golyandina 2001).

The main stages in SSA are (a) decomposition and (b) reconstruction. The decomposition has two steps (i) embedding and (ii) SVD. The reconstruction phase of SSA involves two steps (i) grouping and (ii) diagonal averaging. The flowchart for methodology is given in Fig. 2.

[1] Research Scholar, Department of Civil Engineering, Indian Institute of Technology Guwahati, INDIA 781039
[2] Associate Professor, Department of Civil Engineering, Indian Institute of Technology Guwahati, INDIA 781039

 https://doi.org/10.1142/9789811275449_0025

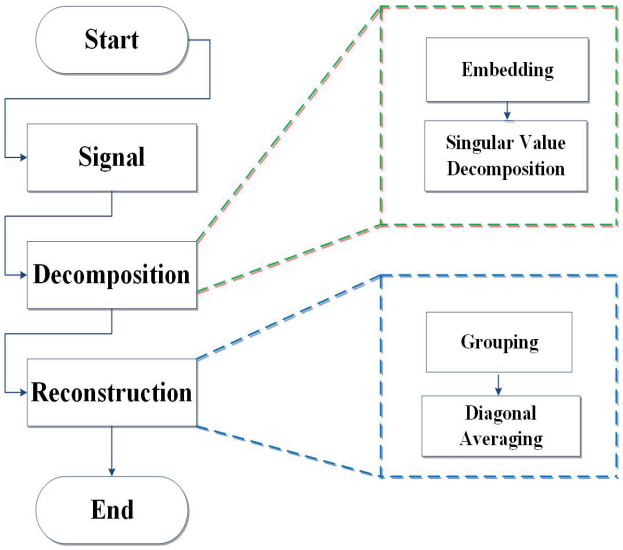

Fig. 2. Flowchart for singular spectrum analysis

Forecasting algorithm

The recurrent forecast method is applied to forecast rainfall for next 'T' steps. The basis of method is that last component of any vector z can be expressed as linear combination of past components $\left(z_1, z_2 \ldots z_{L-1}\right)$. The linear recurrent formula is given as follows:

$$F = \frac{1}{1-\pi^2} \sum_{i=1}^{L} P_i U_i \qquad (1)$$

$$\pi^2 = P_1^2 + \ldots\ldots + P_L^2 \qquad (2)$$

Where P_i is the last component of eigen vector U_i for $\left(i = 1, 2, \ldots, L\right)$ and vector $F = \beta_1, \ldots\ldots, \beta_{L-1}$. Here L is window length and N is the length of known data points.

$$z_i = \begin{cases} \tilde{z}_i & for\ i = 1, \ldots, N; \\ \sum_{j=1}^{L-1} \beta_j x_{i-j} & for\ i = N+1, \ldots, N+T \end{cases} \qquad (3)$$

RESULTS AND DISCUSSION

Application of SSA

The SSA is a powerful method, which can separate the noise component from the raw signal. Decomposition of SSA enables us to identify the trend, periodicity and, peak values in the data series. Based on the properties of time series, trend component is extracted by SSA as shown in Fig. 3. Trend plot helps to understand whether there is increase or decrease in magnitude over longer period of time. Traditional methods fail to predict the shape of variation which can be overcome by SSA.

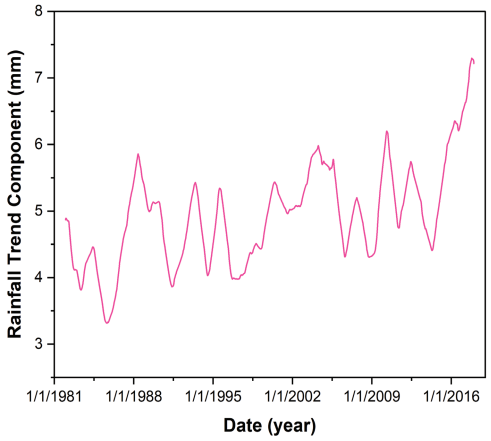

Fig. 3. Rainfall trend component for Guwahati city

Fig. 4. shows the range of cyclic component which represents rise or fall of rainfall series over longer period of time (Woodward et al. 2012).

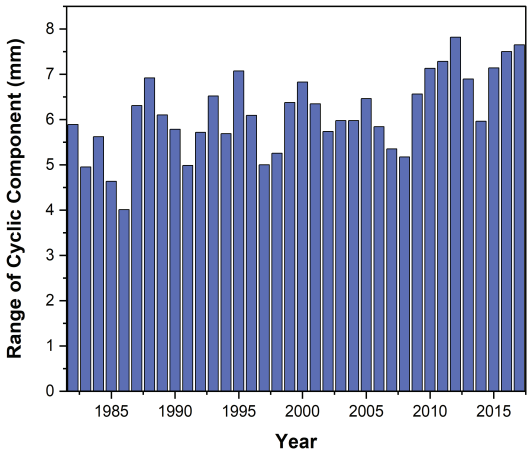

Fig. 4. Range of cyclic component

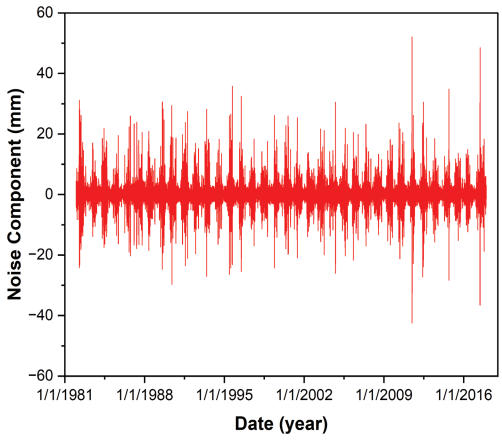

Fig. 5. Noise component

Noise is the irregular fluctuations present in the data series. Identification of noise is the difficult task as it does not follow any specific pattern. The Fig. 5, shows the extracted noise component of the given rainfall series.

Rainfall is consisting of important components such as trend, periodic, cyclic component and noise. To check how well the components are separated weighted-correlation matrix is plotted. From Fig. 6, it is observed that first few eigen functions are correlated to only themselves after eigen function 12, the spread suggests intermixing. The increase spread denotes the random correlation among the eigen functions.

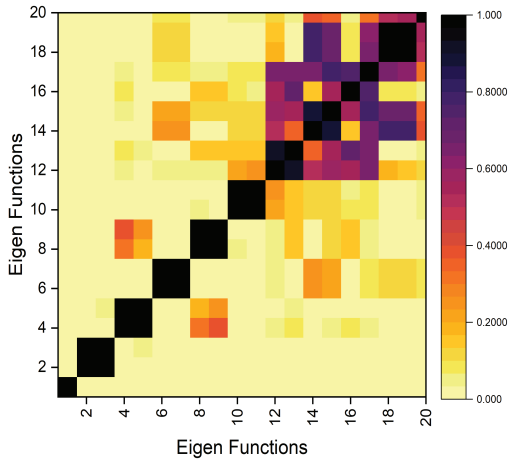

Fig. 6. Weighted-correlation matrix

The trend, periodic and cyclic component together forms a rainfall signal. The forecasted rainfall signal for the year 2018 and extracted rainfall signal from available 2018-year data are compared in Fig. 7. It shows the slight over prediction in peak values. However, the extracted and forecasted signal are well correlated with R^2 value of 0.97,

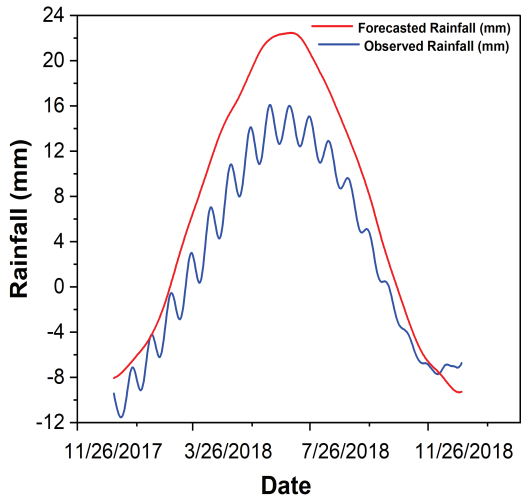

Fig.7. Comparison of rainfall signal components

indicating good agreement between observed and forecasted rainfall signal. Similarly, noise also compared. By adding signal and noise component, rainfall series is obtained. The rainfall is forecasted with reasonable accuracy with R^2 value of 0.61. This is may be due to the addition of chaotic noise to the signal component. The statistical measures used for the model assessment is shown in Table 1.

Table 1. Model performance measure

Performance measure	Value
Coefficient of Determination (Signal)	0.9700
Coefficient of Determination (Rainfall)	0.6100
Mean Absolute Error (MAE) (mm)	3.5270
Root Mean Square Error (RMSE) (mm)	5.9026

CONCLUSIONS

In the present study an attempt has been made to forecast rainfall by application of singular spectrum analysis. Results shows that:

- The various components are extracted and forecasted well with reasonable accuracy on daily scale for 365 days for the study area.
- The SSA helps us to understand the positive or negative trend along with the shape of variation over longer period of time.
- The method successfully displays the repetition pattern of rainfall, rise and fall in rainfall magnitude.

The above results suggest that SSA can be successfully applied to understand the internal structure of rainfall series.

References

Golyandina, N., Nekrutkin, V., and Zhigljavsky, A. (2001). “Analysis of Time Series Structure: SSA and Related Techniques.” Chapman & Hall/CRC.

Pachauri, Rajendra K., Myles R. Allen, Vicente R. Barros, John Broome, Wolfgang Cramer, Renate Christ, John A. Church et al. Climate change 2014: synthesis report. “Contribution of Working Groups I, II and III to the fifth assessment report of the Intergovernmental Panel on Climate Change.” IPCC, 2014.

Woodward, W.A., Gray, H.L., Elliott, A.C., (2012). “Applied Time Series Analysis.” CRC Press LLC, Boca Raton.

DISTRIBUTION AND RISK ASSESSMENT OF TRACE ELEMENTS IN SEDIMENT CORES FROM A COASTAL WATERSHED: AN EXAMPLE FROM THE LIAN RIVER, SOUTH CHINA

L. Xie[1,2], D. Rosado[2], J. Chen[3], G. Hörmann[2] and N. Fohrer[2]

ABSTRACT: The Lian river catchment hold one of the largest e-waste recycling centers in the world between 1995 and 2015. Valuable elements were extracted and much of the residues were discarded into the Lian watershed. These practices may have released toxic trace elements to water bodies nearby, as it has been reported for flame retardants in the area before. Therefore, our aim was to evaluate the distribution, potential risks and sources of 7 trace metals (Cr, Ni, Cu, Zn, As, Cd and Pb) known to be linked to these effluents in the Lian river. Sediments cores from 5 sites from the upper to the lower reaches of the river were collected. The total concentrations of trace metals were determined by means of a digestion with HNO_3-HF followed by measurement with an ICP-MS. The results showed that the sediments of the river were significantly polluted by Cr (18.32–83.73 mg/kg), Ni (6.45–50.6 mg/kg), Cu (9.36–531.5 mg/kg), Zn (38.57–441.9 mg/kg), Cd (0.209–1.135 mg/kg) and Pb (54.02–492.8 mg/kg). The pollution load index showed values higher than 4 in the middle section and between 2 and 3 in the lower sections of the study area. Source identification based on principal components analysis showed strong positive correlations among al metals except of Cd, that showed a different behavior, suggesting industrial pollution for the formers and agriculture pollution for the latter.

Keywords: sediment pollution, heavy metal pollution, environmental pollution, Guangdong Province, risk assessment

INTRODUCTION

Riverine sediment is one of the primary components of river ecosystems (Song et al., 2019). However, with expanding urbanization, rapid industrialization and intense human activities, numerous toxic metals have been transported into river water and have accumulated in sediment, leading to severe deterioration of sediment quality (Debnath et al., 2021).

In recent years, the amount of e-waste has risen significantly. In parallel, an industry to recover its valuable materials was developed, especially in developing countries like China. The Lian river catchment held one of the largest e-waste recycling centres in the world from 1995 to 2015, when a central industrial park with stricter environmental controls was built (Li et al., 2019). The components of the e-wastes were usually subjected to roasting, burning and acid dissolution to extract valuable elements and much of the residues were discarded into the Lian watershed before flowing into the South China Sea at Haimen Bay (Sthiannopkao and Wong, 2013).

Therefore, our aim was to evaluate the distribution, potential risks and sources of 7 trace metals (Cr, Ni, Cu, Zn, As, Cd and Pb) known to be linked to these effluents in the Lian river.

MATERIAL AND METHODS

Sediments cores from 5 sites from the upper to the lower reaches in Lian river catchment (Figure 1) were collected using a gravity sampler equipped with a polycarbonate tube with an inner diameter of 6.5 cm and a length of 80 cm. After sampling, overlying water was extracted using a tubule and syringe. All sediment cores were sectioned at 1-cm intervals, and the sub-samples were sealed separately in polyethylene bags.

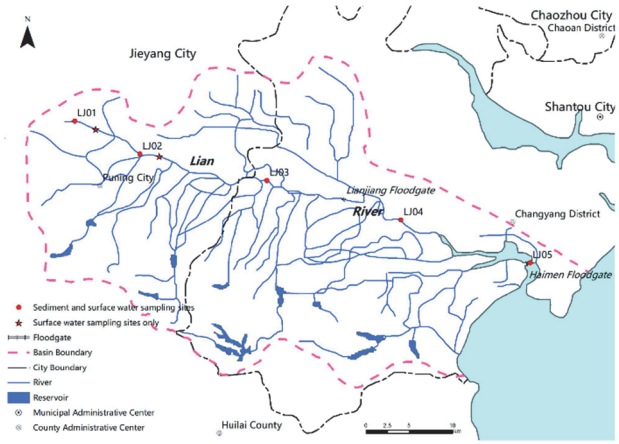

Fig. 1. Sampling points in the Lian river (South China).

[1] School of Geography and Tourism, Guangdong University of Finance & Economics, Guangzhou 510320, CHINA
[2] Department of Hydrology and Water Resources Management, Kiel University, D-24118 Kiel, GERMANY
[3] School of Geography and Planning, Sun Yat-Sen University, Guangzhou 510275, CHINA

 https://doi.org/10.1142/9789811275449_0026

After freeze drying, each sample was ground with a pestle and mortar until all particles passed through a 0.149-mm nylon sieve. About 50 mg of sample was digested in a HNO_3-HF mixture under high temperature and pressure conditions in Teflon tubes, such that residual metals trapped within the crystal structure of minerals were digested and dissolved in the concentrated HNO_3-HF solution. The total concentrations of heavy metals were analyzed using inductively coupled plasma mass spectrometry, i.e. ICP-MS (X-2, Thermo, USA).

The pollution Load Index (Tomlinson et al., 1980), abbreviated as PLI, was calculated at each sampling site as the geometric mean of the contamination factor (C_f^i) of each metal (i). The C_f^i is the ratio between the concentration of the metal i in the sediment (C_s^i) and their environmental background value (C_{bv}^i) for soils in Guangdong Province (China National Environmental Monitoring Centre, 1990; Kang et al., 2022).

$$PLI_{site} = \sqrt[i]{{C_f}^1 \times {C_f}^2 \times {C_f}^3 \ldots \times {C_f}^i} \quad (1)$$

$${C_f}^i = \frac{{C_s}^i}{{C_{bv}}^i} \quad (2)$$

Finally, a principal component analysis (PCA) was carried out to find similar behaviours and origins of metals in the sediment sites.

RESULTS AND DISCUSSION

The results showed that the sediments of the river have high levels of Cr (18.32–83.73 mg/kg), Ni (6.45–50.6 mg/kg), Cu (9.36–531.5 mg/kg), Zn (38.57–441.9 mg/kg), Cd (0.209–1.135 mg/kg) and Pb (54.02–492.8 mg/kg) as shown in Figure 2.

The mean values of the contamination factors followed the descending order Cd (8.6) > Cu (4.97) > Zn (3.23) > Pb (2.59) > Ni (1.53) > As (1.26) > Cr (0.90). It means that the mean concentrations of Cr, Ni and As were close to the ranges of soil background values for Guangdong Province, whereas Cd concentrations is about 4-20 times higher than the soil background values for Guangdong Province.

The PLI was higher in the middle reaches (point 3), with an PLI > 4, that indicates metal concentrations more than 4 times higher than expected in Guangdong Province and therefore, a high level of pollution (Figure 3). The major source of pollution in this site seems to be Guiyu e-waste recycling zone that is located close upstream. On the other hand, in the upper reaches, the PLI was close to 1, indicating metal values similar to the values expected in Guangdong Province and, therefore, lower anthropogenic influence.

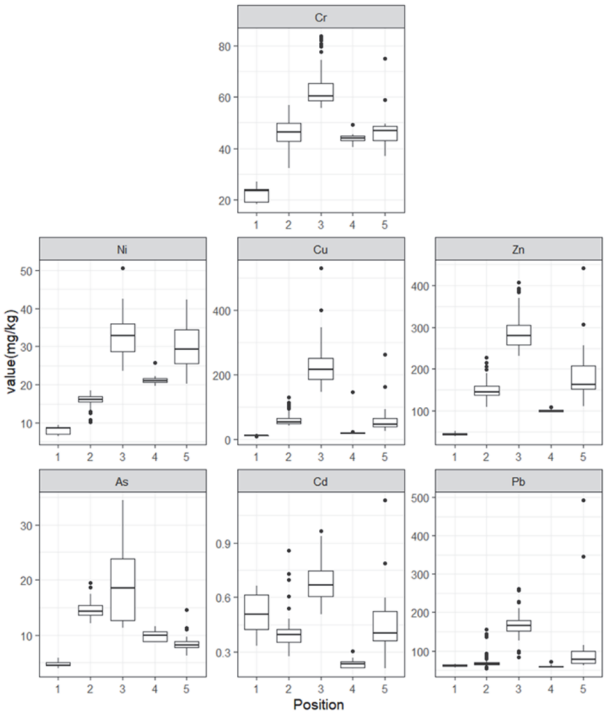

Fig. 2. Distribution of trace elements in sediments of 5 sampling points of the Lian River (South China).

In sampling points 2, 4 and 5, PLIs were within 2 and 3, indicating higher values than those expected for the Guangdong Province and a likely anthropogenic influence.

In the principal components analysis, strong positive correlations with high correlation coefficients were found between pairs of Cr, Ni, Cu, Zn, As, and Pb, suggesting industrial pollution as a similar source for all these metals. However, results suggest a different source for Cd, that might be connected to fertilizers in agriculture.

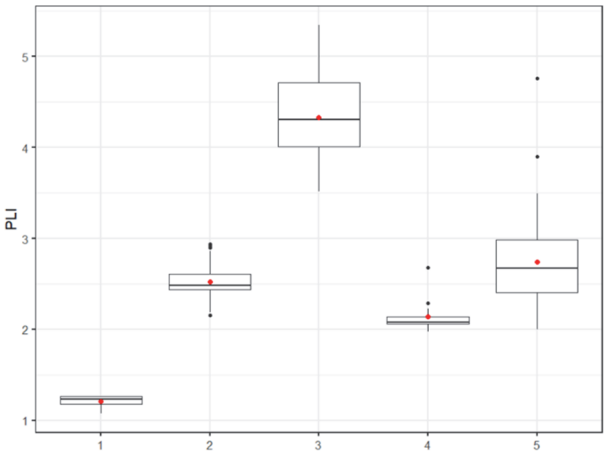

Fig. 3. Pollution load indices (PLIs) of trace elements in 5 sampling points of the sediments of the Lian River (South China).

CONCLUSIONS

The spatial and vertical distributions of heavy metals exhibited significant variability among sampling sites. Based on the PLIs of sediment samples, more severe metal pollution was found in samples of points 3 and 5. Of these metals, Cd, Cu, Zn and Pb exhibited higher enrichment levels.

The excess accumulation of Cr, Ni, Cu and Zn, Pb in sediment was associated with the discharge of industrial effluents while Cd is supposed to be linked to the application of fertilizers.

References

China National Environmental Monitoring Centre, 1990. Chinese Soil Element Background Value. Beijing, China.

Debnath, A., Singh, P.K., Sharma, Y.C., 2021. Metallic contamination of global river sediments and latest developments for their remediation. J. Environ. Manage. https://doi.org/10.1016/j.jenvman.2021.113378

Kang, J., Ding, X., Ma, H., Dai, Z., Li, X., Huang, J., 2022. Characteristics and Risk of Forest Soil Heavy Metal Pollution in Western Guangdong Province, China. Forests 13, 884. https://doi.org/10.3390/f13060884

Li, H., La Guardia, M.J., Liu, H., Hale, R.C., Mainor, T.M., Harvey, E., Sheng, G., Fu, J., Peng, P., 2019. Brominated and organophosphate flame retardants along a sediment transect encompassing the Guiyu, China e-waste recycling zone. Sci. Total Environ. 646, 58–67. https://doi.org/10.1016/j.scitotenv.2018.07.276

Song, J., Liu, Q., Sheng, Y., 2019. Distribution and risk assessment of trace metals in riverine surface sediments in gold mining area. Environ. Monit. Assess. 191, 1–13. https://doi.org/10.1007/s10661-019-7311-9

Sthiannopkao, S., Wong, M.H., 2013. Handling e-waste in developed and developing countries: Initiatives, practices, and consequences. Sci. Total Environ. 463–464, 1147–1153. https://doi.org/10.1016/j.scitotenv.2012.06.088

Tomlinson, D.L., Wilson, J.G., Harris, C.R., Jeffrey, D.W., 1980. Problems in the assessment of heavy-metal levels in estuaries and the formation of a pollution index. Helgoländer Meeresuntersuchungen 33, 566–575. https://doi.org/10.1007/BF02414780

STUDY ON THE INFLUENCE OF WIND SPEED ON THE MEASUREMENT OF SURFACE VELOCITY

Y. Roh[1] and K. Choi[2]

ABSTRACT: Surface velocimetry has been steadily increasing interest and research on its applicability to stationary discharge measurement due to its measurement efficiency and economy. However, it has not yet been widely used due to some uncertainties in the measurement of surface velocity. The first is the uncertainty of the relation between the surface and mean velocity, and the others is for wind effect on surface velocity.
In the case of measurement of water surface velocity, the direction and height of the wave on water surface can be changed by wind, which may cause an error in the surface velocity value. For higher velocity in flood flow, the influence of the wind speed is negligible on surface velocity, but as the velocity decreases, the influence of the wind effect on the surface velocity increases relatively.
In this study, in order to analyze the effect of wind speed and direction on the surface velocity under constant flow conditions when measuring discharge using surface velocity meter, wind direction anemometer(150WX of AIRMAR Co.) was installed with radar surface velocimetry(RQ-30 of SOMMER co.) in an test river.
From the results, speed and direction of wind was found to affect the measured surface velocity in low flow condition. Wind speeds of 2.5 m/s or more caused fluctuations of 20.0~71.4 % of the surface velocity depending on the wind direction, while the effect was not significant as 2.9~8.6 % at less than 1 m/s of wind speed. Therefore, for calculating the discharge by measuring the surface velocity, the effect of wind speed and direction should be considered, especially in low flow conditions where the influence of wind is relatively large.

Keywords: discharge, surface velocity, wind speed, radar surface velocimetry

INTRODUCTION

There are many advantages to using a surface velocimeter to measure the flow discharge, because it does not contact with the flow and can measure without flow disturbance. This type of measuring instrument can be easily installed in the river. However, in order to use of surface velocity meter to measure flow discharge of rivers, there are still problems to be solved, such as the calculation of mean velocity from surface velocity and the effect of wind on the surface velocity. Surface velocity can be over- or under measured because winds blowing at the water surface affect the measurement of velocity. This effect is more greater at the lower flow conditions. For higher velocity in flood flow, the influence of the wind speed is negligible on surface velocity, but as the velocity decreases, the influence of the wind effect on the surface velocity increases relatively. In this study, in order to analyze the effect of wind speed and direction on the surface velocity under constant flow conditions when measuring discharge using surface velocity meter, wind direction anemometer was installed with radar surface velocimetry in an test river.

EQUIPMENTS AND INSTALLATION

RQ-30d of Sommer Ltd. was used to measure surface velocity and 150WX of AIRMAR Tec. was installed to monitor wind speed and direction in test bed.

The radar sensors of the RQ-30d measures continuously and contact-free the surface velocity of rivers, streams, open channels or canals. RQ-30d measures surface velocity and water level and together with a known cross section it can calculate discharge Q of flow. The measurement of the surface flow velocity is based on the Doppler frequency shift method: A radar signal is transmitted to the water surface at a constant frequency of 24 GHz. The sensor measures the partially reflected signal whose frequency is shifted due to the water movement. The surface velocity is determined through a spectral analysis.

[1]Advanced Infrastructure, Korea Institute of Hydrological Survey, Kintex-ro 217-59, Goyangsi, REPUBLIC OF KOREA
[2] River&Sea Co.LTD., 603 Keumkang Penterium IT Tower, 282 Hagui-ro, Dongan-gu, Anyang-si, REPUBLIC OF KOREA

 https://doi.org/10.1142/9789811275449_0027

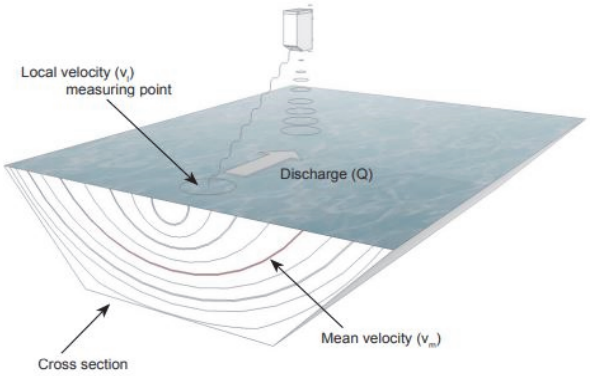

Fig. 1 Measurement of the surface velocity by RQ-30d (SOMMER MESSTECHNIK, 2017)

150WX measures apparent and theoretical wind speed and direction with internal compass and GPS. It can measure range of wind speed 0 to 40m/s with 0.1m/s resolution.

Fig. 2 Wind sensor150WX, (AIRMAR, 2020) installed in test bed

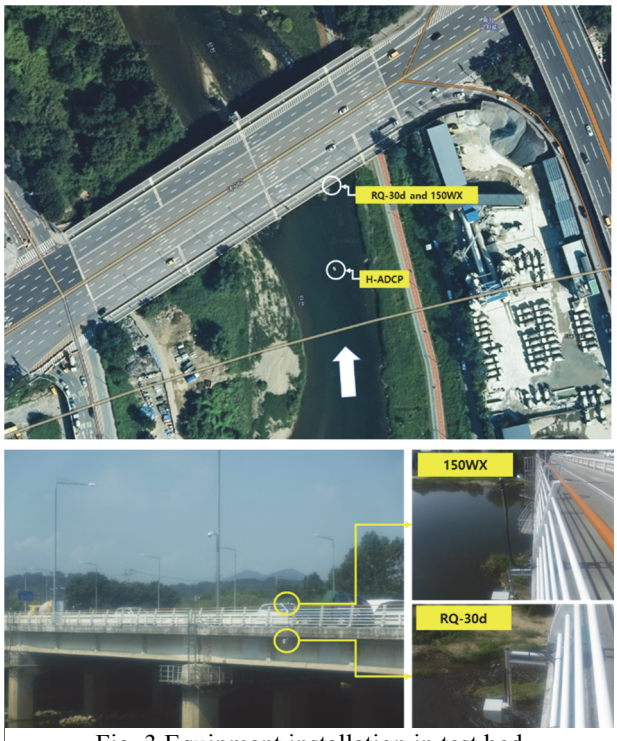

Fig. 3 Equipment installation in test bed

Test bed for this study, the Daegok Station located in a small stream with a river width of about 50m, as shown in Fig.3. In this station, H-ADCP system has been installed and operating for measuring discharge(MOLIT, 2017). In order to analyze the trend of velocity variation, measured velocity by H-ADCP was compared with surface velocity measured by RQ-30d.

MEASUREMENT OF SURFACE VELOCITY

Test bed operated during 2021.01.01~2021.09.30 and surface velocity was measured every 10 minute. As shown in shown in Fig. 4, 5, surface velocity showed similar trend with the mean velocity measured by H-ADCP. However, instantaneous wind speed changes affect surface velocity measurements.

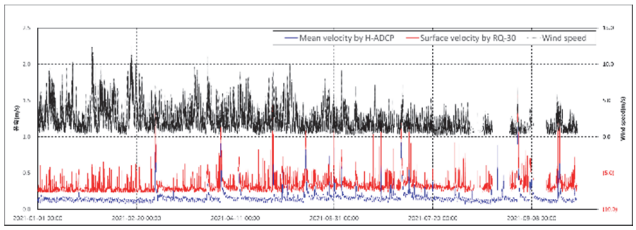

Fig. 4 Surface and mean velocity, wind speed measured during whole period

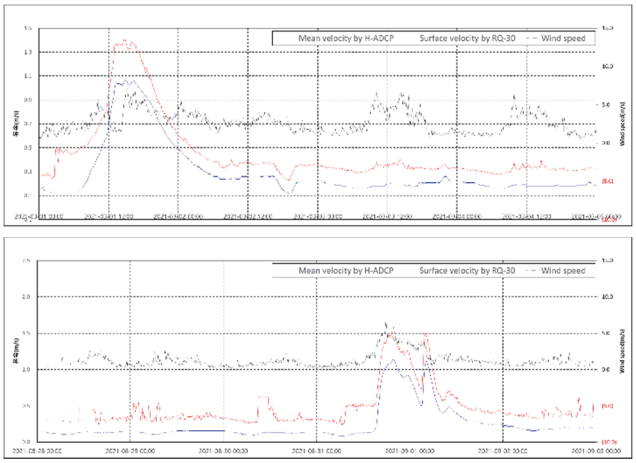

Fig. 5 Surface and mean velocity, wind speed measured during high flow events

The effect of wind speed on the surface velocity measurement was significant when the wind speed was over 2.5 m/s and the flow velocity was below 0.3 m/s.

DISCHARGE CALCULATION USING INDEX VELOCITY METHOD

In order to calculate discharge, relation between surface velocity measured by RQ-30 with mean velocity was developed as shown in Fig.6. The range of below 0.3 m/s greatly affected by wind speed was excluded from the development of the index relation.

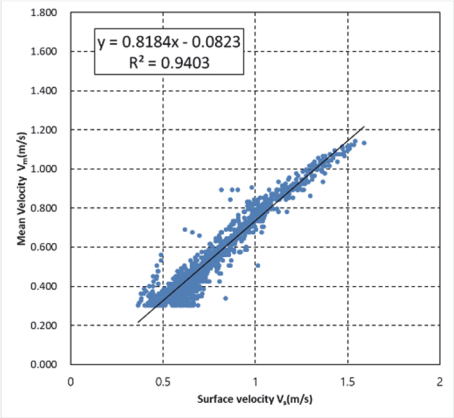

Fig. 6 Index relation

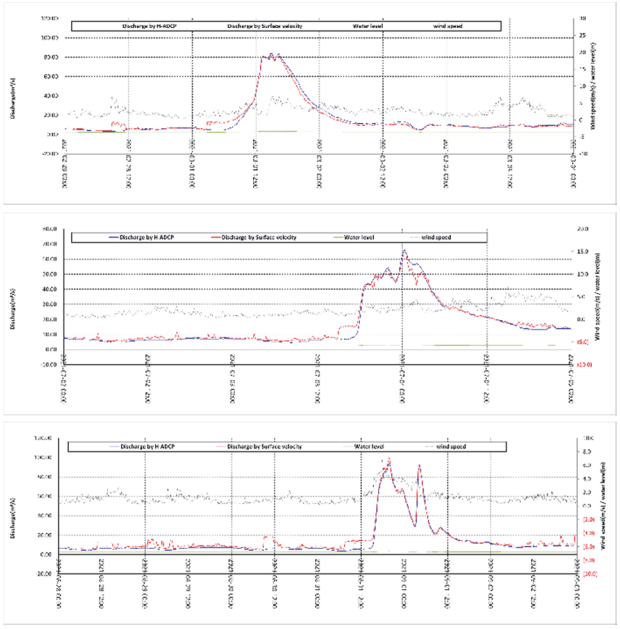

Fig. 7 Discharge by IVM

Fig. 7 is result of discharge calculation by IVM developed using surface velocity. As shown in figures, discharge by surface velocity showed good agreement with H-ADCP measurement. However, it was found that there was a large deviation in the low-flow condition, which is greatly affected by wind speed

CONCLUSION

From the results, speed and direction of wind was found to affect the measured surface velocity in low flow condition. Wind speeds of 2.5 m/s or more caused fluctuations of 20.0~71.4 % of the surface velocity depending on the wind direction, while the effect was not significant as 2.9~8.6 % at less than 1 m/s of wind speed. Therefore, for calculating the discharge by measuring the surface velocity, the effect of wind speed and direction should be considered, especially in low flow conditions where the influence of wind is relatively large.

ACKNOWLEDGEMENTS

This study was supported by Korea Environment Industry & Technology Institute(KEITI) as "Service Program for Demand-Responsive Water Supply", funded by the Korea Ministry of Environment(MOE). [2020002650003]

References

MOLIT., (2017), Annual Report of Hydrological Survey in Korea., Minister of Land, Infrastructure & Transportation., VII Construction and Operation of Automatic Discharge Measurement System.

SOMMER MESSTECHNIK, (2017), Brochure of Sensors for Water Discharge., https://www.sommer.at/en/.

AIRMAR, (2020), Brochure of WeatherStation Multisensor-Ultrasonic Instruments for Land Applications., https://www.airmar.com/weather-description.html?id=155.

SEA SURFACE TEMPERATURES IN THE NINO REGIONS AND ANNUAL PRECIPITATION IN EQUATORIAL PACIFIC ATOLLS

Ian White[1], Tony Falkland[2] and Farran Redfern[3]

ABSTRACT: Water resources in equatorial atolls are amongst the most vulnerable globally, partly because of extreme variability of annual precipitation (P) due to frequent ENSO events. IPCC projections for the central and western tropical Pacific indicate mean annual rainfall will increase as sea surface temperatures (SSTs) rise. Projections of the intensity and frequency of ENSO events and hydrological droughts are of low confidence. Here, relationships between 12-month May to April precipitation ($P_{M\text{-}A}$) in two equatorial atolls, Tarawa and Kiritimati in Kiribati, and 12-month $SST_{M\text{-}A}$ in the Nino regions surrounding the atolls are examined between 1950 and 2022. Only the Nino4 region has as significant temporal trend in $SST_{M\text{-}A}$. There are no significant trends in $P_{M\text{-}A}$ in either atoll due to large ENSO-related interannual variability. In both atolls, strong, highly significant correlations are found between $P_{M\text{-}A}$ and $SST_{M\text{-}A}$ in the Nino regions eastward of the atolls. These show $\partial P_{M\text{-}A}/\partial SST_{M\text{-}A}$ for both atolls over 1,000 mm/°C. The relationship for Kiritimati appears nonlinear. Comparison of ranked very much above normal (VMAN, percentile > 0.9) and very much below normal (VMBN, percentile < 0.1) $SST_{M\text{-}A}$ with ranked VMAN and VMBN $P_{M\text{-}A}$ revealed poor correspondence for both atolls, suggesting that extreme $SST_{M\text{-}A}$ are not a sole determinant of extreme $P_{M\text{-}A}$. The nonlinearity of the relation is shown by $\partial P_{M\text{-}A}/\partial SST_{M\text{-}A}$ for below normal $P_{M\text{-}A}$ being an order of magnitude smaller than trends for above normal $P_{M\text{-}A}$.

Keywords: Equatorial atolls, precipitation, sea-surface-temperatures, extreme events.

INTRODUCTION

Water resources in small island developing states are vulnerable (UNGA 2014). Atolls in equatorial Pacific are especially vulnerable, partly due to their unique hydrogeology and to very variable precipitation (P) during ENSO events (Falkland and White 2020). IPCC projections for the central and western tropical Pacific indicate mean annual rainfall is likely to increase as sea surface temperatures (SSTs) warm. ENSO influence on precipitation over the Indo–Pacific is projected (medium confidence) to strengthen and shift eastward but projected changes in hydrological drought are less certain (IPCC, 2021). Kiribati, in June 2022, declared a State of Disaster due to severe water shortages, illustrating the critical impacts of droughts on water availability in atolls.

By the end of this century, worst-case projections are that SSTs in equatorial Pacific could rise by 2 to 3°C relative to 1981-2000 (Brown et al. 2014). What will be the potential impact of these increases on longer-term P and droughts in equatorial Pacific atolls?

Here, data over the period 1950 to 2022 is used to examine the impact of SST in the Nino regions on P in two equatorial atolls located in those Nino regions. We focus on the extreme 12-month SST events and extreme 12-month P events relevant to droughts.

STUDY LOCATIONS

Two equatorial atolls in the Republic of Kiribati, Tarawa (1°52'N, 173°E) and Kiritimati (1°55'N, 157°22'W), 3,300 km apart, were chosen for study. Their location relative to the Nino regions is shown in Fig 1.

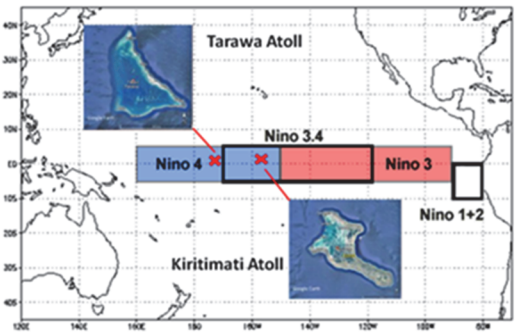

Fig. 1 Location of Tarawa and Kiritimati atolls in relation to the Nino SST regions

Tarawa and Kiritimati lie in the Nino4 region and Kiritimati is also in the Nino3.4 region used to identify ENSO events. Maximum land elevations in both atolls are less than 14m above mean sea level with large areas below 5m, so orographic effects are expected to be minimal.

DATA USED

Monthly precipitation for Tarawa from 1950 to 2022 was used. In Kiritimati, continuous monthly precipitation

[1] Institute for Climate, Energy and Disaster Solutions, Pacific Institute, Fenner School of Environment and Society, Australian National University, Canberra, ACT 0200, AUSTRALIA
[2] Island Hydrology Services, 6 Tivey Place, Hughes, ACT, 2605, AUSTRALIA
[3] Ministry of Infrastructure and Sustainable Energy, Betio, South Tarawa, KIRIBATI

 https://doi.org/10.1142/9789811275449_0028

was available from 1951 to 2022. Monthly ERSSTv5 values of Nino region SSTs were available from 1950: (https://www.cpc.ncep.noaa.gov/data/indices/ersst5.nino.mth.91-20.ascii).

Because of the importance of ENSO-related droughts, we use 12-month data running from May to April, designated as $P_{M\text{-}A}$ for cumulative precipitation, and $SST_{M\text{-}A}$ for average sea surface temperatures. Using 12-month data eliminates seasonal influences and any short lags between $P_{M\text{-}A}$ and $SST_{M\text{-}A}$ and is relevant to changes in groundwater storage.

TEMPORAL TRENDS IN $SST_{M\text{-}A}$ AND $P_{M\text{-}A}$

Fig. 2 compares $P_{M\text{-}A}$ in Tarawa and Kiritimati with $SST_{M\text{-}A}$ in the Nino4 region surrounding the atolls.

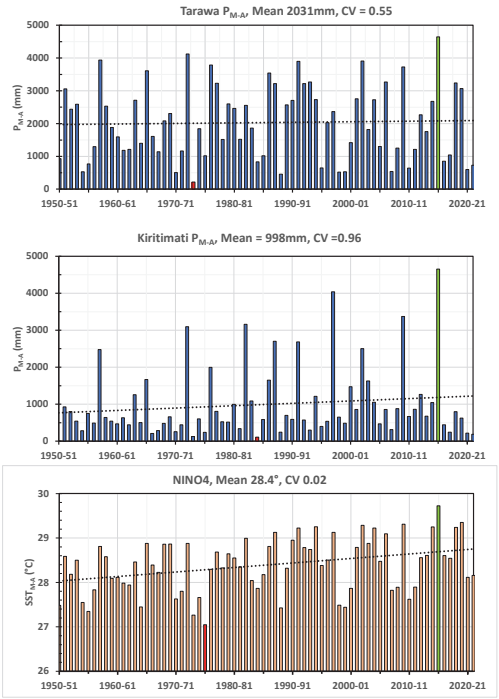

Fig. 2 $P_{M\text{-}A}$ in Tarawa (top) and Kiritimati (middle) compared with $SST_{M\text{-}A}$ in the Nino4 region over the period 1950-2021. Dotted lines show trends. Maximum values shown in green, minimum values in red.

There are no significant ($p > 0.05$) trends in $P_{M\text{-}A}$ in either atoll or for $SST_{M\text{-}A}$ in Nino3 and Nino3.4. There is, however, a significant trend ($p < 0.005$) in $SST_{M\text{-}A}$ in the Nino4 region of 1.0±0.3°C/century, much less than the worst-case projections for climate change (CC) at the end of this century (Brown et al. 2014). The huge variability in $P_{M\text{-}A}$ in both atolls (over 40 times in Kiritimati and 20 times in Tarawa between maximum and minimum) statistically swamps detection of any trends (ABoM and CSIRO, 2014).

Since 1950, the maximum variation in Nino4 $SST_{M\text{-}A}$ is 2.7°C while $SST_{M\text{-}A}$ in Nino3 and Nino3.4 varied by up to 3.9°C. These ranges are comparable or even greater than end of century worst-case projections. Given these historic $SST_{M\text{-}A}$ excursions how has $P_{M\text{-}A}$ responded?

RELATIONS BETWEEN $P_{M\text{-}A}$ AND $SST_{M\text{-}A}$

Fig. 3 shows the relation between $P_{M\text{-}A}$ and Nino $SST_{M\text{-}A}$ at the same date with the maximum correlation.

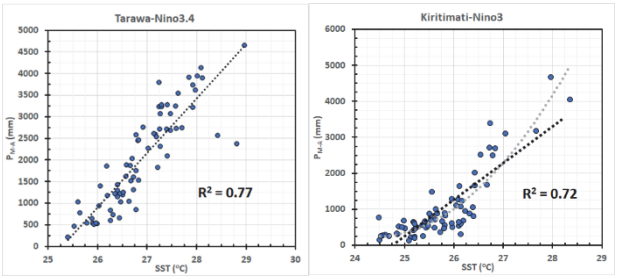

Fig.3 Relation between $P_{M\text{-}A}$ and $SST_{M\text{-}A}$ for Tarawa with Nino3.4 (left) and Kiritimati with Nino3 (right).

The relationships shown in Fig.3 are highly significant ($p << 10^{-6}$). For Tarawa, $\partial P_{M\text{-}A}/\partial T_{M\text{-}A}$ = 1260±80mm/°C while for Kiritimati, $\partial P_{M\text{-}A}/\partial T_{M\text{-}A}$ = 1030±80mm/°C, although for the latter the relation appears nonlinear. The maximum correlation between $P_{M\text{-}A}$ and $SST_{M\text{-}A}$ was found with the Nino region to the east of each atoll. This may be due to the prevailing easterly trade winds.

EXTREME $SST_{M\text{-}A}$ AND EXTREME $P_{M\text{-}A}$

The data in Fig. 2 suggest ranked extreme $SST_{M\text{-}A}$ may correspond to the same ranked extreme $P_{M\text{-}A}$. The largest Nino4 $SST_{M\text{-}A}$ in Fig. 2 in 2015-16 corresponds to the largest $P_{M\text{-}A}$ in both atolls also in 2015-16. The smallest Nino4 $SST_{M\text{-}A}$ in 1975-6, however, does not correspond with the smallest $P_{M\text{-}A}$ in Tarawa in 1973-4 or in Kiritimati in 1984-5. This implies a difference in relationships between extreme values in La Niñas (low precipitation) and in El Niños (high precipitation). To examine this, we compare the ranking between very much above normal events (VMAN, percentile > 0.9) and very much below normal events (VMBN, percentile < 0.1) in Fig. 4.

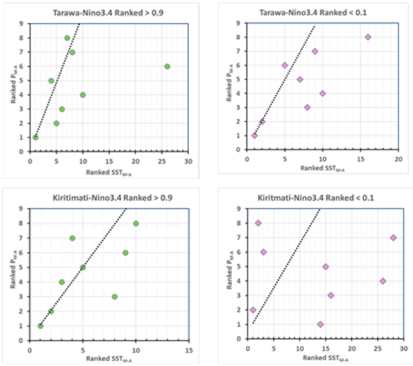

Fig 4. Comparison of the ranking of VMAN (green points) and VMBN (pink points) $P_{M\text{-}A}$ with the ranking of VMAN and VMBN $SST_{M\text{-}A}$ in Nino3.4 for Tarawa (top row) and Kiritimati (bottom row). The dotted lines show one to one correspondence.

In general, in Fig. 4, correspondence between the ranking of extreme P_{M-A} and ranking of extreme SST_{M-A} is poor. In Tarawa, the lowest two ranked P_{M-A} events corresponded to the lowest two ranked SST_{M-A} while in Kiritimati the highest two ranked P_{M-A} together with the fifth ranked P_{M-A} corresponded to identical VMAN rankings of SST_{M-A}. So, despite the highly significant general relations between P_{M-A} and SST_{M-A} in Fig. 3 for both atolls, ranked VMAN and VMBN SST_{M-A} events do not in general correspond to the same ranked VMAN and VMBN P_{M-A} events over 12-month time scales.

ARE P_{M-A} AND SST_{M-A} RELATIONS LINEAR?

Saturated vapor pressure of water increases almost exponentially with SST. Relationships between atoll P_{M-A} and SST_{M-A} might be expected to be non-linear. Fig. 3 seems to suggest that for Kiritimati. To examine the linearity, we analyze the relationships between above normal (AN, percentile > 0.7), normal (N, 0.3 ≤ percentile ≤ 0.7), and below normal (BN, percentile < 0.3) P_{M-A} with SST_{M-A} at the same date in Fig. 5.

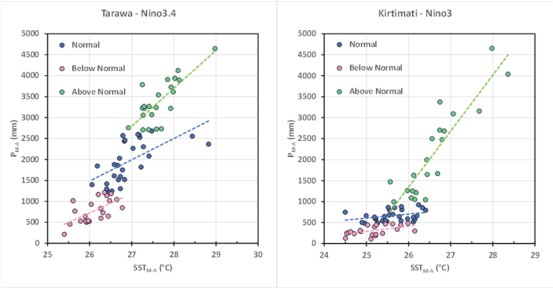

Fig. 5 Relationships between AN (green), N (blue) and BN (pink) P_{M-A} with SST_{M-A} at the same date.

Fig. 5 reveals that the apparent linear relations in Fig. 3 are composed of separate trends dominated by the above normal P_{M-A} components. The relationships between P_{M-A} and SST_{M-A} are statistically different for AN, N, and BN P_{M-A} in both atolls (Table 1).

Table 1 Increasing trends of AN, N, BN P_{M-A} with increasing SST_{M-A} in Tarawa, and Kiritimati

Atoll	P_{M-A} Range	$\partial P_{M-A}/\partial SST_{M-A}$ (mm/°C)	Significance
Tarawa	Above Normal	910±170	$p < 0.00005$
	Normal	510±130	$p < 0.0005$
	Below Normal	120±40	$p < 0.05$
Kiritimati	Above Normal	1300±150	$p < 10^{-7}$
	Normal	100±50	NS, $p > 0.05$
	Below Normal	130±50	$p < 0.05$

The relation for the normal range P_{M-A} at Kiritimati was not significant. Table 1 shows an approximately order of magnitude difference in $\partial P_{M-A}/\partial SST_{M-A}$ between above and below normal rainfalls in both atolls. It clearly demonstrates that both $\partial P_{M-A}/\partial SST_{M-A}$ in Fig. 3 are dominated by above normal precipitation. Fig. 5 also shows a puzzling overlap in SST_{M-A} for different P_{M-A}.

CONCLUSIONS

IPCC projects mean annual rainfalls in the tropical Pacific will increase as SST rise. The magnitudes of increases are uncertain. Worst case projections suggest equatorial SST may increase by 2 to 3°C. In the Nino regions, between 1950 and 2022, SST_{M-A} have varied by up to 4°C but only in the Nino4 region is there a significant trend of 1.0±0.3°C/century. Huge ENSO-related variability masks any trends in P_{M-A} in Tarawa and Kiritimati. P_{M-A} in both atolls is strongly related to corresponding SST_{M-A} with the historic trends of at least 1,000 mm/°C. These trends are dominated by above normal rainfalls whose trends are an order of magnitude larger than below normal rainfalls in both atolls. Strongest correlations were with the Nino region to the east of each atoll, possible due to the prevailing trade winds, demonstrating the complexity of relations between rainfall and SST in the equatorial Pacific.

References

ABoM and CSIRO (2014). *Climate Variability, Extremes and Change in the Western Tropical Pacific: New Science and Updated Country Reports*. Pacific-Australia Climate Change Science and Adaptation Planning Program Technical Report, Australian Bureau of Meteorology and Commonwealth Scientific and Industrial Research Organisation, Melbourne, Australia, 372pp.

Brown, J.N., Langlais, C. and Gupta, A.S. (2014). Projected sea surface temperature changes in the equatorial Pacific relative to the Warm Pool edge. Deep Sea Research Part II: Topical Studies in Oceanography, 113, 47-58.

Falkland, A. and White, I. (2020). Freshwater availability under climate change. In L. Kumar (Editor), Climate change and impacts in the Pacific. Springer, 403-448.

IPCC (2021). In Masson-Delmotte, V., P. Zhai, A. Pirani, S.L. Connors, C. Péan, S. Berger, N. Caud, Y. Chen, L. Goldfarb, M.I. Gomis, M. Huang, K. Leitzell, E. Lonnoy, J.B.R. Matthews, T.K. Maycock, T. Waterfield, O. Yelekçi, R. Yu, and B. Zhou (Editors). Climate Change 2021: The Physical Science Basis. Contribution of Working Group I to the Sixth Assessment Report of the Intergovernmental Panel on Climate Change. Cambridge University Press, Cambridge, United Kingdom and New York, NY, USA, In press,

UNGA (2014). Report of the Third International Conference on Small Island Developing States, Apia, Samoa, 1-4 September 2014, UN General Assembly. United Nations General Assembly, 70pp.

DYNAMIC DECISION SUPPORT SYSTEM FOR DISASTER RESPONSE "DDS4D" - BEYOND THE INFORMATION SHARING

Makoto Hanashima[1], Hiroaki Sano[1], Yuichiro Usuda[1]

ABSTRACT: The information sharing capability is the highest priority feature for the disaster information system. Even if the system has excellent functions, without information sharing capability, it may not work in a serious disaster situation. However, by only information sharing, it is not enough to invoke effective disaster response activities, thus the information products to support the decision makers on the front-line of disaster response is needed. According to this concept, we have been developing the "Dynamic Decision-support System for Disaster Response (DDS4D)" since 2019. DDS4D has capabilities that are implementation of three technological elements; captures and stores dynamic disaster data in real time, analyzes disaster dynamics according to analysis scenarios defined by users and visualize results of analysis in real time. By having these capabilities, DDS4D can demonstrate the decision support for disaster response in the "real" disaster situation. It can be said that these features are fundamental functions of the "Disaster Digital Twin." In this paper, we present the overview of DDS4D and the results of feasibility demonstration.

Keywords: Information Sharing, Disaster Response, Digital Twin, Decision Support.

THE CONCEPTS OF INFORMATION SHARING

The information sharing capability is the highest priority feature for the disaster information system. Even if the system has excellent functions, without information sharing capability, it may not work in a serious disaster situation.

Since the word, "Information Sharing", is used in various contexts, so we have to clarify the concept and purpose of "Information Sharing" before discussion.

In the disaster situation, various organizations work in parallel. Without information sharing, each organization decides its activity based on own information only. Situational awareness is different by each organization; thus, effective disaster response cannot be achieved.

The purpose of "Information Sharing" is to build a common situational awareness of the disaster between various response organizations, immediately (Hanashima et al. 2017).

SIP4D: Shared Information Platform for Disaster Management

Over the years, the government has made a great deal of effort to reinforce the resilient functions of society. However, information sharing among disaster response organizations has not been established yet.

Therefore, we have aimed to build up "Shared Information Platform for Disaster Management (SIP4D)". SIP4D is an information pipeline that enables collecting disaster related data from various sources, generating "ready-to-use" information products and distributing them to disaster response organizations (Fig. 1).

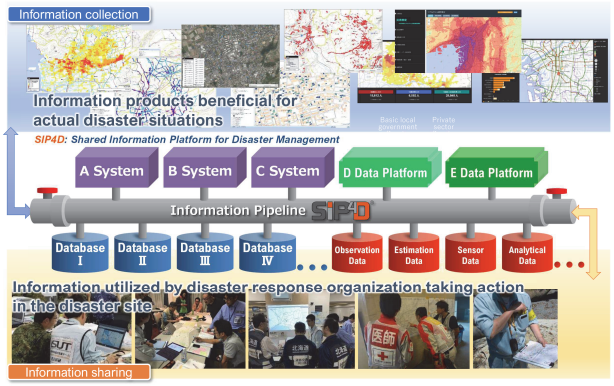

Fig. 1 SIP4D provides the "information pipeline" for disaster response organization.

Now SIP4D is described as the national information sharing platform for disaster response in the Disaster Prevention Basic Plan of Japan. SIP4D contributes to establish sharing information among various disaster response organizations, and to build common situational awareness (Usuda et al. 2019).

However, by only information sharing, it is not enough to invoke effective disaster response activities, thus the information products to support the decision makers on the front-line of disaster response is needed. To resolve this issue, we set our next goal to construct the dynamic decision support to drive disaster response activities.

[1] National Research Institute for Earth Science and Disaster Resilience (NIED), JAPAN

 https://doi.org/10.1142/9789811275449_0029

Next Concept: Cyber Physical Synthesis for Disaster Resilience

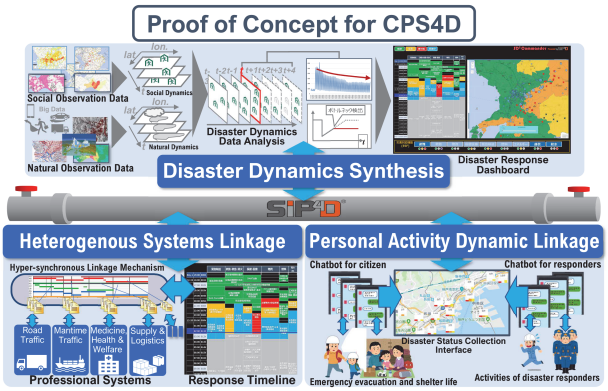

Fig. 2 The proof of concept for "Cyber Physical Synthesis for Disaster Resilience (CPS4D)".

The new concept of our current project is "Cyber Physical Synthesis for Disaster Resilience", CPS4D.

Fig. 2 shows the overview of proof of concept for CPS4D. We have designed CPS4D as a set of technologies to reconstruct the natural and societal phenomena occurring in the physical space as "digital twin" in the cyberspace, to analyze the dynamics of disaster, and to feed forward the solutions from the cyberspace into the physical space.

According to this concept, we have been developing the "Dynamic Decision-support System for Disaster Response (DDS4D)" as an enhanced module of SIP4D. DDS4D has capabilities that captures and stores dynamic disaster data in real time, analyzes disaster dynamics according to analysis scenarios defined by users and visualize results of analysis in real time. By having these capabilities, DDS4D can demonstrate the decision support for disaster response in the real disaster situation.

SYSTEM OVERVIEW OF DDS4D

To utilize the shared information in disaster response, each organization needs to process the information according to its activities. In emergency situations, it is often difficult for disaster response organizations to process information, resulting in situations where information is shared but not fully utilized.

Therefore, we planned to build DDS4D as a platform for agile production of information products to support decision making in disaster response. To do so, we believed the following issues needed to be addressed.

a. Bring information closer to decision making
b. Make it the decision unit (granularity) of the decision maker
c. Respond immediately to issues that arise in the field

If we respond to these issues, currently, we must create handmade content for decision makers. It is easy to imagine that such a response would be impossible in the event of a catastrophe such as the Nankai Trough earthquake.

After considering these issues, we have established the following three functional requirements for DDS4D.

1. Generate information on disaster dynamics by integrating natural and social information
2. Aggregate by decision-making unit (granularity and resolution)
3. Modify and expand in response to on-site requests

DDS4D is constructed from three sub systems, DDS-DB, DDS-SY and DDS-VI.

Disaster Dynamics Spatiotemporal Database, DDS-DB, is a large-size spatiotemporal database which records dynamic disaster data as time series geospatial data.

Disaster Dynamics Synthesizer-SY, is an agile data analysis infrastructure which operates dynamic analysis based on the user-definable analysis scenario.

User can create and modify scenarios according to data processing flow. Once defined, the scenario is automatically executed when the data is updated.

Disaster Dynamics Visualizer, DDS-VI, is a visualization sub-system for decision support that can draw maps and graphs in real time based on the information products created by DDS-SY. User can define the screen layout and presentation of information using GUI on their purpose (Fig. 3).

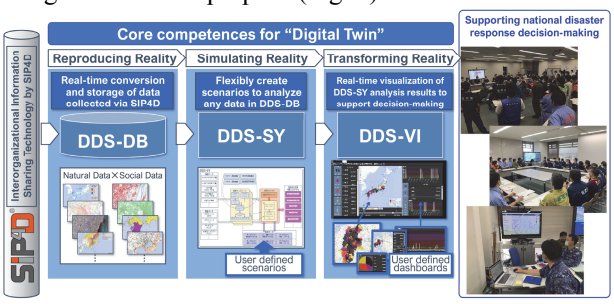

Fig. 3 System Architecture of "DDS4D".

To demonstrate the implementation of functional requirements, we set three demands of decision supporting.

The first is "Foresight on potential municipalities to support." For the demonstration, DDS4D estimates damage using forecast data and estimate municipalities that should be supported. This analysis will be useful for quantitative decisions such as the number of dispatching supports. We show the example of this demonstration, supporting decisions based on Disaster Relief Act application predictions.

The second is "Nationwide, uniform, comprehensive and quantitative monitoring of abnormalities." For the demonstration, DDS4D continuously and automatically detects municipalities where evacuation instructions have

not been issued even though there is a considerable risk of disaster. It will prevent omissions of evacuation instructions. We show the example of this demonstration, preventing delay of issuing the evacuation instructions.

The third is “Automatic detection of municipalities that will require support changes.” For the demonstration, DDS4D detects that even if the estimated scale of damage is the same, there is a significant difference in the response of basic local governments, such as the investigation of damage certification. This analysis will be utilized to detect the need to dispatch specialist staff, etc.

FEASIBIULITY DEMONSTRATION OF DDS4D

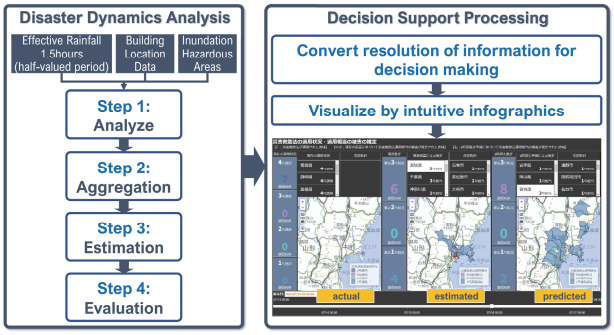

Fig. 4 Analytic framework of “Rapid evaluation of the Disaster Relief Act”.

Fig. 4 shows the analytic framework of demonstration, the “Rapid evaluation of the Disaster Relief Act”. We defined the following process as the analysis scenario on DDS4D.

Step 1: Analyze the number of buildings will be exposed heavy rainfall within the inundation hazardous areas.

Step 2: Aggregate the number of buildings analyzed in “Step1” by municipalities.

Step 3: Estimate the number of households will lose housings based on the result of “Step2” by applying the evaluation model.

Step 4: Based on the result of “Step3”, evaluate which clause of the Disaster Relief Act will be applied.

If the rain fall forecast is used instead of the effective rainfall, these analytics could predict the status hours later.

DDS4D performs this scenario every 30 min. This information products may contribute to the national level decision making, to conduct a nationwide estimation of damage in the disaster and to provide support to local governments.

For disaster responses, it is necessary to aggregate data by appropriate unit. In this case, the effective rainfall data indicates the intensity of rainfall by each 250m square grids. If the building damage estimation presented in 250m square grids, it might be not useful for decision makers. Thus, DDS4D aggregates the data to the administration area. Also, to the prefectural level, to assist municipalities by the quantitative estimation of damage at the early timing of disaster response.

The estimated number of exposed buildings by heavy rain indicates the relative level of damage, but it is not intuitive for the decision makers. They need some administrative criteria to evaluate the damage level.

Each three map shows actual, estimated, and predicted data for local governments which are applied the Disaster Relief Act, generated by the scenario shown in the previous slide. DDS4D estimates the number of households that will lose their housings due to flooding and evaluates which municipalities are eligible to apply for the Disaster Relief Act.

CONCLUSION

This paper provided an overview of DDS4D and a demonstration case study. We believe that DDS4D is a demonstration of fundamental technology for realizing a digital twin in the field of disaster resilience.

Up to now, SIP4D and DDS4D have been developed in phases, but in the next phase, we aim to integrate the functions of both so that the latest research results and technologies can be immediately implemented in the disaster response field. We are discussing with the "Information Support Team (ISUT)" of the Cabinet Office of the Japanese government to utilize the information products generated by DDS4D for the rainy season of this year. SIP4D and DDS4D will bridge the gap between researchers and disaster response sites, thereby contributing to even more effective disaster response.

ACKNOWLEDGEMENTS

The content of this paper was conducted as a part of “Enhancement of National Resilience against Natural Disasters” of the Cross-ministerial Strategic Innovation promotion Program (SIP) by the Council for Science, Technology, and Innovation.

References

Makoto, H., Ryota, S., and Yuichiro, U. (20171). The Standardized Disaster-Information Products for Disaster Management: Concept and Formulation. Journal of Disaster Research 12:1015-1027.

Usuda, Y., Matsui, T., Deguchi, H., Hori, T., and Suzuki, S. (2019). The Shared Information Platform for Disaster Management –The Research and Development Regarding Technologies for Utilization of Disaster Information–. Journal of Disaster Research 14: 279–291.

AN EMPIRICAL ANALYSIS OF SPATIAL AND TEMPORAL HETEROGENEITY OF METEOROLOGICAL FACTORS AFFECTING AIR QUALITY IN CHINA

Jin Lin[1], Xiang Que[1,2*], Jinfu Liu[1*], Xiaogang Ma[2] ,Tingting Fei[1], Xuanhui Yan[3]

ABSTRACT: Air pollution is a severe environmental problem in China. Meteorological factors that directly affect the dispersion of air pollutants are closely related to the air quality index(AQI). Extensive literature describes the non-stationarities between meteorological factors and air quality by employing the geographically weighted regression (GWR) or geographically and temporally weighted regression (GTWR). However, most previous studies have ignored the case where the rate of numerical variations has spatial heterogeneity. To better reveal the potential spatiotemporal patterns of the impacts of some selected meteorological factors, such as ground pressure, relative humidity, temperature, wind speed, on air quality in China from 2013 to 2018, we utilized the spatiotemporal weighted regression (STWR) to explore the spatio-temporal non-stationary. Results show that the R-squared (R^2) of the STWR model are higher than that of GWR and OLS especially when the rate of change of AQI is fast. Some spatial coefficient surfaces corresponding to different variables show obvious seasonal variations. Their spatial distribution also varies significantly over time. Some interesting findings are as follows: 1) The impacts of humidity on AQI are more obvious in northwestern China from April to June and July to September. 2) Before 2016, humidity had a positive effect on the AQI in most of the northwest, but since then there has been a negative effect. 3) In most southern China areas, the negative correlation between temperature and AQI tends to weaken, which may be caused by the gradual weakening of the temperature inversion phenomenon under climate warming.

Keywords: Spatiotemporal Weighted Regression, Air Quality Index, Meteorological Factors

INTRODUCTION

With the acceleration of urbanization, air pollution has become increasingly serious, and it has gradually become a factor that threatens human life and health (Kahn and Yardley, 2007). The concentration of atmosphere pollutants generally exceeds the clean standard in some cities or provinces of China (Zhang et al., 2020; Chen et al., 2016).

Meteorological factors such as temperature, pressure, humidity, and wind speed that directly affect the diffusion of air pollutants are closely related to the Air Quality Index (AQI). The rate of air quality change caused by meteorological factors may vary over time in different regions (Xu et al., 2017). Most previous studies generally employed the ordinary least squares (OLS) or geographically weighted regression (GWR) to investigate the relationships between meteorological factors and air quality (Hajiloo et al., 2019, Guo et al., 2021), while ignoring temporal heterogeneity. These studies failed to finely capture the situation that the change rate of in air quality caused by meteorological factors may vary over time in different regions. Our study is dedicated to fill this gap by utilizing an numerical rate-of-change decay based weighted model to explore the effects of temporal non-stationarity in more detail.

STUDY AREA AND DATA

Our study area covers 33 provinces and autonomous regions in China except Macau. As shown in Figure 1, it can be divided into three areas like a ladder from west to east. The first step of the ladder is mainly in the Qinghai-Tibet Plateau. The second step of the ladder is mainly in the plateau areas of China, and the third step of the ladder is mainly in the plain and hilly areas of China. Besides, it can also be divided into 6 parts according to the orientation.

Our daily air pollutants and meteorological data from January 1, 2013 to December 31, 2018 were mostly collected from the Chinese Air Quality Reanalysis dataset (CAQRA), the Institute of Atmospheric Physics, and the China National Environmental Monitoring Centre (CNEMC) (https://doi.org/10.11922/sciencedb.00053) with a spatial resolutions of 15km. We calculated the AQI based on six conventional air pollutants (i.e. $PM_{2.5}$, PM_{10}, SO_2, NO_2, CO, and O_3) in the dataset. Explanatory variables included simulated surface fields of wind speed (U, V), surface pressure (PSFC), relative humidity (RH), and temperature (TEMP) representing meteorological conditions in the dataset. The data were preprocessed before aggregation by 50m and 50m grids and administrative regions, respectively, and the monthly average was calculated point by point. All data were

[1] Computer and Information College, Fujian Agriculture and Forestry University, Fuzhou, Fujian, CHINA
[2] Department of Computer Science, University of Idaho, Moscow, USA
[3] College of Mathematics and Informatics, Fujian Normal University, Fuzhou, Fujian, CHINA

 https://doi.org/10.1142/9789811275449_0030

normalized by using z-scores to remove order of magnitude effects.

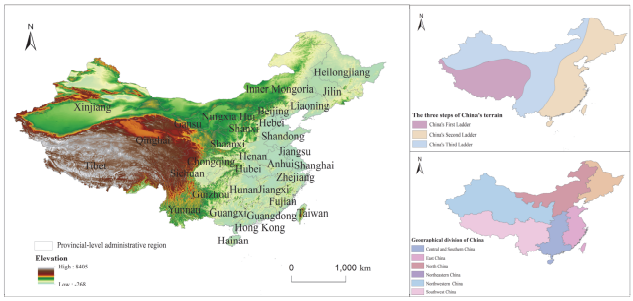

Fig 1. The map of study area.

Method

Our modeling approach proceeds as follows (Figure 2). To better explore the potential spatiotemporal patterns between major meteorological factors and air quality, we adopts the spatiotemporal weighted regression (STWR) (Que X et al., 2020) to analyze the heterogeneity of the influences of major meteorological factors on AQI in China from 2013 to 2018. Next, we explored the seasonal variation of the spatial coefficients. Finally, a dynamic time warping algorithm (DTW)(Petitjean F et al., 2011) is used to cluster the temporal variation of the spatial coefficients.

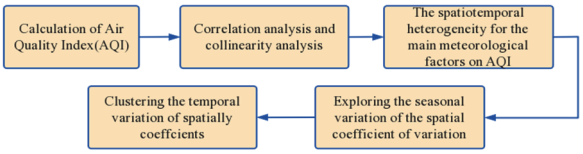

Fig 2. Research framework.

RESULT

Comparison of Models Performances

Trough experiments we found, the STWR model performed better in fitting the relationship between AQI and meteorological factors than OLS and GWR models. and November 2016.

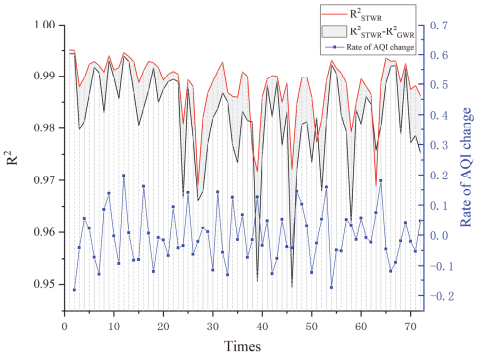

Fig 3. R-squared of models from 2013−2018.

By comparing the AQI rate of change with the R^2 of the GWR and STWR models, as can be seen in the Figure 3, the STWR model more accurately captures the time-varying characteristics than other models when the AQI rate of change is greater, such as July 2015, March 2016.

Seasonal Variation of Spatial Coefficient Corresponding to Different Meteorological Factors

We found that the spatial distribution of each meteorological factor's effect on air quality differs by season. As the Fig 4 a1 and a2 shown, the surface pressure (PSFC) showed a largely positive effect on AQI between January-March and October-December in the central region of China. And in the region of a2 and b2, the positive effect of PSFC on AQI gradually increased with the change of years. Conversely, in the region of c1 and d1, surface pressure has a relatively strong negative effect on the AQI between April-June and July-September.

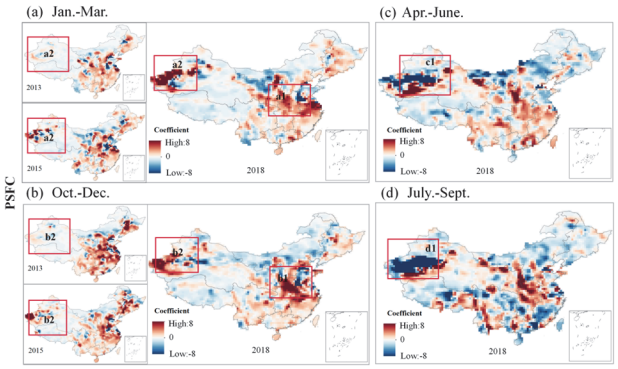

Fig 4. Spatial coefficient surface of PSFC.

As the Fig 5 a1 and a2 shown, temperature (TEMP) has a relatively large range of negative values from January to March and October to December in each year. In the region of a2 and b2, the degree of negative influence gradually increased with times. On the contrary, in the region of c1 and d1, the regression coefficients of temperatures from April to June and from July to September of each year generally have a larger positive influence range.

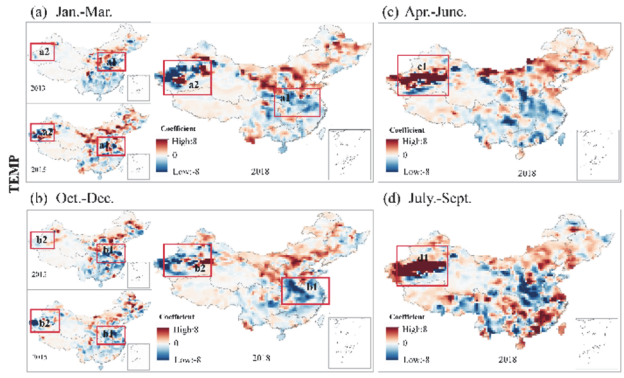

Fig 5. Spatial coefficient surface of TEMP.

CONCLUSION

Our study shows that the surface pressure has a favorable effect on AQI in central and southern China, and the intensity of the effect increases in autumn and winter. In contrast, the atmospheric structure is suitable for the diffusion of pollutants during spring and summer in northwest China because of high ground pressure. Falling temperatures in autumn and winter in northern and northwestern China exacerbate air pollution. Conversely, if the temperature in western China is higher from April to September, the air quality will be worse.

Besides, this study confirms that STWR can be well applied to the analysis of spatiotemporal heterogeneity between meteorological factors and air quality. An interesting finding is that the average R^2 of STWR are higher than that of GWR and OLS, especially at those when the rate of change of AQI is fast.

In this study, we do not consider the interaction and transformation of different meteorological factors and pollutants. However, it should be possible to combine physical models to compensate for the limitations of statistical models. In addition, factors such as regional carbon emission increase, economic development level, and human activities (characterized by night lights) can be further considered to reveal the driving mechanism of air pollution more comprehensively.

References

Chen, T., He, J., Lu, X., She, J., & Guan, Z. (2016). Spatial and temporal variations of PM2. 5 and its relation to meteorological factors in the urban area of Nanjing, China. International journal of environmental research and public health, 13(9), 921.

Guo, B., Wang, X., Pei, L., Su, Y., Zhang, D., & Wang, Y. (2021). Identifying the spatiotemporal dynamic of PM2. 5 concentrations at multiple scales using geographically and temporally weighted regression model across China during 2015‐2018. Science of The Total Environment, 751, 141765.

Hajiloo, F., Hamzeh, S., & Gheysari, M. (2019). Impact assessment of meteorological and environmental parameters on PM2. 5 concentrations using remote sensing data and GWR analysis (case study of Tehran). Environmental Science and Pollution Research, 26(24), 24331-24345.

Petitjean, F., Ketterlin, A., & Gançarski, P. (2011). A global averaging method for dynamic time warping, with applications to clustering. Pattern recognition, 44(3), 678-693.

Que, X., Ma, X., Ma, C., & Chen, Q. (2020). A spatiotemporal weighted regression model (STWR v1. 0) for analyzing local nonstationarity in space and time. Geoscientific Model Development, 13(12), 6149-6164.

Kahn, J., & Yardley, J. (2007). As China roars, pollution reaches deadly extremes. New York Times, 26(8), A1.

Xu, L. J., Zhou, J. X., Guo, Y., Wu, T. M., Chen, T. T., Zhong, Q. J., ... & Ou, C. Q. (2017). Spatiotemporal pattern of air quality index and its associated factors in 31 Chinese provincial capital cities. Air Quality, Atmosphere & Health, 10(5), 601-609.

Zhang, L., An, J., Liu, M., Li, Z., Liu, Y., Tao, L., ... & Luo, Y. (2020). Spatiotemporal variations and influencing factors of PM2. 5 concentrations in Beijing, China. Environmental Pollution, 262, 114276.

VALIDATION OF REAL-TIME PRECISION POSITIONING USING INEXPENSIVE SINGLE-FREQUENCY TYPE LOCAL−AREA RTK SYSTEM AND NETWORKS

T. Shinmura[1] and M. Nasu[1]

ABSTRACT: We constructed a low-cost and easy-to-handle local-area RTK-GNSS positioning system which can automatically perform RTK positioning every second. The positioning was conducted at two reference stations to evaluate the accuracy and reliability of the real-time data: (1) at the university campus (ground fixed point) with obstacles such as buildings and trees, hindering a GNSS satellite signal reception and (2) at the open-sky rooftop of a 11-story school building (rooftop fixed point), where the reference station had been set up with only few obstacles to GNSS satellite signal reception. At the ground station, the network connection status, temperature, and relative humidity were also simultaneously measured. Consequently, 600 data were acquired in 10 min, and the data with the highest ratio were further selected for analysis. For the ground-based fixed points, the standard errors of all the data were >10 times more accurate than those of D-GNSS; however, such result is unsatisfactory, as previously anticipated for RTK positioning. We further filtered the data with less than 15 satellites and less than 9 ratio values and found that the data quality and reliability were improved to a satisfactory level. For the rooftop fixed point, the standard error of all the data was approximately 1 mm in both horizontal and vertical directions, thereby indicating higher accuracy than the data from the ground fixed point. Consequently, we obtained accurate and reliable data with less scatter. Overall, it is possible to obtain accurate and reliable RTK positioning data in real time using statistical processing to eliminate outliers.

Keywords: Network RTK, Local-Area RTK, Low-Cost Precise Survey System, RTKLIB

INTRODUCTION

Japan is located in a geologically active zone, where earthquakes and volcanic activity are frequent, and the resulting natural disasters constantly threaten the citizens and property of Japan. Densely allocated precise positioning devices should be introduced for monitoring subtle crustal deformation throughout the country toward more accurate prediction of the volcanic activity. To this end, we assembled an inexpensive and easy-to-handle precision positioning system and evaluated its performance. Shinmura and Nasu (2020) have previously constructed a low-cost and easy-to-handle RTK precise positioning system. Shinmura and Nasu (2021) have validated reproduction of accuracy of coordinate values and Shinmura and Nasu (2022) have demonstrated the continuity, stability of supplying of precise positioning data. In this study, we used these systems to perform real-time positioning every second at a fixed point with good reception of satellite signals and analyzed the results to explore the specific conditions for stable and continuous reception of precise positioning data.

SYSTEM OVERVIEW

Fig. 1 shows the devices that make up the system and the data flow, and Fig. 2 shows photos and the corresponding descriptions of the antenna and devices used in this system. The details of this system were described in Shinmura and Nasu (2020). Both stations were connected to the Internet via 4G lines. The base station reference data are being sent to the caster (NTRIP server), and the rover station constantly receives this via

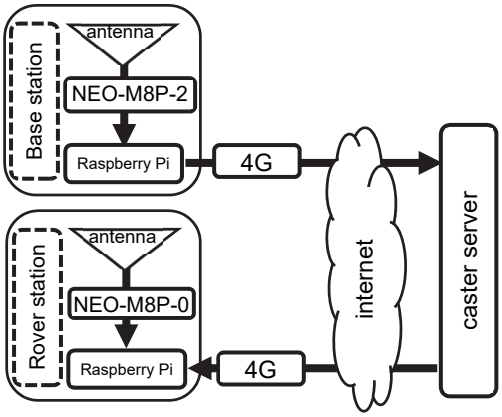

Fig. 1 System overview of this study.

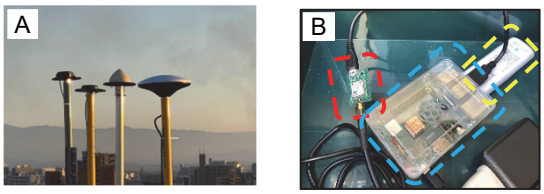

Fig. 2 Reference station and mobile station installed at a fixed point on the rooftop
A: Antennas used in this study are the second (for the reference station) and fourth (for the mobile station) from the front.
B: Equipment for processing and transmitting data for the mobile station. Red dashed line – RTK receiver (NEO-M8P-2), Blue dashed line – Raspberry Pi running the data processing and transmission programs, Yellow dashed line – USB router for mobile communication (4G) connection.

[1] Faculty of Economics, Kumamoto Gakuen University, 2-5-1 Oe Chuo-ku Kumamoto, JAPAN

 https://doi.org/10.1142/9789811275449_0031

the Internet. The price at the rate of beginning of 2021 was approximately 800 US dollars.

RESULTS AND DISCUSSION

Determination of representative values as provisional true values

To ensure the stable operation of the program, the program was allowed to run for 10 min with positioning every second. Subsequently, the data were tabulated and the resultant output alongside the measurement were started again for the next 10 min. Such measurements were performed continuously. Fig 3. illustrates the latitudinal data, recorded from the continuous measurement for ~1 month from November 5, 2021.

Fig. 3A demonstrates all the data obtained along the horizontal axis of time. Except few outliers, the data are concentrated at 32.803790°. In Fig. 3B, the vertical axis was restricted to the degree range of 3.0×10^{-7} of the above concentrated latitudes. As observed, the yellow and blue plots with low ratio values are relatively scattered; however, the black plots with ratios above 300 are clustered at approximately 32.80379055°. Figure 3C shows a histogram of the data over approximately the same range as the vertical axis in Figure 3B. As the data are normally distributed, the average estimate (32.80379056°N) is hereafter considered as the representative value after outliers were removed from the total. The same results were obtained for longitude and altitude, with 130.73054082° east longitude and 86.375 meters altitude, respectively, as the representative values.

Evaluation of real-time data acquired every second

All the real-time data acquired every second for ~24 h on November 1, 2001, were evaluated for the difference between the representative values obtained by statistical methods as the error.

In the entire dataset, 91.8% of horizontal data exhibited an error of < 1 cm and 75.5% of vertical data. In the range where the ratio value, normally reflecting the Fix value, is ≥ 3, it was found that 97.8% of the data exhibited the error of < 1 cm in the horizontal direction and 80.5% in the vertical direction. In both cases, the percentage of the accurate data generally increases for Fix values. Hereafter, the ratio value of ≥3 or higher is referred to as a Fix value, while the ratio value of ≤ 3 is referred to as a Float value. However, some exceptional data with very small errors were identified even for the Float value while the Float data were generally classified as the data with poor accuracy. In GNSS satellite positioning, the number of acquired satellites strongly affects the accuracy of positioning data. However, in this measurement, the number of acquired satellites exceeded 15 for the entire period. In addition, the antenna was installed on the roof

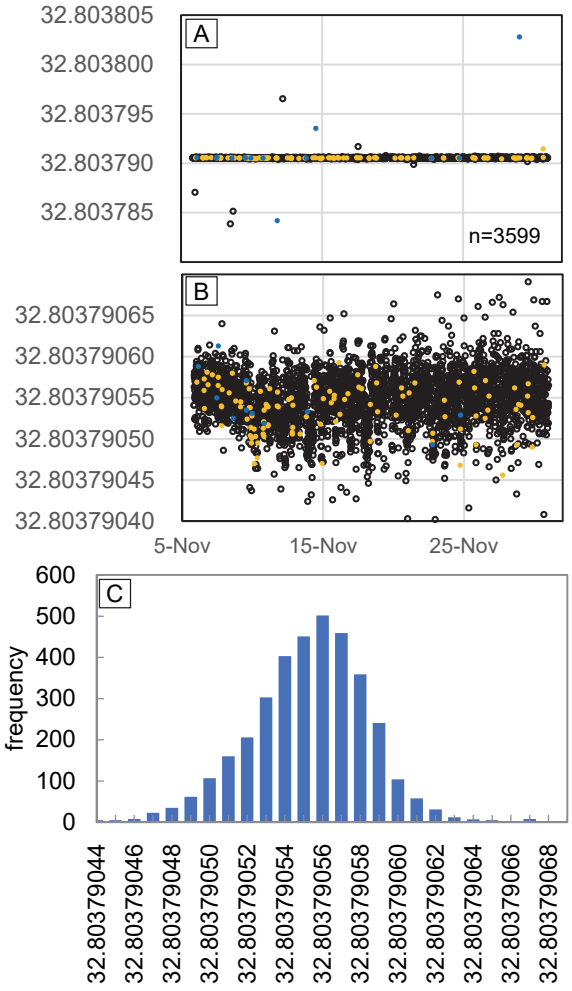

Fig. 3 Latitude data continuously measured for approximately one month from November 5, 2021.
A: All the data obtained along the horizontal axis of time.
B: Vertical axis was restricted to the degree range of 3.0×10^{-7} of the concentrated latitudes of Fig. A.
C: Histogram of data over approximately the same range as the vertical axis in Fig. B.
Blue, yellow, and black circles show obtained data, and the colors and shapes show their ratio values as follows: blue is 4–10, yellow is 80–100, and black is over 300.

of a 7-story building with a good view, thereby nearly refuting any multipath effect.

Fig. 4 displays only the Float data, separated according to Age, namely, the Age of the reference station data used when analyzing the positioning values. As seen, both horizontal and vertical data with the Age of > 30 exhibited larger errors, while the errors for the data with the Age < 30 was distributed around 0 with only few exceptions. Much of the data with the Age of < 30, characterized by low errors, exhibited different times, compared to that of the continuous vertical columns of data with Age greater < 30 and a large error on the column were also identified.

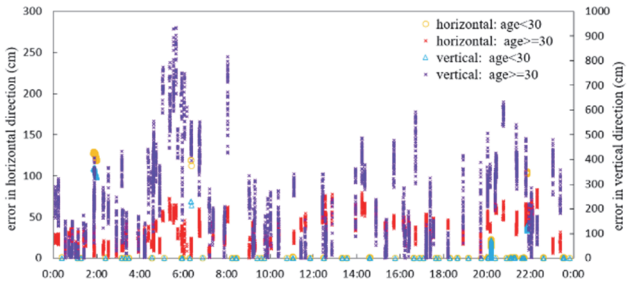

Fig. 4 Errors of Float data in 1-s measurement in 1-s RTK positioning on November 1, 2021.

The magnitude of the error is expressed as the difference from the representative value. In total, 4,733 Float values are divided and displayed according to whether the Age is < 30 or the Age is > 30 (RTK relative positioning or single positioning).

In other words, the data were calculated at consecutive times to the data whose Age was >30 and whose error was continuously large, and was potentially related to an unidentified phenomenon, which increased the Age above 30.

Although the Float values accounted for only 6.5% of the 72,640 pieces of total data, if continually accurate data are required, these percentages should be maximally reduced. Based on this, the Float data were classified by the Age and simultaneously analyzed to elucidate their occurrence. The number of consecutive Float values was expressed as the number of cases. As one piece of data was measured per second, the number of data per case corresponds to the duration of the Float value. Therefore, the average number of data per case is expressed as the average duration of the Float value.

The Float value with the Age of < 30 divided the latter into two categories including those, seemingly attributed to the Age fluctuations (A) and those that were unrelated (B), based on the magnitude of the Age value, how it fluctuated, and whether it was continuous with data exceeding 30.

	Age > 30	Age ≦ 30	
		(A) Age fluctuations are related	(B) Age fluctuations are unrelated
number of cases	83	37	34
overall count	4025	496	212
average duration (sec)	48.5	70.9	6.2

(A) The average duration was 70.9 s. As for the causes of Float solutions, those caused by an increase in Age or its effect due to the stagnant reception of reference station data were numerous and long-lasting. Numerous horizontal errors were > 10 cm.

(B) The average duration was 6.2 s. The cases in which the ratio value somehow decreased, probably unrelated to Age, yielding a Float value, were infrequent and did not persist for long periods of time. They also exhibited the horizontal error of 1 cm, the same accuracy as the Fix value.

During the observation period, the system was running stable and the periodic ping results indicated stable network connectivity. Therefore, the operation of an external free caster server was likely the driver of the identified Age increase. Lastly, it was found that in real-time precision positioning for inexpensive operation, it is necessary to set up and use our own caster server for solving the degradation of Age.

CONCLUSIONS

Our analysis demonstrated that for precise positioning it is required to

1) Provide a good reception environment
2) Not miss the Fix data (the ratio values of ≥ 9)
3) Ensure a little or no delay in reference data

We concluded that when these three conditions are accomplished, our local-area network RTK-GNSS positioning system provides the data in real-time every second with the errors of < ~1 cm in horizontal dimension with enough for observing very small displacements.

ACKNOWLEDGMENTS

We would like to express our gratitude to the administration department of Kumamoto Gakuen University for their understanding and cooperation on the installation and access to the roof of the building for the installation of the base station. This research was funded by the FY2022 Kumamoto Gakuen University Research Grant and Educational Research Support Program (President's Discretionary Funds).

References

Shinmura, T. and Nasu, M. (2020) Construction and Verification of Precise Survey System Using Low Cost Receivers for Local-Area RTK-GNSS and the Internet. The Kumamoto Gakuen University Journal of Liberal Arts and Sciences, 26(1), 15-50.

Shinmura, T. and Nasu, M. (2021) Verification of the Accuracy and Reproducibility of Local-Area RTK-GNSS over 4G Lines over Time, The Kumamoto Gakuen University Journal of Liberal Arts and Sciences, 26(2), 1-12.

Shinmura, T. and Nasu, M. (2022) Validation of Real-Time Precision Surveying Using Inexpensive Single-Frequency Type Local Area RTK System and Networks, The Kumamoto Gakuen University Journal of Liberal Arts and Sciences, 27(2), 25-60.

JOINT INVERSION OF ELECTRICAL RESISTIVITY AND SEISMIC REFRACTION TOMOGRAPHY IN REDUCING INTERPRETATION AMBIGUITY

Yonatan Garkebo Doyoro[1,2,3] and Ping-Yu Chang[1,4]

ABSTRACT: A single geophysical method is limited in providing adequate model accuracy and resolution for inversion of subsurface structure. Using multi-geophysical techniques with different sensitivity to subsurface structures can complement each other and obtain more relevant results. We numerically perform joint inversion of electrical resistivity tomography (ERT) and seismic refraction tomography (SRT). The joint inversion approach is used to detect horizontally layered sedimentary units. The result shows unclear and considerably merged layer interfaces for separate inversion of the ERT and SRT. However, jointly inverted results exhibit relatively improved layer structures, reducing model ambiguity. In addition, the numerical experiment shows the adequacy of regularization selection on model resolution.

Keywords: Electrical resistivity tomography, seismic refraction tomography, joint inversion, uncertainty.

INTRODUCTION

In particular conditions, it is well known that all geophysical methods produce ambiguity in model interpretation because of the inherent uncertainty in data inversion (Doyoro et al., 2021; Vozoff and Jupp, 1975). Using multi-geophysical techniques can combine the strengths of different methods to reduce the effect of non-uniqueness and uncertainty with respect to single-domain inversions (Gallardo and Meju, 2004; Vozoff and Jupp, 1975).

Seismic and electrical methods have complementary sensitivities and are often combined differently (Garofalo et al., 2015; Ronczka et al., 2018). For instance, the use of combining electrical resistivity tomography (ERT) and seismic refraction tomography (SRT) data derived using the main assumptions that indirectly correlate the relationship between the electrical resistivity and the velocity of the seismic waves through direct linkages of both parameters with the porosity (Archie, 1942; Wyllie et al., 1956). Wagner et al. (2019) developed petrophysical joint inversion for four-phase (rock matrix, water, ice, and air) volumetric fraction for permafrost quantification from electrical resistivity and seismic refraction data. In this study, we numerically evaluate the uncertainty of single-domain inversion with regard to petrophysical joint inversion of ERT and SRT data for three-phase (rock matrix, water, and air) volumetric fraction of saturated sedimentary rock units.

Using low regularization weight for horizontal structures and high weight for vertical structures is a common technique to improve the inversion results (Mollaret et al., 2020). However, the effect of properly or improperly selected regularization weight on the model resolution has not been assessed. We analyze the suitability of appropriately choosing anisotropic smoothing (zWeight regularization) in recovering horizontal or vertical structures. Therefore, in addition to petrophysical joint inversion, the present study evaluates the effect of regularization parameters on model resolution.

METHODOLOGY

We perform a numerical experiment for the geological model obtained from the Touqiao industrial area of central Taiwan, consisting of horizontally stratified sediments such as mud, gravel, clay, and sand from top to bottom (Fig. 1a). Since the groundwater is observed at a 3 m depth, the mud layer is characterized as a vadose and saturated layer. Wagner et al. (2019) and Mollaret et al. (2020) used a four-phase (rock matrix, water, ice, and air) volumetric fraction, but this study uses a three-phase (rock matrix, water, and air) volumetric fraction for saturated sedimentary rock units. We follow Wagner et al. (2019) approach for apparent numerical resistivity and travel time data generation.

The petrophysical joint inversion is based on Wagner et al. (2019), and the forward modelling and inversion capabilities are available in the open-source pyGIMLi package (Doyoro et al., 2022; Rücker et al., 2017). The joint inversion minimizes the following objective function (Wagner et al., 2019):

[1] Department of Earth Science, National Central University, Taoyuan, TAIWAN
[2] Earth System Science, Taiwan International Graduate Program (TIGP), Academia Sinica, Taipei, TAIWAN
[3] Department of Applied Geology, School of Natural Sciences, Adama Science and Technology University, Adama, ETHIOPIA
[4] Earthquake-Disaster, Risk Evaluation and Management Centre, National Central University, Taoyuan, TAIWAN

 https://doi.org/10.1142/9789811275449_0032

$$\left\|W_d\left(d-F(m)\right)\right\|_2^2+\alpha^2\|W_m m\|_2^2+\beta^2\left\|W_p^{sum}p-1\right\|_2^2+\gamma^2\left\|W_p^{sum}p-p_0\right\|_2^2\rightarrow min \quad (1)$$

where the first term represents data misfit, the second term corresponds to model smoothness regularization, the third term indicates a supplementary regularization to fulfill the volume conservation constraint, and the fourth term is optional for porosity constraining. We refer the reader to Wagner et al. (2019) for more details on the petrophysical joint inversion scheme.

RESULTS AND DISCUSSION

Conventional inversion

Fig. 1b shows the conventional or separate inversion of apparent resistivity and seismic travel time data. The inversion result shows that the horizontally stratified layers are not properly reproduced, particularly for the refraction tomography. In addition, the inverted velocity model shows a gradual increase of velocity as the survey depth increases instead of resolving the low-velocity clay and sand layers. It indicates the failure of conventional seismic refraction tomography to detect the low-velocity (hidden) layers. However, resistivity tomography recovers the clay and sand layers as a single low resistivity layer, showing better results than refraction tomography. Finally, the inverted resistivity and seismic travel time data are transformed into water, air, and rock content models, estimating each content's volumetric fraction.

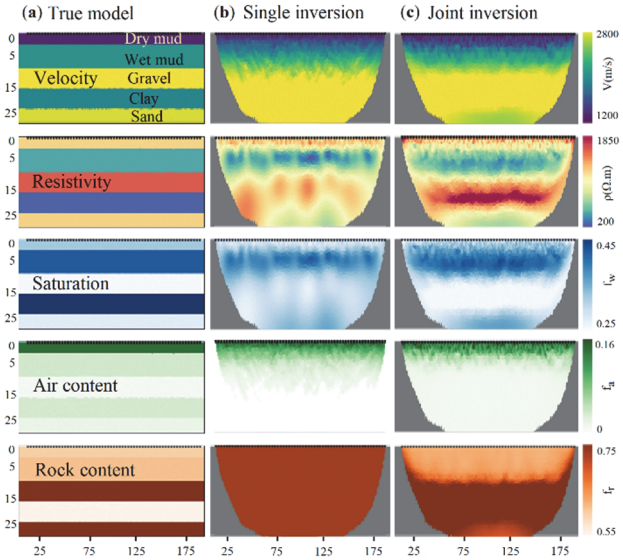

Fig. 1. (**a**) True model for layered sedimentary units, (**b**) conventional inversion, and (**c**) petrophysical joint inversion. The x-axis represents depth (m), while the y-axis represents profile distance (m).

Petrophysical joint inversion

We perform petrophysical joint inversion using apparent resistivity and seismic travel time data to examine its model improvement on conventional inversion. The resistivity information is incorporated in the jointly inverted refraction tomogram and vice versa. Fig. 1c exhibits the jointly inverted results for the layered sedimentary model. The jointly inverted SRT model indicates four layers: the dry mud layer is identified as very low velocity, the wet mud is designated as low velocity, and the relatively high-velocity layer specifies the gravel layer. The bottom clay and sand layers are recovered as a single layer with the low-velocity signature, which is not recovered in the conventional inversion. The jointly inverted ERT also determines four layers. Relatively high resistive top layer (dry mud), very low resistive second layer (wet mud), relatively resistive third layer (gravel), and low resistive bottom layer wherein the clay and sand layers are combined. The jointly inverted SRT and ERT models are more adequately resolved the layered structures and interfaces compared to the conventional inversion. Besides, the transformed water, air content, and rock matrix are well estimated in the jointly inverted model (Fig. 1c).

Seismic refraction fails to detect a hidden layer (low-velocity layer) that could be distinguished by resistivity imaging, similar to other studies (Gallardo and Meju, 2004; Hellman et al., 2017). On the other hand, resistivity imaging may fail to determine low-contrast resistivity boundary that could be sensed by seismic refraction. Under these conditions, joint inversion can improve the overall resolution and reduce each method's inherent uncertainty (Doyoro et al., 2021).

Regularization constraint

Geophysical inversion schemes, in general, noticeably depend on the choice of regularization parameters (Mollaret et al., 2020). Anisotropic smoothing (zWeight) is a regularization parameter used to enhance horizontal or vertical structures by incorporating it into the objective function (Equation 1).

We test various regularization weights for petrophysical joint inversion and assess model resolution. This study presents results for three zWeight constraints: 0.25 for known *prior* geologic conditions, 0.5 for unknown geologic information, and 0.75 for improperly used geologic information. The numerical test uses a layered sedimentary model shown in Fig. 1a.

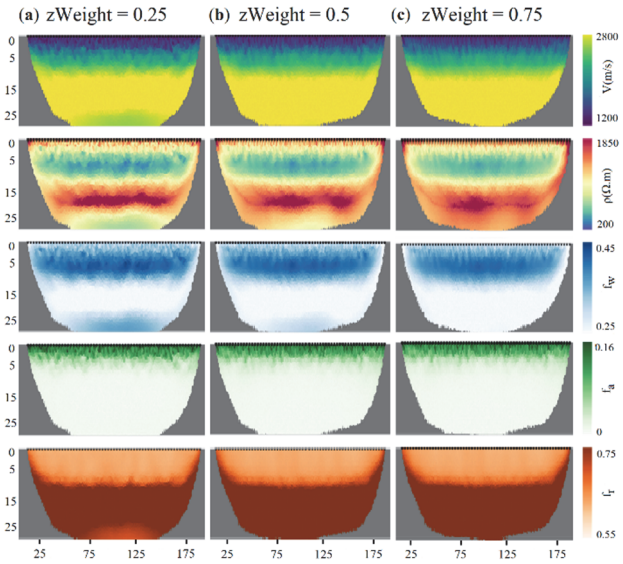

Fig. 2. Inverted models for petrophysical joint inversion of ERT and SRT using anisotropic smoothing of zWeight = 0.25, 0.5, and 0.75. The model shows the seismic, resistivity, saturation, air content, and rock matrix from top to bottom. The x-axis represents depth (m), while the y-axis represents profile distance (m).

The joint inversion using 0.25 zWeight anisotropy smoothing (Fig. 2a) shows a high model resolution that adequately recovers the layer structures and interfaces. However, joint inversion using 0.5 zWeight depicts smeared quality with less layer accuracy (Fig. 2b); deeper depth layer structures are not reproduced in the SRT model. On the contrary, a low model resolution and poor layer structures are obtained through joint inversion using 0.75 zWeight regularization constraints (Fig. 2c). Thus, properly selected anisotropy smoothing can enhance model resolution. If *prio*r geologic information is known, an anisotropy smoothing zWeight of 0.25 can be used for horizontally situated structures while 0.75 zWeight for vertical structures. Whereas 0.5 zWeight can be used for unknown prior geologic information.

CONCLUSIONS

This study examines how petrophysical joint inversion of the ERT and SRT reduces model ambiguity of single-domain inversion and evaluates the regularization parameter effects on resolution. Since the ERT and SRT have different sensitivities, they complement each other in the joint inversion and improves the model resolution. SRT adequately detects gravel and clay boundary that is unclear in ERT. On the contrary, ERT identifies a clay layer that is a hidden layer for SRT. In addition, the appropriately chosen anisotropy smoothing regularization (zWeight) can affect the model resolution. A zWeight of 0.25 can be used for horizontally oriented structures, 0.5 for unknown subsurface conditions, and 0.75 for vertically situated structures. This study presents how petrophysical joint inversion and appropriately selected regularization parameters can considerably reduce model ambiguity.

ACKNOWLEDGEMENTS

We would like to thank the Minister of Science and Technology (MOST) of Taiwan for supporting this study under project number MOST 108-2638-E-008-001-MY2.

References

Archie, G.E., 1942. The electrical resistivity log as an aid in determining some reservoir characteristics. Transac. AIME, 146(01): 54-62.

Doyoro, Y.G., Chang, P.-Y. and Puntu, J.M., 2021. Uncertainty of the 2D resistivity survey on the subsurface cavities. Appl. Sci., 11(7): 3143.

Doyoro, Y.G., Chang, P.-Y., Puntu, J.M., Lin, D.-J., Van Huu, T., Rahmalia, D.A. and Shie, M.-S., 2022. A review of open software resources in python for electrical resistivity modelling. Geosci. Lett., 9(1): 1-16.

Gallardo, L.A. and Meju, M.A., 2004. Joint two-dimensional DC resistivity and seismic travel time inversion with cross-gradients constraints. Geophys. Res. Solid Earth, 109(B3).

Garofalo, F., Sauvin, G., Socco, L.V. and Lecomte, I., 2015. Joint inversion of seismic and electric data applied to 2D mediaseismic and electric data joint inversion. Geophys., 80(4): EN93-EN104.

Hellman, K., Ronczka, M., Günther, T., Wennermark, M., Rücker, C. and Dahlin, T., 2017. Structurally coupled inversion of ERT and refraction seismic data combined with cluster-based model integration. Appl. Geophy., 143: 169-181.

Mollaret, C., Wagner, F.M., Hilbich, C., Scapozza, C. and Hauck, C., 2020. Petrophysical joint inversion applied to alpine permafrost field sites to image subsurface ice, water, air, and rock contents. Front. Earth Sci., 8: 85.

Ronczka, M., Wisén, R. and Dahlin, T., 2018. Geophysical pre-investigation for a Stockholm tunnel project: joint inversion and interpretation of geoelectric and seismic refraction data in an urban environment. Near Surf. Geophys., 16(3): 258-268.

Rücker, C., Günther, T. and Wagner, F.M., 2017. pyGIMLi: An open-source library for modelling and inversion in geophysics. Comput. and Geosci., 109: 106-123.

Vozoff, K. and Jupp, D., 1975. Joint inversion of geophysical data. Geophys., 42(3): 977-991.

Wagner, F., Mollaret, C., Günther, T., Kemna, A. and Hauck, C., 2019. Quantitative imaging of water, ice and air in permafrost systems through petrophysical joint inversion of seismic refraction and electrical resistivity data. Geophys. J. Int., 219(3): 1866-1875.

Wyllie, M.R.J., Gregory, A.R. and Gardner, L.W.J.G., 1956. Elastic wave velocities in heterogeneous and porous media. Geophys., 21(1): 41-70.

RECENT ACTIVITIES OF THE REGIONAL ADVISORY COMMITTEE (RAC)

Wing-Huen Ip[1, 2]

ABSTRACT: The Regional Advisory Committee (RAC) has been established in 2018 to promote the attendance and participation in the AOGS annual meetings by researchers and students from the ASEAN countries and India that constitute the largest population of the AOGS geographic area. In addition, RAC is interested in building research networks on scientific issues of common interest and importance in the Asian geoscience community. In spite of the COVID 19 pandemic, we have gradually introduced a number of projects that will form the building blocks of the RAC program in the coming years. These include the launch of new publications, the organization of working groups on the coastal zone risk mitigation and management and on the low-latitudinal ionospheric research, respectively. Furthermore, it is planned that a series of satellite meetings on topical areas of interest to the local scientific communities will be organized in coordination with the Scientific Sections in complement to the AOGS annual meetings.

Keywords: ASEAN, India, research networks, working groups

INTRODUCTION

Even though the main purpose of the Asia Oceania Geosciences Society is to promote research and cooperation of scientists in Asia and Oceania ranging from Kathmandu to Wellington, the attendance and hence membership are dominated by researchers from China, Japan, South Korea and Taiwan with about a quarter from Europe and the USA. Scientists from India, Thailand, Vietnam, Indonesia, Philippines and Malaysia tend to attend annual meetings held in Singapore but the ratio is generally low (<5%). There are many factors leading to the less than ideal attendance. They include the cost to attend an international meeting like AOGS and the scientific topics of special interest to the local communities might not be in the main stream of the AOGS annual meetings. As an international non-profit organization supporting an inclusive and equitable community of Earth and space scientists with a view to make scientific discoveries and social changes as in the case of the American Geophysical Union, what should AOGS do? It is out of this thought that the Regional Advisory Committee was created by the AOGS Council in 2018. Its membership is composed of leading scientists from different countries with expertises covering a wide swap of scientific areas and its main purpose is to give advice to AOGS on how to make its scientific program more attractive to the ASEAN and Indian scientists.

Figure 1 shows the original concept of the structure of TAC. That is each RAC member will lead a subcommittee called the Local Advisory Committee (LAC) to help organize and integrate the geoscience communities in individual countries. Also, some RAC members could come from major universities or research institutions to provide support and inputs.

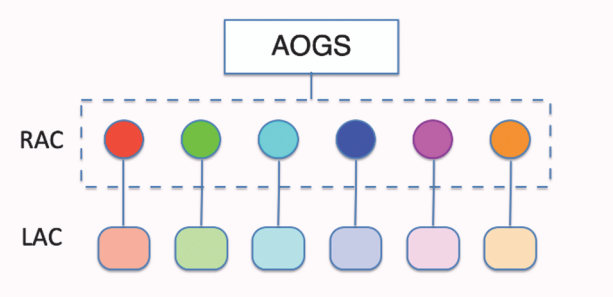

Fig. 1 The original concept of the RAC organization.

Figure 2 shows the current RAC membership with Wing Ip (National Central University) as the Chair and Punyasloke Bhadury (Indian Institute of Science Education and Research Kolkata) as the Vice Chair/CEO. (Note: Information on RAC and its activities can also be found at www.aogsrac.org). All members have been active in mounting a number of initiatives as described below.

[1] Institute of Astronomy, National Central University, Taoyuan City, TAIWAN (R.O.C.).

[2] Department of Space Science and Engineering, National Central University, Taoyuan City, TAIWAN (R.O.C.)

 https://doi.org/10.1142/9789811275449_0033

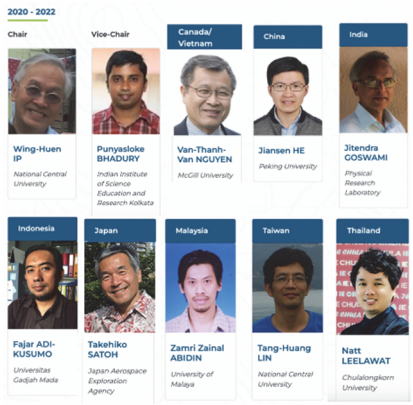

Fig. 2 The membership of RAC.

RECENT ACTIVITIES

The brief history of RAC can be divided into the pre-pandemic era (before 2020) and the pandemic era (after 2020 until now). In order to advertise the new committee and its function, an exhibition booth called "AOGS Infinity" was set up at the 2019 AOGS annual meeting in Singapore. Figure 3 shows RAC member Natt Lelawatt standing enthusiastically in front of the booth displaying posters introducing some research programs and facilities in India and ASEAN countries. The plan to continue such exhibition booth and organizing accompanying scientific sessions to highlight opportunities for cooperation and personal exchange in succeeding annual meetings from 2020 to 2022 was unfortunately disrupted by the COVID-19 pandemic forcing in-person meetings to be replaced by virtual meetings.

Fig. 3 Prof. Natt Leelawat and the RAC exhibition booth "AOGS Infinity" at the 2019 annual meeting in Singapore.

During this extraordinary time, RAC organized two online activities with the support of AOGS Secretariat Office. These include the presentations on January 27, 2021, by Section Presidents on the aspects of regional cooperation in different disciplines of geoscience. The videos of the online talks can be found at: https://www.asiaoceania.org/aogs2021/public.asp?page=whos_talking_to.asp. As a pilot project (called Young Scientist Showcase) we have also invited a number of PhD students and ECRs (early career researchers) in 2021 to give short presentations on their research work. The idea is to raise the interest of individual scientific sections to follow up.

In parallel to these online projects in lieu of in-person meetings, we have also proposed to the AOGS Council on the desirability of introducing a publication project to compile the extended abstracts into a proceedings volume. This is because many funding agencies in Asia requite publication record to support the applications for attending international meetings like AOGS. It is quite probable that the realization of such an extended abstract volume series will attract more researchers from ASEAN, India and other countries to attend AOGS. In addition, it is a good way for long-term information exchange.

Another publication project that RAC has played a role is the negotiation with Springer-Nature on the starting of a society book program called "Interdisciplinary Geosciences" in its Springer Briefs series. This book project opened to all fields in Earth and space sciences has been approved by the AOGS Council and Prof. Yoshifumi Omura is to be the Editor-in-Chief. It should be mentioned that RAC member Prof. Van Thanh-Van Nguyen, as Chair of the Publication Committee, has been instrumental in beginning and finalizing these two new publication projects that could enhance the scientific impact and visibility of AOGS.

Fig. 4 The Proceedings volume for extended abstracts and the "Interdisciplinary Geosciences" book series are two publication projects promoted by RAC.

As we proceeded with the RAC business, it has become clear that the original concept of forming LACs under individual RAC members does not work. This is because it is difficult for researchers to connect to experts

outside their specialized fields and institutions. As a consequence, the momentum can never be built up. We have therefore opted for a different operational mode which is to organize working groups by recruiting specialists from different countries and institutions to address some unified themes. The new scheme of the RAC organization is shown below.

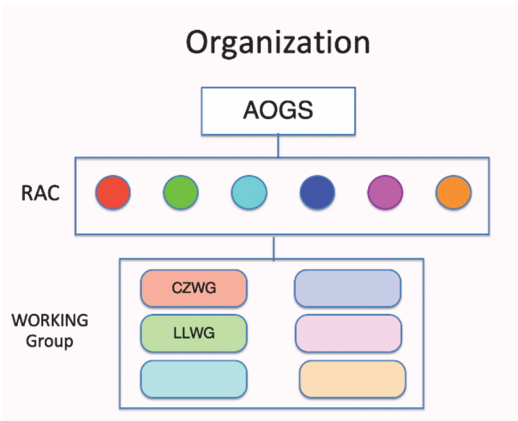

Fig. 5 The projected-oriented structure of RAC.

Briefly speaking, because of the threat of sea, level rise (SLR) to the coastal regions of many Asian countries, coastal zone risk mitigation and management is going to be a mounting issue as the climate crisis deepens. A working group with CZWG as the abbreviated name is formed. Current CZWG members include scientists from China, India, Indonesia, New Zealand, Singapore, Taiwan and Vietnam. At this point in time, except for the fact that it is an informal group, the organization and agenda of CZWG are still being defined. But the main goals can be assessed to be: (1) to exchange information; (2) to heighten the sensitivity to coastal zone protection by scientific analyses and discussions; (3) to activate governmental/intra-governmental activities in some urgent areas; and (4) to educate and reach out to the general public.

Point (1) can be addressed by exchanging information on the research results and publications such that the scientific communities covered by AOGS can be more or less on the same page as far as coastal zone risk mitigation and management are concerned. The annual AOGS meeting is therefore an important channel for this purpose. Point (2) will rely on the scientific expertise of the CZWG members to identify areas not yet well understood or discussed for further examination/monitoring. Topical sessions or satellite meetings can be organized for this purpose. Point (3) means that CZWG should be able to produce study reports or white papers on behalf of AOGS to promote regional/international cooperation with the support of NGO or governmental agencies. This is perhaps where the impact of CZWG will be felt in the context of science and technology policy. Finally, Point (4) can be started by organizing online public talks or short courses.

Along the same line, RAC has formed a second working group (LLWG) for Low-Latitude Ionospheric Research, currently, with members from China, Malaysia, Nepal, Pakistan, and Taiwan. More researchers from other countries are expected to join. While the general purpose and agenda are similar to those of CZWG, LLWG has the task to energize regional cooperation in solar-terrestrial physics. This is because, with the increasing solar activity in Cycle 25, the corresponding space weather effects will become more and more frequent and interesting. Ground-based scientific infrastructures and facilities in our region can conduct coordinated observations as well as in conjunction with satellite measurements. These data are very useful in the study of ionospheric disturbances, hurricanes, lightning and tsunamis, etc. From the point of view of RAC, LLWG will be unique in its ability to develop regional scientific networks and capacity building. If successful, we can extend the collaboration to the low-latitude regions around the world with this working group as the main driver.

FUTURE PROSPECTS

Last but not the least, we must mention the satellite meeting program which is especially set up to meet the need of scientific communities in ASEAN and India (plus other countries). According to the guidelines from the AOGS Council, such small-sized topical workshops should have at least one RAC member and one section president or the section president's designate in their respective organizing committees. The minimum workshop duration is one day and maximum is two days. Other administrative conditions are given in the AOGS webpage. We look forward to the first satellite meeting with scientific focus on biogeochemistry which is to be held in Kolkata.

As described previously, it is planned that all initiatives and activities mentioned here, if proven viable, will be incorporated into different scientific sections with increasing numbers of members from ASEAN and India while RAC will move on to other business.

ACKNOWLEDGMENT

I thank RAC colleagues, in particular, Prof. Punyasloke Bhadury and Prof. Van Nguyen, for kind help and supports.

RESEARCH ON THE SPATIOTEMPORAL HETEROGENEITY OF INFLUENZA AND ITS MAIN DRIVING FACTORS —— AN EMPIRICAL ANALYSIS BASED ON STWR MODEL

Tingting Fei[1], Xiang Que[1,2,3], Xiaogang Ma[3] ,Youqiong Xu[4], Jin Lin[1], Xuanhui Yan[5]

ABSTRACT: Influenza virus has the characteristics of easy mutation, easy transmission and high morbidity, and has caused many disease outbreaks around the world. Influenza outbreaks are closely related to the environment and meteorology with obvious spatiotemporal heterogeneity. Little research has been done on the main drivers of influenza outbreaks and the extent of their effects in both spatial and temporal dimension. If the temporal characteristics of influenza data are ignored, this not only leads to insufficient extraction of spatiotemporal information, but also may lead to misinterpretation of the spread and prevalence of infectious diseases. Therefore, we employed the spatiotemporal weighted regression (STWR) model to explore the response mechanism of influenza on a certain spatiotemporal scale, and analyzed the relationships between the numbers of influenza at county level in Fuzhou and major meteorological factors such as temperature and humidity, social factors, and NDBI from 2013 to 2019. Results show that the main factor affecting the flu in Fuzhou is the large temperature difference between winter and spring caused by the subtropical monsoon climate. The high population and dense buildings in urban areas were also an important incentive for the rapid spread of influenza in Fuzhou.

Keywords: Influenza, Spatiotemporal weighted regression, Spatial heterogeneity, Temporal heterogeneity

INTRODUCTION

Influenza is an acute respiratory infection caused by influenza viruses. Influenza viruses, characterized by easy mutation, easy transmission, and high morbidity, which has caused many disease outbreaks around the world (Jennings et al. 2018). Influenza outbreaks are closely related to the environment and meteorology, and have obvious spatiotemporal heterogeneity.

Few studies have been conducted on the main driving factors of the outbreaks of influenza and their effects in both temporal and spatial dimensions. Ibarra Zapata et al. (2021) identified 19 areas at high risk of influenza A (EOITA) by using the geographically weighted regression (GWR) (Brunsdon et al. 1996), along with a transmission type analysis. This method obtains the spatially varying coefficient surfaces corresponding to different variables, but it does not consider time dimension. Guo et al. (2021) employed the geographically and temporally weighted regression (GTWR)(Huang et al. 2010; Fotheringham et al. 2015) to explore the impacts of some socioeconomic and environmental factors on the mortality of chronic obstructive pulmonary disease (COPD). Although taking the time dimension into account, current GTWR ignores the spatial non-stationary of the rate of numerical variations, which in results the configuration of weight matrix is imprecise. The spatiotemporal weighted regression (STWR) proposed by Xiang et al. (2020; 2021) adopts the time-varying numerical difference rate attenuation weighting strategy, and constructs the spatiotemporal kernel function through the weighted average form, which can better capture the mixed effects of time and space.

If the time dimension of influenza data is ignored, it will not only lead to a waste of information, but also may lead to misunderstanding of the transmission and prevalence of infectious diseases. Therefore, it is of practical significance to explore the temporal and spatial distribution characteristics of influenza, to find the main driving factors leading to influenza aggregation, and to provide a scientific basis for influenza prevention and control.

STUDY AREA

We choose Fuzhou, the capital of Fujian Province in China, as the study area for its typical subtropical monsoon climate and the increasing number of people suffering from influenza, especially in winter and spring.

[1] Computer and Information College, Fujian Agriculture and Forestry University, Fuzhou, Fujian, China
[2] Key Laboratory of Fujian Universities for Ecology and Resource Statistics, Fuzhou, China
[3] Department of Computer Science, University of Idaho, Moscow, USA
[4] Fuzhou Center for Disease Control and Prevention, Fuzhou, Fujian, China
[5] College of Mathematics and Informatics, Fujian Normal University, Fuzhou, Fujian, China

 https://doi.org/10.1142/9789811275449_0034

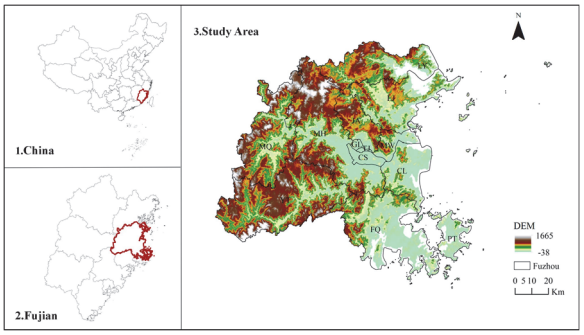

Fig. 1. Study Area.

DATA AND METHODS

Research framework

In this study, principle component analysis was used to downscale the dimensions of main natural factors such as temperature and humidity and social factors such as nighttime lighting to generate four comprehensive factors (F1-F4). Then, a spatiotemporal weighted regression (STWR) model was introduced to explore the spatiotemporal relationship between the comprehensive factors of influenza cases in Fuzhou. This method represents the time distance by the numerical difference rate within the time interval, which can more effectively capture the problem of spatial heterogeneity in the rate of change, and has better fitting and prediction effects on the regression coefficient surface.

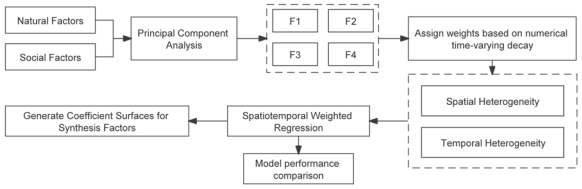

Fig. 2. Research framework.

Selection of indicators

Table 1. Description of the data used in this study.

Index	Indicator	Data Sources
Influenza dataset	Influenza cases	Fuzhou Center for Disease Control and Prevention
F1	PM2.5	https://doi.org/10.11922/sciencedb.00053
	NO2	
	Temperature	
	SO2	
	CO	
	Humidity	
F2	Nighttime lighting	https://eogdata.mines.edu/products/vnl/
	Density of population	https://www.worldpop.org/
	NDVI	http://www.resdc.cn/
	NDBI	http://www.gscloud.cn/
	Urbanization rate	http://tjj.fuzhou.gov.cn/
F3	The meridional wind	https://doi.org/10.11922/sciencedb.00053
	The zonal wind	
F4	Average per capita income.	http://tjj.fuzhou.gov.cn/

RESULT

Through the study of cases information, we found that the influenza in Fuzhou mainly occurred in urban areas, especially Cangshan and Gulou districts (Figure 3). In addition, as shown in Figure 4, we found that after 2014, Fuzhou had two peak incidence periods in summer, winter and spring, but the influenza epidemic season was mainly from November of the current year to January of the following year. The distribution of cases has spatial autocorrelation. In December 2017, 2018 and 2019, the number of influenza cases increased sharply, showing year-to-year upward trend.

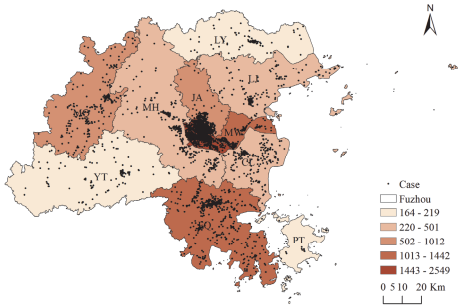

Fig. 3. Distribution of cumulative number of Influenza cases in Fuzhou.

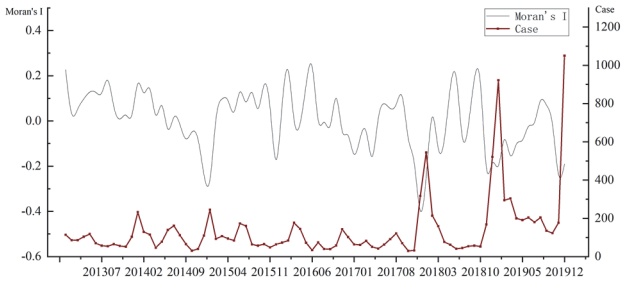

Fig. 4. Distribution and spatial autocorrelation of Influenza cases in Fuzhou City.

Figure 5 shows that the local fitting effect of STWR has obvious advantages in the urban area of Fuzhou. Combined with Figure 4, it is found that the local determination coefficient of STWR is significantly higher than that of the GWR model in the area and time where the number of influenza cases surges.

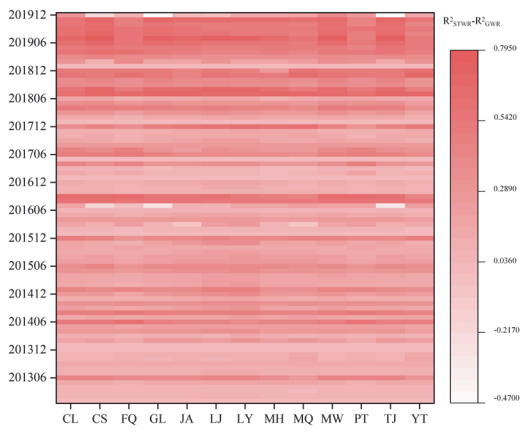

Fig. 5. Distribution and spatial autocorrelation of Influenza cases in Fuzhou City.

According to the regression coefficient of the comprehensive factor F1-F2 (Fig. 6), influenza is more sensitive to the change of F1 and F2. Until 2019, the areas where the F1 coefficient changed from negative to positive were CS, FQ, TJ and CL, indicating that the air quality and climate change in that part of the region can exacerbate the spread of influenza. However, the two regions, YT and LY, which are far away from the urban area, turned positive to negative. The areas where the F2 coefficient changes from negative to positive are YT, LY and LJ. These areas are affected by geographical location and resources, and their development speed is slower than other districts in Fuzhou. Therefore, the spread of influenza is greatly affected by human activities.

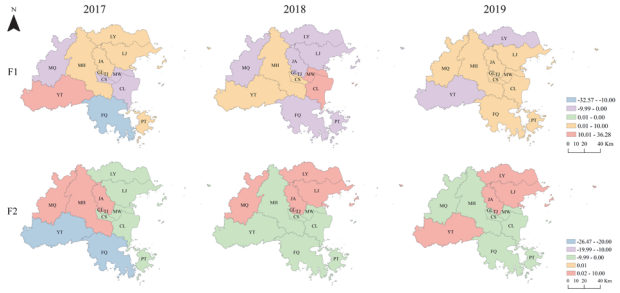

Fig.6.Principal components (F1-F2) coefficient surface.

CONCLUSION

Our study shows that the process of influenza outbreaks has significant spatiotemporal heterogeneity. The main factor affecting influenza in Fuzhou is the large temperature difference between winter and spring caused by the subtropical monsoon climate. In addition, the large population and dense buildings in the urban area are also important incentive for the rapid spread of influenza in Fuzhou. Compared with OLS and GWR, the significant areas in the spatial coefficient surfaces generated by STWR are more interpretive, especially in those areas where high influenza prevalence. And these areas are strongly affected by socioeconomic and environmental drivers. These findings highlight the importance of influenza prevention measures in areas with high population density in Fuzhou during periods of large temperature differences between winter and spring.

References

Brunsdon, C., Fotheringham, A. S., & Charlton, M. E. (1996). Geographically weighted regression: a method for exploring spatial nonstationarity. Geographical analysis, 28(4), 281-298.

Fotheringham, A. S., Crespo, R., & Yao, J. (2015). Geographical and temporal weighted regression (GTWR). Geographical Analysis, 47(4), 431-452.

Guo, B., Wang, Y., Pei, L., Yu, Y., Liu, F., Zhang, D., ... & Guo, H. (2021). Determining the effects of socioeconomic and environmental determinants on chronic obstructive pulmonary disease (COPD) mortality using geographically and temporally weighted regression model across Xi'an during 2014–2016. Science of The Total Environment, 756, 143869.

Huang, B., Wu, B., & Barry, M. (2010). Geographically and temporally weighted regression for modeling spatio-temporal variation in house prices. International journal of geographical information science, 24(3), 383-401.

Ibarra-Zapata, E., Gaytán-Hernández, D., Gallegos-García, V., González-Acevedo, C. E., Meza-Menchaca, T., Rios-Lugo, M. J., & Hernández-Mendoza, H. (2021). Geospatial modelling to estimate the territory at risk of establishment of influenza type A in Mexico-An ecological study. Geospatial Health, 16(1).

Jennings, L., Huang, Q. S., Barr, I., Lee, P. I., Kim, W. J., Buchy, P., ... & Chen, J. (2018). Literature review of the epidemiology of influenza B disease in 15 countries in the Asia - Pacific region. Influenza and other respiratory viruses, 12(3), 383-411.

Que, X., Ma, C., Ma, X., & Chen, Q. (2021). Parallel computing for fast spatiotemporal weighted regression. Computers & Geosciences, 150, 104723.

Que, X., Ma, X., Ma, C., & Chen, Q. (2020). A spatiotemporal weighted regression model (STWR v1. 0) for analyzing local nonstationarity in space and time. Geoscientific Model Development, 13(12), 6149-6164.

THE RESPONSES OF THREE MAJOR PROJECTS ON THE HORIZONTAL SALINITY FRONT IN THE YANGTZE RIVER ESTUARY

C.P. Kuang[1], H.Y. Li[1], J. Wang[1,*], Y.L. Wu[1] and J.D. Fan[1]

ABSTRACT: The Yangtze River Delta is the most densely populated and economically developed region in China, where the interaction mechanism between the river and the sea has been a hotspot in recent years. As a key physical phenomenon of the Yangtze River Estuary (YRE), the salinity front has an important influence on salinity distribution and sediment transport. There are three major projects around the mouth in the YRE, the North Passage Deepwater Channel Project (NPDCP), the Hengsha East Shoal Reclamation Project (HESRP) and the Nanhui East Shoal Reclamation Project (NESRP), which have different impacts on salinity front due to the different locations and scales. In this study, a two dimensional hydrodynamic and salinity transport model of the YRE was established by MIKE21 to study the influence of the responses of the three major projects on the horizontal salinity front in the YRE. The model has been well validated by the measured data of tidal level, current speed and direction and salinity. The numerical results show that: (1) the salinity front in the North Channel (NC) is akin to a single-front pattern, however, the salinity fronts in the North Passage (NP), the South Passage (SP) and the North Branch (NB) almost have a double-front pattern. (2) the three joint projects can make the main salinity front of the NP and NB move downstream, and decrease main salinity front intensity of the NB, NP and SP.

Keywords: horizontal salinity front; Yangtze River Estuary; numerical model

INTRODUCTION

The Yangtze River Estuary (YRE) is a moderate-tidal-controlled estuary, the fresh water from upstream and saline water from the offshore form a barrier which is often called plume front. The Yangtze River plume has a large range, which can extend nearly 100 km, and the front at the maximum salinity gradient is called the salinity front. As an important physical phenomenon occurred in the YRE, the salinity front has a significant influence on tidal current, mass migration and deposition process. Since the 1990s, a large number of projects have been constructed, including the North Passage Deepwater Channel Project (NPDCP), the Hengsha East Shoal Reclamation Project (HESRP) and the Nanhui East Shoal Reclamation Project (NESRP). These projects change the original dynamic conditions of the estuary, and then affect the salinity front at the mouth, which has a direct impact on sediment deposition and water quality (Luan et al., 2017). Many studies have investigated the influence of the constructions in the YRE by using numerical model. Fan (2011) investigated the influence of each stage of the NPDCP on salinity distribution in the North Passage (NP). It was found that the ebb tidal current in the channel increased significantly after the project. The range of low saline water (1-5 psu) in the upstream of the NP expanded, while the intrusion of high salt water in the downstream was intensified. Wang (2018) based on a small scale three-dimensional baroclinic numerical model of the YRE, concluded that the HESRP would increase the flow velocity of the NP, the South Passage (SP) and the South Channel (SC), and lower the salinity of the midstream and the downstream of the North Channel (NC) and the SC. Li and Shen (2017) explored the influence of the North Branch Middling Narrowing Project on hydrodynamics and water quality by using MIKE3. They revealed that both the saline water intrusion in the North Branch (NB) and in the South Branch (SB) would be reduced after the project.

In this study, a two-dimensional hydrodynamic and salinity transport model of the YRE based on MIKE21 is used to explore the combined effects of the NPDCP, the HESRP and the NESRP (shown in Fig.1) on the salinity and salinity front of the four branches (the NP, SP, NC and NB).

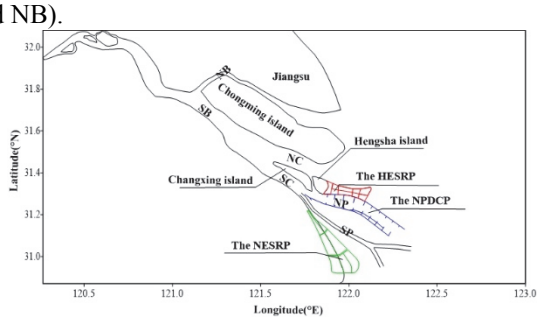

Fig.1 Locations of the three main projects in the YRE.

[1] College of Civil Engineering, Tongji University, Shanghai, CHINA; Email: 2011141@tongji.edu.cn

 https://doi.org/10.1142/9789811275449_0035

METHODOLOGY

In order to study the salinity and salinity front in the YRE, the MIKE21 FLOW MODEL (FM) is used to simulate the changes of tide, current and salinity in the YRE. The model covers the whole YRE, including the Hangzhou Bay and Zhoushan islands with the range from 120°E to 125.5°E in the longitudinal direction and from 27°N to 34.3°N in the latitudinal direction. The unstructured triangular grid is chosen to describe the complicated shore line with 46066 nodes and 89710 elements. The range of the mesh size is from 10-33000 m, decreasing from the open sea boundary to the estuary for both the simulation time and accuracy. The time step is set as automatic adjustment in the range of 0.01-10 s, and the Courant number is set as 0.8. Surface wind data is selected by the atmospheric reanalysis products of European Centre for Medium-Range Weather Forecasts (ECMWF). The ECMWF-Interim is one of the most commonly used atmospheric reanalysis product with a spatial resolution of 0.125° and a temporal resolution of 6 h. The depth thresholds in each element are used to classify each element as drying, flooding and wetting, with threshold depths of 0.005 m, 0.05 m and 0.1 m respectively. The bottom stress is determined by a quadratic friction law, and the Manning number is range from 60 to 98 $m^{1/3}/s$. In the model verification, the open sea boundaries are specified as time-varying tidal levels derived from a harmonic model covering the entire China Sea and its adjacent seas, whose open boundary is driven by the Global Tidal Model, which accounts for 8 main astronomic components (M2, K2, S2, N2, K1, P1, O1, Q1). The real monthly average river discharges at the upstream boundaries are used for the model validation. The salinity at the upstream boundaries is set as zero. At the open sea boundary, the salinity is interpolated based on the measured data. For comparison of impacts of the projects, a typical dry season discharge of 10,000 m^3/s is used at the upstream boundary of the YRE and M2 tide is used at the open boundary. The salinity transport model applies a hot start, which is the result of running for 2 months from a cold start to get relatively realistic salinity distribution.

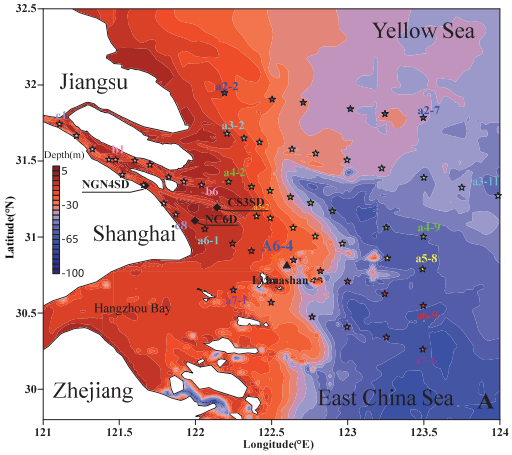

Fig.2 Main study area and observation points.

The measured hourly tidal level, current and salinity in 2014 (observation points shown in Fig.2) have been collected to validate the YRE model (Kuang et al. 2017; Wu et al. 2022), which has been quantitatively assessed using the skill model (Willmott, 1981). The skill values indicate that hydrodynamic model is excellent, and salinity transport model is very good (Chen et al. 2016).

RESULTS

Among the four branches of the YRE, four longitudinal sections are chosen along the talweg of each branch, the starting point locates at the bifurcation point of the NB and SB. The horizontal salinity gradient (Hgs) is chosen as the criterion to define the salinity front, where $Hgs = \Delta\bar{s} / \Delta x$, $\Delta\bar{s}$ is the variation of vertical-averaged salinity in the distance Δx. The maximum value of Hgs is taken as the location of the salinity front.

Fig.3 is the simulated salinity and salinity gradient along each longitudinal section before and after the constructions of three projects. It indicates that the salinity front in the NC is akin to a single-front pattern, however, it almost has a double-front pattern in the NP, SP and NB. The location and intensity of salinity front in the four branches are shown in Table 1.

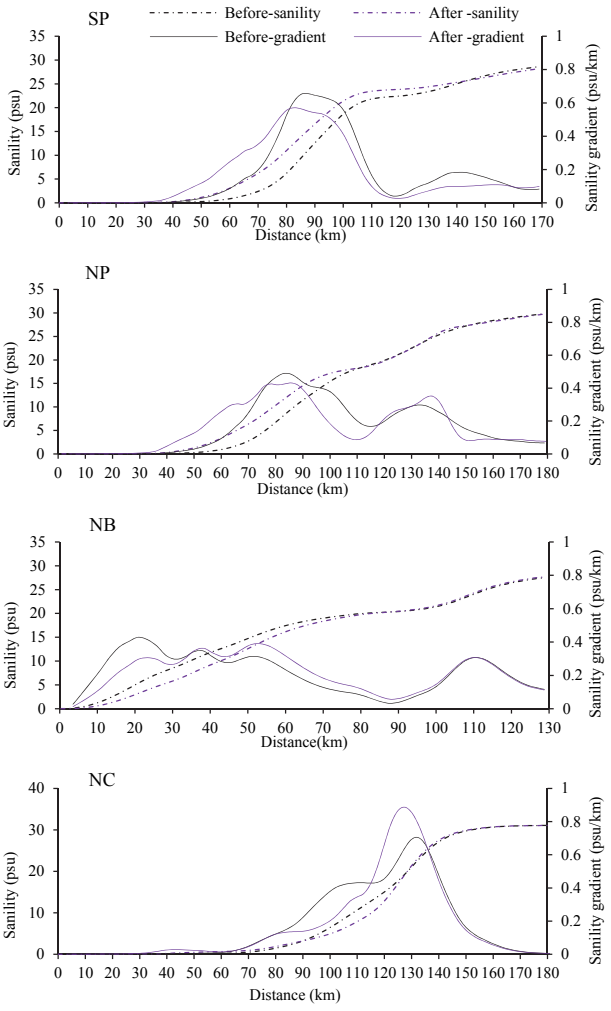

Fig.3 The variation of salinity and salinity gradient along the talweg of the SP, the NP, the NB and the NC before and after three projects.

From Fig.3 and Table 1, as for the first front, under the coupled action of three projects, the front of the SP moves upstream while the fronts of the NP and NB move downstream, moreover, the salinity front intensity of these branches decrease. As for the second front, the three joint projects caused the salinity fronts of the SP and NP move downstream 14km and 4km respectively, while the salinity front of the NC and NB move upstream 5km and 2km respectively. The salinity front intensity of the SP is decreased by 0.07 psu/km, and the intensity of the NP and NC are both strengthened.

Table 1. Position and intensity of salinity fronts before and after three projects

		SP	NP	NC	NB
First front position (km)	Before	87	84	-	20
	After	83	86	-	53
First front intensity (psu/km)	Before	0.66	0.49	-	0.43
	After	0.57	0.43	-	0.39
Second front position (km)	Before	141	134	132	112
	After	155	138	127	110
Second front intensity (psu/km)	Before	0.18	0.30	0.71	0.31
	After	0.11	0.35	0.89	0.31

CONCLUSIONS

In this study, a well-validated hydrodynamic and salinity transport model is used to investigate the influence of the three main projects on the horizontal salinity front in the YRE. When the three project works together, the effect of the coupled action on each branch salinity front is not a linear superposition of the separate action of each project. The salinity front in the NC is akin to a single-front pattern, however, the salinity fronts in the NP, SP and NB almost have a double-front pattern. The three projects can make the first front of the SP move upstream and decrease its intensity, while they make the second front of the NP move toward the sea and strengthen its intensity.

ACKNOWLEDGEMENTS: This study was supported by Innovation Program of Shanghai Municipal Education Commission (2021-01-07-00-07-E00093) and Interdisciplinary Project in Ocean Research of Tongji University (2022- 2-ZD-04).

References

Chen, W., Chen, K., Kuang, C.P., Zhu, D.Z., He, L.L., Mao, X.D., Liang H.D., and Song, H.L. (2016). Influence of sea level rise on saline water intrusion in the Yangtze River Estuary, China. Applied Ocean Research. 54: 12-25.

Fan, Z.Y. (2011). The effect of Deep Waterway project on current and salinity in Changjiang Estuary. Master's Thesis, East China Normal Univ. Shanghai, China.

Kuang, C. P., Chen, W., Gu, J., Su, T.C., Song, H.L., Ma, Y., and Dong, Z.C. (2017). River discharge contribution to sea-level rise in the Yangtze River Estuary, China. Continental Shelf Research. 134: 63-75.

Luan, H.L., Ke, K.T., Ge, J.Z., Chen, L.G., Yang, W.L. and Ding, P.X. (2018). 3D numerical simulation of the impacts of planned estuarine project on saltwater intrusion in the Yangtze River Estuary. Advances in Marine Science. 36(04): 525-539.

Li W.J. and Shen Y.M. (2017). Influence of the North Branch middling narrowing on hydrodynamics and seawater quality in the Yangtze Estuary. Post & Waterway Engineering. 12: 42-50.

Wang, ZH (2018). Numerical simulation of the effects of the reclamation in Hengsha Shoal on hydrodynamic environment. Ph.D. Thesis, Dalian University of Technology. Dalian, Liaoning.

Willmott, C. (1981). On the validation of models. Physical Geography. 2(2):184-194.

Wu YL, Chen K, Kuang CP and Wang J. (2022). Response characteristic of salinity front to Deep-Water Channel and Hengsha East Shoal siltation project in dry season of the Yangtze River Estuary. Chinese Journal of Hydrodynamics. 37(01): 115-124.

SIMULATING THE STORM-SURGE IN THE BAY OF BENGAL

Guangquan Qiao[1], Zhaofei Ren[1], Yabin Sun[1] and Jinfeng Zhang[2]

ABSTRACT: In order to simulate the storm surge in the Bay of Bengal (BoB), the Wind-Wave-Water level coupling model is introduced in this paper. In this study, an Atmosphere-Wave-Hydrodynamic real-time coupled model (WRF + SWAN + FVCOM) is established using the Model Coupling Toolkit (MCT) coupler, and by this coupled model, the storm surge during tropical storms considering the wave radiation stress was calculated. The cyclone path, wave height, wind speed and water level of this coupled model was verified using the typhoon path of JTWC, the wave height and wind data of Jason satellite data and the site-measured water level data of several nearshore stations. Using this model, the storm surge caused by 38 Cyclones affecting the BoB from 1987 to 2018 was calculated, and the distribution of BoB extreme storm-surge of various return years was analyzed according to the calculation results. This paper also discussed the influence of wave radiation stress on storm surge for some severe cyclones. This study can guide the disaster prevention and engineering design of nearshore projects.

Keywords: storm surge, Bay of Bengal, MCT coupler, return years, wave radiation stress

INTRODUCTION

Tropical Cyclone (TC) is one of the disastrous weather systems that often occur on the tropical ocean surface. During its process, it is often accompanied by strong winds, heavy rains, huge waves and storm surges, which seriously threaten the navigation safety of ships at sea and the life and property safety of people in coastal countries, causing huge losses of life and property to the local people. The Bay of Bengal (BoB) is one of the most cyclone-prone areas.

BoB is located in the North Indian Ocean, with a broad continental shelf and a triangular shape in space. Due to the terrain, the water level at the top of the bay is accumulated, and the tidal range is sharply increased. The southwest monsoon prevails in summer, and the tropical cyclones occur frequently, which intensifies the tidal potential. Due to the combined effect of large tidal range and storm surge, BoB has become one of the most severely affected areas by storm surge in the world.

Among the coastal countries in BoB, Bangladesh is particularly affected by TC. Because the coastline of the country is located at the top of the funnel-shaped BoB, and the funnel effect is easy to aggravate the surge caused by the storm [1]. As the terrain of Bangladesh is low, once the storm surge is formed, the inundated area is more likely to go further inland. Moreover, the population density of the country is very high, which increases the disaster and economic impact caused by the storm surge.

The study of storm surge caused by TC in the area reveals their propagation laws and extreme value distribution characteristics, which can provide reference for local disaster prevention and reduction. It can also provide design basis for the design and construction of coastal engineering.

Therefore, it is essential with a broad application prospect to establish a coupled near shore hydrodynamic model, which can fully consider the influence of wind, wave on storm surge, and by using this model to study the law of storm surge in BoB under the consideration of wave radiation stress.

This paper establishes a real-time coupling model of Atmosphere-Wave-Hydrodynamic in BoB based on the Model Coupling Toolkit (MCT) coupler, and verifies the model using the measured data and satellite data. The model is also used to study the effect of wave radiation stress on storm surge and the distribution characteristics of extreme storm surge (with a return period of 50 or 100 years) in BoB.

METHODOLOGY

Model Establish

The Atmosphere-Wave-Hydrodynamic real-time coupling model adopts three sub-models of atmosphere, wave and hydrodynamic. The atmosphere model adopts WRF, the wave adopts SWAN, and the surge adopts FVCOM hydrodynamic model. The three models establish data exchange channels through the MCT

[1] CCCC-FHDI Engineering Co., Ltd., No.292, Lijiao Road, Haizhu District, Guangzhou City, Guangzhou, 510290, CHINA.
[2] Tianjin University, No.135, Yaguan Road, Jinnan District, Tianjin City, Tianjin, 300350, CHINA.

 https://doi.org/10.1142/9789811275449_0036

coupler. The data exchange variables between the three models are shown in Figure 2 [2].

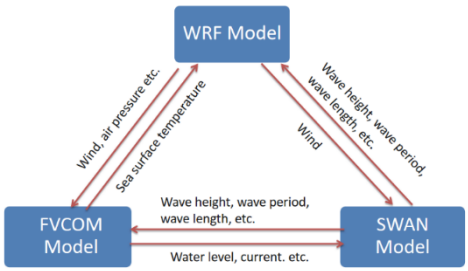

Fig. 2 Exchange variables between the three models

Model Setup

The calculation range covers the north part (≥ 16.8°N) of BoB, in which the focus is on the coastal results north of 21.1°N.

WRF is a structural grid with a space accuracy of 0.1° (about 11.0km), 123 and 62 grids in the longitude and latitude respectively. Fig. 3 shows the calculation scope.

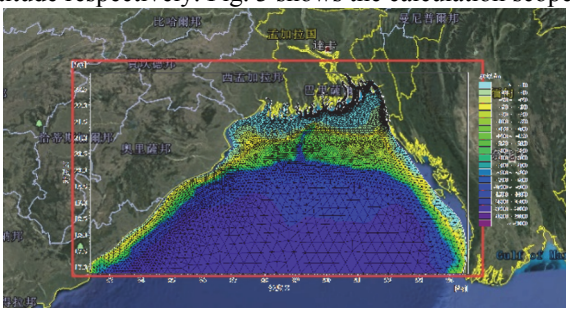

Fig. 3 Model extent and bathymetry

SWAN and FVCOM share the same unstructured grid. The south boundary is 16.8°N, about 650km away from the bay top. The East, North and West boundaries are all land boundaries, with a length of about 1200km in the east-west direction. The offshore boundary grid is 0.1 ~ 0.4°, and the grid along the Bangladesh coast (north of 21.1° N and east of 89.1°E) is within 0.05° (5.5km), and the grid in the key research area is densified to 0.01° ~ 0.002° (1100m ~ 220m). The model has 48772 grids and 27087 nodes. Fig. 3 also shows the unstructured grids.

ETOP1 data is used for deep-water bathymetry, and C-MAP water depth from DHI is used for near shore bathymetry.

WRF model uses the historical reanalysis data from the National Center for Environmental Prediction (NCEP), providing 3D atmospheric initial conditions and time-varying boundary conditions; and the NEAR-GOOS daily average sea surface temperature data provides sea surface temperature data for this model; ADP global surface and upper air observation meteorological data are used to provide 3D variational assimilation data. The deep-water tide level boundary adopts the tide prediction module including 8 basic tidal constituents provided by MIKE21 of DHI, and the runoff boundaries are ignored. The wave in SWAN model is completely driven by wind, and the JONSWAP spectral is used to generate wind waves.

Model Calibration/Validation

The verification data of cyclone path comes from IBTrACS (international best track archive for climate stewardship), wind speed and wave verification are based on seven typhoon waves captured by Jason satellite data from 2004 to 2017, and the measured wind speed data of two cyclone storms in 199102 and 200706 by Paul G C [3]. The water level verification adopts the site observation data of Char Chenga station, Cox's Bazar station, Chittagong station and Hirion point of cyclone 199102 in the existing literature [4].

Figure 4 presents the time series comparison between measured and simulated data, which shows the simulated data fit well with the measured ones.

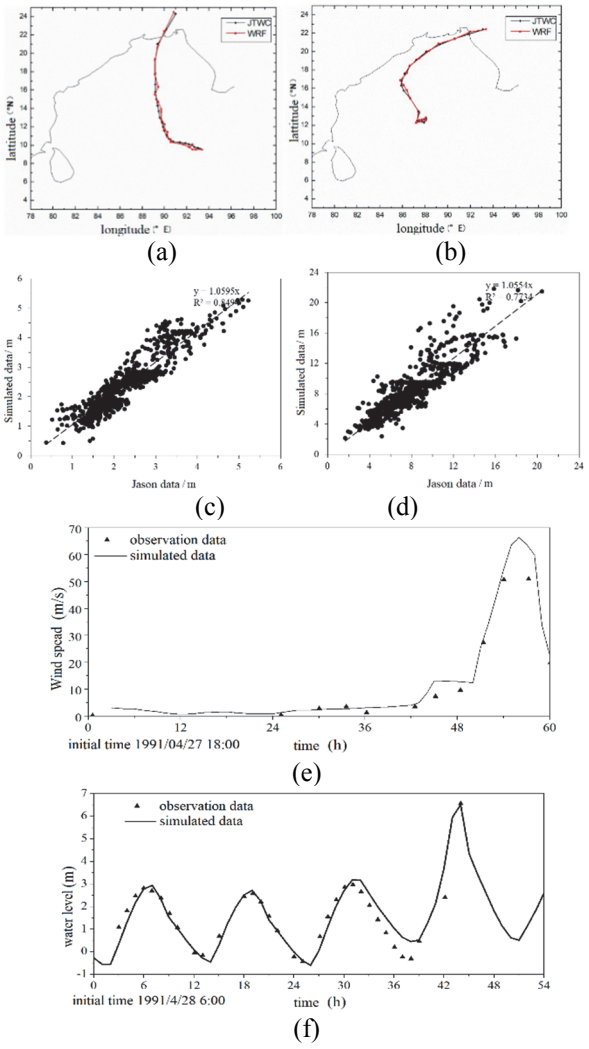

Fig. 4 Simulated vs measured time series (a/b Cyclone paths of 200706 and 200901; c/d Wave and wind speed verified by Jason satellite data; e Wind speed verified by measured data (199101 cyclone Kutubdia station); f Water level verified by measured data (199101 cyclone Chittagong station)).

RESULTS AND DISCUSSION

Influence of wave on storm surge

As an example, the influence of wave on storm surge during Cyclone 199102 is presented in Figure 5. It can be mainly concluded that:

(1) The wave radiation stress on the right side of the cyclone path is stronger than that on the left side due to the large wave height caused by deep water;

(2) The spatial difference of wave radiation stress makes the water flow from the strong radiation stress area to the weak radiation stress area, as a result that the water level on the left side of the path increases.

(3) The shallow water area is more sensitive to the wave radiation stress, and the increased value of storm surge on the left side is higher than that on the right.

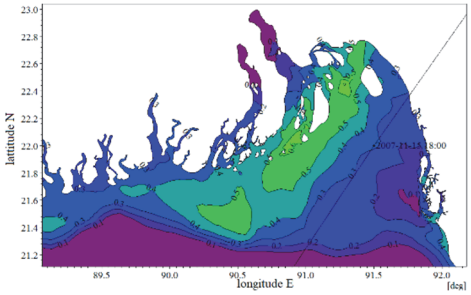

Fig. 5 Effect of wave on maximum storm surge (TC 199102, difference between storm surge with wave and without wave)

Extreme storm surge

Figure 6 summarizes the analyzed extreme storm surge of 100 return years based on the results of 38 cyclones by the above model from 1978 to 2018 via Poisson-Gumbel joint distribution. Table 1 shows the test parameters of Poisson-Gumbel joint distribution and PIII distribution

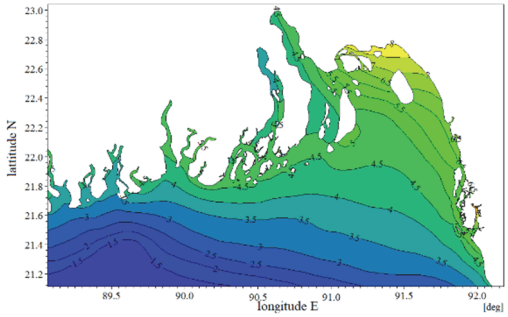

Fig. 6 100 return years storm surge distribution

It can be mainly concluded that:

(1) The results obtained by PIII distribution are significantly larger than the results of composite extreme value distribution. According to the hypothesis test parameters and the comparison with the results of other researchers [6], the extreme storm surge obtained by PIII distribution statistics is more reasonable;

(2) In general, the cyclone affected the east coast of Bangladesh more severely than the west coast.

(3) The extreme surge values with the period of 50-year and 100-year along the top of the Bay of Bengal is above 7.5m and 9.5m, respectively.

Table 1 Test parameters of the distributions

Parameters	Poisson-Gumbel joint distribution		Pearson III distribution	
	With wave	Without wave	With wave	Without wave
K-S test,Ks	0.062~0.074	0.062~0.074	0.03~0.05	0.04~0.06
Stv, Sf^2	0.1~1.5	0.1~1.5	0.1~1.7	0.1~1.8

CONCLUSIONS

The MCT model can well simulate the storm surge in BoB as the computed results are verified by cyclone path data, wave height, wind speed and water level data.

The wave impacts the storm surge by residual momentum flow due to wave radiation stress difference on the left and right sides of the path. This effect is more obvious in shallow water than in deep water.

The probability analysis of extreme storm surge shows that PIII distribution is better for extreme surge analysis as the test parameters shows that PIII has lower deviation. The cyclone affected the east coast of Bengal more severely than the west coast with higher storm surge.

References

Assalek J A. Coastal Trapping and Funneling Effects on Storm Surges in the Meghna Estuary in Relation to Cyclones Hitting Noakhali Cox's Bazar Coast of Bangladesh[J]. Journal of Physical Oceanography, 2010, 28(28):227-249.

Liu B, Liu H, Xie L, et al. A coupled atmosphere-wave-ocean modeling system: Simulation of the intensity of an idealized tropical cyclone[J]. Monthly Weather Review, 2011, 139(1): 132-152.

Institute of Water Modelling, Water Environment and Climate, Techno-economical Feasibility Study for Development of The Land at Moheshkhali Island by Dredging Chars, Shoals for Land Based L.N.G. Terminal[R]. January, 2017.

Paul G C, Ismail A I M. Contribution of offshore islands in the prediction of water levels due to tide–surge interaction for the coastal region of Bangladesh[J]. Natural Hazards, 2013, 65(1):13-25.

Volvaiker S, Ponnumony V, Charls A, et al. Wave–current interaction during Hudhud cyclone in the Bay of Bengal[J]. Natural Hazards and Earth System Sciences, 2017, 17(12):2059-2074.

DEVELOPING A HIGH RESOLUTION NON-HYDROSTATIC OCEAN CIRCULATION MODELLING SYSTEM: A CASE STUDY FOR VIZAG

Shailee Patel[1], Bhasha Vachharajani[2], Neeraj Agarwal[3] and Rashmi Sharma[3]

ABSTRACT: Fine scale eddies and circulation features in the ocean govern many small and large-scale processes, which get modulated due to small-scale horizontal variations in density. Some of these phenomena are responsible for nutrient upwelling, while some have implications on acoustic propagation. Three-dimensional observations at such a fine scale (~ < 1 km) are hard to obtain in continuity from in-situ or satellite measurements. Numerical models of the ocean provide an opportunity to simulate the small-scale features of the oceanic circulation. In this study, we present a very high-resolution model for the ocean surrounding Vishakhapatnam (Vizag) region at the East Coast of India. The objective is to test and evaluate the configuration that has been prepared for this domain and then to nest/couple it within a larger/coarser domain model. We have made use of the Massachusetts Institute of Technology general circulation model (MITgcm) for this study. Open boundary conditions are prescribed from a regional ocean model for the Indian Ocean (IO) Region. The model is forced with ERA-interim winds and fluxes for a period of around 40 days. Ocean surface currents simulated from the model are compared with the Nucleus for European Modelling of the Ocean (NEMO) observations as well as from the outputs of the larger domain IO model

Keywords: MITgcm, Vizag, Circulation

MITgcm Configuration and Methodology

The model is configured along the east coast of India extending from 81.70°E - 84.70°E in longitude and 17°N - 19°N in latitude bearing 720x480x66 grid points in x, y and z axis respectively with a horizontal resolution of 400m x 400m shown in Figure 1with blue box.

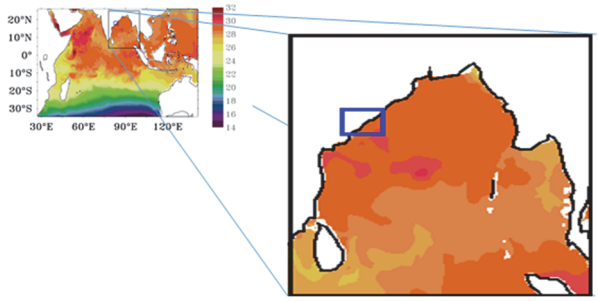

Figure 1: IO model domain with nested domain Bay of Bengal (black box) and Vizag (blue box) overlaid temperature field.

The model uses a very high-resolution bathymetry from GeBCO which is essential for accurate representation of the bottom bathymetry. Domain open boundaries are integrated by prescribing the temperature, salinity and velocities from IO model simulations on the open boundaries (eastern and southern). The IO model was configured from 30°S - 30°N and 28°E - 115°E with a horizontal resolution of 10km x 10km as shown in Fig.1. The model is initialized from 7th Jan 2018 using temperature, salinity and velocity values interpolated from the regional ocean model and is integrated forward in time using atmospheric forcing from the ECMWF Re-Analysis (ERA-intrim). First 15 days are considered as required spin-up time (Mohanty et. al. 2017). Thus the simulation period from 21st Jan 2018 to 15th Feb 2018 is used for comparison.

Result and Discussion

Initially the IO model validation is performed by using available satellite and in-situ data for 2018. Statistical analysis suggest that the model simulation is good enough for the use of nesting smaller domain boundary conditions.

Further, the domain averaged zonal and meridional velocities from the Vizag model are compared with with same configuration of low resolution (10km) IO simulations and NEMO ocean model (Fig.2). Results suggest that there are positive biases in the zonal velocity of the IO model and NEMO. This influence can be seen in the initial few days of the high resolution model simulations which are basically initialized by the IO model (Fig.2a). However, with longer integration, the high resolution model simulations of zonal velocity fields converge to the NEMO analysis. In contrast, the meridional velocity fields have biases maintained until the end of the simulations (Fig.2b). One of the reason behind

[1] Senior Research Fellow, Pandit Deendayal Energy University, Ghandhinagar, 382007, INDIA
[2] Department of Mathematics, Pandit Deendayal Energy University, Ghandhinagar, 382007, INDIA
[3] Space Application Center, Indian Space Research Organization, Ahmedabad, 380015, INDIA

 https://doi.org/10.1142/9789811275449_0037

these biases is different initial condition for Vizag and IO model. This aspect needs to be investigated.

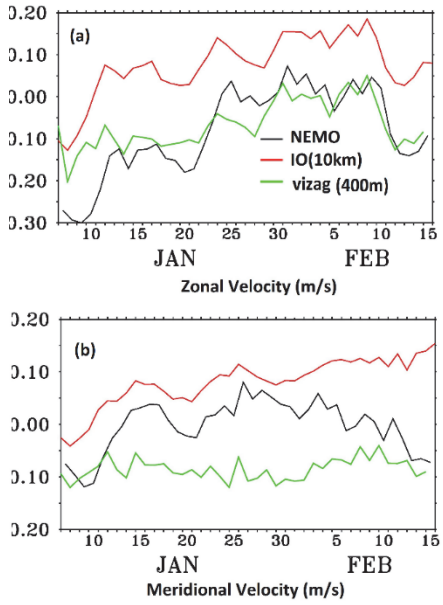

Figure 2: Vizag domain averaged (a) zonal and (b) meridional velocities compared with IO simulations and NEMO model.

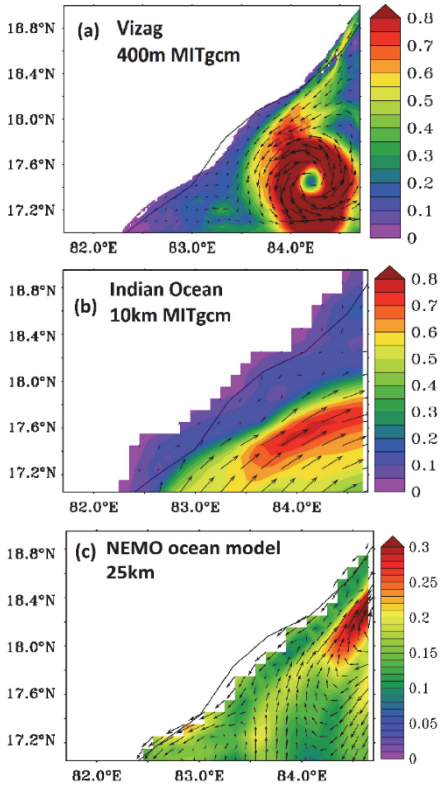

Figure 3: Temporal average picture of (a) Vizag (b) IO (c) NEMO current speed (m/s) overlaid with direction during study period (21st Jan 2018 to 15th Feb 2018)

Temporally averaged surface current speed overlaid with vector after considering short spin up of 15 days from high-resolution model, IO model and NEMO model are shown in Fig.3. It can be seen that the high resolution model shows a strong cyclonic eddy which is neither seen in the IO model (from which the high resolution model is initialized) nor in the NEMO analysis. This needs to be ascertained whether the eddy generated is a real one, which is not captured in the coarser model or is it created due to instabilities in the high resolution model.

Conclusion and Future Scope

We reported here very preliminary results from a high resolution region specific model initialized and forced at the boundaries from the outputs of a coarse resolution IO model. Simulated velocity fields are compared with the state of art available analysis and there is a large mismatch in the meridional flow. Spatial current structure shows he presence of a very strong cyclonic eddy feature in the high resolution model simulations, which are absent in the IO model and NEMO analysis. These discrepancies need a relook at the model configuration and proper tuning of model parameters. More careful experiments, may be with higher resolution (2km x 2km) Bay of Bengal configuration (Ratheesh et.al 2020) initial and boundary conditions can be planned. Longer simulations and validation with satellite and insitu observations will also be carried out in future. Further, tidal boundary conditions will be incorporated at high resolution with non-hydrostatic configuration. The long term objective of this exercise is to develop a satellite data assimilative high resolution nested modelling framework for the Indian Ocean.

ACKNOWLEDGEMENTS

The Authors would like to thank the Space Application Center's High Performance Computing facility for computational resources for carrying the model simulations.

References

Sachiko Mohanty, A.D. Rao and Himanshu K. Pradhan (2017). Estimates of internal tide energetics in the western Bay of Bengal. IEEE Journal of Oceanic Engineering, 43(4):1015-1023

Smitha Ratheesh, Neeraj Agarwal, Aditya Chaudhary, J.Lijin, J.sreelekha, Manikandan Mathur, Rashmi Sharma, Raj Kumar (2020). Response of high-resolution ocean circulation model to winds from different sources in simulating summer monsoon freshening in the North Bay of Bengal: A case study. Deep Sea Research Part-II: Topical Studies in Oceanography, 172(8):104727.

TIDE INDUCED MIXING AND AIR-SEA FLUXES IN THE BAY OF BENGAL

Bijan Kumar Das[1] and Arun Chakraborty[2]

ABSTRACT: The upper ocean mixing in the Bay of Bengal (BoB) gets substantial influence from the local winds, huge fresh water influx and tidal forcing that makes the mixing more complex and dynamic. This study aims to understand the role of tidal forcing on upper ocean mixing in the BoB and how this mixing process changes in presence of river fresh water. Moreover, it is also seen that how this tidal forcing modulates the air-sea interactions in the region. The analysis includes three high resolution (1/12°) Regional Ocean Modelling System (ROMS) simulations, a control run, a tide run and a river-tide run. In the tide forcing simulations, the tidal components included are M2, S2, N2, K2, K1, O1, P1, Q1, Mf and Mm. Again, the river-tide simulation additionally has the discharge from the major rivers (Ganges, Brahmaputra, Irrawaddy, Godavari, Krishna, Mahanadi and Subarnarekha) in the region. The analyses show that the tidal buoyancy deepens the mixed layer increasing the integrated upper ocean temperature, while the surface temperature reduces. The upper ocean temperature profile further reduces in the tidal vertical mixing process in presence of river fresh water. The tidal mixing increases the surface salinity, whereas the addition of low saline river discharge largely reduces the surface and subsurface salinity. The warmer upper ocean layers in the tidal forcing simulation radiates more surface longwave, sensible and latent surface heat fluxes over the region. Therefore, the study shows that the tidal forcing has major influence in the upper ocean mixing as well as the air-sea fluxes over the BoB.

Keywords: Mixing, Air-Sea fluxes, Tidal forcing, River fresh water, Bay of Bengal, ROMS.

INTRODUCTION

The Bay of Bengal (BoB) is the northeastern part of the Indian Ocean and contributes substantially to the South-East Asian monsoon, tropical cyclogenesis and regional livelihood. The BoB exhibits a complex upper ocean dynamics and air-sea interactions owing to the seasonally reversing monsoon winds, fresh water influx, tidal forcing and equatorial remote influence. Earlier studies have mentioned that the assessment of upper ocean mixing and air-sea exchanges in the BoB still remains challenging (Mahadevan et al. 2016). Again, the increase in accumulated heat energy in the BoB impacts the air-sea interactions as well as the upper ocean dynamics (Anandh et al. 2018). Further, the climate change induced inhomogeneity in the sub-continental monsoon is also reported by Nair et al. (2018). Therefore, the assessment, understanding and prediction of the BoB mixing and its interaction with the atmosphere are of great interest.

The tidal forcing contributes huge energy for ocean mixing and modulates the whole upper ocean processes. Earlier studies with the assessment of tidal contributions over the BoB are mostly limited to the circulations (Bhagawati et al. 2018; Das et al. 2020). So, this study focuses on the tide induced upper ocean mixing and the air-sea exchanges in the BoB. Moreover, the study also discusses the changes in tidal contribution over the region in presence of fresh water influx.

DATA AND METHOD

The study uses three Regional Ocean Modelling System (ROMS) simulations (1/12°), a climatological control simulation (Clim) and two sensitivity experiments with tides (Tide) and with river-tide (RiTd). The model configurations and the validations of the simulated outcomes can be found at Das et al. (2020).

The tidal forcing in the simulation (Tide, RiTd) includes ten tidal components M2, S2, N2, K2, K1, O1, P1, Q1, Mf and Mm. Whereas the river influx simulation (RiTd) has the seven major (in terms of discharge amount) rivers in the BoB basin and are Ganges, Brahmaputra, Irrawaddy, Godavari, Krishna, Mahanadi and Subarnarekha.

RESULTS AND DISCUSSIONS

Temperature and salinity

The Sea Surface Temperature (SST) shows mostly the similar values till May in all the simulations (Fig. 1a). Whereas from June onwards, the tidal simulations reduce the average SST up to .25°C. Presence of river fresh water helped in reducing the SST. The depth integrated temperature shows the maximum value in

[1] Department of Mathematics, Midnapore College (Autonomous), Midnapore-721101, INDIA
[2] Centre for Oceans, Rivers, Atmosphere and Land Sciences, Indian Institute of Technology Kharagpur, Kharagpur-721301, INDIA

 https://doi.org/10.1142/9789811275449_0038

standalone tidal simulation and minimum value in the control run (Fig. 1b). Clearly, tidal forcing increases the upper ocean temperature (up to .5°C), which is reduced in presence of fresh water influx.

Standalone tidal forcing increases the Sea surface Salinity (SSS) compared to the control run as seen in Fig. 1c. The SSS in RiTd is much less (up to 1.5 psu) here due to the low saline river discharge. In case of depth integrated salinity, the overall values are increased in all three simulations and showed similar like surface pattern (Fig. 1d).

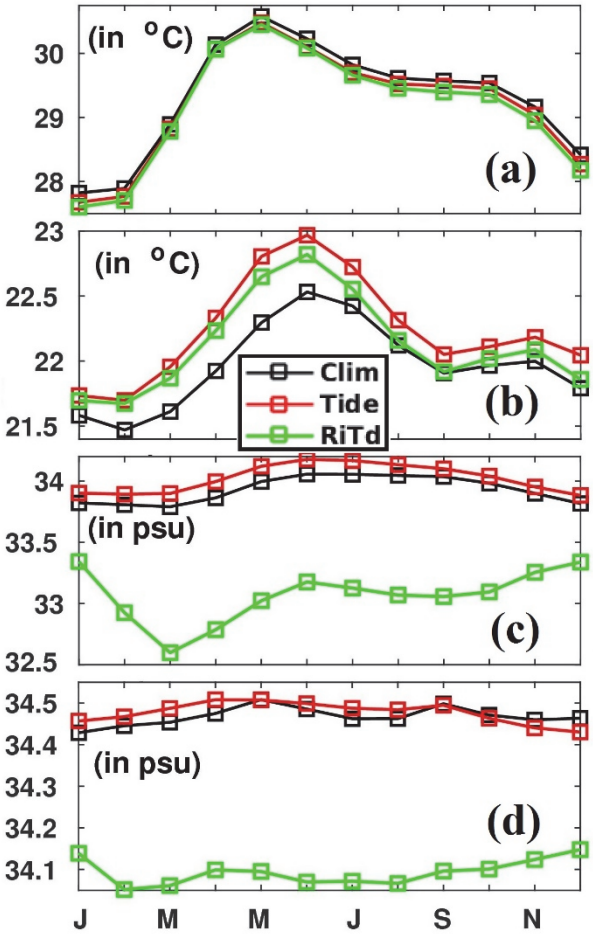

Fig. 1. Simulated SST (a), depth integrated temperature (b), SSS (c) and depth integrated salinity (d) from control (Clim in black), tide forcing (Tide in red) and combined river-tide forcing (RiTd in green) simulations.

Mixed Layer Depth (MLD)

The seasonal changes in MLD are seen from all the simulations in Fig. 2. It is found that the tidal vertical mixing has deepened (5 to10 m) the MLD compared to the control simulation (Fig. 2a-b). But the fresh water significantly contributes in the combined forcing for shallowing (10 to 15 m) the MLD (Fig. 2c). The maximum discharge in monsoon (June-September) makes the MLD shallowest in the BoB during ISM.

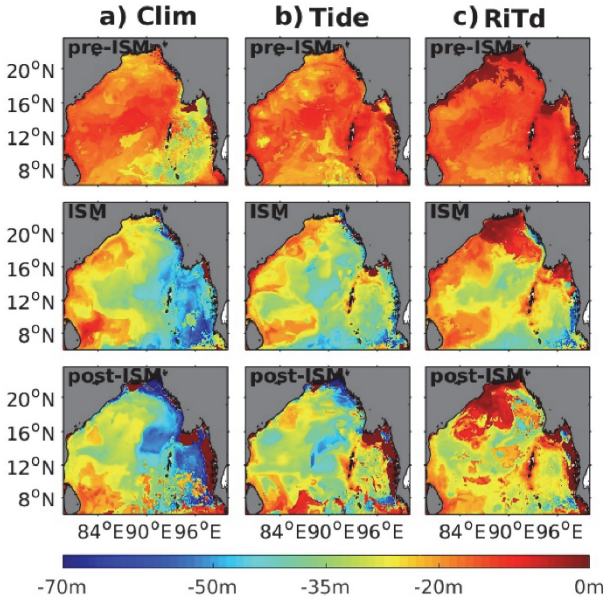

Fig. 2. The seasonal (pre-Indian Summer Monsoon (ISM), ISM and post-ISM) MLD from a) control, b) tide forcing and c) river-tide forcing simulations.

Upper Ocean Heat Content (UOHC)

The warm upper layer in the standalone tide forcing simulation (as seen in Fig. 1b) makes the UOHC (300 m) comparatively high (Fig. 3b). In contrast, the addition of river discharge with the tide forcing simulation reduces the heat content (Fig. 3c). But the UOHC in the combined forcing simulation remains high than the control run (Fig. 3a). The monthly time series of the net UOHC also shows the similar pattern as of the spatial distributions throughout the year (Fig. 3d). The net heat content is maximum during the ISM in all simulations.

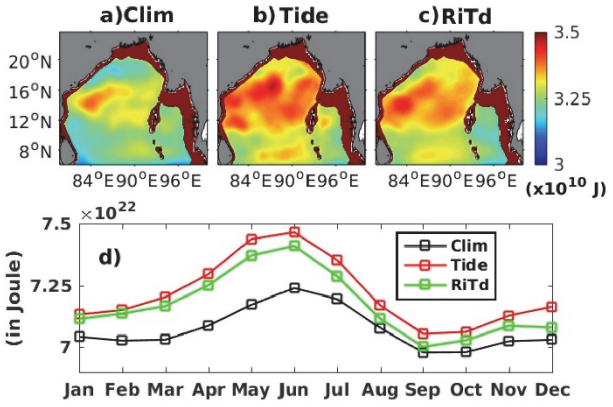

Fig. 3. The UOHC (300 m) in a) control, b) tide forcing and c) river-tide forcing simulations. The monthly time series of net UOHC is shown in (d).

Air-Sea fluxes

The components of the net heat flux are analysed and given in Fig. 4. The incoming short wave remained same in all simulations. The outgoing long wave radiation, sensible and latent heat fluxes are shown in Fig. 4a-c, respectively.

The long wave radiation has increased in both the sensitivity experiments without having any changes due to the river discharge in the combined forcing (Fig. 4a). The tide forcing has increased the sensible heat flux reasonably and the maximum increment is noticed during ISM (Fig 4b). Fresh water inclusion has increased the release of sensible heat flux. The latent heat flux is also increased in both the sensitivity simulations (Fig. 4c). Both the tide and river-tide forcing simulations are showing almost similar values for the latent heat flux.

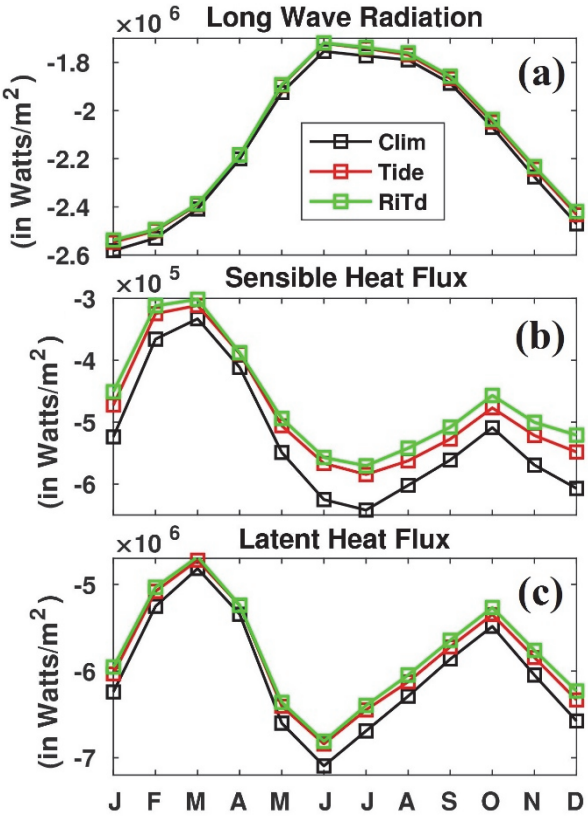

Fig. 4. Monthly average a) long wave radiation, b) sensible heat flux and c) latent heat flux is shown from control (black), tide forcing (red) and combined river-tide forcing (green) simulation. The heat released are upward for all these heat flux components.

CONCLUSIONS

The study examines the tide induced mixing and air-sea fluxes in the BoB by using ROMS simulations. The analysis shows that the tidal vertical mixing reduces the SST while increases the upper ocean temperature. The river discharge helps to reduce the SST as well as depth integrated temperature when added with the tidal forcing. Although the SSS is increased slightly by the tidal forcing, river discharge remains dominant in determining the surface and depth integrated salinity. The MLD is deepened in the standalone tide forcing simulation compared to the control run, but further becomes shallower in presence of river influx. The warm upper layers in the tide forcing simulation make the UOHC relatively high followed by the combined river-tide forcing and control simulation. The high UOHC stimulates the upward heat fluxes in the bay. The long wave radiation, sensible and latent heat fluxes are increased in the standalone and combined river-tide forcing simulations. The combined forcing simulation shows the maximum release of sensible heat fluxes. Overall, the study shows significant impact of tidal forcing in the mixing and air-sea fluxes in the BoB. Further, it is also noticed that the inclusion of river discharge also modulates the tidal influences.

References

Anandh, TS., Das, B. K., Kumar, B., Kuttippurath, J., and Chakraborty, A. (2018). Analyses of the oceanic heat content during 1980–2014 and satellite-era cyclones over Bay of Bengal. Int. J. Climatolo., 38(15), 5619-5632. https://doi.org/10.1002/joc.5767

Bhagawati, C., Pandey, S., Dandapat, S., and Chakraborty, A. (2018). Dynamical significance of tides over the Bay of Bengal. Dyn. Atmospheres Oceans, 82, 89-106. https://doi.org/10.1016/j.dynatmoce.2018.05.002

Das, B. K., Anandh, T. S., Kuttippurath, J., and Chakraborty, A. (2020). Influence of river discharge and tides on the summertime discontinuity of Western Boundary Current in the Bay of Bengal. J. Phys. Oceanogr., 50(12), 3513-3528. https://doi.org/10.1175/JPO-D-20-0133.1

Mahadevan, A., Paluszkiewicz, T., Ravichandran, M., Sengupta, D., and Tandon, A. (2016). Introduction to the special issue on the Bay of Bengal: From monsoons to mixing. Oceanography, 29(2), 14-17. http://dx.doi.org/10.5670/oceanog.2016.34

Nair, P. J., A. Chakraborty, H. Varikoden, P. A. Francis, and J. Kuttippurath, 2018: The local and global climate forcings induced inhomogeneity of Indian rainfall. Sci. Rep., 8, 6026, https://doi.org/10.1038/s41598-018-24021-x

A HYBRID ML-PHYSICAL MODELLING APPROACH FOR EFFICIENT PROBABILISTIC TSUNAMI HAZARD AND RISK ASSESSMENT

Naveen Ragu Ramalingam[1], Anirudh Rao[2], Kendra Johnson[2], Marco Pagani[2,3] and Mario Martina[1]

ABSTRACT: Probabilistic tsunami hazard and risk assessment (PTHA/PTRA) are vital tools for understanding tsunami risk and planning measures to mitigate impacts. At large-scales their use and scope are currently limited by the computational costs of numerically intensive simulations which are not always feasible without large computational resources like HPCs and may require reductions in resolution, number of scenarios modelled or use of simpler approximation schemes. To conduct the PTHA/PTRA for large proportions of a coast, we need therefore to develop concepts and algorithms for reducing the number of events simulated and more rapidly approximating the needed simulation results. This case study for a coastal region of Tohoku, Japan utilizes a limited number of tsunami simulations from submarine earthquakes along the subduction interface to generate a wave propagation and inundation database at different depths and fits these simulation results to a machine learning (ML) based variational autoencoder model to predict the intensity measure (water depth, velocity, etc.) of the tsunami at the location of interest. Such a hybrid ML-physical model can be further extended to compute the inundation for probabilistic tsunami hazard and risk onshore.

Keywords: Tsunami hazard, machine learning, autoencoders

INTRODUCTION

The computational demands of probabilistic tsunami modelling currently limit their widespread application for onshore tsunami hazard and risk assessment. The ability of autoencoders in dimensional reduction, feature representation and transformation can be exploited for approximating the non-linear processes in the shallow water regions nearshore and the inundation processes onshore. In this contribution we describe how a variational autoencoder (VAE) type neural network model is trained on the simulated time series of tsunami amplitudes at points of different depths offshore and the inundation maps onshore for a location along the coastal Tohoku region in Japan. Further, the model is tested against the simulation of different realistic historical events to evaluate the efficacy and requirements of this novel approach.

GENERATION OF SYNTHETIC DATA

Tsunami Model and Test Locations

For the simulation of the synthetic events, their wave amplitude time series and onshore flood footprint, a tsunami model based on GeoClaw Version 5.7.1, (Clawpack Development Team, 2020) was developed. The model covers the Pacific Side of the Honshu Island with a nested domain approach of 1350 m-850 m-100 m grids as in Figure 1. Model development and calibration are based on local information related to topo-bathymetry, tsunami defences, 2011 Tohoku historical event's gauge and survey data.

The virtual gauges are setup at different depths of 5m, 25m, 50m and 100m as shown in Figure 2. Each simulation is run for a 6-hour duration from onset of the tsunami. Tides and waves components are ignored and the initial water level condition is zero mean sea level.

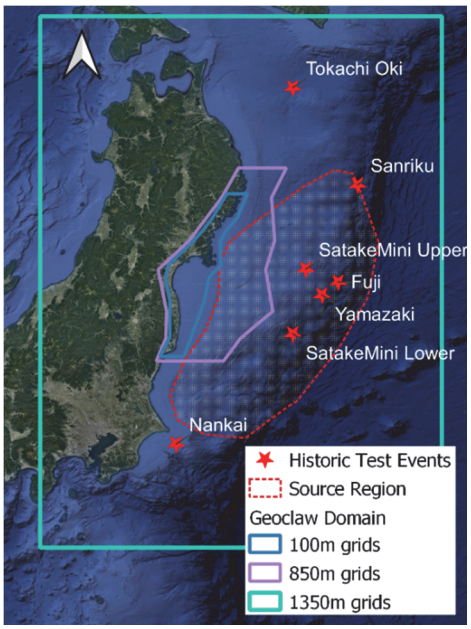

Fig. 1 Tsunami model coverage, location of source region and historical test events

[1] University School for Advanced Studies Pavia, Piazza della Vittoria 15, 27100 Pavia, ITALY (naveen.raguramalingam@iusspavia.it)
[2] GEM Foundation, Via Ferrata 1, 27100, Pavia, ITALY
[3] Institute of Catastrophe Risk Management, Nanyang Technological University, SINGAPORE

 https://doi.org/10.1142/9789811275449_0039

Three locations with different coastal configuration are identified for the case study – Rikuzentakata (enclosed bay), Ishinomaki (shielded) and Sendai (open bay) – where different coastal processes (like shoaling, refraction, reflection, and resonance) are expected to impact the tsunami nearshore results. Due to the limited scope of this article only the results related to Rikuzentakata, with offshore gauge 5832 and nearshore gauge 6042 are discussed.

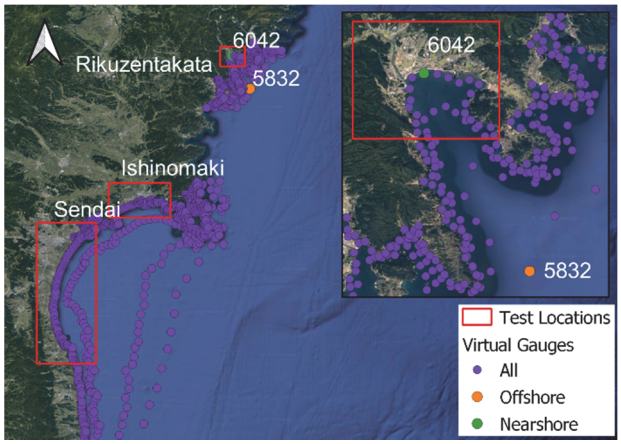

Fig. 2 Virtual gauges and the test locations in Japan (Rikuzentakata in the inset)

Design of Experiments

To train the VAE neural network model, 383 hypothetical tsunamigenic earthquake events are simulated, with M_w 7.5-9.0 and uniformly distributed over the Tohoku subduction interface earthquake source.

Information on depth, slip, strike and dip (see Table 1) are taken from the Slab2 model of the Japan trench (Hayes et al., 2018), and rake is always 90 degrees. The rupture planes are constrained to depths shallower than 16 km for M_w 9.0 events, assumed to be the lower seismogenic limit of the subduction interface. The deformation is modelled assuming homogenous slip for the rupture using Okada solution (Okada 1985) with the value of rupture length, width and slip scaled based on the magnitude of the event (Strasser et al. 2010).

Table 1 EQ event parameters

Range	Mw	Lat	Long	Depth	Dip	Strike
Min	7.5	35.73	141.15	10.2	5.54	187.20
Max	9	39.48	143.90	45.7	17	225.78

Test Events

To evaluate the performance of the VAE model on a generalized dataset, eight heterogenous slip and one homogenous slip events are used for testing:

1. 2011 Tohoku EQ – (Fujii et al. 2011), (Yamazaki et al. 2018), and four variations of (Satake et al. 2013) by varying the sub-fault location and slip distribution.
2. Events outside the Tohoku source region – 1968 Tokachi-Oki EQ (Nagai et al. 2001), 1896 Sanriku EQ (Satake et al. 2017) and a synthetic homogenous slip rupture event outside the training source region (Nankai 2022).

METHODS

Data Preprocessing

For a given gauge location and tsunami event, the wave amplitude time series is checked for a threshold (0.1 m at deep gauges, 0.5 m at shallow gauges). From the time instance when threshold is crossed, an observation window of 240 mins is selected for calculating a uniformly sampled wave amplitude time series with 1024 data points. For the inundation footprint, all flooded grid points from the overall simulation set for the region are selected and converted into a single 1D array. For each event, the 1D array element values represent the depth at these grid points. This wave propagation and inundation dataset in the learning framework is divided into 80:20 split of training and test events.

Variational Autoencoder Model (VAE)

This work extends an already existing ML approach (Liu et al. 2021) used for tsunami forecasting. Our objective is to approximate the tsunami wave amplitudes and event inundation footprints. The VAE model implementation from (Liu et al. 2021) was taken as the base model and further adapted and calibrated to this use case (refer to Figure 3 and Table 2). The current framework tries to limit the need for a large number of simulations and prescribes some additional steps to ease and improve the training of the model, like pretraining, curriculum learning, and moving mask learning which will be tested in future work.

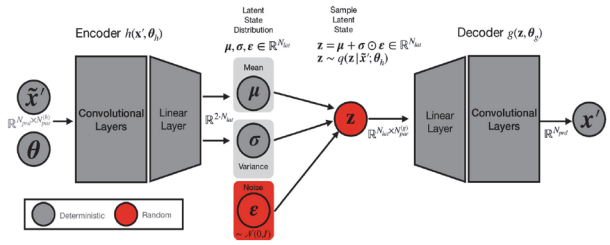

Fig. 3 Schematic of a Variational Autoencoder (Liu et al. 2021)

Table 2 CNN channel parameters of the VAE Model

	Layers	1	2	3	4	5
Encoder	In	Inputs	64	64	128	128
Network	Out	64	64	128	128	256
Decoder	In	256	128	128	64	64
Network	Out	128	128	64	64	Outputs

The main changes to the learning framework and design of VAE by Liu et al 2021 are:

1. Observation window - 240 mins.
2. Number of CNN layers - 5.
3. Number of z-latent variables - 50.

RESULTS AND DISCUSSION

For the test events, maximum amplitude and the timing of local peaks is well captured by the model, as shown in Figure 5 for the test event (#123) and Tohoku event (Yamazaki et al. 2018) at the test nearshore gauge (6042). Further, the model is able to extrapolate beyond the training information, predicting water levels higher than those in the training events, as shown in the results for the full Tohoku test event set in Figure 4.

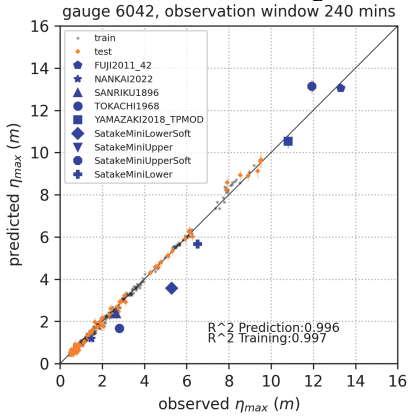

Fig. 4 Scatter plot of the observed vs predicated tsunami max amplitude at the nearshore gauge (6042)

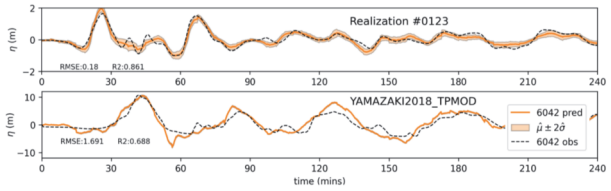

Fig. 5 Time series realization of a test event (#123) and historic Tohoku event (Yamazaki et al. 2018)

Figure 6 shows results for inundation prediction at Rikuzentakata for a low and high inundation test event. There is a minor depth error of 0.1-0.2 m reported by the model at grid cells not inundated, locations seen in the absolute error maps.

While the nearshore approximation approach is useful as hazard proxy at the coast, its application is currently limited by the need to train the model for each location and calibrate the VAE model architecture, hindering the application at a large scale, but the possibility to predict the inundation maps provides a more transferrable scheme for a larger region.

Such an approach can help extend offshore tsunami hazard information available at deep offshore points to much needed onshore hazard and risk, with a relatively limited number of simulations and associated computational costs.

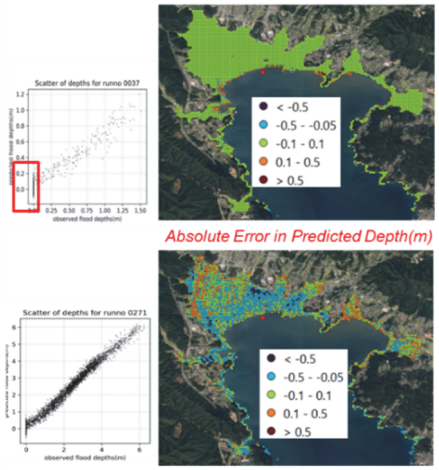

Fig. 6 Scatter plot of the observed vs predicated tsunami inundation depths of a low (#37) and high (#271) magnitude event and the absolute error map for the floodable grid locations.

References

Clawpack Development Team (2020),Clawpack v5.7.1, http://www.clawpack.org,doi:10.5281/zenodo.4025432

Fujii, Y., K. Satake, S. Sakai,M. Shinohara, and T. Kanazawa (2011) Tsunami source of the 2011 off the Pacific coast of Tohoku EQ, Earth Planets Space, 63, 815–820.

Liu, C. M., Rim, D., Baraldi, R., & LeVeque, R. J. (2021). Comparison of machine learning approaches for tsunami forecasting from sparse observations. Pure and Applied Geophysics, 178(12), 5129-5153.

Nagai, R., M. Kikuchi, and Y. Yamanaka. 2001. Comparative Study on the Source Processes of Reccurent Large Earthquakes in Sariku-oki Region: 1968 Tokachi-oki Earthquake and 1994 Sanriku-oki Earthquake. (Journal of the Seism. Society of Japan) 54:267-280.

Okada, Y. (1985). Surface deformation due to shear and tensile faults in a half-space. Bulletin of the seismological society of America, 75(4), 1135-1154.

Satake, K., Fujii, Y., & Yamaki, S. (2017). Different depths of near-trench slips of the 1896 Sanriku and 2011 Tohoku Earthquakes. Geoscience Letters, 4(1), 1-10.

Satake, K., Fujii, Y., Harada, T. and Namegaya Y. (2013),Time and Space Distribution of Coseismic Slip of the 2011 Tohoku EQ as Inferred from Tsunami Waveform Data, Bulletin of the seismological society of America, 103(2B) 1473–1492.

Strasser, F. O., Arango, M. C., & Bommer, J. J. (2010). Scaling of the source dimensions of interface and intraslab subduction-zone earthquakes with moment magnitude. Seismol Research Letters, 81(6), 941-950.

Hayes, G., 2018, Slab2 - A Comprehensive Subduction Zone Geometry Model: U.S. Geological Survey data release.

Yamazaki, Y., Cheung, K. F., & Lay, T. (2018). A self-consistent fault slip model for the 2011 Tohoku earthquake and tsunami. Journal of Geophysical Research: Solid Earth, 123(2), 1435-1458.

GENOMIC ANALYSIS OF COASTAL SEDIMENT ISOLATES FOR IDENTIFYING AMR GENE TRANSFER FROM TERRESTRIAL TO MARINE BACTERIAL SPECIES

F. W. Wong[1], K. M. Leung[1] G. K. K. Lai[1], S. D. J. Griffin[1], D. L. Ibarra[1*]

ABSTRACT: Non-point source microbial pollution damages the overall health of marine ecosystems. Beyond their direct effects, contaminating microbes can introduce antimicrobial resistance and virulence genes into resident species by horizontal gene transfer, a process that may be enhanced by co-pollutants such as heavy metals. In this work, a number of heavy metal- and antimicrobial-resistant (AMR) strains of *E. coli* were isolated from water and sediment samples collected in the Causeway Bay, Hong Kong (22.2833 N, 114.1847 E) and their complete genomes obtained by hybrid assembly using both Illumina MiSeq and Oxford Nanopore MinION sequencing platforms. Genomic analysis showed an abundance of plasmids and mobile elements bearing heavy metal- and AMR genes, such as the *mer* operon and *tetR-tetA* efflux system, with these features frequently co-located. In addition, NCBIBLAST–using isolates collected from in-land soil, freshwater, and animal faeces in Hong Kong, as well as the NCBI database – showed that these genes, while common amongst human and animal-derived *Enterobacteriaceae*, could also be shown present in a number of strains of obligate halophilic *Vibrio* spp.. Previous water chemistry analysis at this location showed high levels of heavy metal contamination (98 ppm Pb, 0.12 ppm Hg, and 0.4 ppm Cd), which has been shown to promote AMR transfer by selecting for co- resistance. Further isolation and characterisation of marine bacterial species from Hong Kong coastal waters will help to determine the extent of this process.

Keywords: antimicrobial resistance, heavy metal resistance, horizontal gene transfer, *E. coli*, *Vibrio*

INTRODUCTION

Escherichia coli is a Gram-negative, non-sporulating, facultative anaerobe found in the intestines and faeces of mammals, birds and reptiles. Although strictly anaerobic bacteria dominate the human gut microbiome, the ability of *E. coli* to survive under aerobic conditions means that it is often used as an indicator of faecal pollution of water (Tenaillon et al. 2010).

While Hong Kong's Water Pollution Control Ordinance Cap. 358 aims to regulate sewage contamination, overflow and run-off after seasonal heavy rainfall leads to some very high peak *E. coli* levels in inland and coastal waters. And while *E. coli* does not proliferate in seawater, adaptive responses have been shown to allow virulent and multi-drug resistant strains to persist (Alves et al. 2014; Lothigius et al. 2010).

In addition to biological waste, many coastal areas of South China suffer from serious heavy metal contamination, with Hong Kong recording especially high levels of Cu, Zn, Cd and Hg (Wang et al. 2013). In bacteria, heavy metals have been shown to co-select for antimicrobial resistance (AMR) because they may induce similar mechanisms of resistance such as efflux pumps (Seiler and Berendonk 2012). Hence, heavy metal pollution may exacerbate a biological hazard.

In a previous survey, sediment recovered from the Typhoon Shelter in Causeway Bay, Hong Kong, was found to show high levels of heavy metal contamination (98 ppm Pb, 0.12 ppm Hg, and 0.4 ppm Cd) (Au Yeung 2019). Hence, this study has revisited the site to examine any microbiological impact by using whole genome sequencing of recovered bacterial isolates. First, genomic analysis of selected *E. coli* isolates has looked especially at possible links between AMR and heavy metal resistance. Second, genomic analysis of isolates of *Vibrio* spp. (obligate halophiles abundant in seawater) recovered from the same location, as well as of sequences curated on the NCBI database, makes it possible to explore examples of gene transfer from sewage-borne *E. coli* to an exclusively marine bacterial genus. Given the selection pressure presented by the levels of pollution, a high degree of horizontal gene transfer might be expected (Aminov 2011; Soucy et al. 2015).

MATERIALS AND METHODS

Samples and selection

Two sediment samples (#5 and #6) were recovered from the Typhoon Shelter in Causeway Bay, Hong Kong at 22.2833469 N, 114.1847401 E. Similar samples from Chai Wan Breakwater (22.2720916 N, 114.2456090 E) and between Ferry Piers 3 and 4 (22.2877925 N, 114.1578774 E) did not yield high levels of *E. coli* on the day of sampling. After suspension in 0.9% saline, *E. coli* colonies were enumerated and identified using 3M Petrifilm *E. coli*/coliform plates. Antibiotic-resistant bacteria were identified by spreading 100 µL aliquots of the suspension on Luria agar containing 0.1% *w/v*

[1] The ISF Academy, 1 Kong Sin Wan Road, Pokfulam, HONG KONG
* Correspondence: Diana Ibarra, dlibarra@isf.edu.hk

 https://doi.org/10.1142/9789811275449_0040

tetracycline and incubating overnight at 27 °C. Resistant colonies were transferred to Luria agar containing copper(II) sulphate.

Using CHROMagar Vibrio plates, *Vibrio* spp. isolates were recovered from water and sediment samples as mauve, blue and white colonies.

Genomic sequencing and analysis

Isolates were passaged to purity on Luria agar (with 3.5% *w/v* NaCl for *Vibrio* spp.) before DNA extraction using the Qiagen DNeasy PowerSoil Pro Kit. Complete genomes were obtained by hybrid assembly via Unicycler, using reads from both Illumina MiSeq and Oxford Nanopore MinION sequencing platforms. NCBI BLAST, PATRIC and the CARD database were used for genomic analysis.

RESULTS

Complete genomes were obtained for four *E. coli* isolates (DLI.6n, DLI.5a, DLI.5h and DLI.5p) showing resistance to tetracycline as well as unrestricted growth in 0.1 M $CuSO_4$. In addition, draft genome sequences were obtained for 22 *Vibrio* spp. isolates, including *V. cyclitrophicus* (4), *V. harveyi* (4), *V. natriegens* (3), *V. campbellii* (2), *V. diazotrophicus* (2) and *V. parahaemolyticus* (2).

DLI.6n comprises a chromosome of 5.01 Mbp and a circular 104 kbp IncFII(pCoo) plasmid. Isolates 5a, 5h and 5p are closely-related variants with chromosomes of 4.94 Mbp and an identical 57 kbp IncFII(pCoo) plasmid.

An association between heavy metal and antibiotic resistance

The 6n plasmid contains the *mer* (mercury resistance) operon adjacent to the tetracycline resistance genes (*tetA-tetR*) (Fig. 1), all between a pair of mobile elements. A similar motif is found in the *chromosomes* of 5a, 5h and 5p, also flanked by a pair of insertion sequences (the IS186n transposase InsL). Interestingly, the *cusRS* and *cusCFBA* operons, responsible for copper homeostasis/resistance, are positioned close to the *mer*

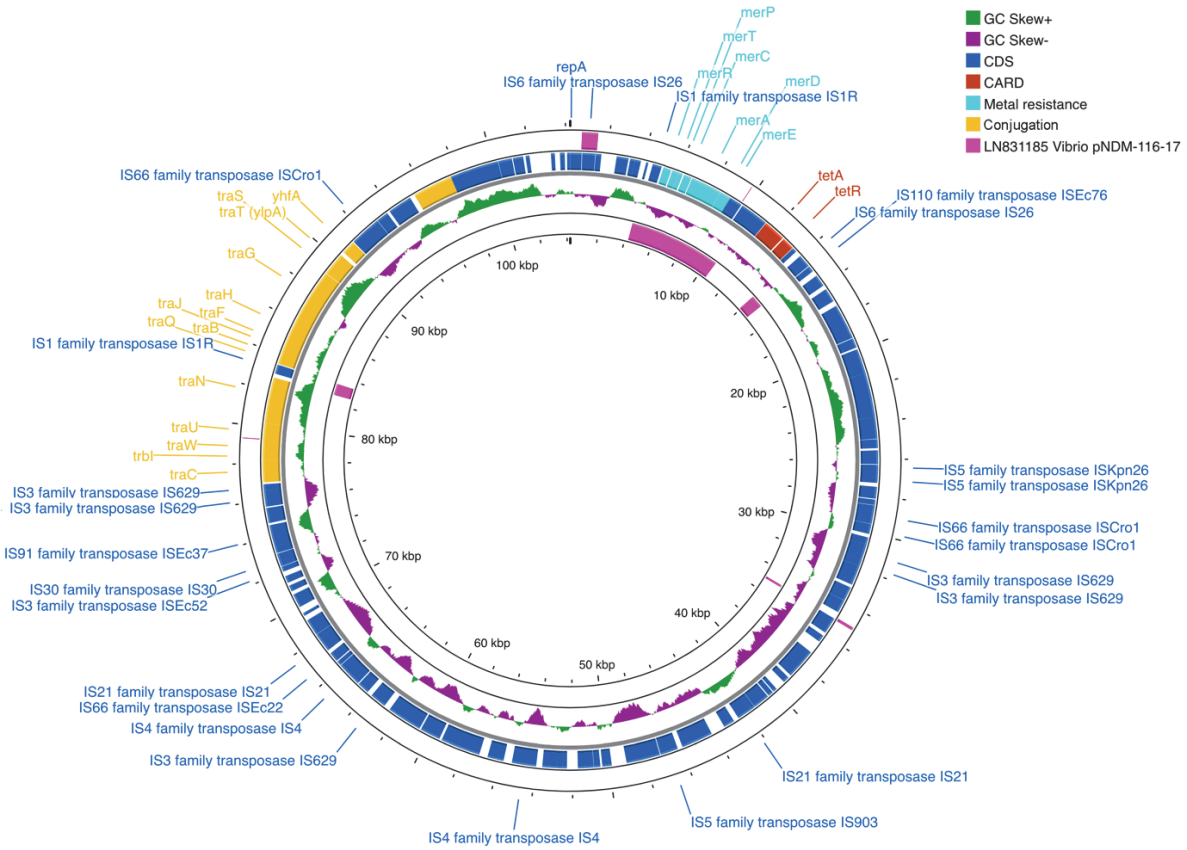

Fig. 1. The *mer* (mercury resistance) operon and tetracycline resistance genes *tetA-tetR* are co-located between transposable elements on the 104 kbp IncFII(pCoo) plasmid of *E. coli* 6n (pDLI.6n), but the same motif is chromosomally encoded in *E. coli* isolates 5a, 5h and 5p.

operon in 5a, 5h and 5p. In 6n, *cusRS* and *cusCFBA* are likewise chromosomally-encoded and so not associated with the *mer* operon.

Evidence for gene transfer to *Vibrio*

A homologous *mer* operon-*tetA*-*tetR* motif can be found in the *Vibrio cholerae* plasmid pNDM-116-17 (Walsh et al. 2011). In addition, the identical pair of mobile elements, flanking alternate resistance genes, has been found in IncQ plasmids from *Vibrio* sp. recovered from shrimps from southern China (Li et al. 2017). In the *Vibrio* isolates we have collected, analysis of AMR genes by CARD suggests a possible origin for some in *Enterobacteriaceae*: for example, the cAMP receptor protein (CRP), thought to play a role in the intestinal colonisation of humans by *Vibrio cholerae* (Manneh-Roussel et al. 2018).

CONCLUSION

Heavy metal and antibiotic resistance genes appear to be co-selected in *E. coli* in Hong Kong coastal waters. The high levels of heavy metal contamination at the Causeway Bay site are likely to encourage horizontal gene transfer.

Ease of transfer of AMR genes between sewage-borne *E. coli* and marine *Vibrio* spp. may have far-reaching consequences for public health and marine ecosystems.

Our continuing work will be looking further at the pathways and dynamics of gene transfer, as well as the relationship between AMR and heavy metal concentrations.

Data availability

The complete genome sequences and raw read data for *Escherichia coli* strain 5a and *Escherichia coli* strain 6n, including plasmids pDLI.6n and pDLI.5a, are available through NCBI under BioProject PRJNA875216.

References

Alves, M. S., Pereira, A., Araújo, S. M., Castro, B. B., Correia, A. C. and Henriques, I. (2014). Seawater is a reservoir of multi-resistant *Escherichia coli*, including strains hosting plasmid-mediated quinolones resistance and extended-spectrum beta-lactamases genes. Front. Microbiol., 5: 426.

Aminov R. I. (2011). Horizontal gene exchange in environmental microbiota. Front. Microbiol., 2: 158.

Au Yeung, F. J. (2019). Study of Sediment in Hong Kong Waters for Heavy Metals and Bacteria using an ROV. AGU Fall Meeting 2019

Li, R., Ye, L., Zheng, Z., Chan, E.W.C. and Chen, S. (2017). Genetic Characterization of Broad-Host-Range IncQ Plasmids Harboring blaVEB-18 in Vibrio Species. Antimicrob. Agents Chemother., 61(7): e00708-17.

Lothigius, A., Sjöling, A., Svennerholm, A. M. and Bölin, I. (2010). Survival and gene expression of enterotoxigenic *Escherichia coli* during long-term incubation in sea water and freshwater. J. Appl. Microbiol., 108(4), 1441–1449.

Manneh-Roussel, J., Haycocks, J., Magán, A., Perez-Soto, N., Voelz, K., Camilli, A., Krachler, A. M., Grainger, D. C. (2018). cAMP Receptor Protein Controls *Vibrio cholerae* Gene Expression in Response to Host Colonization. mBio, 9(4): e00966-18.

Seiler, C. and Berendonk, T. U. (2012). Heavy metal driven co-selection of antibiotic resistance in soil and water bodies impacted by agriculture and aquaculture. Front. Microbiol., 3: 399.

Soucy, S. M., Huang, J. and Gogarten, J. P. (2015). Horizontal gene transfer: building the web of life. Nat. Rev. Genet., 16(8), 472–482.

Tenaillon, O., Skurnik, D., Picard, B. and Denamu, E. (2010) The population genetics of commensal *Escherichia coli*, Nat. Rev. Microbiol., 8(3), 207-217.

Walsh, T. R., Weeks, J., Livermore, D. M. and Toleman, M. A. (2011). Dissemination of NDM-1 positive bacteria in the New Delhi environment and its implications for human health: an environmental point prevalence study. Lancet Infect. Dis., 11(5), 355–362.

Wang, S.-L., Xu, X.-R., Sun, Y.-X., Liu, J.-L. and Li, H.-B. (2013). Heavy metal pollution in coastal areas of South China: A review. Mar. Pollut. Bull., 76(1-2), 7– 15.

PHYTOPLANKTON HABITATS RESPONSE TO THE VARIABILITY OF ESTUARINE HYDRODYNAMIC CONDITION IN THE MACROTIDAL CHIKUGO RIVER ESTUARY

Lett Wai Nwe[1*], Katsuhide Yokoyama[1] and Gubash Azhikodan[1]

ABSTRACT: The effects of hydrodynamic and mixing conditions on the variation of phytoplankton composition and their habitats were investigated in the tide-dominated macrotidal Chikugo River estuary during a neap-spring tidal cycle in 2021. The estuary changed from stratified to well-mixed conditions during a neap-spring transition. The river discharge was < 60 m^3s^{-1} during the study period. Seawater intruded towards 17 km (upstream) during neap tide and until 16 km during spring tide. Surface suspended sediment concentration (SSC) was low during neap tide and maximum (~400 mg/L) during spring tide corresponding with changes in mixing and an estuarine turbidity maximum (ETM) was developed between 8-12 km during spring tide. Marine habitats diatoms were the major group with 20-89% of total phytoplankton. During a neap-spring tidal cycle, the maximum abundance of freshwater green algae was found during neap tide while diatoms (both marine and freshwater habitats) was in two days after neap tide and freshwater blue-green algae was in intermediate tide in response to changes in mixing conditions. The distribution of marine habitat diatoms and freshwater blue-green algae were positively correlated with salinity whereas freshwater green algae and freshwater habitat diatoms were negatively correlated with salinity. This study concludes that saltwater intrusion and mixing conditions driven by tidal forcing mainly controlled the species composition and their habitats in the Chikugo River estuary.

Keywords: ETM, habitats, mixing condition, salinity intrusion

INTRODUCTION

An estuary is a highly complex and the most productive ecosystem providing spawning and nursery areas for a variety of fisheries as well as protecting humans from the impact of waves, winds, and storms although it experiences tides. Recently, sea level rise, flooding and drought, and sea surface temperature rise can affect the estuarine hydrodynamic conditions which contribute to the spatial and temporal variation of estuarine habitats, especially phytoplankton communities that serve as a primary food source of estuarine trophic levels.

These changes in phytoplankton dynamics can lead to threatening the estuarine ecosystem such as growth and production rates, replacing small size species that impact energy transfer to the entire food web and harmful algae bloom. Additionally, phytoplankton plays as a bio-indicator of environmental variations by climate.

Therefore, the study aims to investigate the effects of hydrodynamic conditions on the variation of phytoplankton composition and their habitats in the highly turbid Chikugo River estuary.

METHODOLOGY

The study area, the Chikugo River estuary is the largest estuary in the Kyushu district of southwestern Japan, and Japan's one of the most fishery productive areas (**Fig. 1**).

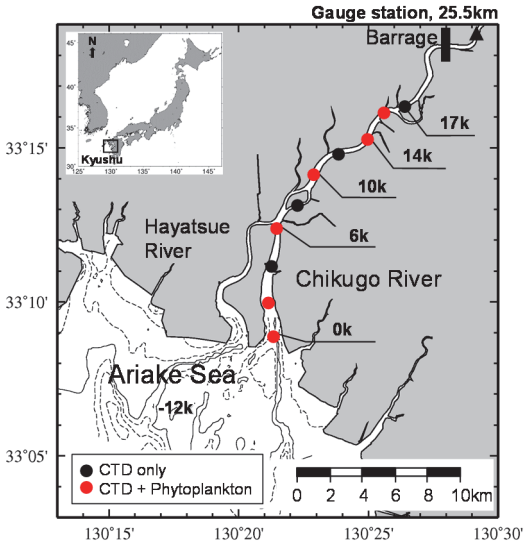

Fig. 1 Location of the study area

The field survey was conducted from a neap tide spring tide (21st to 26th April 2021) in the Chikugo River estuary. Ten stations were designated from the downstream (0 km) to the upstream (17 km): 0-4 km as lower estuary, 5-10 km as middle estuary and 11-17 km as upper estuary (**Fig. 1**).

[1] Department of Civil and Environmental Engineering, Tokyo Metropolitan University, JAPAN

 https://doi.org/10.1142/9789811275449_0041

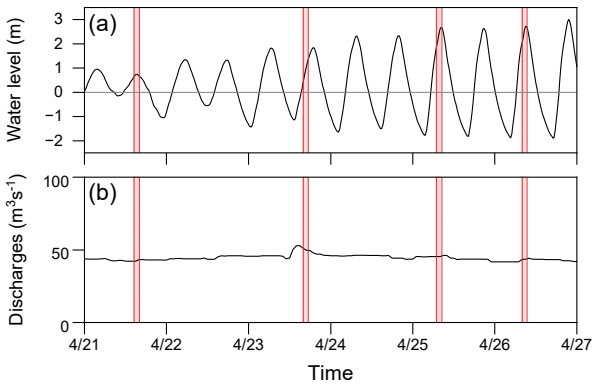

Fig. 2 a) water levels and b) discharges during a neap tide to spring tide. Shaded areas show the field survey periods

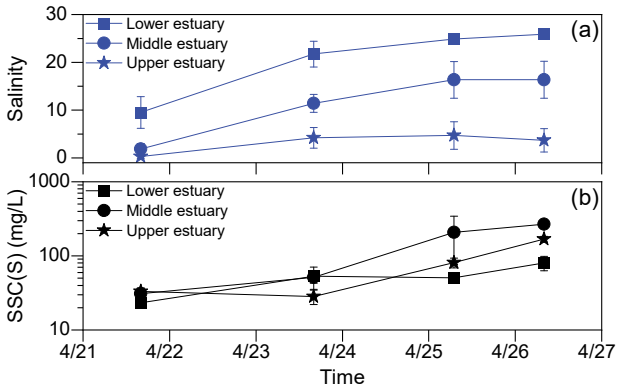

Fig. 3 Variation of a) salinity and b) SSC during a neap-spring tidal cycle

The vertical profiles of salinity and turbidity at every 0.1 m depth from 10 stations using a CTD with turbidity sensor (AAQ175-Z57, JFE Advantech, Japan) and water level using a HOBO logger (Onset, USA) were measured. Further, 1 L of surface water samples were collected by Van Dorn water sampler from 6 stations: 0 km, 2 km, 6.5 km, 10 km, 14 km, and 16 km for phytoplankton analysis. These 1L water samples were concentrated by a plankton net (20 µm mesh size) into 1-5 ml. The subsamples (1 ml) collected from each concentrated sample were placed in a counting chamber (50mm × 20mm × 1mm) and analyzed under a light microscope (NIKON: ECLIPSE series, E*i*, Japan) using the literature (Janse van Vuuren et al., 2006; Tomas, 1997).

The cell density of individual phytoplankton was calculated using the following equation:

$$\text{No. of cells ml}^{-1} = \frac{\text{cell counted} \times 1000}{\text{no. of grids} \times \text{CF}} \qquad (1)$$

where CF is the concentration factor of a water sample.

The suspended sediment concentration (SSC) was calculated from the in-situ turbidity (TB) by the following formula (Azhikodan and Yokoyam, 2016):

$$\text{SSC} = 1.0 \times \text{TB} + 4 \times 10^{-4}\text{TB}^2 + 6 \times 10^{-14}\text{TB}^5 \qquad (2)$$

The euphotic depth (Z_e, m), the depth of 1% of surface light intensity, was calculated ($Z_e = 4.61/k$), where k is the light attenuation coefficient.

The relationship between environmental parameters and the abundance of different phytoplankton habitats was calculated using a correlation test (r).

RESULTS AND DISCUSSION

Tide and river discharge

The estuary changed from a stratified condition during the neap tide to a well-mixed condition during the spring tide with tidal amplitude of 1 m and 4.7 m, respectively (**Fig. 2a**). The river discharge was low (<60 m^3s^{-1}) during the study period (**Fig. 2b**) due to the absence of rainfall.

Salinity and SSC

The saltwater intrusion reaches over 17 km (upstream) during neap tide and 16 km during spring tide due to low discharge. The surface salinity was found to be 9.54±3.32 in downstream, 1.9±1.12 in the middle estuary and 0.30±0.36 in upstream during the neap tide (**Fig. 3a**). The salinity varied from 24.88±0.95 (downstream) to 4.72±2.88 (upstream) during intermediate tide (**Fig. 3a**). The highest salinity was found at downstream (25.93 ± 0.86) during the spring tide (**Fig. 3a**).

The surface SSC varied from 23.33±1.67 mg/L (downstream) to 33.25±3.83 mg/L (upstream) during the neap tide (**Fig. 3b**). The SSC values gradually increased during the intermediate tide (**Fig. 3b**). The highest SSC was found during the spring tide at the middle estuary (268.58±33.77 mg/L) (**Fig. 3b**) under strong mixing, which led to the formation of an estuarine turbidity maximum (ETM) zone. The changes in salinity, mixing condition, and SSC have been reported by Azhikodan and Yokoyama (2015, 2016) in the Chikugo River estuary and the present results followed their discussion and findings.

Phytoplankton habitats distribution

The total density of phytoplankton changed from 45.36 to 208.85 cells/ml during the neap to spring tides. Among phytoplankton, marine habitats diatoms were found as the major group with 20-89%.

The temporal changes in phytoplankton habitats distribution are shown in **Fig. 4**. The density of freshwater green algae (FW green) was maximum (20.54 cells/ml) in the neap tide when the water column was vertically stratified with high water clarity (**Fig. 3b**, **Fig. 4a**). On the other hand, the highest density of marine habitat diatoms (MW diatoms) (164.57 cells/ml) and freshwater habitat diatoms (FW diatoms) (38.90 cells/ml) were found in the

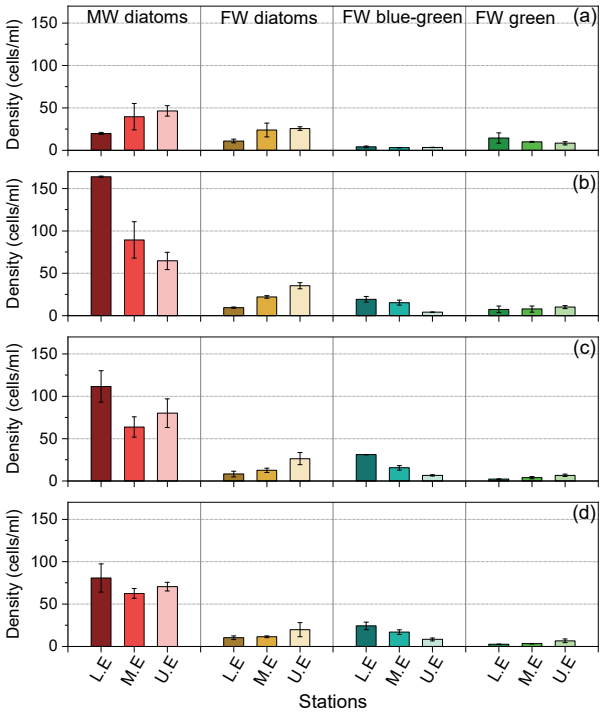

Fig. 4 Spatio-temporal variation of different phytoplankton habitats during a) neap tide, b) two days after neap tide, c) intermediate tide and d) spring tide. L.E = lower estuary, M.E = middle estuary and U.E = upper estuary

two days after neap tide (**Fig. 4b**) and freshwater blue-green algae (FW blue-green) was in the intermediate tide (31.20 cells/ml), respectively (**Fig. 4c**). After that the density of all habitats decreased towards the spring tide (**Fig. 4d**). This indicates that the distribution of phytoplankton was influenced by the changes in water mixing during a neap-spring transition.

Spatially, the densities of MW diatoms and FW blue-green decreased from downstream to upstream and their densities positively correlated with salinity distribution (r = 0.48 and r = 0.74, p<0.01) (**Table 1**). Conversely, the densities of FW diatoms and FW green showed opposite trend and their densities were negatively related to salinity (r = -0.71 and r = -0.56, p<0.01) (**Table 1**). The salinity becomes the main factor of phytoplankton distribution in the Chikugo River estuary. In addition, the densities of all habitats decreased at the middle estuary during the ETM formation (**Fig. 3b**, **4d**). This explains that the dense concentration of fine particles during ETM formation can affect the distribution and activities of phytoplankton.

Therefore, mixing conditions, salinity intrusion and ETM formation by a tidal forcing mainly controlled the abundance and distribution of phytoplankton that linked to the survival of phytoplankton habitats in the tide-dominated Chikugo River estuary.

Table 1 Correlation between the environmental parameters and density of different phytoplankton habitats. Z_e = euphotic depth (m), * p<0.05, ** p<0.01.

	Salinity	SSC	Z_e
Salinity	1		
SSC	0.04	1	
Z_e	-0.16	**-0.7****	1
FW blue-green	**0.74****	0.26	**-0.50****
FW green	**-0.56****	**-0.38***	**0.47****
FW diatoms	**-0.72****	-0.17	0.05
MW diatoms	**0.48****	0.01	**-0.38***

CONCLUSION

This study analyzed the distribution of different phytoplankton habitats in relation to environmental conditions during the neap to spring tides in 2021. The estuarine water varied from stratified condition to well-mixed condition and the salinity intrusion reached upstream due to low river discharge. The SSC increased from neap to spring tides and the ETM zone developed at the middle estuary during spring tide. The abundance of different phytoplankton habitats was affected by the changes in the mixing condition of a neap-spring tidal cycle. Salinity was the main controlling factor in the distribution of phytoplankton habitats together with the ETM formation in the Chikugo River estuary. This finding can be contributed to estimating the source of different phytoplankton species in the estuaries.

ACKNOWLEDGEMENTS

This research was supported by the River Fund of the Foundation of River and Watershed Environment Management (FOREM), Japan (No. 2021-5211-014) and the JSPS KAKENHI Grant No. JP20K14840. The authors thank the Chikugo River Work Office, Ministry of Land, Infrastructure, Transport, and Tourism, Japan for the data.

References

Azhikodan, G. and Yokoyama, K. (2015). Temporal and spatial variation of mixing and movement of suspended sediment in the macrotidal Chikugo River estuary. J. Coast. Res. 313: 680–689.

Azhikodan, G. and Yokoyama, K. (2016). Spatio-temporal variability of phytoplankton (Chlorophyll-a) in relation to salinity, suspended sediment concentration, and light intensity in a macrotidal estuary. Cont. Shelf Res. 126: 15-26.

Janse van Vuuren S., Taylor J., Gerber A. and Van Ginkel C. (2006). Easy identification of the most common freshwater algae. A guide for the identification of microscopic algae in South African freshwaters. ISBN 0-621-35471-6.

Tomas, C.R. (1997). Identifying marine diatoms and dinoflagellates. Academic Press. Inc. Harcourt Brace & Company. pp. 598.

NEAP-SPRING TIDAL AND SEASONAL VARIATIONS IN SALINITY INTRUSION AND MIXING CONDITION AT THE TROPICAL MACROTIDAL TANINTHARYI RIVER ESTUARY

N. O. Hlaing[1], G. Azhikodan[1] and K. Yokoyama[1]

ABSTRACT: Estuaries in developing countries have a strong impact on the livelihood of local people and the economic growth of the country through small-scale fisheries and farming. However, these estuaries are currently facing with a major problem of decline in fish stock due to the over-exploitation of fish resources. Additionally, the saltwater intrusion in the estuary will affect the freshwater supply and agriculture. A large amount of saltwater intrusion also causes tidal flooding and resulting in the coastal population homeless. The recent trend of changes in rainfall patterns associated with climate change can exacerbate the above issues. A deep understanding of the hydrodynamic processes in these estuaries is required for the better planning and management of their aquatic environment. Hence, the seasonal and tidal (neap-spring) variation of salinity intrusion and mixing conditions in the Tanintharyi River estuary (TRE), Myanmar was studied from 2017-2019. The study area was influenced by the monsoon-generated high river discharge from the Tanintharyi river (90% during the wet season) and high tidal ranges from the Andaman Sea. The results reveal that the salinity intrusion in the TRE was maximum during dry periods (>35km) and minimum (0.6-16km) during peak monsoon. The salinity intrusion during pre-monsoon and post-monsoon exhibits 17.4 km and 28.4 km, respectively. From a neap-spring tidal perspective, the mixing conditions in the TRE varied from partially mixed to well-mixed conditions in dry periods and from stratified to partially mixed conditions in peak monsoon. Therefore, the seasonal changes in rainfall patterns are a major influencing factor of salinity intrusion, and the combined effects of rainfall and tidal forces were responsible for mixing in the TRE. It was concluded that the narrower duration of monsoon periods with increased rainfall intensity patterns and strong tidal forces are responsible for the hydrodynamic changes in estuaries of Southeast Asian regions.

Keywords: estuary, hydrodynamics, Indian summer monsoon.

INTRODUCTION

The estuaries are essential as a nursery area for commercial fish larvae and valuable for the local small-scale fisheries in developing Asian countries. According to the report of the Food and Agriculture Organization (FAO 2019), the over-exploitation of fish populations results in declines in fish resources which can impact the food security issue in low-income countries. Nowadays, the estuaries in these countries suffer a severe problem of salinity intrusion, although it provides food and income for coastal populations. The salinity intrusion causes serious catastrophic impacts on human societies such as freshwater degradation, frequent tidal flooding, and the coastal population becoming homeless.

According to World Meteorological Organization (WMO 2019), the recent changes in rainfall patterns can exacerbate the above-mentioned problems in estuaries. Understanding the temporal and spatial trend of salinity intrusion and mixing conditions are of fundamental importance to achieving sustainable management, especially in developing countries. Hence, this study aims to investigates the neap-spring tidal and seasonal variation in salinity intrusion and mixing conditions at the Tanintharyi River estuary, Myanmar.

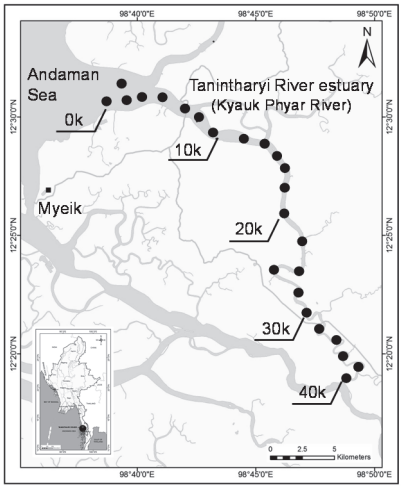

Fig. 1. Location of study area - Tanintharyi River estuary.

[1] Dept. of Civil and Environmental Eng., Tokyo Metropolitan University, 1-1, Minami-Osawa, Hachioji, Tokyo 192-0397, JAPAN

 https://doi.org/10.1142/9789811275449_0042

MATERIALS AND METHODS

The study area, Tanintharyi River estuary (TRE) is situated in the Southeast Asia region of Myanmar. It is important for coastal small-scale fisheries and freshwater supply for paddy fields (Nwe et al. 2021). The upstream regions of TRE received huge fluvial discharge during monsoon season (4000-6000 mm/year) and low discharge during the rest of the entire year. The downstream regions of TRE received saltwater intrusion from the Andaman Sea with a maximum tidal range of about 5 m (spring) and a minimum of 1.5 m (neap).

The field measurement conducted at TRE (2017-2019) includes different seasonal and tidal (neap-spring) time scales (Table. 1). The vertical profile of salinity was measured from the river mouth (0 km) to upstream (40 km) of TRE by using conductivity, temperature, depth, CTD probe (AAQ 119, JFE Advantech, Japan). The daily rainfall data at upstream TRE (Dawei) was collected from the Dept. of Meteorology and Hydrology of Myanmar. The rainfall data was averaged for 14-days rainfall to represent the fluvial discharge conditions. To represent the tidal condition, the water level data were collected at downstream of TRE by using a water level sensor (HOBO-U20-L-02, Onset, USA). The salinity intrusion length, *SIL* was determined as a distance from the river mouth (0 km) to upstream where the bottom salinity was 10 (Azhikodan et al. 2014). The mixing conditions are defined by using the salinity interface gradient (SIG) method, which calculates the slope of salinity ten isohaline (Azhikodan et al. 2014).

$$SIG = \frac{H}{Xb - Xs} \quad (1)$$

where X_b is the distance from 0 km to the place where salinity 10 appears at the bottom, X_s is the distance from 0 km to the place where salinity 10 appears at the surface, and H is the water depth around 10 isohaline area. If the SIG value was greater than 0.005, the estuary was well-mixed. If the SIG value was between 0.005 and 0.001, the estuary was partially mixed. The estuary was stratified if the SIG value was less than 0.001.

RESULTS AND DISCUSSION

Hydrographic conditions

The estuary received maximum rainfall (44.5 mm/day) during the monsoon season, and very little rainfall (1.4 mm/day) during dry seasons (Fig. 2b, Table 1). The pre-monsoon season showed an increasing trend of rainfall, but the post-monsoon season showed a decreasing trend of rainfall. The estuary was influenced by the maximum tidal range during the spring tide (4.7-5.9 m) and the minimum (1.3-2 m) during neap tide (Fig. 2a, Table 1). The salinity intrusion was maximum (SIL=34-37 km) during the dry season and minimum (SIL=0.6-16 km) during the monsoon season (Fig. 2b, Fig. 3). According to neap-spring tidal transitions, the SIL during the post-monsoon season showed an increasing trend from neap to intermediate tide and expect to increase during spring tide, although the data was limited. Otherwise, the SIL during pre-monsoon showed a similar trend to that during the monsoon season. The three types of mixing conditions were found at TRE where the estuary was vertically well-mixed during dry seasons, and it was stratified to partially mixed during the monsoon season (Fig. 2c, Fig. 3). According to neap-spring tidal transitions, the mixing conditions during the post-

Table 1. Detail Explanation of field measurement (2017-2019).

No	Date	Total Stations	Seasons	Tidal conditions	Rainfall (mm/day)	Tidal range (m)
1	01-Jun 2017	10	Pre-monsoon	Neap	9.3	2.47
2	01-Dec 2017	10	Post-monsoon	Intermediate	2.01	4.06
3	14-Dec 2018	17	Post-monsoon	Neap	0.26	2.53
4	28-Feb 2019	15	Dry	Neap	1.41	1.30
5	03-Mar 2019	11	Dry	Intermediate	0	2.30
6	07-Mar 2019	10	Dry	Spring	0	4.77
7	26-Aug 2019	10	Monsoon	Neap	33.94	2.09
8	28-Aug 2019	10	Monsoon	Intermediate	41.96	3.61
9	02-Sep 2019	16	Monsoon	Spring	44.57	5.98

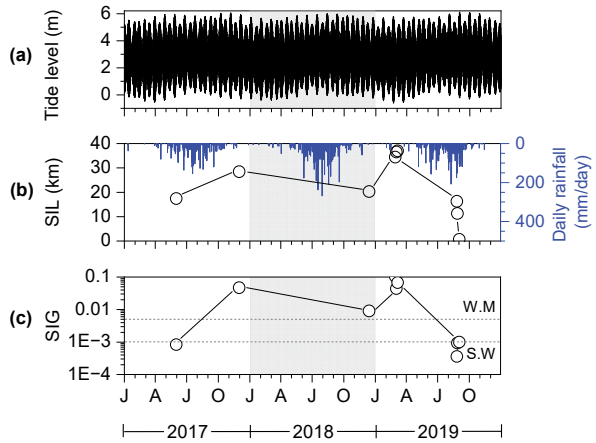

Fig. 2. Time-series of (a) tidal range, (b) SIL and rainfall, (c) SIG.

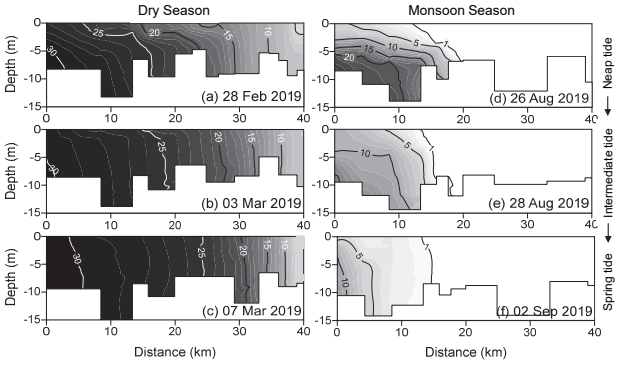

Fig. 3. Vertical and horizontal variations of salinity intrusion and mixing conditions.

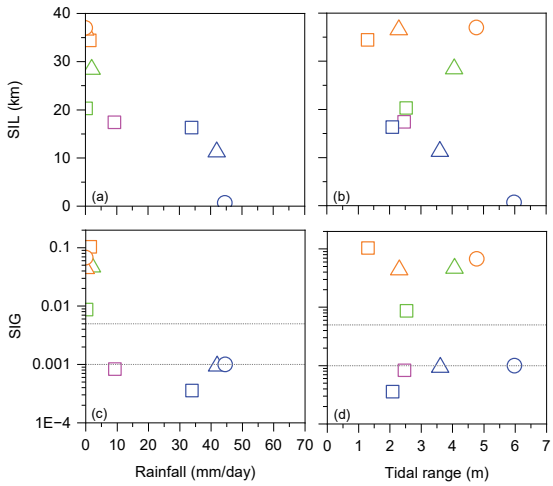

Fig. 4. Effect of rainfall and tidal range on salinity intrusion (SIL) and mixing condition (SIG).

monsoon season have a similar mixing trend with the dry season and the SIG increased from neap tide to intermediate tide and expect larger SIG during spring tide, although the data was insufficient. The mixing condition during pre-monsoon seasons was stratified at neap tide.

Salinity intrusion based on rainfall and tidal range

The salinity intrusion was maximum during the dry season and minimum during the wet season (Fig. 4a). The pre-monsoon season was expected to have a similar trend to the monsoon season and the post-monsoon season had weaker salinity intrusion than the dry season. According to neap-spring tidal time scales, the salinity intrusion showed a strong decreasing trend with tidal range, especially during the monsoon season and it was a weak increasing trend during the dry season (Fig. 4b). The salinity intrusion during the post-monsoon season showed a strong increasing trend from neap-intermediate tide and expected to have stronger salinity intrusion during the spring tide (Fig. 4b). Hence, the rainfall was a major influencing factor for the salinity intrusion at TRE.

Mixing condition based on rainfall and tidal range

Depending on the rainfall intensity, the mixing condition changed from stratified to partially mixed condition during the monsoon season and it was vertically well-mixed condition during the dry season (Fig. 4c). The mixing condition during pre-monsoon was stratified condition and the post-monsoon season was well-mixed condition based on the influence of rainfall. These two transition seasons (pre and post) may follow the trend of the monsoon and dry seasons, although the data was insufficient. According to neap-spring tidal time scales, the mixing condition during monsoon season indicated an increasing trend with tidal range but the dry season showed vertically well-mixed conditions (Fig. 4d). Therefore, the mixing condition was combinedly influenced by both tidal forcing and rainfall, especially during monsoon season at TRE.

CONCLUSIONS

The seasonal and neap-spring tidal transition of salinity intrusion and mixing conditions at TRE, Myanmar was investigated during 2017-2019. The outcomes from this study discussed the effect of rainfall and tidal range. The salinity intrusion was maximum during the dry season and minimum during monsoon seasons. The pre-monsoon and post-monsoon seasons showed a similar trend to the monsoon and dry seasons. According to neap-spring tidal time scales, the salinity intrusion exhibited an increasing trend during the dry season and decreasing trend during the monsoon season.

The TRE exhibited all three mixing conditions during the dry to monsoon seasons. The neap-spring transition of mixing conditions does not change (i.e., well-mixed) during the dry season. However, it varied from stratified to partially mixed conditions based on the increased rainfall during the monsoon season. Therefore, the seasonal rainfall pattern was a major influencing factor on the salinity intrusion, and it was partly influenced along with tidal forcing on the mixing condition, especially during monsoon seasons.

ACKNOWLEDGEMENTS

The authors would like to thank the Japan International Research Center for Agricultural Sciences (JIRCAS) for the research funding and for providing the necessary facilities to conduct this research work. Thanks to Dept. of Marine Science (Myeik University), Dept. of Meteorology and Hydrology of Myanmar, and Hydraulics laboratory (Dept. of Civil and Environmental Eng., Tokyo Metropolitan University) for the data and guidance during field measurement.

References

Azhikodan, G., Yokoyama, K., and Morimura, Y. (2014). Effect of mixing on turbidity maximum movement during semilunar tidal cycle in the Chikugo River estuary. Journal of Japan Society of Civil Engineers, Ser. B1 (Hydraulic engineering). **70**(**4**): 37-42.

FAO (2019): Securing sustainable small-scale fisheries report.

Nwe, L. W., Azhikodan, G., Yokoyama, K., and Kodama, M. (2021). Spatio-temporal distribution of diatoms and dinoflagellates in the macrotidal Tanintharyi River estuary, Myanmar. Regional studies in Marine Science. **42**: 1-12.

WMO (2019): State of the global climate in 2019 report.

LONG-TERM (1953-2020) MORPHOLOGICAL CHANGES OF CHIKUGO RIVER, JAPAN

P.E. Phyu[1], K. Yokoyama[1] and G. Azhikodan[1]

ABSTRACT: This study aims to predict the long-term morphological changes of the Chikugo River using river cross-sectional surveyed data from 1953-2020. The study area was divided into the estuary (0-23 km), middle stream (23-50 km) and upstream (50-64 km). The mean bed elevation of every cross-section in each surveyed year was calculated to analyze the long-term longitudinal elevation changes. Spatial (0-64km) and temporal (1953-2020) changes in channel shapes were found. In addition, three different morphological trends were found during the study period of 67 years. From 1953 to 1993, dredging, sand & gravel mining, and dam construction decreased the bed elevation of Chikugo River; 1-4 m for estuary, 2-4 m for middle stream and 1-3 m for upstream. From 1993-2009, elevation changes became less compared to the first period and elevation increased uniformly (about 0.5 m). From 2009-2020, non-uniform morphological changes were observed due to changes in river flow and sediment supply by climate change disasters. The disaster events not only increase the river flow but also carries more sediments from the watershed. Most of these sediments were deposited in the middle stream (50-64 km) increasing the bed elevation by about 1-1.5 m. The upstream (50-64 km) showed a quick and significant response to the type of disasters although elevation change was almost stable due to the net result of deposition by landslide disaster and erosion by the flood. However, the elevation of the estuary (8-23 km) decreased due to net erosion by high river flow and insufficient sediment supply from upstream while the elevation of 0-8 km increased slightly due to the deposition of eroded sediments from 8-23 km. Therefore, climate change disasters affect the morpho dynamic equilibrium of Chikugo River non-uniformly although elevation changes were less compared to that of human activities.

Keywords: bed elevation, river flow, sediment supply

INTRODUCTION

Long-term morphological changes in rivers depend not only on the natural processes but also on anthropogenic activities since rivers are very dynamic to changes in river flow and sediment supply (Hai et al., 2019). Recently, global climate change has become a hot topic for the morphological changes of rivers worldwide due to frequent floods and droughts affecting the river flow and sediment supply.

The study area, Chikugo River also has a lot of experience in river improvement works since the Meiji era (1603-1868) (Yutaka, 2009). Moreover, during recent years, several flooding and landslide disasters had occurred in the Chikugo River basin due to heavy rainfall events by climate change. Further, morpho-dynamics in estuaries consisting of sand base and mud layer has not been studied well in the world, although sand bar near the river mouth or muddy bed fluctuation in the estuaries have been studied well.

Therefore, this study aims to predict the long-term morphological changes of the Chikugo River using field measurement of river cross-section data to prevent impacts of morphological changes.

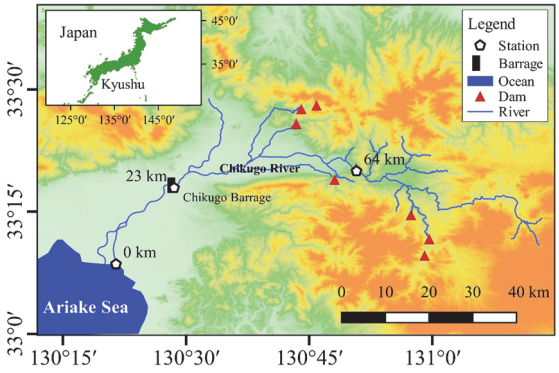

Fig. 1 Location of the Study Area

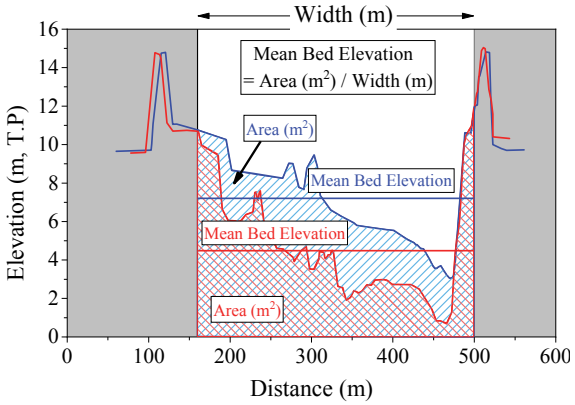

Fig. 2 Calculation of Mean Bed Elevation

[1] Dept. of Civil and Environmental Eng., Tokyo Metropolitan University, 1-1, Minami-Osawa, Hachioji-Shi, Tokyo 192-0397, JAPAN

 https://doi.org/10.1142/9789811275449_0043

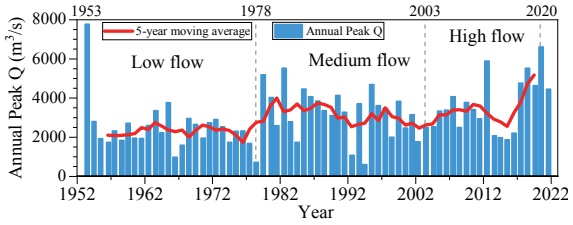

Fig. 3 Annual Maximum River Flow (1953-2021)

METHODOLOGY

The Chikugo River, the largest river in the western part of Japan, is surrounded by four prefectures in the Kyushu region **(Fig.1)**. It initiates from Mt. Aso and flowed downstream into the Ariake Sea with a total length of 143 km and watershed area of 2860 km^2. The upstream of 64 km is a mountainous region mainly occupied by dams and the downstream of 64 km (study area) is a flat plain region with agricultural land and an estuary extends up to 23 km with a tidal range of 1.5-5 m from neap tide to spring tide (Azhikodan and Yokoyama, 2019).

The study period was divided into the low flow (1953-1978), medium flow (1978-2003) and high flow (2003-2020) periods based on river flow data (**Fig.3**) collected at Senoshita station (25.5 km). The government has measured the topography of river cross-sections in 200 m intervals from 0 km (river mouth) to 64 km upstream since 1953 with 3-5 years intervals. To understand the long-term morphological changes, the mean bed elevation of each cross-section for every surveyed year was calculated as shown in **Fig. 2**. In addition, longitudinal elevation changes in each period were also calculated since it is very difficult to distinguish the elevation changes from the longitudinal profile.

RESULTS AND DISCUSSION

Spatial (0-64 km) and Temporal (1953-2020) Changes in Channel Shape

After analyzing the measured cross-sections figures, spatial and temporal changes of channel shapes along the river was noticed and changes in two representative cross-sections (17 km for estuary, 34.6 km for middle stream) were shown in **Fig. 4**.

The most changes in channel shape of 17 km station were found during 1953-1993. The elevation of the whole channel was lowered about 8 m during that period. During the period of 1993-2003, the bed elevation decreased about 1 m while banks elevation increased about 1 m for left bank and 3 m for right bank. Starting from 2003, bank erosion occurred instead of riverbed erosion and approximately 2.5 m of left bank and 6 m of right bank were eroded during 2003-2019. Similar to that of 17 km

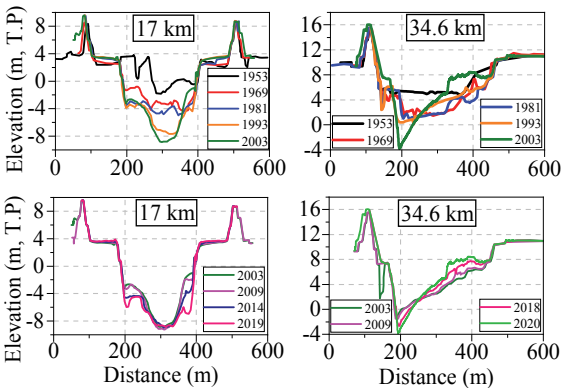

Fig. 4 Spatial and Temporal Changes in Channel Shape

station, most changes of 34.6 km were also found during the period of 1953-1993. Starting from 1993, the channel shape of 34.6 km changed from trapezoidal to triangular shape.

The different morphological responses show that there are other factors affecting the channel shape other than river flow and sediment supply. The bank erosion at the 17 km station might be the effect of the bed sill located upstream of 17 km. In the case of the 34.6 km station, meandering properties of deposition at the inner bend and erosion at the outer bend were observed. Therefore, the long-term pattern of changes in channel shape is depending not only on the river flow and sediment supply but also on the hydraulic structures and geological conditions of the location.

Longitudinal Elevation Changes (1953-2020)

The longitudinal bed elevation profiles of surveyed years were shown in **Fig.5 and Fig. 6**. Regardless of the study period division by river flow, three patterns of morphological changes such as (i) riverbed incision by human activities (1953-1993), (ii) stable channel with slightly increased elevation (1993-2009) and (iii) non-uniform morphological changes by disaster events (2009-2020) were found. The results of each trend were discussed as follows.

Riverbed incision by human activities (1953-1993)

The longitudinal elevation profile of the Chikugo River and elevation changes from 1953-1993 were shown in **Fig.5 and 5a**. The decrease in bed elevation from 1953-1969 was mainly caused by river improvement works (dredging, sand & gravel mining, and dam construction) after the occurrence of the severe flood in 1953. Exactly four dams were constructed upstream of the Chikugo River for flood control. In addition, channel widening, and riverbed dredging were performed when the Chikugo barrage was constructed at 23 km from 1977-1985 (Japan Water Agency). The decrease in elevation was reduced

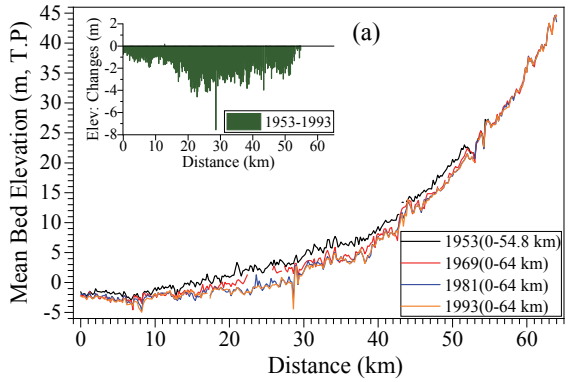

Fig. 5 Longitudinal Elevation Changes (1953-1993)

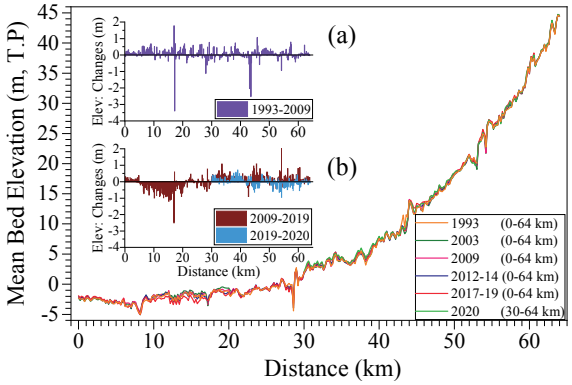

Fig. 6 Longitudinal Elevation Changes (1993-2020)

during 1981-1993, as there were no large-scale channel improvement works except in some locations. Hence, these small-scale decreases in bed elevation might be the after-effects of human activities during the earlier period.

Stable channel period with uniformly increased elevation (1993-2009)

The longitudinal elevation profile and elevation changes from 1993-2009 were shown in **Fig.6 and 6a**. During the period of 1993-2009, annual maximum river flow varied from 2000-4500 m^3/s. The longitudinal bed elevation increased uniformly about 0.5 m except some locations. Therefore, this period can be assumed as the period of the equilibrium state of river flow and sediment supply.

Non-uniform morphological changes by disaster events (2009-2020)

The longitudinal elevation profile and elevation changes from 2009-2020 were also shown in **Fig.6 and 6b**. During this period, three main disasters were occurred in the Chikugo River basin: 2012 torrential rainfall, 2017 landslide disaster and 2020 heavy rainfall flood. Further, the river flow in 2018 and 2019 (**Fig.3**) were as high as in 2017 although there were no disaster events during those periods. Non-uniform longitudinal elevation changes were observed due to the sudden change in river flow and sediment supply by these disasters.

The upstream 50-64 km was almost stable although it showed a significant response to the type of disasters such as deposition occurred after landslide disaster and erosion occurred after the flood. However, most of the sediments carried from the watershed and upstream (gravel and coarse sand) were deposited in the middle stream (30-50 km) and increased the bed elevation (1-1.5 m) after every disaster while 23-30 km was just stable with a slight decrease in elevation. Conversely, the amount of erosion was higher than that of deposition for the estuary (8-23 km) which resulted in a decrease in elevation (0.5-1 m) while 0-8 km was stable with a slightly increased elevation due to deposition of eroded sediments from 8-23 km (silt and clay).

These non-uniform elevation changes showed that, although disasters increased both river flow and sediment supply, it was only enough to deposit on the middle stream and insufficient to keep the estuary in an equilibrium state.

CONCLUSION

This study found out following three morphological changes trends; (i) human activities decreased the bed elevation of Chikugo River regardless of the river flow during 1953-1993, (ii), morphological changes along the river were uniform with the medium flow condition during 1993-2009, and (iii) non-uniform morphological changes (stable channel in the upstream, aggradation in the middle stream and degrading trend in the estuary) were found along the river during 2009-2020 due to effects disasters with the high flow condition.

ACKNOWLEDGEMENTS

The authors sincerely thank the Chikugo River Work Office, Ministry of Land, Infrastructure, Transport and Tourism of Japan and the Japan Water Agency for providing the valuable data. The authors are very grateful to the Japanese Government for supporting the Master study of Pan Ei Phyu through Ministry of Education, Culture, Sports, Science and Technology.

References

Azhikodan, G., & Yokoyama, K. (2019). Seasonal morphodynamic evolution in a meandering channel of a macrotidal estuary. Science of the Total Environment, 684, 281–295.

Hai, D. M., Umeda, S., & Yuhi, M. (2019). Morphological changes of the lower Tedori River, Japan, over 50 years. Water (Switzerland), 11(9).

Yutaka, T. (2009). History of water management in Japan from the end of World War II. International Journal of Water Resources Development, 25:4, 547-553.

NUMERICAL MODELLING OF SALTWATER AND FRESHWATER FLOW DYNAMICS AT THE CONFLUENCE OF TIDAL RIVERS

Haruka Inoue[1], Katsuhide Yokoyama[1] and Gubash Azhikodan[1]

ABSTRACT: The interaction between saltwater and freshwater related to complex topography at the confluence of Arakawa and Sumida River estuaries were studied using a 3D hydrodynamic model Fantom Refined and analyzed the flow characteristics using particle tracking. The analysis results showed that the saltwater distribution in the Arakawa River was well-mixed during spring tide and partially mixed during neap tide. The results of the particle tracking revealed that most of the river water flowing from the upstream to downstream of Arakawa River flows into the mainstream Arakawa River itself instead of splitting into Sumida River. In other words, it flows into a wide river with wide and straight channel. When the particles are released from the Sumida River at downstream of the confluence during the flood tide, all the particles in the surface layer pass through the Iwabuchi gate and flow into the Arakawa, while about 80% of the particles in the bottom layer flow into the upstream of the Sumida River (known as Shingashi River). In addition, the surface layer is more affected by freshwater inflow in spring tide. Furthermore, the impact of freshwater inflow at neap tide was greater than at spring tide.

Keywords: Saltwater intrusion, Computational fluid dynamics, Three-dimensional fluid simulation

INTRODUCTION

Saltwater intrusion in estuaries has various effects on our lives, such as salt damage to crops and contamination of drinking water. To prevent salt damage, estuary weirs are built, but they cause other problems such as deterioration of water quality damage to ecosystems, etc. In order to prevent such damages, it is necessary to understand the flow dynamics in the estuarine channel in detail. For a simple river channel, a two-dimensional, vertical-longitudinal simulation is useful, but for a complex river with many branches and meanders and tributary inflows, three-dimensional analysis is necessary. This is because saltwater and freshwater movements are complicatedly distributed not only longitudinally but also horizontally across several channels.

Therefore, a three-dimensional hydrodynamic simulation was conducted at the confluence of two urban rivers (Arakawa River and Sumida River) in Tokyo to investigate the relationship between saltwater intrusion, topography, and flow velocity.

METHODOLOGY

Research Area

The study area is the Arakawa River estuary (Fig. 1). Arakawa River provides water for many urban and agricultural uses and supports the political and economic centers of Japan. It is also home to many living organisms in its downstream waters. Furthermore, they play a major role in flood control.

The topography of the study area is very complicated as the confluence of Arakawa River (mainstream) and Sumida River (branch downstream) as well as the confluence of Shingashi River (branch upstream) and Sumida River (branch downstream) are located close to each other at the branch confluence point.

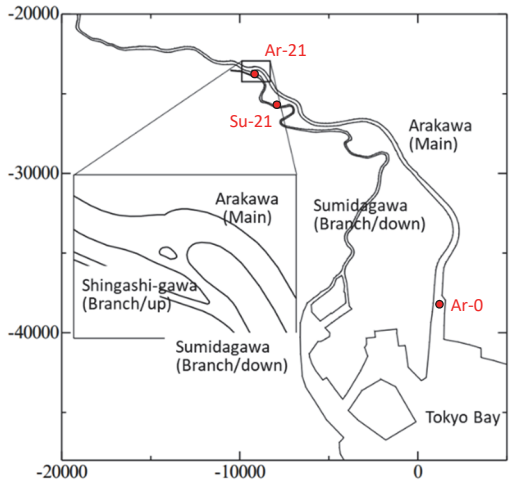

Fig.1 Location map of Arakawa River and Sumida River

[1] Civil and Environmental Engineering, Tokyo Metropolitan University, 1-1 Minamiosawa, Hachioji-shi, Tokyo, JAPAN

 https://doi.org/10.1142/9789811275449_0044

Analysis Method

A three-dimensional hydrodynamic simulator, Fantom Refined (Shintani, 2017; Veerapaga et al., 2019) was used in this study. The basic equations are the continuity equation, the Navier-Stokes equation, and the salinity transport equation. The discretization method is a collocated-grid finite volume method with second-order accuracy for the time progression and third-order accuracy for the advection term. A generalized two-equation model, GLS turbulent closure, was used as the turbulence model.

In this study, a three-dimensional simulation of river water flow at the branch confluence during the period from 5:00 on September 7, 2017 to 24:00 on September 21, 2017 was conducted to analyze the river water flow by particle tracking to consider the particle dispersal conditions at spring and neap tides, respectively.

VERIFICATION OF ACCURACY

The measured water level (at the river mouth and upstream) and salinity (at three sites along the estuary) data (Fig. 1) were compared with calculated values. The salinity at Ar-0 was measured from both the surface and bottom layers.

The water level fluctuation was well reproduced by the model (Fig. 2). In the case of salinity values, the simulated data generally agree with the observations (Fig. 3). However, peak salinity was not well reproduced by the model. Overall, the results are considered to be acceptable for conducting the case study.

FLOW CHARACTERISTICS

Mixing and Form of saltwater intrusion

Fig. 4(a) shows the longitudinal distribution of salinity during spring tide. During spring tide, the difference in salinity between the surface and bottom layers is small, indicating that the estuary was vertically well-mixed. Further, saltwater intrudes until 12 km upstream. Fig. 4(b) shows the longitudinal distribution of salinity during neap tide. This figure shows that the salinity is low in the surface layer and high in the bottom layer during the neap tide, which indicates the partially mixed condition of the estuary. The saltwater reaches until 16 km upstream during the neap tide.

Result of particle tracking

The divergence characteristics of river water at the branch confluence was analyzed using hypothetical particles. Fig. 5(a) shows the percentage of particles flowing into each river when particles flow from upstream of the Arakawa River (mainstream) during the ebb tide of spring tide. Most of the river water flows directly into the Arakawa River (mainstream) along the topography. Particles placed in the lower layer do not flow into Sumida River (branch downstream). Even for particles placed on the surface layer, only 1.6% flow into the Sumida River (branch downstream). Fig. 5(b) shows the percentage of particles flowing into each river when particles flow from upstream of the Arakawa River (mainstream) during the ebb tide of the neap tide. In the case of neap tide, no particles flowed into Sumida River (branch downstream).

Fig. 6(a) shows the percentage of particles flowing into each river when particles flow from downstream of Sumida River (branch downstream) during the flood tide of spring tide. As shown in Fig. 7, comparing the velocities of the surface and bottom layers, the velocity at

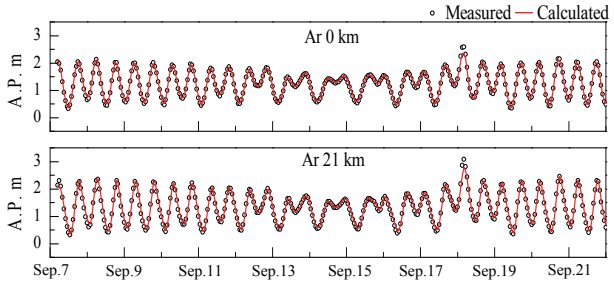

Fig.3 Comparison of calculated and measured salinity

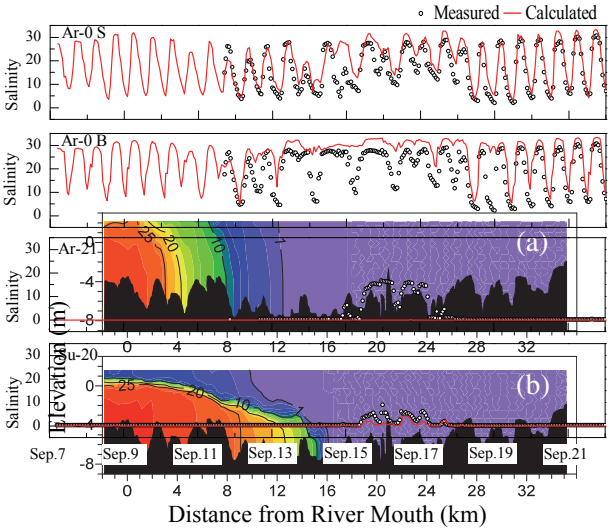

Fig.4 Longitudinal salinity distribution (a: Spring tide, Sep.7 / b: Neap tide, Sep.15)

Fig.2 Comparison of calculated and measured water level

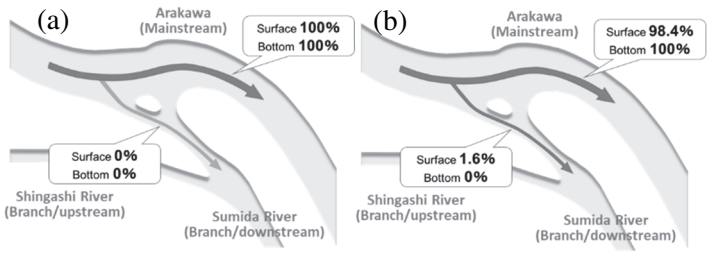

Fig.5 Percentage of particles flowing into each river when particles flow from upstream of Arakawa River during ebb tide (a: Spring tide, Sep.19 / b: Neap tide, Sep.14)

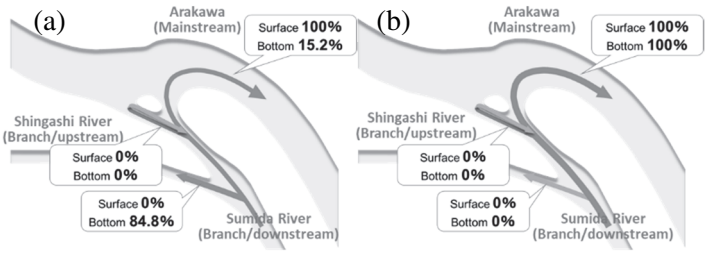

Fig.6 Percentage of particles flowing into each river when particles flow from downstream of Sumida River during flood tide (a: Spring tide, Sep.19 / b: Neap tide, Sep.14)

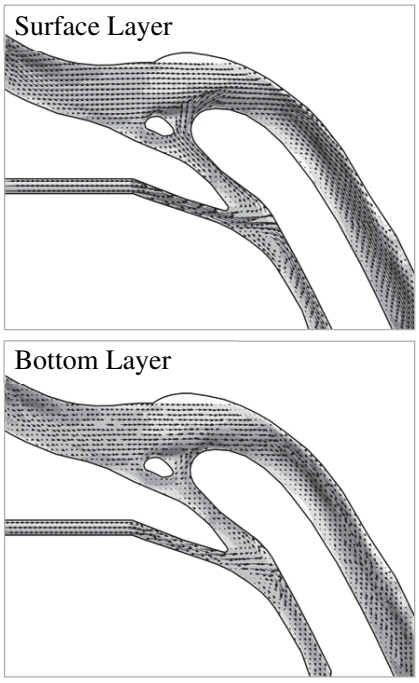

Fig.7 Velocity vectors for each layer

the surface is relatively large, and the river water flowing in from Shingashi River (branch upstream) pushes the particles away. At the bottom, the inflow from Shingashi River (branch upstream) is weaker than at the surface, so particles are dispersed. These results suggest that the surface layer is more strongly affected by freshwater inflow.

Fig. 6(b) shows the percentage of particles flowing into each river when particles flow from downstream of Sumida River (branch downstream) during the flood tide of the neap tide. During neap tide, the freshwater inflow from Shingashi River (branch upstream) is relatively larger than during spring tide because of the weaker momentum of the water flowing upstream from Sumida River (branch downstream), and the particles are pushed towards the Arakawa River (mainstream). Hence, the water from the Sumida River does not flow into the Shingashi River but instead flows into the Arakawa River. This suggests that the effect of freshwater inflow is greater at neap tide than at spring tide.

Consideration of particle tracking

Fig. 1 shows that the Arakawa River (mainstream) is relatively straight and wide. In contrast, Sumida River (branch downstream) has many meanders and its channel width is narrow. From this, it can be said that at bifurcation points, most river water tends to flow into rivers with straighter bed topography and wider river widths.

CONCLUSION

(1) The saltwater distribution in the Arakawa River was well-mixed during spring tide and partially mixed during neap tide.

(2) River water flowing from upstream of the mainstream (Arakawa River) is rarely diverted into the branch (Sumida River) and most of the water flows straight down the mainstream, because the channel is wide and straight.

(3) The surface layer is more affected by freshwater inflow during spring tide.

(4) Impact of freshwater inflow at neap tide is more significant than at spring tide.

References

Shintani, T., (2017). An unstructured-cartesian hydrodynamic simulator with local mesh refinement technique. J. JSCE, Ser. B1 (Hydraul. Eng.) 73 (4), 967–972.

Veerapaga, N., Azhikodan, G., Shintani, T., Iwamoto, N., Yokoyama, K., 2019. A three-dimensional environmental hydrodynamic model, Fantom-Refined: validation and application for saltwater intrusion in a meso-macrotidal estuary. Ocean Modelling 141, 101425.

ASSOCIATION OF EUTROPHICATION PARAMETERS AND WATER QUALITY PARAMETERS OF TWO SELECTED ESTUARIES

A. Gayathri H.[1], B. Sreelekshmi S.[1], C. Gowtham Mohan[1], D. Gopika Sankar M. S.[1], E. Priya K. L.[1], F. Gubash Azhikodan[2], G.Katsuhide Yokoyama[2]

ABSTRACT: The productivity of an aquatic system is often measured in terms of Chlorophyll-a, which is supplemented by the nutrients like nitrogen and phosphorous. An excess amount of Chlorophyll-a is often caused as a consequence of nutrient enrichment, termed as eutrophication. However, the measurement of Chlorophyll-a is not included in the monitoring programs of the Pollution Control Board (Central and State) and hence assessing the eutrophication status of an estuary is difficult. This necessitates the prediction of Chlorophyll-a from its influential parameters that are monitored regularly. In this study, the possible influence of salinity on Chlorophyll-a was studied and an Artificial Neural Network (ANN) model for prediction of Chlorophyll-a using parameters like Total Phosphorous (TP), Turbidity and Salinity was developed based on data from Pollution Control Board (PCB). The proposed model was tested using the field data from Ashtamudi estuary and a hydrodynamically and geographically different estuarine system, the Chikugo estuary Japan. From the study, it was found that salinity has an influence on Chl-a. Also, the prediction model needs to be modified according to the unique characteristics of estuaries for better prediction. The developed model is envisaged to support monitoring agencies, planning agencies and decision makers in the assessment of eutrophication status of estuarine systems.

Keywords: Chlorophyll-a, Eutrophication, Artificial Neural Network, Salinity, Total Phosphorus, Turbidity

INTRODUCTION

Eutrophication is the enrichment of nutrients, mainly nitrogen and phosphorus, in water bodies mainly caused due to human activities, increased land usage and the application of fertilizers, which is a major source of nutrients. It results in habitat degradation, loss of biodiversity, and harmful algal blooms. It also degrades water quality, resulting in increased turbidity, health risks, diminished aquatic growth due to oxygen depletion, and a foul taste and odour.

This study aims to do a relative analysis of eutrophication parameters and the influence of salinity on Chlorophyll-a between Ashtamudi estuary, in India and Chikugo estuary, in Japan. Ashtamudi estuary, is the second largest and most deep (7m) estuary in Kerala with its freshwater inflow from Kallada River. Chikugo River estuary is located in the Kyushu prefecture of south western Japan with its freshwater input from Chikugo river. Data from Ashtamudi estuary was collected, to compare its water quality and eutrophication parameters and understand the influence of salinity on Chlorophyll-a content. Based on that, a model was developed for Chl-a and it was validated using data from another estuary which is in a different geographic and hydrodynamic conditions as compared to Ashtamudi to give an insight to the possibility of extending the study.

MATERIALS AND METHODS

Study Area

The Ashtamudi Estuary, stands out for its distinctive biodiversity and hydrographic features. Greater levels of urbanization and dense population density in the surrounding areas result in excessive human influence and eventual environmental degradation. Ashtamudi estuary is a microtidal estuary and tides in the estuary are semidiurnal with a range of about 1m. It has 8 branches with an average width of each lobe 3km. (Figure 1)The Chikugo River Estuary is a mesotidal\macrotidal estuary, 1,000 metres wide at the mouth and 250 metres wide 23 kilometres upstream.

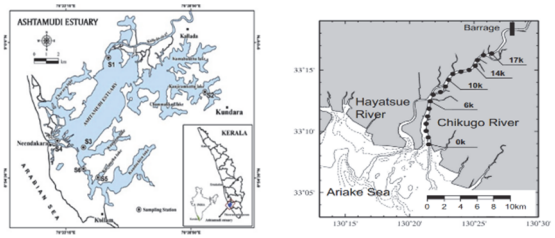

Fig 1: Location map of Ashtamudi estuary and Chikugo estuary respectively.

A branch from the main estuarine waterway joins it at 6.8 kilometres, 10 kilometres upstream. At 6.1 kilometres, a second branch emerges and empties into the Ariake Sea.

[1]Department of Civil Engineering, TKM College of Engineering, INDIA
[2]Department of Civil and Environmental Engineering, Tokyo Metropolitan University, JAPAN

 https://doi.org/10.1142/9789811275449_0045

(Figure 1). Semidiurnal tides occur in the estuary, with tidal amplitudes of 5 m at spring tide and 1.5 m at low tide.

Methodology

Major components of the methodology were field visit, various laboratory analyses and model making to be performed. (Figure 2).

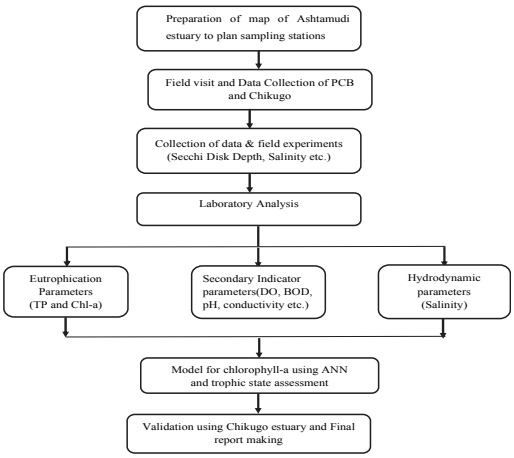

Fig 2: Flowchart of Methodology of the study.

Initially, the geographical map of the region, was studied and stations were marked on the map before the field visit (Figure 3). The data was collected during a neap tide during pre-monsoon season on 11th April,2022 from 12 stations. Two sets of data were collected from each station -one from the surface and the other from Secchi disk depth (SDD). The DO fixation of collected samples were done. At the same time the previous years' data from Pollution Control Board (PCB) was collected and the corresponding data of Chikugo estuary Japan was also acquired for complete analysis. The field SDD was calculated using Secchi disk.

All laboratory analysis were based on the American Public Health Association (APHA) standard methods. The collected data from the Ashtamudi was tested in lab for analysis for the following parameters: TP using spectrophotometry, Chl-a by centrifugation; pH using pH meter, dissolved oxygen and Biochemical oxygen demand (BOD) after 5-day incubation in lab; salinity using Water Quality Analyzer.

Fig 3: Sampling stations in Ashtamudi estuary

The values obtained in each experimental analysis were analysed and data cleaning was done to eliminate the anomalies in the data. Using the PCB data, the inter-relationship between the selected parameters and Chl-a was arrived at and further trophic assessment of the Ashtamudi estuary was done. The influence of salinity on Chl-a was made to study using Total Dissolved Solids (TDS) from the data. The variation of Chlorophyll-a with the influencing parameters was studied and a suitable model using Artificial Neural Networks (ANN) toolbox in MATLAB was developed to predict the concentration of Chlorophyll-a using the PCB data. The data obtained from the Ashtamudi and Chikugo estuaries was then used to validate the predictability of the model.

Table 1: Data for modelling

ESTUARY	DATA PERIOD
Ashtamudi (PCB) data	2013-2018
Ashtamudi (field visit)	Neap tide April 2022
Chikugo	Neap tide April 2010

RESULTS AND DISCUSSION

SSD vs turbidity: The graph in figure 4 is a SSD v/s turbidity graph, and clearly represents an inverse relationship between SSD and turbidity. A power relation with an R^2 value of 0.9889, has been obtained. The equation obtained from this graph was further used to model the input turbidity values of the data from the Pollution Control Board.

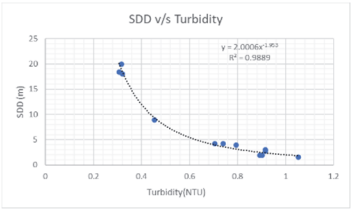

Fig 4: SSD v/s Turbidity graph.

Influence of salinity on Chl-a (with TDS model and without TDS model)

One objective of the study was to identify the influence of salinity on Chlorophyll-a. Two models for Chl-a were developed to showcase the influence of salinity on Chl-a- case (i) considering TDS as an input variable and case(ii) eliminating the TDS input.

Case (i) had three input variables-TP, TDS and turbidity. The ANN model having 10 neurons in the network with R values of 0.99692, 0.99993, 0.99859 for training, validation and testing respectively showed better performance. Figure 4 shows the actual v/s predicted Chl-a of the estuary.

Case (ii) had two input variables- TP and turbidity. The ANN model having R values of 0.98056.0.95233, 0.9945

for training, validation and testing respectively showed better performance. Figure 5 shows the Predicted v/s Measured Chl-a values of case (i) model with a R^2 value 0.9964 and the Predicted v/s Measured Chl-a values of Case (ii) model with an R^2 value of 0.2338

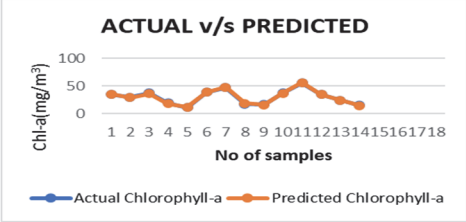

Fig 4: Comparison curve for TDS included Model

Predicting Chlorophyll values using both models yielded the observation that the model considering TDS as input gives a better prediction of Chl-a indicating its strong influence on the same. Case (i) model was identified the better one and was further used for validation.

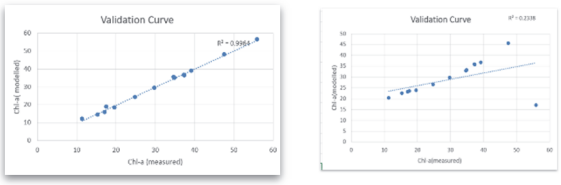

Fig 5: Validation curve for Chl-a (Case (i) and Case (ii))

Validation of Model

Validation using Ashtamudi Data

Case(i) model was validated using the data observed from the neap tide in on Ashtamudi. The Figure 6 shows the comparison curve between measured v/s predicted Chl-a. The validation curve shown in Fig 6 shows that the prediction yielded a regression value of R2=0.9191.

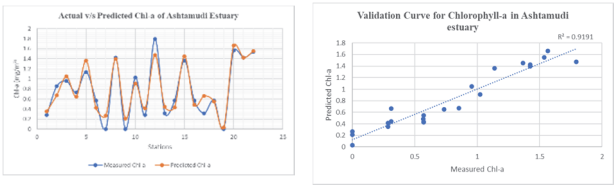

Fig 6: Validation for Ashtamudi

Validation using Chikugo Estuary Data

The case (i) model was further validated using the data from Chikugo estuary Japan. Figure 7 shows the comparison curve between the measured v/s predicted Chl-a. The model predicted the values only with a R^2 value of 0.8147. The decrease in regression value indicates that the model prediction for a different estuary is subject to its unique hydrodynamic and geographic conditions. The variability in measurement techniques for Chl-a is attributed to the change as well.

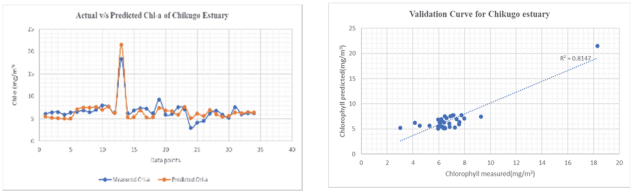

Fig 7: Validation for Chikugo estuary

CONCLUSIONS

The model including TDS as input parameter yielded a R^2 value of 0.9964 and the model omitting TDS yielded a R^2 value of only 0.2338. This indicated that salinity does have a strong influence on Chl-a. The model predicted Chl-a values of Ashtamudi estuary with a R^2 value of 0.9191 and predicted the values of Chikugo estuary with a R^2 value=0.8147. This difference in regression values could be attributed to the fact that for accurate predictions the unique hydrodynamic and geographic conditions of the estuaries must be incorporated. Results obtained from our study indicated that salinity has a strong influence on the Chl-a content in estuaries and it needs to be investigated further considering the salinity variations that can occur in different hydrodynamic states of the estuary.

In conclusion, the ANN modelling technique described above appears to hold promise for the modelling of Chl-a, which could be useful for the inclusive development and maintenance of different estuaries of varying importance.

ACKNOWLEDGEMENTS

APJ KTU CERD Funding worth Rs.50,000/-

References

Azhikodan G. & Yokoyama K. (2016), Spatio-temporal variability of phytoplankton (Ch-a) in relation to salinity, suspended sediment concentration, and light intensity in a macrotidal estuary, Continental Shelf Research 126 (2016) 15–26.

Azhikodan G. & Yokoyama K. (2015), Temporal and Spatial Variation of Mixing and Movement of Suspended Sediment in the Macrotidal Chikugo River Estuary, Journal of Coastal Research, 31-3 680-689; DOI: 10.2112/JCOASTRES-D-14-00097.1.

Shen.J, Kuo A. Y., (1996), Inverse estimation of parameters for an estuarine eutrophication model, Journal of environmental engineering 122(11) 1031-1040.

Sruthy G. S., Priya K. L., Athul M. Madhu, Suchith Chellapan, Adarsh S. and Haddout S., (2021), Fuzzy logic approach for the assessment of trophic state of water bodies, Ecological Eng 169 (2021) 106314.

ON ZONAL WIND DRIVEN CURRENT SYSTEMS IN THE OUTER PLANETARY IONOSPHERES

Chen-Yen Hsu[1], Meng-Tse Yang[2] and Wing-Huen Ip[1,2]

ABSTRACT: During the Cassini Mission, when the spacecraft crossed the D ring, it detected a magnetic perturbation of 15-25 nT. This doesn't arise intrinsically but induced by external currents. Such an unexpected current system can be explained in terms of the dynamo mechanism originated from the difference in the zonal wind speed at the footpoints of the planetary magnetic field lines. In Khurana et al., 2018, the total current is accordingly estimated to be as large as ~7 MA. In this study, we apply the same pattern of the zonal wind-driven currents at the other three outer planets, and find out that the maxima of Jupiter, Uranus and Neptune are 0.20 MA, 0.44 MA and 0.63 MA.

Keywords: Cassini, Field-Aligned Current, Pedersen Current, Zonal Wind, Ionosphere.

INTRODUCTION

During the Grand Finale mission phase of the Cassini project, the Cassini spacecraft moved in a trajectory crossing the equatorial region between the inner edge of the D ring and the upper atmosphere of Saturn. It detected a magnetic perturbation of 15-25 nT, and a strong field-aligned current system is also observed.

This surprising discovery of the magnetic perturbation has to do with the strong magnetic field-aligned current system. The footpoints of Saturn's magnetic field lines are down to the atmosphere; and because of the zonal wind, the two ends of a single field line experience a velocity shear. That will cause the potential differences and thereby generate the Pedersen currents. When the spacecraft flyby, the magnetic field induced by the currents will be detected. In addition, D ring is the innermost ring of Saturn. The magnetic field is relatively strong there. D ring has less dense materials, allowing the currents to pass through. Also, this consequence is related to Cassini's trajectory itself.

According to Khurana et al., 2018, the total current on Saturn is estimated to be ~7 MA. Because Saturn's magnetosphere is axisymmetric, the currents can be expressed as ~1 MA/radian.

Since all outer planets, including Jupiter, Uranus and Neptune, have strong intrinsic magnetic field and zonal wind circulations, it is interesting to explore whether the similar electric currents can be generated as well. In this study, we examine the possible configurations and magnitudes of the zonal wind-driven currents at different outer planets and their possible physical consequences.

ANALYSES

We construct the planetary magnetic field lines and calculate the zonal wind speeds at the footpoints, with the data from the literature.

Spherical Harmonic Models

We use the spherical harmonic (SH) models to build the magnetic field line configurations and surface magnetic fields of the planets. The spherical harmonic models are more advanced than the offset tilted dipole (OTD) models. The formulae in spherical coordinate are expressed as equation (1)~(3).

$$B_r = -\frac{\partial V}{\partial r} = \sum_{n=1}^{\infty}\sum_{m=0}^{n}\left\{(n+1)\left(\frac{a}{r}\right)^{n+2}[g_n^m\, cos(m\phi) + h_n^m\, sin(m\phi)]P_n^m(cos\theta)\right\} \quad (1)$$

$$B_\theta = -\frac{\partial V}{r\partial\theta} = -\sum_{n=1}^{\infty}\sum_{m=0}^{n}\left\{\left(\frac{a}{r}\right)^{n+2}[g_n^m\, cos(m\phi) + h_n^m\, sin(m\phi)]\frac{dP_n^m(cos\theta)}{d\theta}\right\} \quad (2)$$

$$B_\phi = -\frac{1}{rsin\theta}\frac{\partial V}{\partial r} = \frac{1}{sin\theta}\sum_{n=1}^{\infty}\sum_{m=0}^{n}\left\{m\left(\frac{a}{r}\right)^{n+2}[g_n^m\, sin(m\phi) - h_n^m\, cos(m\phi)]P_n^m(cos\theta)\right\} \quad (3)$$

The *g* and *h* values are Schmidt coefficients, which are from in-situ observations and published in literature. The references are listed in Table 1.

[1] Graduate Institute of Astronomy, National Central University, Taoyuan City, TAIWAN
[2] Department of Space Science and Engineering, National Central University, Taoyuan City, TAIWAN

 https://doi.org/10.1142/9789811275449_0046

Table 1. References of used models.

Planet	SH models	Zonal wind
Jupiter	Connerney et al., 2018	Galperin et al., 2001
Uranus	Connerney et al., 1987	Kaspi et al., 2013
Neptune	Connerney et al., 1991 Connerney et al., 1993	

Zonal Wind Speed Distributions

The zonal wind speed distributions are also from in-situ observations and published in literature. The references are listed in Table 1.

Pedersen Current Calculation

With the footpoints of magnetic field lines and zonal wind speeds, we can calculate the Pedersen currents from equation (4) (eq. (3) in Khurana et al., 2018).

$$I_p = \pm \Sigma_p R_{planet} \Delta V_{zonal} B_{eq} cos\theta \quad (4)$$

RESULTS

Due to the tilted magnetospheres, Jupiter, Uranus and Neptune, not like Saturn, have different derived values for each field line (see Fig. 1 and 2-4). Here, we present 16 lines for each planet (separated by 22.5° in azimuth). The magnetic field lines are all at 1.5 planet radius on equatorial plane.

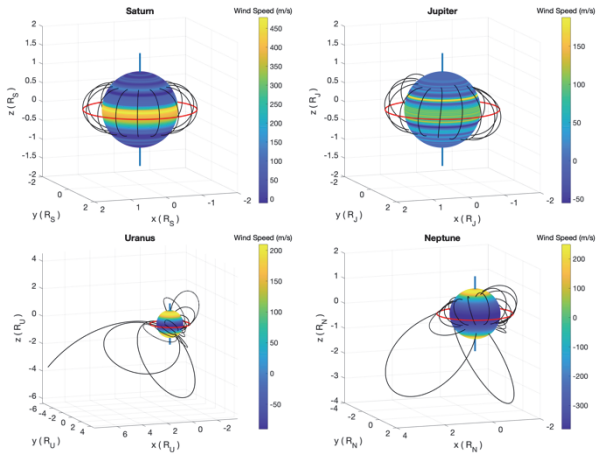

Fig. 1. Field line configurations of Saturn, Jupiter, Uranus and Neptune. The red rings label where L = 1.5.

In our calculations, the currents can reach to 0.20 MA, 0.44 MA and 0.63 MA on Jupiter, Uranus and Neptune, respectively. By integrating the currents or converting to MA/radian, we can obtain the total currents. However, their magnetospheres are tilted and shifted that we cannot derive the total currents simply by multiplied by radian but have to integrate infinite currents.

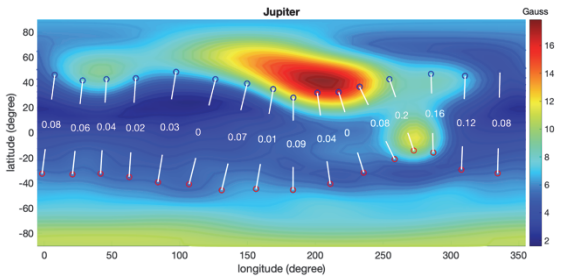

Fig. 2. Calculated Pedersen currents (in MA) of Jupiter. The blue circles represent the northern footpoints; and the red circles represent the southern footpoints.

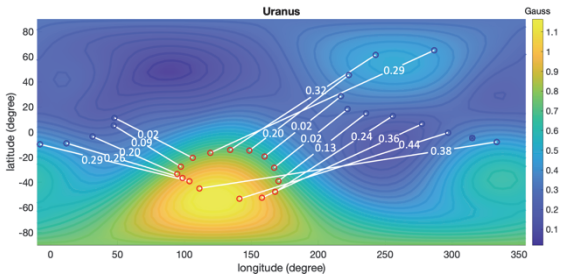

Fig. 3. Calculated Pedersen currents (in MA) of Uranus. The blue cross means that field line has no corresponding southern footpoint. The field line (the open line in Fig.1 Uranus's configuration) is just near the magnetic pole and will be an open line or trace to several R_U away.

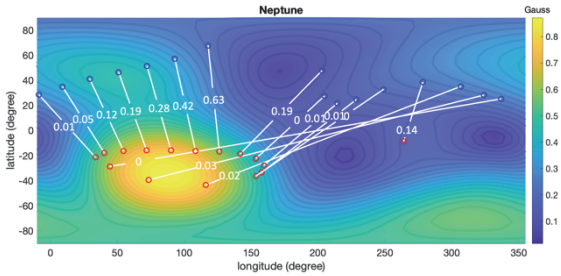

Fig. 4. Calculated Pedersen currents (in MA) of Neptune.

DISCUSSION

Because Saturn's magnetosphere is axisymmetric, as we see in Fig. 1, each line has the same value. If we want to derive the magnetic perturbation of the other three planets, we need to integrate infinite currents with different values. Even if we assume currents are the same everywhere on a single line, it will still be imprecise.

SUMMARY

1. According to Khurana et al., 2018, the detected field-aligned current system on Saturn may be resulted from different zonal wind speeds at the footpoints of

magnetic field lines. We speculate the same phenomenon will also present on the other three giant planets.

2. We utilize the zonal wind speeds and spherical harmonic models to simulate the outer planets' environments.
3. Except for Saturn, the outer planets have tilted magnetospheres. Therefore, all lines have different derived currents. Maximum for each planet:
   - Jupiter: 0.20 MA
   - Uranus: 0.44 MA
   - Neptune: 0.63 MA

References

Connerney, J. E. P. et al., The magnetospheres of Jupiter, Saturn, and Uranus, 1987, Reviews of Geophysics, 25, 615-638

Connerney, J. E. P. et al., The magnetic field of Uranus, 1987, JGR, 92, 15329-15336

Selesnick, Magnetospheric convection in the nondipolar magnetic field of Uranus, 1988, JGR, 93, 9607–9620

Connerney, J. E. P. et al., The magnetic field of Neptune, 1991, JGR, 96, 19023-19042

Connerney, J. E. P. et al., Magnetic fields of the outer planets, 1993, JGR, 98, 18659-18680

Galperin et al., Universal n^{-5} spectrum of zonal flows on giant planets, 2001, Physics of Fluids, 13, 1545-1548

Nichols and Cowley, Magnetosphere-ionosphere coupling currents in Jupiter's middle magnetosphere: effect of precipitation-induced enhancement of the ionospheric Pedersen conductivity, 2004, Annales Geophysicae 22, 1799–1827

Kaspi et al., Atmospheric confinement of jet streams on Uranus and Neptune, 2013, Nature, 497, 344-347

Khurana et al., Discovery of Atmospheric-Wind-Driven Electric Currents in Saturn's Magnetosphere in the Gap Between Saturn and its Rings, 2018, GRL, 45, 10,068-10,074

Cao et al., The landscape of Saturn's internal magnetic field from the Cassini Grand Finale, 2020, Icarus, 344, 113541

NUMERICAL MODELLING OF THE SIZE AND TEMPERATURE VARIATIONS OF STAR SPOTS AND BRIGHT FACULAE OF MAGNETICALLY ACTIVE STARS FROM THE TRANSIT LIGHT CURVES

Tzu-Heng Chang[1], Chia-Lung Lin[1] and Wing-Huen Ip[1,2]

ABSTRACT: It is known that small-scale structures in the transit light curves of exoplanets can be used to infer the sizes and temperatures of dark spots or bright faculae of their host stars. Among many factors, the precision depends on the observational statistics, the ratio of the size of the exoplanet to that of the dark (or bright) spot and the cadence used in the light curve measurements. We have developed a numerical code allowing us to explore the effects and limitations of such a method for stars of different spectral types.

Keywords: Exoplanet, Transit, Starspots

INTRODUCTION

In addition to the radial velocity method which has been used to discover the first exoplanet, 51 Pegasi b, by Mayor & Queloz (1995), the transit measurement is another method to detect exoplanets. Indeed, since the finding of HD 209458b by Charbonneau et al. (2000) and Henry et al. (2000), the number of detected exoplanets has mushroomed dramatically, especially, because of the high photometric light curve data provided by the Kepler space telescope. The study of the physical properties of exoplanets has also advanced from the determination of the sizes, masses, and orbital parameters of the exoplanets to the compositions and structures of their atmospheres by the new method of transmission spectroscopy (Kreidberg(2018)). As consequence, it is also clear that the heterogeneous structures of the stellar surfaces because of magnetic activities such as dark spots and bright faculae could have strong effects on the interpretation of the transmission spectra of the exoplanetary atmospheres to be obtained by missions like JWST and ARIEL. It is for this reason that we have embarked on the construction of a numerical code that will allow us to simulate the light curves and spectra of the host stars of exoplanets under different conditions. As disk-resolved stellar photometry or spectra go, the most basic thing is to in-build the limb darkening effect as it will affect the general structures of the transit light curves. The next thing is to synthesize fine features in the exoplanet transit curves resulting from occultation of dark (cold) spots or bright (hot) active regions or faculae. A comparison of the computational results with high-quality transit light curves will lead to a better understanding of the temperature and size distributions of such small-scaled regions.

LIMB-DARKENING EFFECT

Because of the optical depth effect, the brightness intensity of a star is maximum at the disk center ($\theta = 0°$) and decreases gradually until reaching the limb ($\theta = 90°$).

There are many different ways to describe the limb darkening effect (Sing (2010)). One most often used is the wavelength-dependent quadratic law,

$$\frac{I(\mu)}{I} = 1 - a(1-\mu) - b(1-\mu)^2 \qquad (1)$$

where I_c is the central intensity at the disk center, and $\mu = \cos\theta$, and a and b are the limb-darkening coefficients characteristic of the central star.

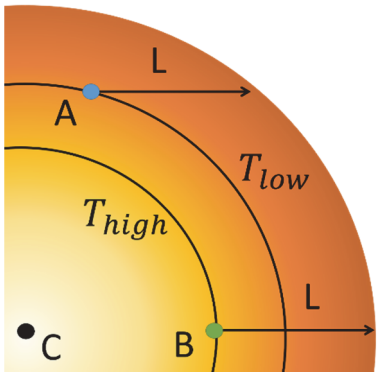

Fig. 1. An illustration of the limb darkening effect with C being the stellar disk center, L being the lights-of-sight, a and b are locations where the respective optical depth is about unity; finally, T_{high} and T_{low} are referred to the temperature profile in the stellar atmosphere.

SIMULATION

In order to simulate the brightness intensity distribution of a host star with a transiting exoplanet, a code with a set of 600x600 grids is generated as illustrated

[1] Graduate Institute of Astronomy, National Central University, Taoyuan, TAIWAN (R.O.C.).
[2] Department of Space science and Engineering, National Central University, Taoyuan, TAIWAN (R.O.C.).

 https://doi.org/10.1142/9789811275449_0047

in Figure 2. The stellar effective temperature is given to be T_* from which the brightness intensity can be approximated by the blackbody radiation. As an example, the physical parameters of the central star are adopted from the work of Valio et al. (2017). Also listed in Table 1 are the physical parameters of the exoplanet assumed to be in circular orbit on the equatorial plane with the stellar rotation axis assumed to be exactly perpendicular to the light-of-sight.

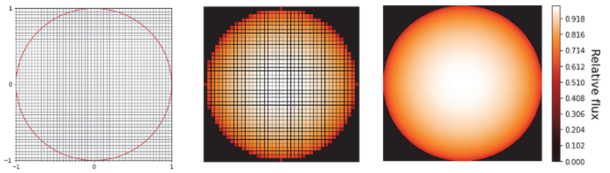

Fig. 2 Schematic views of the numerical model produced to generate exoplanet transit light curves. Left: a simplified computational model with 50×50 grids. Middle: The grid model superimposed on the stellar disk with the limb darkening effect. Right: The brightness intensity of the stellar disk without the grids.

Table 1. Planetary parameters of simulation.

Parameters	Values
Star	
Mass ($M_\odot$)	1.16
Radius ($R_\odot$)	1.05
Effective Temperature (K)	5780
Rotation Period (day)	12.4
Linear limb-darkening Coefficient a	0.44
Quadratic limb-darkening Coefficient b	0.1
Planet	
Mass (M_J)	2.45
Radius (R_{star})	0.1
Orbital Period (day)	1.48571
Semi-major Axis (R_{star})	5.738
Inclination Angle (degree)	90

Figure 3 compares the transit lights obtained by assuming different sizes of the exoplanet, namely, $R_p = 0.05\ R_*$, $R_p = 0.10\ R_*$ and $R_p = 0.15\ R_*$ indicating the sensitivity of the planetary radius to the transit light curve depth (σ).

SPOTS AND FACULAE

As shown in previous studies of the light curves with periodic variations from the Kepler observations, low-mass stars can have very large dark spots on their surfaces (Schmieder(2018)). Crossing of these localized regions with cooler temperatures (i.e., $T_{spot} < T_*$) can produce interesting features in the transit light curves (Namekata et al.(2019)).

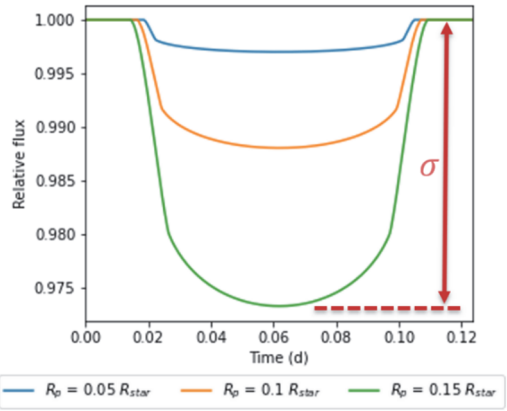

Fig. 3. Simulation results of three different radii of the transiting exoplanet.

That is, the light curve during the time interval of spot transit will actually display an intensity increase because of an over-subtraction effect. By the same token, an intensity drop will appear during crossing of a bright facula or active region of higher temperature (i.e., $T_{facula} > T_*$). Such temperature-dependent brightness variations can be demonstrated by considering three different "spot" temperatures, namely, $T_{spot} = 4780$ K, 5100 K and 6780 K, by noting that $T_* = 5780$ K (see Table 1). Figure 4 compares these three cases by assuming $R_p = 0.1\ R_*$.

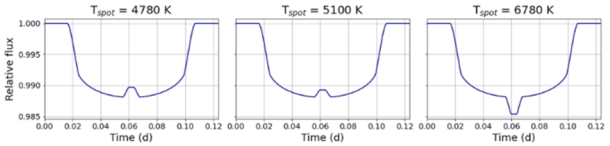

Fig. 4. Simulation results of three different spot temperatures on the stellar disk.

Other parameters in the shape of the small-scaled structures as described above have to do with the sizes of the exoplanet and the spot, respectively. If the exoplanet radius is known beforehand but not the spot size, different shape models will result as shown in Figure 5. It is possible that with transit light curves of high photometric accuracy, the spot size and temperature might be derived by best-fitting the observational data with the synthetic curves.

SUMMARY AND FUTURE WORKS

In preparation for new measurements of transmission spectroscopy of exoplanetary atmospheres that might be "contaminated" by spatially and temporally variable heterogeneous features on the surfaces of the host stars, we have built a grid model of the brightness intensity distribution of the stellar disks with limb darkening effects. The basic structure of the numerical model and its potential applications in the photometric determination of

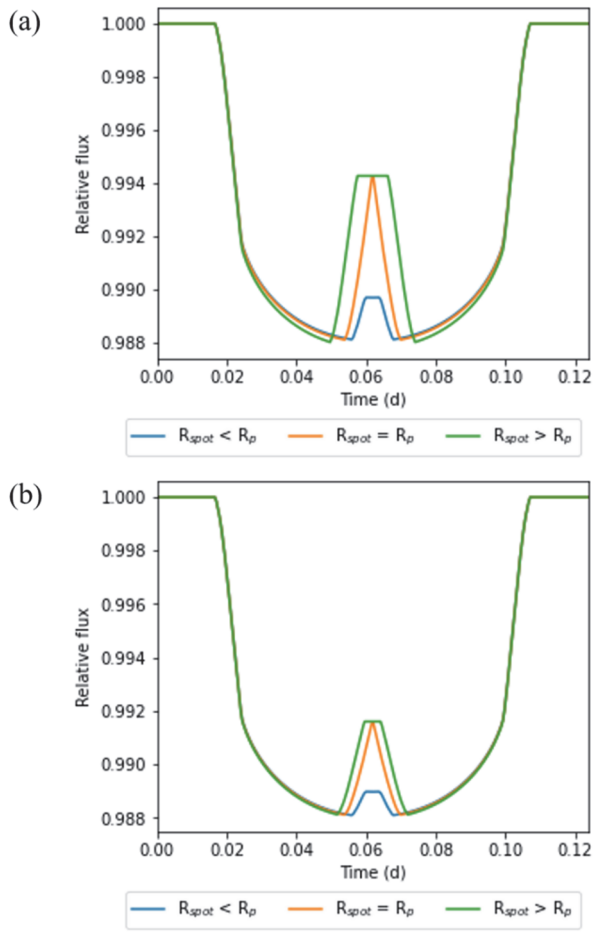

Fig. 5. Simulation results of three different spot sizes, i.e., $R_{spot} = 1.5\ R_p$, $1.0\ R_p$ and $1.5\ R_p$, respectively: (a) $T_{spot} = 4780$ K; (b) $T_{spot} = 5280$ K.

the spot sizes and temperatures are briefly described here. In a future publication, we will report on the preliminary results obtained from the analysis of the Kepler light curves of two solar-type stars, Kepler-17 and Kepler-71. We know that our grid model can, in principle, be modified to implement stellar spectral distribution across the stellar disks. Such an application will provide us the exciting prospects of investigating the physical properties of the spots and faculae in detail as well as the atmospheric compositions and structures of a wide range of exoplanets - including those super-Earth with potential habitability.

ACKNOWLEDGEMENTS

We wish to thank Chia-Lung Lin, Yu-Hsiang Weng, and Yao Hsiao for the information and useful discussions. This work is supported in part by MOST 111-2112-M-008-014.

References

Brown, T. M., Charbonneau, D., Gilliland, R. L., et al. 2001, ApJ, 552, 699.

Charbonneau, D., Brown, T. M., Latham, D. W., et al. 2000, ApJL, 529, L45.

Henry, G. W., Marcy, G. W., Butler, R. P., et al. 2000, ApJL, 529, L41.

Jha, S., Charbonneau, D., Garnavich, P. M., et al. 2000, ApJL, 540, L45.

Kreidberg, L. 2018, Handbook of Exoplanets, 100.

Mayor, M. & Queloz D. 1995, Nature, 378,355.

Namekata, K., Maehara, H., Davenport, J., et al. 2019, Solar Heliospheric and INterplanetary Environment (SHINE 2019).

Schmieder, B. 2018, Journal of Atmospheric and Solar-Terrestrial Physics, 18

Silva, A. V. R. 2003, ApJL, 585, L147.

Sing, D. K. 2010, A&A, 510, A21

Valio, A., Estrela, R., Netto, Y., et al. 2017, ApJ, 835, 294.

NON-THERMAL ESCAPE OF HOT OXYGEN FROM MARTIAN ATMOSPHERE

H.S. Shi[1], Y. Ma[2] and W.H. Ip [1,3]

ABSTRACT: The non-thermal escape via the production of hot oxygen atoms from the electron recombination dissociation of the O_2^+ molecules is known to be the most important atmospheric loss mechanism of Mars. The numerical modelling of such a dynamical process usually used to be done by assuming a static Martian ionosphere. In this study, we examine the effect caused by the flow field in the lower Martian ionosphere by coupling the standard collisional dynamics of the hot oxygen atoms to the MHD model of the Martian ionosphere according to Ma et al. 2004. We will compare hot oxygen escape rate with and without ionospheric flows.

Keywords: Mars, Martian Atmosphere, Hot Oxygen, Particles

INTRODUCTION

Mars was once rich in the liquid water on its surface, and there were studies discussed the process of losing water molecules, such as Jeans escape of hydrogen and ion sputtering of oxygen. One of a critical process of the oxygen loss in the Martian atmosphere is the photochemical escape of oxygen atoms (Wallis, 1978; Ip, 1988; Cravens et al., 2017; Jakosky et al., 2018). The O_2^+ ion is the chemical consequence of $O^+ + CO_2 \rightarrow O_2^+ + CO$ and $CO_2^+ + O \rightarrow O_2^+ + CO$ which provide a large amount of O_2^+ ions in CO_2-rich atmosphere on Mars, and the oxygen atoms will get the excess energy from the process of electron dissociative recombination reaction of the major components of the Martian ionosphere, O_2^+. Table 1 shows the four reaction channels of the oxygen ions (O_2^+) electron dissociative recombination (DR) with their likelihood. It was suggested that if the by-product, oxygen atoms (O), receive more than 2 eV, it will receive the kinetic energy exceeding the required energy to escape Mars. (McElroy, 1972) .

Table 1 Four channel of dissociative recombination reaction of oxygen ions with electrons (Lillis et al. 2017)

Initial State	Final State	Likelihood
$O_2^+ + e \rightarrow$	$O(^3P)+O(^3P)+6.99$ eV	26.5%
	$O(^1D)+O(^1P)+5.02$ eV	47.3%
	$O(^1D)+O(^1D)+3.06$ eV	20.4%
	$O(^1D)+O(^1S)+0.83$ eV	5.8%

In the first part, we calculate the production rate of the hot oxygen and distribute the energy from the reaction likelihood at the altitude between 100 km and 450 km above the surface of Mars. In the second part, the dynamic process of the hot oxygen atoms which collide with the neutral gas in Martian atmosphere would be simulated. The influence with and without the plasma flow also will be considered in this step. The discussions and the comparisons with the ionospheric flows are given in the last section.

PRODUCTION OF HOT OXYGEN

The production rate of the hot oxygen atoms is related to the environment as function of electron temperature and the molecules density, which can be calculated by the following equation :

$$R_{Hot\,O}(z) = 2n_e(z)n_{O_2^+}(z)k(T_e(z)) \quad (1)$$

where $n_{O_2^+}$ is the O_2^+ ion density, n_e is the electron density, and k is the dissociative recombination (DR) rate coefficient, which is a function of electron temperature (Petrignani et al., 2005):

$$k = 1.95 \times 10^{-7}\left(\frac{300}{T_e}\right)^{0.70} cm^3 s^{-1} \quad (2)$$

We use the data of O_2^+ ions density and electron temperature from Ma et al. 2004. Figure 1 shows the distribution of the hot oxygen production rate in the equatorial plane (90 degree toward to the Sun) at the Martian altitude from 100 km to 450 km. The large number density of O_2^+ ions is supported by the electron transfer reactions on the sun-lit facing side of the carbon dioxide-rich atmosphere in lower altitude, and thus

[1] Department of Space Science & Engineering, National Central University, No.300, Zhongda Rd., Zhongli Dist., 32001, TAIWAN
[2] Department of Earth, Planetary and Space Sciences, University of California, Los Angeles, CA, 90095, UNITED STATES
[3] Institute of Astronomy, National Central University, No.300, Zhongda Rd., Zhongli Dist., Taoyuan City 32001, TAIWAN

 https://doi.org/10.1142/9789811275449_0048

contributes to the high production rate of the post-DR hot oxygen. In this figure, the highest production rate of hot oxygen atoms is concentrated at the altitudes of 140 km to 160 km at 90 degree.

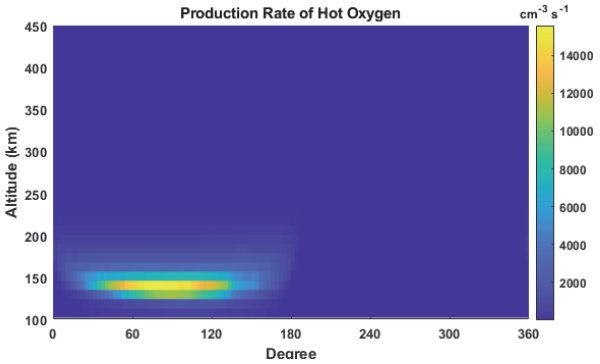

Figure 1 The production rate of hot oxygen by considering the oxygen ions and the electron temperature from Ma et al. (2004).

PARTICLE MOTION SIMULATION

A Monte Carlo method is developed to judge the motion of the hot oxygen atoms. The oxygen fragments of DR reaction share the excess energy which is determined by the ratio of four reaction channels. Because the motion of the oxygen ion will be accelerated by the DR reaction to increase the velocity, v_{DR}, based on the speeds of Maxwell–Boltzmann distribution with isotropic distribution in the Martian ionosphere, v_0, the initial velocity of an oxygen atom will be:

$$v_{Hot\,o} = v_0 + v_{DR} \tag{3}$$

Two new oxygen atoms will move in opposite direction, colliding with the Martian atmospheric molecules such as carbon dioxide and carbon monoxide during their motion. The collision probability (P) of an oxygen atom traveling for a distance S is given by:

$$P = 1 - \exp\left(-\frac{S}{\lambda}\right) \tag{4}$$

where S is the moving distance of an oxygen atom between two collisions, and λ is the local mean free path of the oxygen in different altitude, which is related to the number density and the velocity of collided molecules:

$$\lambda = \frac{v_{th}}{v_r \sigma n_{air}} \tag{5}$$

where v_{th} is the thermal velocity of the hot oxygen, v_r is the relative velocity between hot oxygen and the background gas molecules, n_{air} is the local atmospheric number density, and σ is the collisional cross section. (Bird, 1994) In this model, the oxygen ions also flow with the plasma flow field, U_{flow}, which was constructed by Ma et al. (2004) and shown in Figure 2. The plasma velocity in the lower Martian ionosphere is roughly less than 0.1 km/s. Thus, the total velocity of a hot oxygen can be written as:

$$v_{Hot\,o} = v_0 + v_{DR} + U_{flow} \tag{6}$$

In this test particles simulation, we choose the profile with the highest production rate of the hot oxygen on Mars (at 90 degree, shown in Figure 1). We divide the altitudes from 100 km to 350 km into 24 grids, and generate 1000 test particles in each grid for a series of chemical reactions and collisions. The upper boundary of the simulation is set to be an altitude of 450 km.

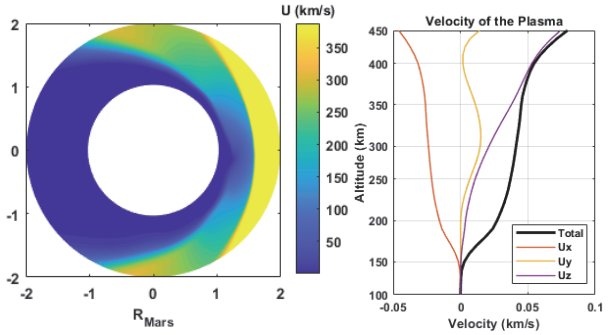

Figure 2 (Left) The total velocity distribution of plasma in the equatorial plane (Right) The velocity component profile of plasma at the altitude of 100 km to 450 km on the sun-lit facing side.

RESULTS

An example on the sun-lit facing side of the hot oxygen energy probability distribution below the altitude of 450 km without the effect of ionospheric plasma is shown in Figure 3.

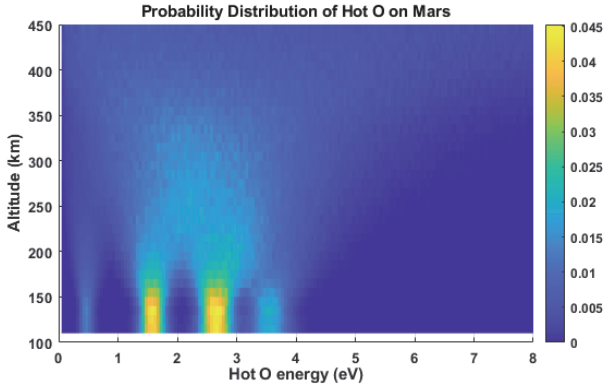

Figure 3 The energy probability (probability of per 0.05 eV) of hot oxygen at the altitude from 100 km to 450 km through the Maxwell-Boltzmann distribution on the sun-lit facing side (in 90 degree).

Below the altitude of 200 km, the energy distribution presents four distinct channels with an average about 0.5 eV, 1.7 eV, 2.6 eV, and 3.7 eV, respectively, while more than the altitude of 250 km of energy distribution becomes uniform. The escape energy on the surface of Mars is 2.1 eV, and that at an altitude of 450 km on Mars is reduced 1.85 eV. Therefore, it means that the escape probability of the hot oxygen at higher altitudes will be higher than those at lower altitudes.

Figure 4 presents the preliminary results of the ratio of the hot oxygen velocity of in 90 degree with and without the plasma flow field at the altitude of 450 km. In this simulation, only 88% of the 24,000 test particles had enough energy to reach the upper boundary at 450 km altitudes. The three peaks in Figure 4 are 4.6 km/s, 5.8 km/s, and 6.6 km/s. The escape velocity of Mars at 450 km altitude is 4.78 km/s. In this terminal velocity distribution, about 72.3% of the hot oxygen atoms exceed the escape speed in the case with the plasma flow, and 70.6% without the flow field. The ratio of the escape oxygen with flow field is about 2% higher than that without flow field.

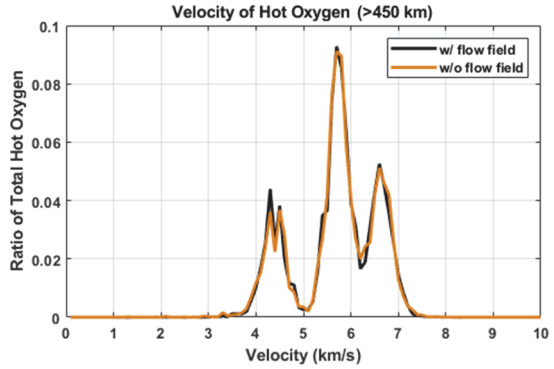

Figure 4 A comparison of the velocity distributions of the hot oxygen atoms with and without ionospheric flows after dissociation and collisional thermalization.

DISCUSSION AND FUTURE WORK

This study presented the preliminary work of the effect of plasma flow field on hot oxygen in the lower Martian atmosphere. Although the energy distribution of the DR reaction has four channels, the energy provided by the 0.4 eV channel cannot accelerate oxygen atoms much. As a result of collisions between low-energy hot oxygen and the gas particles in Martian atmosphere, most of the hot oxygen will not be able to move up to the altitude of 450 km, so the terminal velocity distribution has only three peaks.

The speed of the flow field in the lower Martian ionosphere at 90 degree is about 0.05 km/s, and has a slight effect on the escape rate of hot oxygen, especially the low-energy hot oxygen. These preliminary results only focus on a single region with high sunlit energy and high atmospheric number density. It presents the number of the hot oxygen atoms that can reach an altitude of 450 km, whether their travel direction allows them to escape Mars should be discussed. In the next step, we will further increase the number of the test particles and apply this simulation to the entire Martian equatorial plane, and compare the oxygen loss rate in these two environments.

ACKNOWLEDGEMENTS

This work is supported by MOST 111-2112-M-008-014.

References

Bird, G. A. (1994). Molecular Gas Dynamics and the Direct Simulation of Gas Flows. Oxford: Clarendon Press.

Cravens, T. E., Rahmati, A., Fox, J. L., Lillis, R., Bougher, S., Luhmann, J., Sakai, S., Deighan, J., Lee, Y., Combi, M., & Jakosky, B. (2017). Hot oxygen escape from Mars: Simple scaling with solar EUV irradiance. Journal of Geophysical Research: Space Physics, 122(1), 1102–1116.

Ip, W.-H. (1988). On a Hot Oxygen Corona of Mars. ICARUS, 76, 135–145.

Jakosky, B. M., Brain, D., Chaffin, M., Curry, S., Deighan, J., Grebowsky, J., Halekas, J., Leblanc, F., Lillis, R., Luhmann, J. G., Andersson, L., Andre, N., Andrews, D., Baird, D., Baker, D., Bell, J., Benna, M., Bhattacharyya, D., Bougher, S., … Zurek, R. (2018). Loss of the Martian atmosphere to space: Present-day loss rates determined from MAVEN observations and integrated loss through time. Icarus, 315, 146–157.

Lillis, R. J., Deighan, J., Fox, J. L., Bougher, S. W., Lee, Y., Combi, M. R., Cravens, T. E., Rahmati, A., Mahaffy, P. R., Benna, M., Elrod, M. K., McFadden, J. P., Ergun, R. E., Andersson, L., Fowler, C. M., Jakosky, B. M., Thiemann, E., Eparvier, F., Halekas, J. S., … Chaufray, J. Y. (2017). Photochemical escape of oxygen from Mars: First results from MAVEN in situ data. Journal of Geophysical Research: Space Physics, 122(3), 3815–3836.

Ma, Y., Nagy, A. F., Sokolov, I. V., & Hansen, K. C. (2004). Three-dimensional, multispecies, high spatial resolution MHD studies of the solar wind interaction with Mars. Journal of Geophysical Research: Space Physics, 109(A7).

McElroy, M. B. (1972). Mars: An evolving atmosphere. Science, 175(4020), 443–445.

Petrignani, A., Hellberg, F., Thomas, R. D., Larsson, M., Cosby, P. C., & van der Zande, W. J. (2005). Electron energy-dependent product state distributions in the dissociative recombination of O +2. Journal of Chemical Physics, 122(23).

Wallis, M. K. (1978). Exospheric density and escape fluxes of atomic isotopes on Venus and Mars. Planetary and Space Science, 26(10), 949–953.

STATUS OF JIANGSU REGIONAL ALL-SKY FIREBALL NETWORK IN CHINA

Zhijian Xu[1,2] and Haibin Zhao[1,3,4]

ABSTRACT: At present, several meteor monitoring networks have been established worldwide. However, in China, the research on fireball monitoring is still unsystematic, and the monitoring network is in its initial stage. Jiangsu Regional All-sky Fireball Network (JRAFN), covering the entire region of Jiangsu Province and surrounding areas, consists of 10 stations with the baseline being 50~110km. The video camera used is QHY5III485C with a 2.5mm/f1.6 fisheye lens to achieve a local all-sky field of view, detecting limiting magnitude -1 for meteors, and +3 for stellar, at 20 frames per second. All observation data are uploaded to the central server at the Purple Mountain Observatory (PMO). Since September 2021, hundreds of meteors and several fireball events were recorded, including a super-bright fireball that occurred in Henan Province. The main purpose of this monitoring network is to perform long-term meteor and fireball surveillance, and to obtain the radiation, flux and size distribution of fireballs. We also aim to determine the fall point of the meteorites and recover them by calculating the trajectories and orbits of the fireballs, from single-station system extended to a future nationwide fireball monitoring network of China.

Keywords: Meteorites, meteors, meteoroids.

INTRODUCTION

From 2017 to 2022, in China, there has been at least one super-bright fireball event per year, which has the potential chance to recover meteorites. These fireball events are captured by security surveillance, car recorders, or inadvertently captured by people, so it is difficult to determine the location of meteorite falling. Those recovered meteorites can provide important clues of nature of planets and small Solar System bodies and help to study the early evolution of the solar system (Wasson 1985). Probability of fireball occurrence can help us assess impact risk of meter or sub-meter NEOs. Several meteor monitoring networks have been established worldwide, such as GFO network (Devillepoix et al. 2020), FRIPON network (Colas et al. 2020), but still unsystematic in China.

We report on developing a prototype network of fireball monitoring: Jiangsu Regional All-sky Fireball Network (JRAFN), to perform long-term meteor and fireball surveillance in the region of Jiangsu province and surrounding areas, China.

INSTRUMENT

In JRAFN, 10 fireball monitoring stations will be constructed, with baselines between two closed stations of 50 ~ 150km, to monitoring an area over Jiangsu and surrounding cities of more than 100,000 km². From September 2021 to July 2022, six stations have been in operation successively (see Fig. 1).

Fig. 1. Geographical location of stations, the stations marked in red are already in operation, and marked in blue will be setup soon.

The video camera is QHY5III485C with Sony IMX485, back-illuminated, color CMOS sensor, a 2.5mm/f1.6 fisheye lens to get a local all-sky field of view, and an industrial mini-computer as a control terminal (see

[1] Key Laboratory of Planetary Sciences, Purple Mountain Observatory, Chinese Academy of Sciences, Nanjing 210023, CHINA
[2] China Three Gorges University, Yichang 443002, CHINA
[3] School of Astronomy and Space Science, University of Science and Technology of China, Hefei 230026, CHINA
[4] CAS Center for Excellence in Comparative Planetology, Chinese Academy of Sciences, Hefei 230026, CHINA

 https://doi.org/10.1142/9789811275449_0049

Fig. 2). The camera recorded at a rate of 20 frames per second (20fps) with a resolution of 1440×1088 pixels (BIN2 of original image) video mode, the system can observe approximately magnitude +3 for stellar and brighter than magnitude -1 for meteor.

The camera and lens protect in a weatherproof metal enclosure, using a flat-roof or pole mount. Only need a USB 3.0 cable to connect to the industrial mini-computer. An SSD to cache video files in recent days, and a 1TB hard disk to store all video files. All observation data also be uploaded to the central server at the Purple Mountain Observatory, the stations and central server are off-site backups of each other.

Fig. 2. Main equipment components.

OBSERVATIONS AND RESULTS

The brightness change triggered by a meteor on the CCD chip can be captured by the moving object detection program. Meteor recording clips are done via a video frame cache queue, some frames (usually set to 45 frames) before the trigger can be recorded. The recording clips typically provide 20 to 40 reference stars brighter than magnitude +3, so we can carry out the astrometric calibration. The astrometric solution is accomplished by the program through an iterative least squares minimization process of the residuals of the distance between the reference stars and catalog stars. Based on time-stamp of detection recording the program has the ability to detect double-station events automatically. A plane can be fit through station and measurement positions of meteor, the intersection of every pair of planes results in a line which describes the trajectory as measured from two stations. For the case of multi-stations, we calculate the weight of each station according to the perspective angles. Having obtained the parameters of the trajectory, the Keplerian orbit of the meteor can be calculated.

From Sep 2021 to Apr 2022, a total of about 1500 meteors were detected in all Stations. The proportion of multi-detections for each station is shown in Fig. 3a. Due to the lower sky-background brightness, Xuyi station detected the most meteors among all the stations, while the proportion of multi-station detections vs all detections is the lowest because many fainter meteors cannot be matched with the other stations. In Fig. 3b of monthly statistics, the peak showing in December is likely explained by the Geminids meteor shower. Fig. 3c is the histogram of the absolute magnitude of all events detected by the network, which shows that the exhaustive detection regime can reach around magnitude -3.

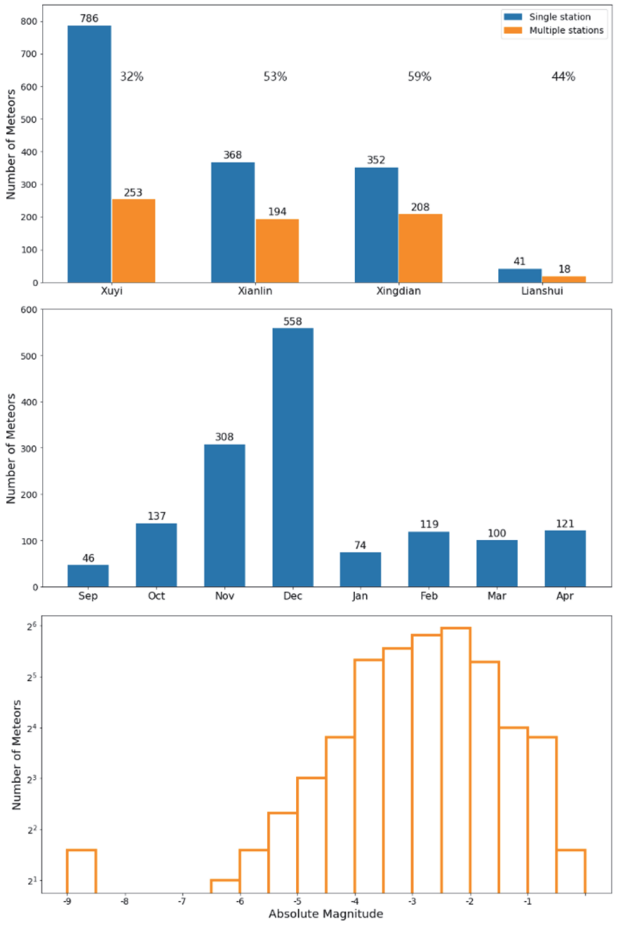

Fig. 3. (a) The proportion of multi-station detections for each station; (b) Monthly statistics of single-station detections for all stations; (c) The exhaustive detection regime of the network.

Until now, nearly 30 fireballs were obtained multi-station detecting. A super-bright fireball occurred in Henan Province was captured at 18:06:48 UTC on November 28, 2021 by Xuyi station. Although the fireball appeared at a very low altitude, with an extreme 450km far away, it still lightened the surroundings (see Fig. 4).

Another bright fireball with brightness of -10 mag was captured by two stations of monitoring network at 13:29:22 UTC, May 22, 2022. Due to the thin cloud, the bright fireball produced a very rare fireball-halo.

The analysis of this fireball is shown in Fig. 5. The second half of the fireball is shaded by cloud, only partial light-curve is available, at Xianlin station. The trajectory is located from Laian County (118.448°E, 32.488°N) to Dingyuan County (117.861°E, 32.503°N), from altitude 91.1 km to 45.4 km. According orbit determination, the meteoroid is an Apollo-type object (a=1.8AU, e=0.636, incl=32.8°) with geocentric velocity of 25.2km/s.

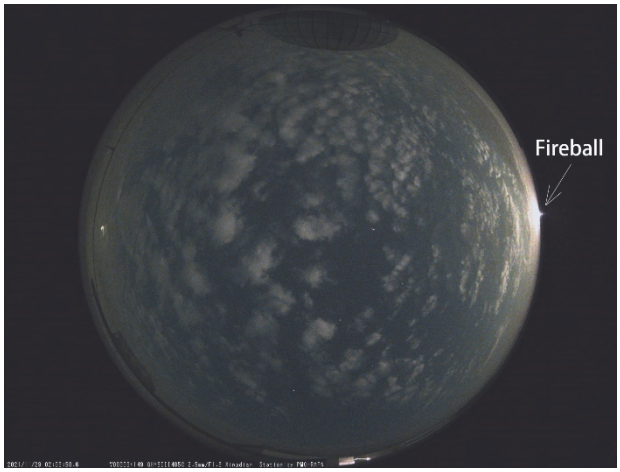

Fig. 4. The super-bright fireball occurred in Henan Province, at the position indicated by the arrow.

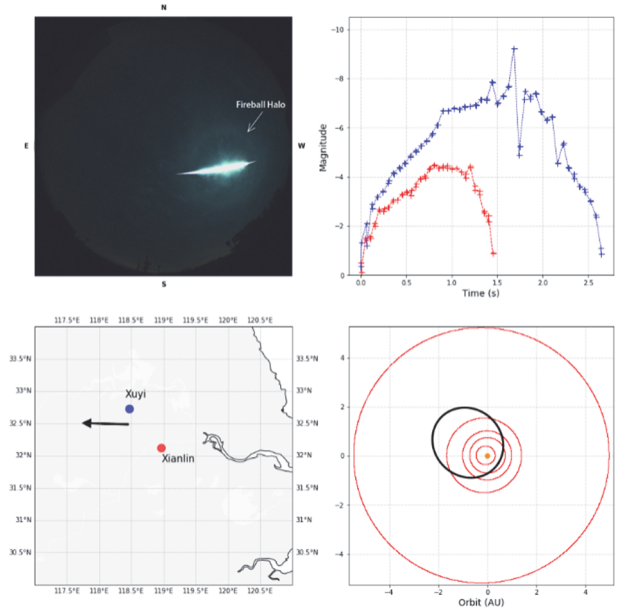

Fig. 5. Analysis results for FB20220522

CONCLUSIONS

The monitoring and investigation of fireballs play an important role in asteroid impact assessment and early solar system research. In this work, a prototype network of fireball monitoring is under construction, detected dozens of fireballs as well as hundreds of meteors, some of which have been obtained trajectories and orbits. The feasibility of the fireball monitoring network is verified. It has laid a solid foundation for the establishment of a region-wide fireball monitoring network in China.

In the future, a plan will address the following action-items: 1. Keep working on software developments and hardware improvements, including software development, multiple mounting alternatives, add 4G wireless module and solar-powered, and add Meteor Spectrum equipment. 2. Complete all station installations and plan new stations in neighboring cities to cover the East China area.

ACKNOWLEDGEMENTS

This research is funded by Space debris and NEO research project (Nos.KJSP2020020204 & KJSP2020020102) and Minor Planet Foundation. In addition, we wish to thank many amateur astronomers and individuals who provide observation stations and maintain the facilities.

References

Wasson, J. T. (1985). Meteorites: Their Record of Early Solar-system History (New York, NY: Freeman).

Devillepoix, H.A.R., Cupák, M., Bland, P.A., et al., (2020). A global fireball observatory. PLANSS 191, 105036.

Colas F., et al., (2020). FRIPON: A worldwide network to track incoming meteoroids. Astronomy & Astrophysics, 644, A53.

A NUMERICAL SIMULATION OF THE 3D STRUCTURE OF THE NEAR-SOLAR DUST ZONE ACCORDING TO β-METEOROID MEASUREMENTS AT HIGH INCLINATION

Yi-Shiang Tzeng[1] and Wing-Huen Ip[2]

ABSTRACT: The β-meteoroids are high-speed submicron dust particles that come from the near-sun region. After breaking up from larger bodies as a result of the collisional process, or sublimation for smaller sizes, these small grains will be accelerated radially forward by solar radiation. Their detectability has been testified by measurements with instruments on multiple spacecraft. Among these spacecraft, Solar Orbiter (SolO) will be the first spacecraft to explore the high-altitude dust distribution with its high inclination orbits in the later phase of the mission. In this work, we examined the 3D structure of the near-solar dust zone with a simple model based on the Parker Solar Probe (PSP) observations and the theoretical dynamics of β-meteoroids governed by gravity-to-radiation ratio β = 0.7. The results show a distribution of β-meteoroid fluxes restricted to ± 36.7° out of the ecliptic plane because of the assumed orbital inclination of grains in the F-corona and demonstrate the impact rates of the first six PSP orbits qualitatively consistent with the observations. Despite further calibrations with the size distribution of the near-solar dust population and the collisional production rates of the sub-micron dust grains being needed, we expect future studies of the physical properties of grains will improve our model.

Keywords: meteoroids, zodiacal dust, numerical simulation, dust impacts

INTRODUCTION

Because of the feeding of dust particles spiraling in from the asteroid belt and cometary meteoroid streams because of the Poynting-Robertson effect, a dust zone near the Sun is formed. Its brightness distribution of this dust cloud ranging up to tens of solar radii called F-corona has been studied by ground-based measurements and space observations in past (see Kimura & Mann, 1998). Solid grains in the F-corona will be lost via thermal sublimation because of the intense solar heating and collisional erosion or breakup. The latter process continuously generates a flux of sub-micron-sized particles that will be accelerated outward by the solar radiation pressure. Such outward-escaping small dust particles in high-speed radial motion (called β-meteoroids) have been detected by instruments on Pioneer 8 and 9 (Berg & Grün 1973), Helios (Grün et al. 1980), Ulysses (Wehry & Mann 1999; Wehry et al. 2004) and STEREO (Zaslavsky et al. 2012). The Parker Solar Probe (PSP) and Solar Orbiter (SolO) have also provided brand-new data (Page et al. 2020; Szalay et al. 2021; Zaslavsky et al. 2021).

Indeed, PSP's plasma wave experiment detected numerous β-meteoroid impact events in its first few orbits around the Sun (Page et al. 2020); its imaging camera also provided a 2D brightness distribution of the F-corona and hence the source region of the β-meteoroids (Stenborg et al. 2021). Interestingly, the SolO's planned inclined orbits will allow a close-up study of the β-meteoroid flux above the ecliptic plane (Zaaslavsky et al. 2021). In this work, we venture to examine how the 3D structure of the near-sun dust zone might be derived by combining the remote-sensing observations, the in-situ dust impact measurements, and theoretical simulation of the orbital dynamics of the β-meteoroids.

MODEL CALCULATION

In our simple model, the near-sun dust cloud's number density distribution follows the description given by Stenborg et al. (2021). The radial interval is given to be between 5 and 30 R_S as shown in Figure 1 whereas the eccentricity (e) and inclination (i) distributions are derived from Mann et al. (2000). A Monte Carlo model is used to select randomly the e-value (0-0.1) and i-value (0-35°) for the initial orbit of a sub-micron grain which equation of motion is given below,

$$\vec{F} = m\frac{d\vec{v}}{dt} = \frac{\mu m}{r^2}(1-\beta)\hat{r},$$

$$\rightarrow \frac{d\vec{v}}{dt} = \frac{\mu}{r^2}(1-\beta)\hat{r},$$

[1] Department of Space Science and Engineering, National Central University, Taoyuan City, TAIWAN (R.O.C.).

[2] Institute of Astronomy, National Central University, Taoyuan City, TAIWAN (R.O.C.).

 https://doi.org/10.1142/9789811275449_0050

where m is the mass of β-meteoroid, $\mu = 1.327 \times 10^{20}\ m^3 s^{-2}$ is the Sun's gravitational parameter, r is the heliocentric distance, and β is the ratio of solar radiation (F_R) and gravitational force (F_G), $\beta = F_R/F_G$. The magnitude of β depends on the particle size, composition, porosity, etc. In our preliminary calculation, the β value is assumed to be 0.7 according to the discussion in Wilck & Mann (1996) and Mann & Czechowski (2021). The physical parameters used in our calculation are summarized in Table 1. In future work, consideration will be given to dust particles of different β values.

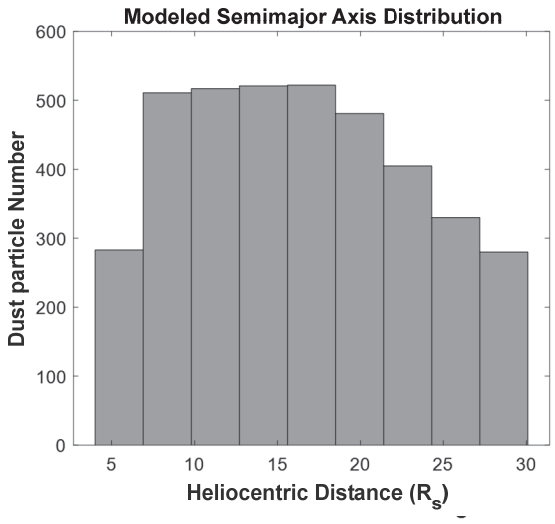

Fig. 1. The near-sun dust number density distribution between 5 and 30 R_S as the semi-major axis distribution.

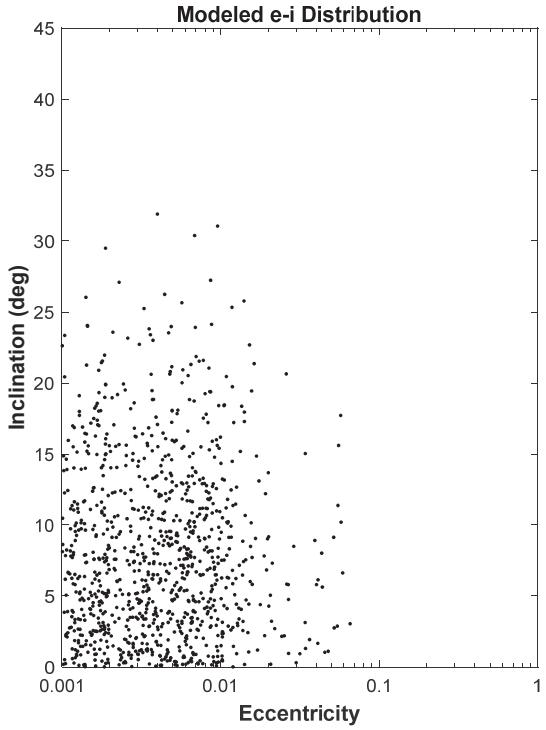

Fig. 2. The eccentricity and inclination distributions for the initial orbit of β-meteoroids.

Table 1. The initial physical parameters of grains.

Model Parameter	Value
Radiation-to-gravity ratio $\boldsymbol{\beta}$	0.7
Semi-major Axis $\boldsymbol{a}$ (R_S)	5~30
Inclination $\boldsymbol{i}$ (deg.)	0~35
Eccentricity $\boldsymbol{e}$	0~0.1
Longitude of the ascending node $\boldsymbol{\Omega}$ (deg.)	0~360
Argument of perigee $\boldsymbol{\omega}$ (deg.)	0~360
True anomaly $\boldsymbol{f}$ (deg.)	0~360

RESULTS

β-meteoroid Flux at Different Solar Distances

Figure 3 depicts the expected β-meteoroid flux distribution at different radial distances and polar angles. Because of the assumed upper limit of the orbital inclinations of the "parent" bodies in the F-corona, the dust impact flux to be measured by SolO will be confined within 36.7° above or below the ecliptic plane. (Please note that the sawtooth feature at the lower and upper boundaries is a result of the spatial resolution of the statistical binning).

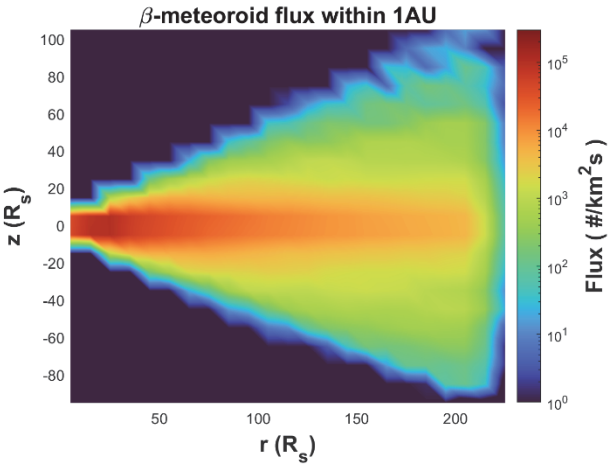

Fig. 3. The β-meteoroid flux at different solar distances (r) with different vertical heights (z).

Prediction of Observations for Spacecraft

Figure 4 shows the radial profiles of the expected β-meteoroid flux for the first six orbits of PSP. They are in qualitative agreement with the observational results reported by Szalay et al. (2021). The absolute magnitudes of the impact fluxes have to be carefully calibrated with the size distribution of the near-sun dust population and the collisional production rates of the sub-micron dust grains.

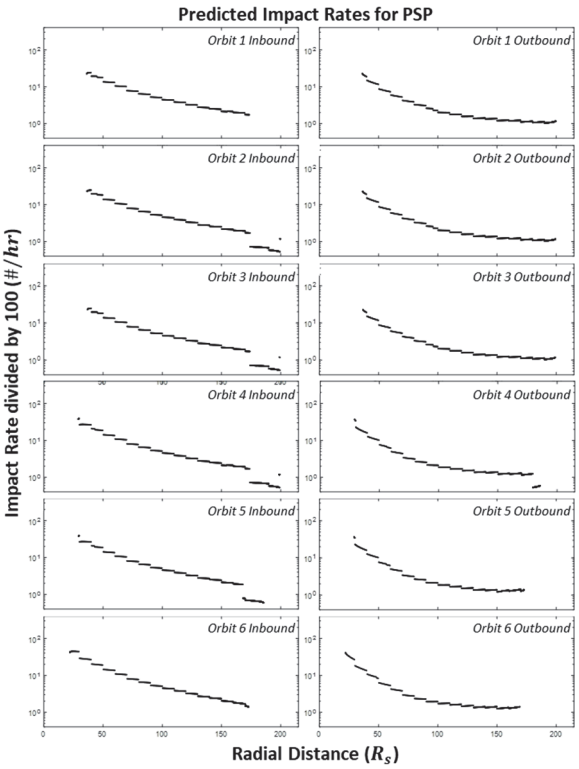

Fig. 4. Impact rate profiles for each PSP orbit from 1 to 6.

DISCUSSION AND SUMMARY

In preparation for the multi-spacecraft measurements of the spatial and temporal variations of the flux of the beta meteoroids by PSP and SolO, we have combined the 3D structure of the F-corona from previous observations (Stenborg et al. 2021) and a theoretical model of the orbital distribution of the small grains in the near-sun dust cloud to stimulate the expected flux values. Our preliminary results show that the synthetic radial profile of dust impact rates compares favorably with the PSP detection of beta meteoroids (Szalay et al. 2021). However, there is a large discrepancy in the absolute value of the estimated impact rates and hence the beta meteoroid flux which might have been caused by the difference in the corresponding dust production rates.

Besides the steady-state model calculations, our numerical method can be applied to transient events sometimes detected in the beta meteoroid flux. It has been suggested that the injection of dust grains by sun-grazing comets or asteroids could be responsible for the burst-like impact rate increases detected by STEREO (Ip & Yan 2012; Zaslavsky et al. 2012). In other words, the near-sun dust cloud which is the last frontier of the interplanetary meteoroid complex can be examined by the numerical method developed here.

ACKNOWLEDGMENT

This work was partially supported by grant No. MOST 105-2119-M-008-003 from the Ministry of Science and Technology, Taiwan.

References

Berg O. E. and Grün E. (1973). Evidence of Hyperbolic Cosmic Dust Particles. Space Research XIII, 1047.

Grün E., Pailer N., Fechtig H., et al. (1980). Orbital and physical characteristics of micrometeoroids in the inner solar system as observed by Helios 1. P&SS, 28, 333.

Ip, W.-H., & Yan, T.-H. (2012). Injection and acceleration of charged nano-dust particles from sungrazing comets. AIP Conference Proceedings, 1436, 30.

Kimura H. and Mann I. (1998). Brightness of the solar F-corona. Earth Planets Space, 50, 493.

Mann I., Krivov A., and Kimura H. (2000). Dust Cloud near the Sun. Icarus, 146, 568.

Mann I. and Czechowski A. (2021). Dust observations from Parker Solar Probe: dust ejection from the inner Solar System. A&A, 650, A29.

Stenborg G., et al. (2021). PSP/WISPR observations of dust density depletion near the Sun I. Remote observations to 8 $R_\odot$ from an observer between 0.13 and 0.35 AU. A&A, 650, A28.

Szalay J. R., et al. (2021). Collisional Evolution of the Inner Zodiacal Cloud. Planet. Sci. J., 2:185.

Wehry A. and Mann I. (1999). Identification of β-meteoroids from measurements of the dust detector onboard the Ulysses spacecraft. A&A, 341, 296.

Wehry A., Krüger H., and Grün E. (2004). Analysis of Ulysses data: Radiation pressure effects on dust particles. A&A, 419, 1169.

Wilck M. and Mann I. (1996). Radiation pressure forces on "typical" interplanetary dust grains. P&SS, 44, 493.

Zaslavsky, A., Meyer-Vernet, N., Mann, I., et al. (2012). Interplanetary dust detection by radio antennas: Mass calibration and fluxes measured by STEREO/WAVES. JGR (Space Physics), 117, 5102.

Zaslavsky A., Mann I., Soucek J., et al. (2021). First dust measurements with the Solar Orbiter Radio and Plasma Wave instrument. A&A, 656, A30.

ONE-DIMENSIONAL INVERSION OF AN AIRBORNE TRANSIENT ELECTROMAGNETIC BY DEEP LEARNING BASED ON UNSUPERVISED AND SUPERVISED COMBINATIONS

Mingzhi Shi[1] and Hui Cao[2]

ABSTRACT: A sample set of stratigraphic structure model airborne transient electromagnetic responses is established, the sample label is attached by unsupervised learning clustering technology, and the multilayer perceptron deep learning network with supervised learning is used to complete multiclassification tasks. Then, the sample set is input into the network for training to establish the inversion from the input response data to the output formation model. Verification results show that the prediction results are consistent with the types of sample stratigraphic models, which proves that the inversion method designed in this paper is correct, and efficient inversion from the test data to the prediction model is realized.

Keywords: inversion, deep learning, airborne transient electromagnetic

INTRODUCTION

In this study, the simulated data of the airborne transient electromagnetic response were first clustered in the form of curves to obtain type labels, and then the mapping of response data to the formation model was established by a deep learning inversion using a multiclassification neural network structure.

The test data set is input into the trained MLP network, and the prediction and classification results of the output stratigraphic model are compared with the types identified by the sample in the original sample set. Verification results show that the prediction results are consistent with the types of sample stratigraphic models, which proves that the inversion method designed in this paper is correct, and efficient inversion from the test data to the prediction model is realized.

METHODOLOGY

Data-driven inversion process

Traditional geophysical inversion methods rely on prior knowledge to make assumptions. Starting from the initial model, the model is continuously modified many times to make the forward modelling results increasingly closer to the measured results. However, as each inversion requires multiple forward calculations, this iterative process consumes considerable time and computing resources, which is the biggest obstacle to real-time inversion. To improve the efficiency of inversion and shorten the inversion time, a data-driven inversion process based on deep learning technology is adopted in this paper to advance the 'model revise-forward iteration' step in the geophysical inversion process to the stage of data pretreatment.

In a data-driven inversion process. The model forward iteration step is advanced to the data preprocessing stage. It only needs to complete one forward iteration step of a large data volume to establish the mapping relationship and only needs to perform one deep learning network mapping for each subsequent inversion of measured data to obtain the inversion prediction results immediately.

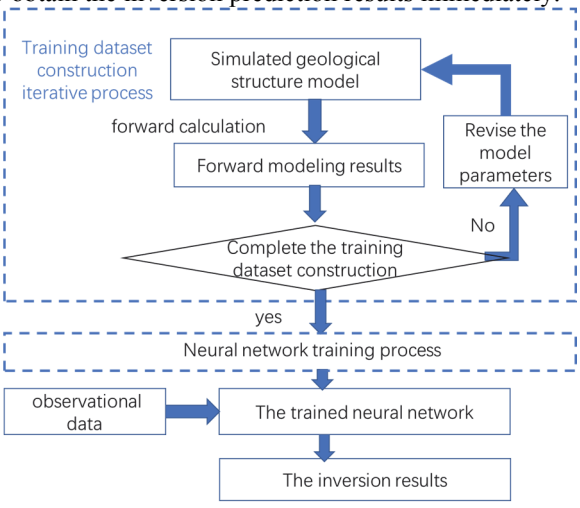

Fig. 1 Data driven inversion process

Deep learning inversion strategy

The steps of DL inversion include the following: I) Construct a deep learning sample set. II) Construct a deep learning network structure. III) Training deep learning networks. IV) Prediction validation.

[1] Nanning College for Vocational Technology, Nanning 530008, CHINA
[2] College of Geophysics, Chengdu University of Technology, Chengdu 610059, CHINA

 https://doi.org/10.1142/9789811275449_0051

RESULTS

To realize one-dimensional inversion of airborne transient electromagnetic based on clustering and a multilayer perceptron neural network, a set of uniform layered underground electrical structure models should be constructed first, and the ATEM forward simulation of the model is carried out to obtain the magnetic field response curve changing with time. These forward results will be used as the training sample set for the subsequent construction of the deep learning network. Then, the K-Means method was used to cluster the response curves to obtain the classification results of the geoelectric structure model by machine. These clustering results are attached to each geoelectric structure model as type labels, and the training sample set containing labels required by the multilayer perceptron neural network is constructed. After that, the data of the training set separated from the sample set are trained. After the training, a mapping from electromagnetic response data to underground electrical structure is constructed. By inputting any group of measured or simulated airborne transient electromagnetic response data into the mapping network, the corresponding geoelectric model output can be obtained in only one step, thus realizing the whole process of one-dimensional inversion of ATEM measurement data by clustering and a multilayer perceptron neural network. Finally, the results are verified, and the correctness of inversion using this mapping model is evaluated.

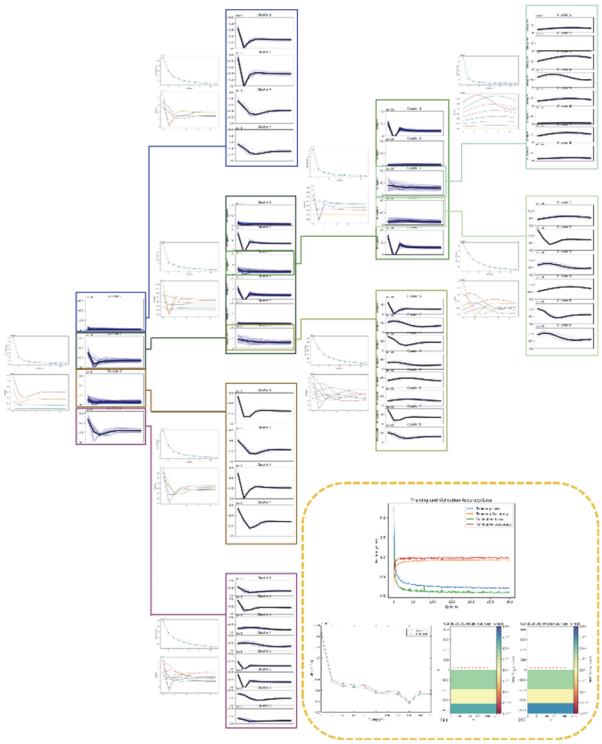

Fig. 2 1D ATEM inversion by DL

DISCUSSION AND CONCLUSIONS

In this study, the simulated data of the airborne transient electromagnetic response were first clustered in the form of curves to obtain type labels, and then the mapping of response data to the formation model was established by deep learning inversion using a multiclassification neural network structure. DL inversion is characterized by being data-driven. At the beginning of the study, it is an efficient and feasible method to construct sample sets using simulated data instead of measured data. In this paper, the test data set is input into the trained MLP network, and the prediction and classification results of the output stratigraphic model are compared with the types identified by the sample in the original sample set. Verification results show that the prediction results are consistent with the types of sample stratigraphic models, which proves that the inversion method designed in this paper is correct, and efficient inversion from the test data to the prediction model is realized.

ACKNOWLEDGEMENTS

This work was financially supported by the National Natural Science Foundation of China (grant no. 41974090).

References

Asif, M.R., Thue S. Bording, Adrian S. Barfod, et al., 2021. Effect of data pre-processing on the performance of neural networks for 1-D transient electromagnetic forward modelling. IEEE Access. 2021(9):34635-34646.

Bai, P., Vignoli, G. & Hansen, T.M., 2021. 1D stochastic inversion of airborne time-domain electromagnetic data with realistic prior and accounting for the forward modeling error. Remote Sensing, 13, article number: 3881.

Cockett, R., Kang, S., Heagy, L. J., Pidlisecky, A., & Oldenburg, D. W., 2015. SimPEG: An open source framework for simulation and gradient based parameter estimation in geophysical applications, Computers & Geosciences, 85, Part A, 142–154.

Puzyrev, V., Swidinsky, A., 2021, Inversion of 1D frequency- and time-domain electromagnetic data with convolutional neural networks. Computers & Geosciences, (2021) 149.

CHANDLER WOBBLE AND LOD ANOMALYES IN 2010-2020S

L. Zotov[1,2], Ch. Bizouard[3] and N. Sidorenkov[4]

ABSTRACT: In early 2000-s the amplitude of the Chandler wobble (CW) started to decrease and in 2017-2020 reached its historic minima, comparable only with the minima of ~1928 yr. In 2021 the CW appeared again. We demonstrate that the phase of the CW is changing now, as during 1920-1930s. Since 2010 it has changed almost by 2 radians, and we expect it will finally reach π radians. This implies splitting of the CW spectra into two pikes. Since 2016 the length of day LOD is decreasing and Earth's rotation velocity is growing. In 2022 it is the highest over the last 90 years. We hypothesize that the anomalies of the CW are interrelated with LOD decrease through some synchronization and/or energy transfer?

Keywords: Earth's rotation, polar motion, Chandler wobble, LOD.

CHANDLER WOBBLE ANOMALYES

Chandler wobble (CW) is a proper component of the Earth's polar motion with 433-day period and average amplitude around 135 mas. It was discovered by S. Chandler in 1891 and has been observed for more than a century with increasing precision. Polar motion (PM) contains annual oscillation and secular trend as well. In the spectrum obtained from EOP C01 data since 1846, presented in Figure 1, we can see that the annual term is a single line, but Chandler spectral line is split and contains several side-lobes. This is related with amplitude and phase variations of the CW.

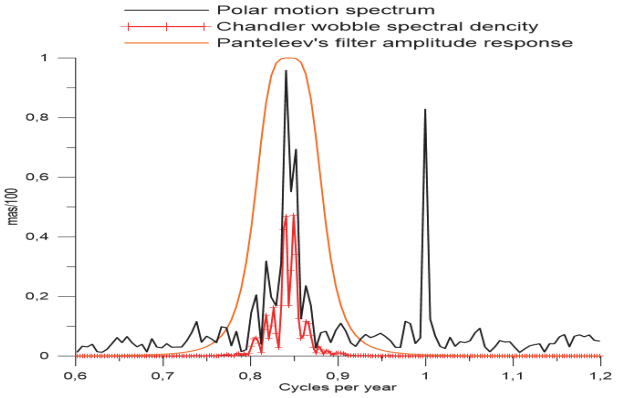

Figure 1. Spectrum of the polar motion with Panteleev's filter superimposed.

The simplest way to see how CW behaves is to subtract trend and annual term from *X* and *Y* components of PM. The result is given in Fig. 2. The major contribution in Fig.2 comes from CW. It is well seen that in 1930s and now days the amplitude of CW decayed almost completely. In 2022 CW appeared again.

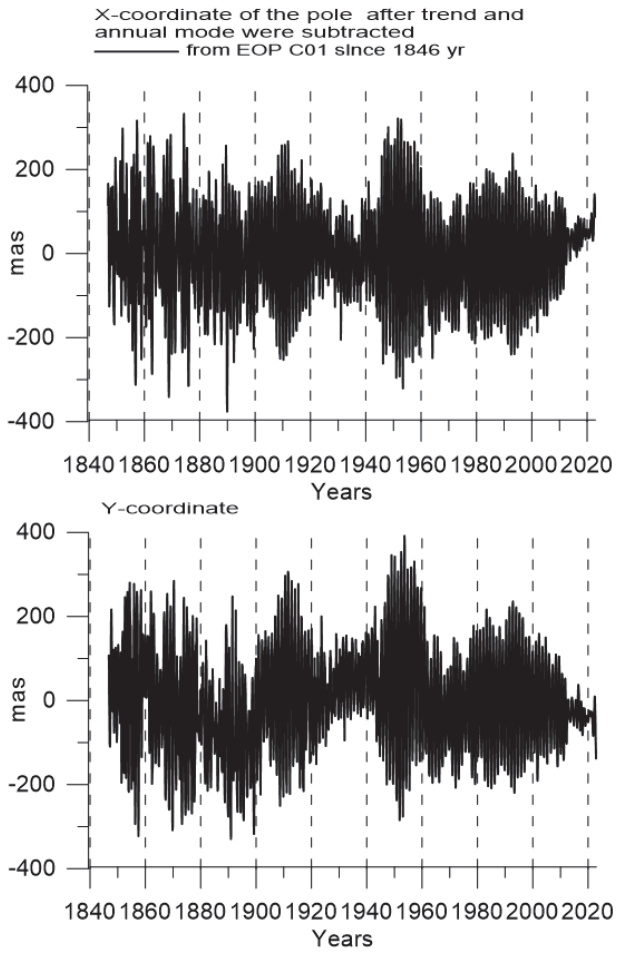

Figure 2. *X* (top) and *Y* (bottom) components of PM after trend and annual term have been removed.

Early data was noisy, but today's accuracy of observations is better than 0.1 mas, what allows to

[1] Sternberg Astronomical Institute, Lomonosov Moscow State University, RUSSIA
[2] National Research University Higher School of Economics, Moscow, RUSSIA
[3] SYRTE, Paris Observatory, University PSL, Sorbonne, UPMC, FRANCE
[4] Hydrometeorological center of RUSSIA

 https://doi.org/10.1142/9789811275449_0052

conclude that in 2017-2020 CW almost disappeared. We call this periods of small amplitude the 'nodes'.

Another strategy to extract Chandler wobble is to filter it out by narrow-band filter. Panteleev's filter was adopted for this. Its response function is shown in Fig. 1 in orange. After CW extraction we can estimate its amplitude and phase in a sliding window. Results are shown in Fig. 3.

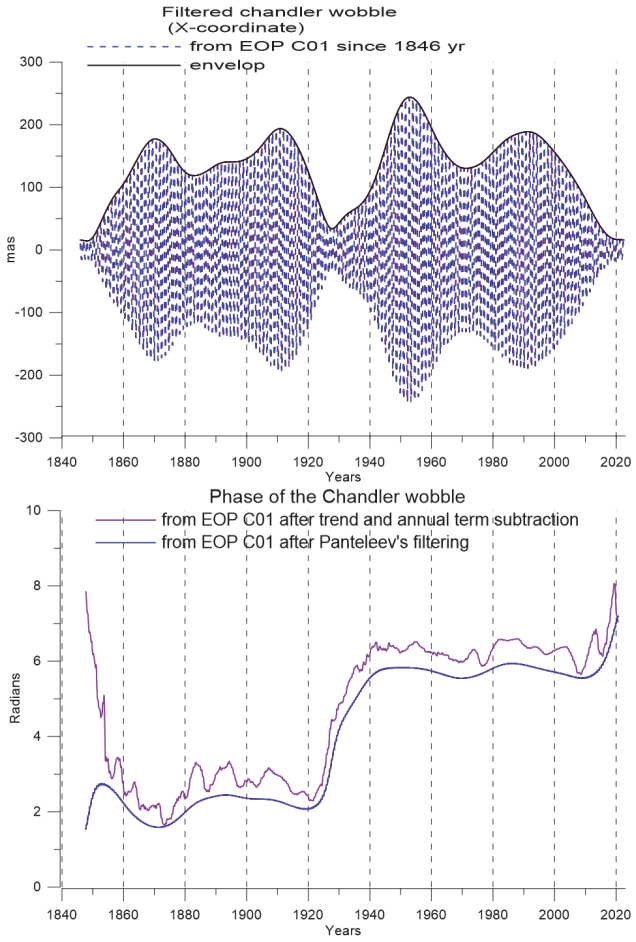

Figure 3. Chandler wobble extracted by Panteleev's filter from PM, estimates of amplitude (top) and phase (bottom) obtained in a sliding window of 3.6-year extent.

Form Fig. 3, top the amplitude variations of the CW can be tracked. Bottom plot shows that in 1930s the phase of CW changed by π and since 2010s it is drifting. Blue curve represents results for Panteleev's - filtered CW. Purple curve represents the results obtained without filtering from the curves given in Fig. 2. Thus, we are concluding: one of the major component of the polar motion, namely CW, is now changing phase and has decayed in amplitude, almost as it did 90 year ago. The phase has changed since 2010 by about 2 radians. Careful reader can ask, what about 1850? It looks like CW decay and phase change occurred then as well. We are hesitating to make this conclusion, because early astrometric data has errors around 0.1 arc seconds.

LOD VARIATIONS

Length of day is an Earth orientation parameter (EOP) used to characterize the rotational velocity of the planet. It decreases, when the latter increases. Standard day contains 86400 conventional seconds. By LOD we mean the discrepancy from this value, it is measured in milliseconds. Fig. 4 represents LOD variations since 1962 (blue) and IERS zonal tide model (orange). Ups and downs of LOD has quasi-20-year periodicity over this time interval. Till now we do not have explanation for these decadal variations. They are supposed to be related with angular momentum exchange at the core-mantle boundary. Nevertheless we want to note, that 18.6-year lunar orbital precession, which is reflected in the amplitude of zonal tide, has some synchronicity with recent variations of LOD. In 2016 rapid acceleration of the Earth rotation begun. On 29 June 2022 LOD curve reached the deepest minimum over 60 years. If this tendency continues, it would be needed to subtract leap second from atomic world time UTC.

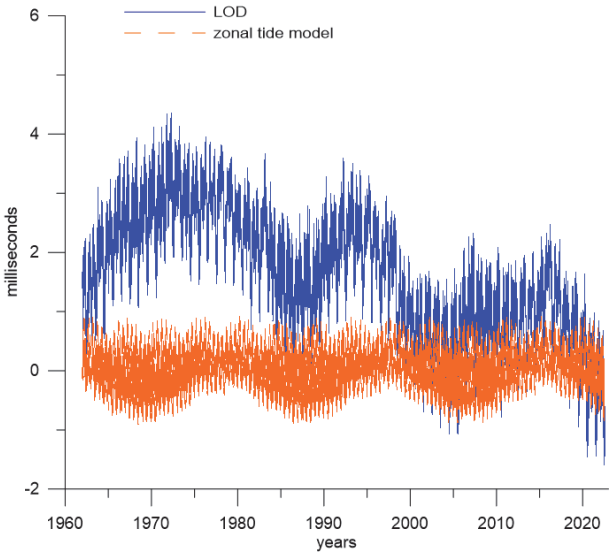

Figure 4. LOD variations and zonal tides.

The mentioned minimum in LOD is a result of superposition of decadal acceleration, annual minimum and tidal fortnightly minimum. Most of the annual, semiannual, monthly variations of LOD can be explained from comparison with atmospheric, oceanic and hydrological angular momentum variations. But decadal variations cannot, they are unpredictable. What is interesting, the acceleration of the Earth started after strong El Nino 2016-2017 and now a series of La Ninas accompanies the quick rotation of the planet.

Today's anomalies in the Earth rotation reminds the situation in the 1930s, when CW was very small and Earth's velocity – quite rapid. We will discuss this subject in the following section.

LONG-TERM TENDENCIES, DISCUSSION

In Fig. 5 we represent long-term variations of LOD from EOP C02 bulletin (purple) and filtered Chandler wobble envelope (red) superimposed.

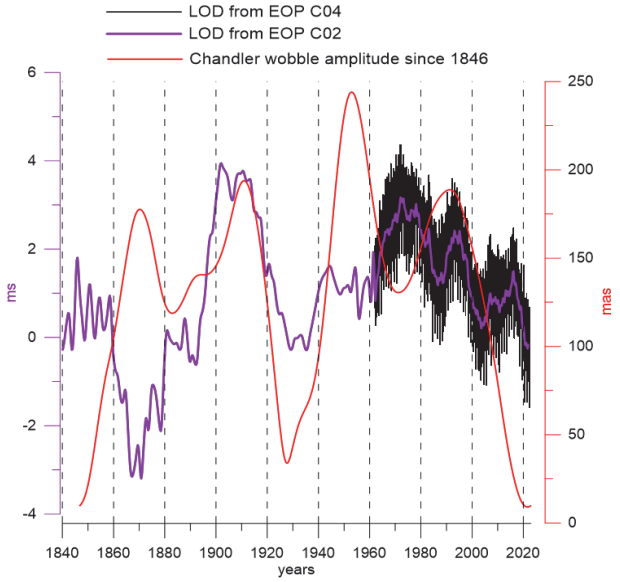

Figure 5. Long-term LOD and CW amplitude variations.

As mentioned earlier, 1930s and end of 2010s are the epochs of minima in both LOD and CW amplitude. Long term LOD determinations made from lunar occultations and eclipses (EOP C02) are less precise, than determinations started in 1962 (EOP C04) from comparisons with atomic clocks. Today minima can be treated as superposition of long-term 90-year quasi-cycle and 20-40 year cycles. We found quasi-40 year variability in the CW amplitude. For around 20 years the amplitude goes up, for 20 years – down. If we compare with LOD decadal variability since 1962 we would see the alternation. Earlier the concept that Earth's rotation velocity changes can be related with Earth's temperature variations, in particular, Atlantic Multidecadal Oscillation (AMO) was hypothesized. When LOD decreases, AMO index increases. Today it adds 0.2°C to global Earth's temperature.

Could it be, that the axial (LOD) and meridional (PM) components of Earth's rotation are coupled? In classical theory of gyroscopes the amplitude of precession can decrease when rotational velocity increases. But Earth's rotation theory based on linearized Euler-Liouville equations decouples LOD and PM variations. Since the velocity changes are around 10^{-8} the terms of the second order can be ignored. But CW, as we know, decays for the real Earth and some energy is required to excite it. Usually it is supposed that noisy processes in the atmosphere and ocean supply it, and variations of CW amplitude are purely random. Now we observe that they repeat after 90 years. This could be a sign of regularity.

Some authors believe that decadal LOD variations are related to the geomagnetic jerks, others refer to long-term variations of angular momentum of the core. Variations of the Chandler wobble amplitude are supposed to be related to oceanic and atmospheric excitations. There are hypothesis that lithosphere drifts over asthenosphere occurs, producing variations in the observable EOPs. Electro-magnetic coupling could potentially join axial and meridional components of the Earth rotation. Synchronization of geophysical processes by external forces and tides is also possible. Further studies are needed to develop the theory and uncover the mechanism.

Anyway, in our present work we show that CW minima has been passed. If LOD minima is related to this, the Earth would start to decelerate in the nearest future.

ACKNOWLEDGEMENTS

This work was supported by the National Natural Science Foundation of China (NSFC), project N B17033; Russian Science Foundation, project no. 21-47-00008; and Cosmos School, Lomonosov Moscow State University.

References

Bizouard Ch., Geophysical modelling of the polar motion, (2020), De Gruyter.

Duan, P., Huang, C. Intradecadal variations in length of day and their correspondence with geomagnetic jerks, (2020), Nat Commun 11, 2273.

Gorshkov V.L., Study of the Interannual Variations of the Earth's Rotation, (2010), Solar System Research, Vol. 44, No. 6, pp. 487–497.

Graham Jones, Earth Sets New Record for Shortest day. https://www.timeanddate.com/news/astronomy/shortest-day-2022 Time&Date, 27 July 2022.

Jamie Carter, The Earth is spinning faster because of a new 'wobble', scientists say, Forbes, 03 Aug 2022.

Malkin Z., Miller N. Chandler wobble: two more large phase jumps revealed, (2010), Earth Planets Space, 62: 943–947.

Sidorenkov N.S., The Interaction Between Earth's Rotation and Geophysical Processes, (2009), Wiley-VCH Verlag, Weinheim.

Zotov L., C. Biouard, Why the Earth does not rotate evenly and how it affects the time counting, (2021), Priroda RAS, N 3: 26-29 in russian.

Zotov L.V., Earth rotation and climate processes, (2022), monography in russian, Moscow, MIEM HSE.

Zotov L.V., Sidorenkov N.S., Bizouard Ch. Anomalies of the Chandler wobble of the pole in 2010-s, (2022) Moscow University Physics Bulletin, N 3: 64-72.

Zotov L.V., C. Bizouard, N. Sidorenkov, Shen WB., Guo ZL, (2020), On the variability of the Chandler wobble, (2019), Proceedings of Journees: 249-254.

SEISMIC HAZARD FUNCTION (SHF) STUDY PRIOR TO LARGE EARTHQUAKE EVENT OF THE YEAR 1994 AND 2006 OFF COAST OF THE JAVA ISLAND: THE SHF ANALYSIS BASED ON THE CHANGE OF THE B-VALUE

Wahyu Triyoso[1] and Osa Yuninda[1]

ABSTRACT: The seismic hazard function analysis around the off coast of Java Island is investigated based on the changes of the b-value using the shallow crustal earthquake catalog data from 1963 to 2016. The study areas took place around M7.8 in 1994 and M7.7 in 2006. The change of the b-value is estimated using the maximum likelihood method with a constant number. First, the b-value surrounding the center area of interest with a radius of about 150 km is calculated based on the earthquake catalog data from 1963 to 2016 (b_{50}). Second, the b-value based on five years with a one-year moving window (b_5) is estimated before M7.8 in 1994 and M7.7 in 2006. The b5 is calculated based on the constant number of events of 25, 50, 75, and 100, and we evaluate the mean b-value. Furthermore, the SHF of b_{50} and b_5 are calculated, and then they are compared. The results showed that the Probability of Exceedance (PE) of SHF b_5 increased by about five years before the two large earthquake events. Therefore, the results obtained in this study might be very beneficial for earthquake mitigation and modeling efforts for the possible potential of the earthquake hazard study and future analysis.

Keywords: Seismic Hazard Function, b-value, Probability of Exceedance, Large Earthquake, Mitigation.

INTRODUCTION

This study is intended to investigate the seismic hazard function analysis around the off coast of Java Island based on the changes of the b-value using the shallow crustal earthquake catalog data of the year 1963 to 2016. The study areas took place around the zones of M7.8 in June 1994 and M7.7 in July 2006. The change of the b-value is estimated using the maximum likelihood method with a constant number.

Nuannin et al. (2012) pointed out that the correspondence between low b and the occurrence of large earthquakes exists. Based on their result, it has been shown that large earthquakes occur when b-values decrease during the study period. The phenomenon is clear enough, as they showed in the diagrams for each catalog data they used.

Triyoso et al. (2022) evaluate the possible correlation between the correlation dimension (D_C) and the seismic moment rate for different late Quaternary active fault data, shallow crustal earthquakes, and GPS on the island of Sumatra Probabilistic Seismic Hazard Analysis (PSHA). The study could characterize a reasonable correlation between two seismotectonic parameters, D_C - b, as follow $D_C = 2.851 - 1.272b$. Furthermore, Triyoso et al. (2022) conclude that the relatively high correlation dimension coincides with a high SHF curve. Therefore, it could be summarized that the areas with relatively high D_C overlap with high seismic moment loading rates, which may imply high tectonic stress loading that could pose the risk of producing significant earthquake hazards in the future.

The most critical finding is that the relatively high D_C or low b-value coincides with the high seismic moment rate model derived from the pre-seismic GPS data. And the SHF curve of total probability of exceedance versus the mean of each observation point's peak ground acceleration (PGA) shows that the relatively high correlation dimension coincides with the high SHF.

Thus, the motivation of this study is to evaluate the SHF that is based on the regional b-value of the year 1963 to 2016 (b_{50}) and the b-value based on five years time windows with about a one-year moving window (b_5) that is estimated prior to both of M7.8 of 1994 and M7.7 of 2006. First, the b5 is calculated based on the constant number of events of 25, 50, 75, and 100, and then we estimate the mean b-value.

The seismicity rate model is based on the declustered shallow earthquake data from 1963 to 2016. First, the seismicity smoothing algorithm (Frankel, 1995) is used, and the SHF is calculated based on b_{50} and b_5. And then they are compared.

DATA AND METHODS

The data utilized in this study is based on The PUSGEN 2017 (The PUSGEN, 2017). The area is around off the south coast of Java Island. The selected data used is based on the magnitude of $M_w \geq 4.7$ with a maximum depth of 50 km from 1963 to 2016, as shown in Figure 1.

[1]Faculty of Mining and Petroleum Engineering, Institut Teknologi Bandung, Jalan Ganesha 10, Bandung 40132, INDONESIA

 https://doi.org/10.1142/9789811275449_0053

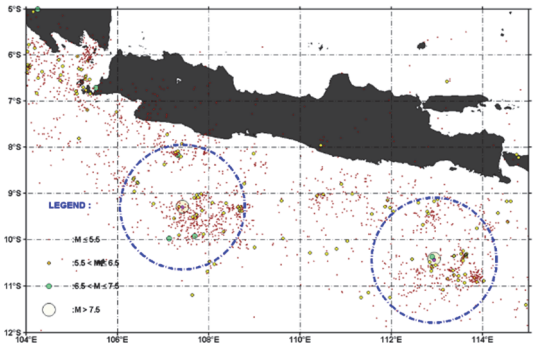

Figure 1. The selected data used is based on the magnitude of $M_w \geq 4.7$ with a maximum depth of 50 km from 1963 to 2016.

The b-value

The b-value of the Gutenberg-Richter Equation (1944) is an essential statistical parameter correlated with the possible size of the scaling properties of seismicity. The average b-value on a regional scale usually ~ 1 (Frohlich and Davis, 1993). The critical findings of an earlier study showing that low b-value and high Dc are closely related to the low degree of heterogeneity of the cracked medium, enormous stress and strain, high deformation rates, large faults, and thus, seismic moment rates. The most robust method for calculating the b-value is the maximum likelihood (Aki K., 1965). The formula can be written as follows:

$$b = \frac{\log_{10}(e)}{(\bar{M} - M_c + 0.05)} \quad (1)$$

where $\bar{M}$ is average magnitude value greater or equal to M_c, and M_c is the minimum magnitude or the magnitude completeness. The 0.05 in Equation (1) is a correction constant.

Seismicity Smoothing

Following Frankel (1995), in this study, the smoothed value $\tilde{n}$ is obtained from:

$$\tilde{n}_i = \frac{\sum_j n_i e^{-\Delta^2 ij/c^2}}{\sum_j e^{-\Delta^2 ij/c^2}} \quad (2)$$

in which $\tilde{n}_i$ is normalized to preserve the total number of events, Δij is the distance between i th and j th cells, and c is the correlation distance. The sum is taken over cell j within a distance of 3c from cell i.

The Occurrence Rate Function and Probability of Exceedance (PE)

The seismicity rate function for a particular cell, v_i ($\geq M_{ref}$), resulted based on seismicity smoothing (Triyoso et al., 2020) and could be formulated by

$$v_i(\geq m) \approx \frac{\tilde{n}_i(\geq M_{ref})}{T.b\ln(10)} 10^{-bm}(1 - 10^{b(m-M\,max)}) \quad (3)$$

Where $\tilde{n}i$ ($\geq M_{ref}$) is the smoothed seismicity value of the grid i of the 10^a earthquakes with a magnitude larger than M_{ref} during the time interval T, and b is the b-value. $M_{max} \sim 8.0$ is used in this study.

The seismicity rate model is estimated based on the declustered shallow earthquake catalog (The PUSGEN, 2017) using the correlation distance of 50km using equation (2).

The annual probability exceedance of peak horizontal ground motion (PGA) u at a site due to events at a particular grid k under the Poisson distribution for a specific time duration T, with the Ground Motion Prediction Equation included, is given by

$$P(u \geq u_0) = 1 - (1 - P(u \geq u_0))^T = 1 - e^{(-T\sum v_i(\geq m(u_0, D_k)))} \quad (4)$$

Where m (u_o, D_k) is the source's earthquake magnitude in a k^{th} grid that can produce a PGA of u_o or larger at the observation grid point (site). D_k is the distance between the observation grid point and the earthquake point at a source grid position that provides a particular PGA's annual PE. The function m(u_o, D_k) is the GMPE.

Ground Motion Prediction Equation (GMPE)

By referring to the recommendation results of Triyoso et al. (2020) and Triyoso and Sahara (2021), the GMPE of Zhao et al. (1997) was used for subduction sources.

RESULT AND DISCUSSION

The SHF in this study is estimated based on M_w of 6 to 8 for the period of five years. Following Triyoso et al. (2020), the source depth of 15 km and the radius of 100km are used. Figure 2 shows the result of SHF estimation based on b_{50} and b_5. It appears that the SHF of the b_5 (1988 to 1993) prior to M7.8 of the 1994 earthquake is larger than the SHF of the b_{50}. Figure 3 shows that the SHF of the b5 (1998 to 2000) prior to M7.7 of the 2006 earthquake is lower than the SHF of the b_{50}. However, the b5 (2001 to 2005) is more significant than the SHF of the b_{50}.

The critical finding of this study shows that both the SHF of the b_5 about five years prior to M7.8 and M7.7 show larger compared to the SHF of the b_{50}.

CONCLUSION

Based on the result of this study, we can conclude that,

- ✓ The Seismic Hazard Function (SHF) based on b_5 increased prior to both large earthquakes of M7.8 and M7.7.

- ✓ The SHF of the b_5 (1988 to 1993) prior to the M7.8-1994 earthquake is larger than the b_{50}.
- ✓ The SHF of the b_5 (1998 to 2000) prior to M7.7 of the 2006 earthquake is lower than the SHF of the b_{50}. However, the b5 (2001 to 2005) is larger than the SHF of the b_{50}.
- ✓ The SHF of the b_5 about five years prior to M7.8 and M7.7 is more significant than the SHF of the b_{50}.
- ✓ The SHF analysis as a function of the b(t) obtained in this study might be very beneficial for earthquake mitigation and the possible potential future of the earthquake hazard study and analysis.

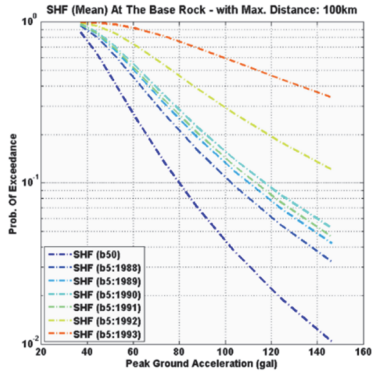

Figure 2: The result of SHF estimation based on b_{50} and the b_5 off the southern coast of East Java Island. The SHF is estimated based on M_w of 6 to 8 for T = 5 years using the source depth of 15 km and the radius of 100km.

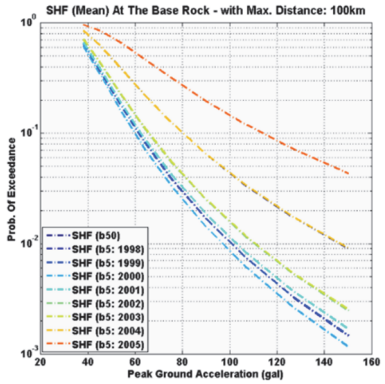

Figure 3: The result of SHF estimation based on b_{50} and the b_5 off the southern coast of West Java Island. The SHF is estimated based on M_w of 6 to 8 for T = 5 years using the source depth of 15 km and the radius of 100km.

References

Aki K. (1965): -Maximum likelihood estimate of b in the formula log N = a-bM and its confidence limits-. Bull Earthq Res Inst Tokyo Univ. 43, 237-239.

Bayrak Y., Ozturk S. (2004): Spatial and temporal variations of the aftershock sequences of the 1999 Izmit and Duzce earthquake. Earth Planets Space. 56, 933-944.

Frankel A (1995) Mapping seismic hazard in the Central and Eastern United States. Seismol Res Lett 66(4):8–21.

Frohlich C., Davis S. (1993): -Teleseismic b-values: Or, much ado about 1.0-. Journal of Geophysical Research 98 (B1), 631-644.

Gutenberg R., Richter C.F. (1944): -Frequency of earthquakes in California-. Bull Seismol Soc Am. 34, 185-188.

Nuannin, P., O. Kulhánek, and L. Persson (2012), Variations of b-values preceding large earthquakes in the Andaman–Sumatra subduction zone. Journal of Asian Earth Sciences (2012).

Tim Pusat Studi Gempa Nasional-2017 (The 2017 PuSGen) (2017) Peta Sumber dan Bahaya Gempa Indonesia Tahun 2017. Jakarta: Kementrian Pekerjaan Umum dan Perumahan Rakyat (In Indonesian).

Triyoso W, Suwondo A, Yudistira T, and Sahara DP. (2020) Seismic Hazard Function (SHF) study of coastal sources of Sumatra Island: SHF evaluation of Padang and Bengkulu cities, Geosci. Lett. (2020) 7:2.

Triyoso, W and Sahara, D.P. (2021) Seismic hazard function mapping using estimated horizontal crustal strain off West Coast Northern Sumatra, Front. Earth Sci. 28 April 2021 | doi: 10.3389/feart.2021.558923

Triyoso, W., Sahara D.P., Sarsito D.A., Natawidjaja D.H and Sukmono, S. Correlation Dimension in Sumatra Island Based on Active Fault, Earthquake Data, and Estimated Horizontal Crustal Strain, GeoHazard, MDPI, Under Review (2022).

Zhao JX, Dowrick DJ, McVerry DH (1997) Attenuation of peak ground acceleration in New Zealand earthquakes. Bull N Z Natl Soc Earthq Eng 30(2):133–158.

ANTHROPOGENIC IMPACTS OF TOURISM TO KARST ENVIRONMENTS IN THE PHILIPPINES

KL Garas[1,3], AC Ondona[1], RDD Agot[1,2], MFB Madrigal[1,2], RAA Rollan[1], AB Abrenica[1], LSJ Manzano[1], NT Ramos[2]

ABSTRACT: Tropical karst is highly sensitive to surface and subsurface changes, with natural and anthropogenic factors contributing to its potential degradation and overexploitation. Thus, the appropriate management and protection of karst environments are needed. This study aims to determine the anthropogenic-driven changes in the karst landscape and groundwater resources of El Nido, Palawan Province. Interferometric Synthetic Aperture Radar (IfSAR), LandSat 8, and Google Earth imagery were used for pre-field geomorphological and land cover delineation. Semi-detailed stratigraphic surveys and rock sampling were conducted. In-situ water quality testing and sampling were done to obtain physicochemical parameters such as pH, conductivity, and total dissolved solids. Focusing on preliminary findings from El Nido, petrographic characterization and microfossil age dating have shown that the limestone is composed of Middle Permian faunal assemblage. Geomorphological analysis shows that the area is dominated by karst towers, remnant valleys, sinkholes, and caves. Georesistivity surveys reveal that the water-saturated layer becomes thicker in the extensive floodplains of Villa Libertad, Dewil Valley, and Villa Paz. In contrast, the town center has a thin and permeable water-saturated layer that is approximately 2-3 m thick. Fecal coliform, nitrates, and sulfates are relatively higher in groundwater collected from karst areas in the urban and tourism center.

Keywords: karst, geomorphology, groundwater, anthropogenic impacts, Philippines

INTRODUCTION

Approximately 1,153 towns in the Philippines are underlain by Permian to Holocene calcareous rock formations. These carbonate rocks typically develop distinct karst features and scenic landscapes that oftentimes serve as the center of tourist attraction in many parts of the country. However, karst areas are considered among the most fragile and vulnerable environments in the world (Goldscheider, 2012). The inherent geologic and climatic conditions in the Philippines, coupled with an unregulated increase in tourism activities, could accelerate the degradation of karst systems, and eventually lead to karst hazards and groundwater contamination. The Climate-responsive Karst Management for Sustainable Tourism (PhilKARST) Program of the MGB aims to understand the effects of natural, climatic, and anthropogenic factors in the development and degradation of karst systems in El Nido, Palawan, one of the top tourist destinations in the Philippines. The study further aims to serve as a science-based guide for reliable ecosystem-based karst management and disaster risk reduction planning.

METHODS

Geological mapping, petrographic and paleontological analyses were employed to determine the horizontal and vertical extent, physical characteristics, and depositional age of the limestone units. IfSAR- and ground-based geomorphological mapping were done to map out karst surface landforms. Geomorphometric parameters such as slope, relief, topographic position index (TPI), terrain ruggedness index were also analyzed from IfSAR-Digital Elevation Models (DEMs) using ArcGIS 10.6.1. An electrical resistivity survey using Syscal Pro Switch 72 from Iris Instruments was carried out to delineate the subsurface water-bearing units in the study areas. The groundwater from several wells and springs was tested in-situ for physical parameters and sampled and analyzed for major ions and heavy metals using the Agilent 55B AA (double beam) flame atomic absorption spectrometer (AAS) and fecal coliform (FC) concentrations using Multiple Tube Fermentation Technique (MTFT).

RESULTS AND DISCUSSION

Characteristics of the Minilog Formation in El Nido

The Minilog Formation (Fig.1) is composed dominantly of small and large benthic foraminifera,

[1]Mines and Geosciences Bureau, Quezon City, PHILIPPINES
[2]National Institute of Geological Sciences, University of the Philippines, Quezon City, PHILIPPINES
[3]Graduate School of Science, Hokkaido University, JAPAN

 https://doi.org/10.1142/9789811275449_0054

dasycladacean, gymnocodiacean, red algae, and fragments of gastropod, pelecypod, and brachiopod. The occurrence of fusulinid species including *Neoschwagerina craticulifera, Neoschwagerina simplex, Verbeekina* sp., and *Schwagerina* sp. in the Minilog Formation indicates that the limestone units were formed during the Middle Permian in a warm, shallow, depositional environment within the inner neritic zone.

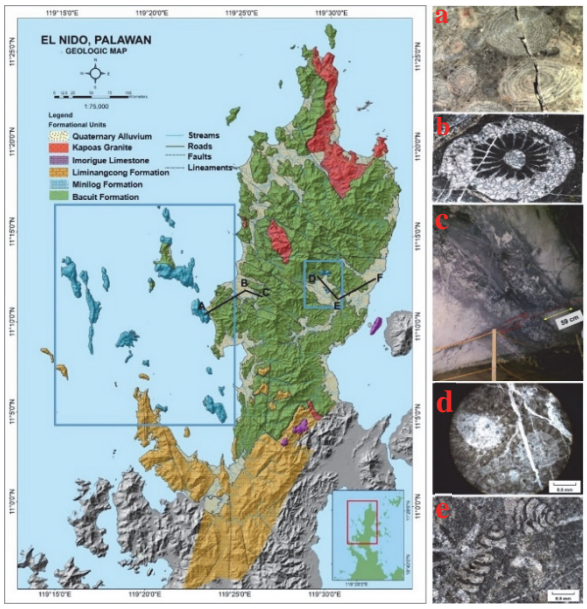

Fig. 1. Geologic map of El Nido, Palawan showing the location of the Minilog Limestone Formation in the study area. Notable fossils include a) fusulinids (LBF); b) rugose corals (*Waagenophyllum sp.*); c) alatoconchid bivalve (*Shikamaia sp.*); d) dasycladacean algae; and e) paleotextulariids (SBF).

Karst geomorphology of El Nido

The karst landscape in El Nido is characterized by numerous steep karst towers and pinnacles, expansive remnant karst plains, large sinkholes, and large cave systems concentrated in Bacuit Bay and Dewil Valley (Fig. 2). It is estimated that karstification in the area commenced during the middle to late Miocene to early Pliocene after the uplift caused by the collision of the Palawan Microcontinental Block and the Philippine Mobile Belt (Yumul et.al., 2003).

Slope-relief shows that topography is characterized by moderately sloping to steep low hills with slope angle ranging from 22.5° to 45°. Topographic position index (TPI), which is used to determine the types of landforms, shows that 41% of the landscape is expressed as ridges while 38% are valleys. The terrain ruggedness index (TRI) further shows that 42% of the landscape is highly rugged thus denoting numerous high landform expressions in the area. Based on the latest field inventory, there are 54 sinkholes and 80 cave openings documented in El Nido.

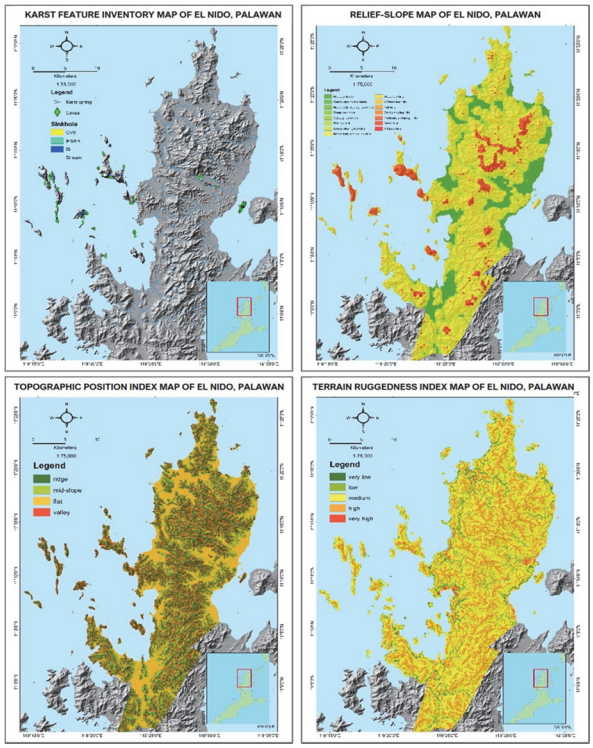

Fig. 2. Maps of the different geomorphometric parameters such as karst features, relief-slope, TPI, TRI used to characterize the karst landscapes in El Nido, Palawan.

Groundwater resources and quality in the urban and tourism centers in El Nido

Georesistivity data collected from seven vertical electrical sounding (VES) stations reveal at least three lithologic units with varying resistivity signatures. Georesistivity profiles (Fig. 3) generated along the VES stations show that the interpreted water-saturated layer (0.6 to 79 meters) becomes thicker in the extensive floodplains of Villa Libertad, Dewil Valley, and Villa Paz. These floodplains are productive sources of groundwater for domestic and agricultural use in the area. In contrast, the town center has a thin, permeable, water-saturated layer with a thickness of approximately 2-3 m.

Thirty-eight (38) wells and springs located in limestone, clastic rocks, and Quaternary alluvium within built-up (i.e., tourism districts and residential centers) and cropland areas in El Nido were tested for physicochemical and fecal coliform (FC) content. Data shows that groundwater samples from karst aquifers generally have pH >7, total dissolved solids (TDS) greater than the standard limit of 600 mg/L, and salinity >0.5 PSU (PNSDW, 2017). Meanwhile, those from non-karst aquifers have pH <7, TDS <600 mg/L, and salinity <0.5 PSU.

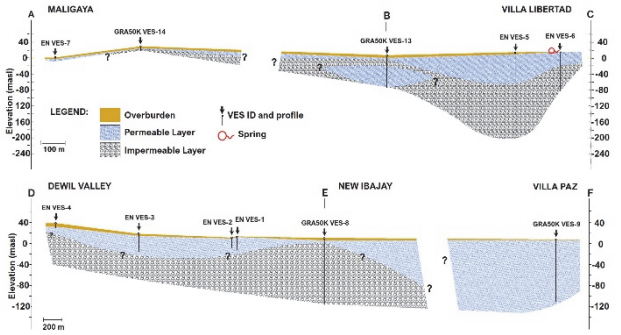

Fig. 3. Georesistivity profiles showing water-saturated layers in Maligaya to Villa Libertad (A-C) and Dewil Valley to Villa Paz (D-F). See Fig. 1 for the location of VES profiles.

Currently, the islands and a portion of the mainland of El Nido underlain by limestone are largely uninhabited with no observed significant extraction of groundwater. The limestone area in Buena Suerte is bordered by settlements founded on alluvial deposits.

The cavities and fractures that characterize the karst formations provide enhanced percolation of rainfall into the subsurface. However, the same features prevent the development of significant storage areas for groundwater. As observed, most islands are surrounded by a thin layer of beach deposits. The water that enters the karst formations seep into the interstices of these thin deposits where it is able to store and transmit a limited amount of groundwater.

Impacts of anthropogenic activities in El Nido

Over the past 10 years, El Nido has seen a rapid growth in tourism (Liabastre and Rieder, 2022). Evaluation of land use and land cover change detection from Sentinel-2 images of the area from 2017 to 2021 show an increase in the total built-up area by 44%.

In urban and tourism centers, TDS, electrical conductivity (EC), and salinity are found to be significantly higher in areas that are underlain by limestone compared to those areas underlain by clastics or alluvium. The presence of limestone and its proximity to the source of contamination also control the nitrate (1.76 - 44.44 mg/L) and sulfate (14 - 345 mg/L) contents in the groundwater. Such behavior may be attributed to the presence of numerous open fractures and network of cavities in limestone which both serve as conduits for the fast transport of contaminants into the karst aquifer.

Fecal coliform (FC) analysis of the groundwater samples collected from this study also shows the high concentrations in tourism centers (<18 - 35000 MPN/100mL), including the samples collected within cropland areas in Dewil Valley (20 - 230 MPN/100 mL). The presence of FC in the groundwater highly indicates anthropogenic activity.

CONCLUSIONS

Tropical island karst is an important asset of the tourism industry in the Philippines. However, this beautiful landscape is also vulnerable to degradation without a sustainable development plan. Geological and geomorphological mapping shows that most of the tourist sites in El Nido are located in areas underlain by Middle Permian limestones. Analysis of the physicochemical parameters and FC contents shows that both land use and geologic conditions affect groundwater quality. The karst aquifer in tourism and urban centers in El Nido is vulnerable to contamination due to the presence of numerous fractures and network of cavities.

ACKNOWLEDGEMENTS

The MGB PhilKARST Program would like to thank the Department of Science and Technology (DOST) for funding this research through its Grants-in-Aid initiatives and the Philippine Council for Industry, Energy, and Emerging Technology Research and Development (PCIEERD) for its support and assistance to the Program. The Program is also grateful to the local government unit of El Nido, Palawan and the DENR-Protected Areas Management Office (DENR-PAMO) for their support during the field survey. We would also like to thank the Environment Management Bureau Region IV for providing the fecal coliform data. Sincere thanks are also extended to Ms. Angela P. Revilla and her colleagues from the Department of Energy (DOE) for their assistance in the identification of fusulinids.

References

Goldscheider, N. (2012). A Holistic Approach to Groundwater Protection and Ecosystem Services in Karst Terrains. Aqua Mundi-Am, 06046, 117-124.

Liabastre, T. and Rieder, L. (2022). Carrying Capacity Assessment for Tourism in Coron and El Nido: A Step toward Sustainable Management of Marine Ecosystems. ADB Briefs. No. 212.

Yumul Jr, G. P., Dimalanta, C. B., Tamayo Jr, R. A., & Maury, R. C. (2003). Collision, subduction and accretion events in the Philippines: a synthesis. Island Arc, 12(2), 77-91.

Philippine National Standards for Drinking Water (PNSDW) (2007). DOH Administrative Order No. 2007-0012.

A GLOBAL COMPARISON OF P- AND S-WAVE VELOCITY STRUCTURES OF THE MANTLE LITHOSPHERE BENEATH MAJOR CRATONS AROUND WORLD

E. Barzgar[1], F. Niu[1,2] and S. Pei[3]

ABSTRACT: We compared Pn and Sn velocities of major cratons of the world to provide constraints on how much these cratons have been modified from their initial states. In particular, we employed pseudowave (PSn) velocity computed from Sn-Pn traveltimes to estimate *Vp/Vs* ratio. We sorted the Pn, Sn, and PSn traveltime data into two groups based on epicentral distance: (1) 2°-12° and (2) 2°-7°. Our results suggest that most cratonic keels show comparable seismic properties with high velocities and low *Vp/Vs* ratio, implying a highly depleted mantle lithosphere. One exception is the Eastern North China Craton (ENCC). The mantle lithosphere beneath the ENCC has the lowest P- and S-wave velocities, as well as distinctly high *Vp/Vs* ratios in both distance groups, suggesting a complete removal of the depleted Archean mantle lithosphere. The Wyoming Craton also has a high *Vp/Vs* ratio close to that of the ENCC but a high P-wave velocity comparable to that of a typical craton, suggesting that its mantle keel has been significantly modified by metasomatism, rather than been completely removed and replaced by a thermal lithosphere. The Ordos Block located in the western part of the North China Craton (WNCC) displays high velocities and low *Vp/Vs* ratio, similar to those of the typical cratons, suggesting that the Ordos Block maintained its Archean mantle lithosphere. The seismic properties of the Trans-North China Orogen (TNCO), located between the WNCC and ENCC, show transitional values between those of the ENCC and the Ordos Block, suggesting an intermediate mantle lithosphere state between that of the ENCC (fertile Early Cretaceous) and the Ordos Block (depleted Archean).

Keywords: Craton, North China Craton, Wyoming Craton, Mantle Lithosphere, Pn and Sn velocity, *Vp/Vs* ratio.

INTRODUCTION

Cratons resulted from a specific melting regime of the primitive mantle with elevated temperature during the Archean. This process formed a unique mantle lithosphere with high strength, depletion, and buoyancy (Carlson et al. 2005; Shulgin and Artemieva, 2019). However, each craton has evolved differently since then. Some processes such as metasomatism can change the initial unique features of the cratons. These changes can reduce the Mg# as well as increase the pyroxene-rich contents, which usually cause lower seismic velocities and higher *Vp/Vs* ratio (Lee, 2003; Carlson et al. 2005; Artemieva, 2009; Shulgin and Artemieva, 2019).

Some studies suggest that the base of the lithosphere, unlike its top, has been universally modified by constant interaction with the asthenospheric flow (Wu et al. 2014; Hu et al. 2018; Celli et al. 2020). Thus, to speculate how much cratons have been modified from their unique initial form, we employed Pn and Sn phases, which are sensitive to the top of the mantle lithosphere.

In this study, we selected several major cratons of the world and compared seismic properties of their mantle lithosphere using Pn, Sn, PSn (i.e., Sn-Pn differential traveltime) velocities as well as *Vp/Vs* ratio to speculate how much they have been modified from their initial form.

CRATONS, DATA AND METHOD

Cratons

We selected eleven cratonic blocks of the world. Acceptable ray coverage was the priority for selecting these blocks and thus we skipped the results for cratons with poor ray coverage such as West African Craton, Congo Craton, and South American Craton. As illustrated in Fig. 1, the selected cratons in this study are Siberian Craton (SIB), North China Craton (NCC), Indian Craton (IND), Yilgarn Craton (YIL), Tanzania Craton (TAN), Kalahari Craton (KAL), East European Craton (EEC), Superior Craton (SUP), and Wyoming Craton (WYO). For the NCC, we divided it into three parts: Eastern NCC (ENCC), Trans-North China Orogen (TNCO), and the Ordos Block of the Western NCC (WNCC). We considered the Ordos Block as representative of the WNCC. All selected cratonic blocks comprise major Archean crustal parts, except for the EEC, which also includes major Paleo-Proterozoic crustal parts.

[1] State Key Laboratory of Petroleum Resources and Prospecting, and Unconventional Petroleum Research Institute, China University of Petroleum Beijing, Beijing, 102249, CHINA
[2] Department of Earth, Environmental and Planetary Sciences, Rice University, Houston, TX 77005, USA
[3] Institute of Tibetan Plateau Research, Chinese Academy of Sciences, Beijing, CHINA

 https://doi.org/10.1142/9789811275449_0055

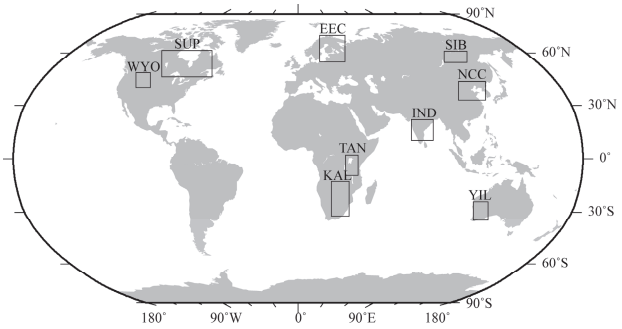

Fig. 1 Approximate location of the selected cratons in this study. The cratons are Siberian Craton (SIB), North China Craton (NCC), Indian Craton (IND), Yilgarn Craton (YIL), Tanzania Craton (TAN), Kalahari Craton (KAL), East European Craton (EEC), Superior Craton (SUP), and Wyoming Craton (WYO).

Data and Method

For the NCC, we extracted data from Annual Bulletin of Chinese Earthquakes (ABCE) between 1985 and 2019. For the other cratons, we extracted data from ISC-Reviewed, ISC-EHB, and ISC Bulletins between 1964 and 2020.

For a fair comparison, we implemented a similar processing approach for all cratons. After pre-processing and controlling the data quality, we corrected the traveltimes by projecting the hypocenter and station elevation to sea level. Then, we implemented a standard linear regression of traveltime and distance for estimating the average slowness (inverse velocity) of the Pn, Sn, and PSn. For the regression process, we imposed a maximum residual constraint of 12 s for the PSn, 10 s for the Sn, and 7 s for the Pn to remove the outliers.

The *Vp/Vs* ratio in this study was estimated using the V_{PSn} and corresponding V_{Pn} by the following equation:

$$\frac{V_p}{V_s} = 1 + \frac{V_{Pn}}{V_{PSn}} \quad (1)$$

The cratonic blocks here are different in size, and larger blocks include more long rays, which usually show higher velocities because they dive into the deeper parts of the mantle lithosphere. To remove this bias, we calculated the average velocities using two datasets based on the epicentral distance: 1) 2°-12° (full dataset) and 2) 2°-7° (short-distance dataset).

RESULTS AND DISCUSSIONS

Fig. 2 shows the average velocities and *Vp/Vs* ratio of the mantle lithosphere of the cratons using the two datasets. The results show that most cratonic blocks present high velocities and low *Vp/Vs* ratio, suggesting a depleted nature of their mantle lithosphere with the most resemblance to the original residue from the melt extraction of the primitive mantle during Archean.

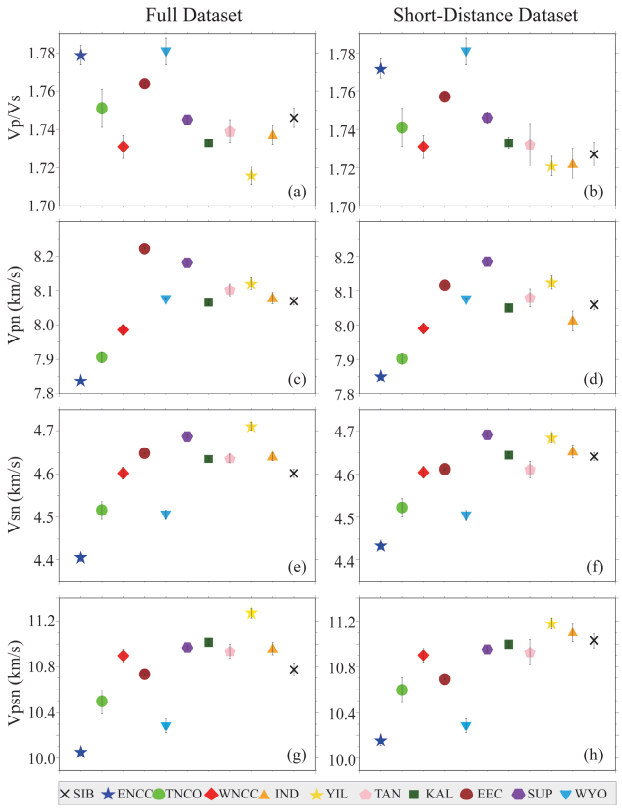

Fig. 2 Seismic properties (Vp/Vs, V_{Pn}, V_{Sn}, V_{PSn}) of the cratons. Full and short-distance datasets refer to the ones using 2°-12° and 2°-7° epicentral distance ranges, respectively. The left figures are with the full datasets, and the right ones are with the short-distance datasets. Note the contrasting seismic properties of the ENCC in all properties compared with those of the other cratons. The Wyoming Craton shows a noticeable high Vp/Vs ratio (a and b) and high V_{Pn} (c and d).

Some cratonic blocks, however, do not fall in this category. For example, the ENCC shows the lowest P- and S-wave velocities as well as a high *Vp/Vs* ratio in both datasets. These features suggest a total removal of the Archean mantle lithosphere beneath it. Low velocities and high *Vp/Vs* ratio of the ENCC using the short-distance dataset refute the possibility of the presence of a thin Archean layer at the mantle lithosphere lid beneath the ENCC. A recent adjoint traveltime tomography study (Dong et al. 2021) is also consistent with this conclusion. The Ordos Block of the WNCC shows comparable velocities and *Vp/Vs* ratio with the typical cratons. These observations suggest that the Ordos Block has maintained its Archean keel. There is no mantle xenolith record within the Ordos Block to confirm this idea. However, high velocities at uppermost mantle depths of seismic studies (e.g., Pei et al. 2007) is consistent with such a scenario. The results of the TNCO are between those of the ENCC and the WNCC. This may imply two scenarios:

1) The mantle lithosphere beneath the TNCO was totally removed and replaced during the collision of the ENCC and WNCC at ~ 1.9 Ga. Some xenolith records (e.g., Gao et al. 2002) also support such a scenario. 2) The mantle lithosphere of the TNCO includes both fertile Early Cretaceous (similar to ENCC) and depleted Archean (similar to Ordos Block) parts. Similar to the ENCC and in contrast to the typical cratons, the Wyoming Craton shows high *Vp/Vs* ratio. However, its P-wave velocity is high, which is comparable with that of the typical cratons. These features suggest that the mantle lithosphere has been highly modified by metasomatism, rather than been totally destroyed and removed. Several seismic studies (e.g., Humphreys et al. 2015) also suggest high velocities down to depths of around 200 km beneath the Wyoming Craton, which is consistent with our results.

CONCLUSIONS

We assessed several major cratonic blocks of the world to speculate how much they have been modified from their unique initial form. To accomplish this, we implemented Pn, Sn, and PSn velocities as well as *Vp/Vs* ratio to derive the seismic properties of the mantle lithosphere of the cratons.

The results suggest that most cratonic blocks show high velocities as well as low *Vp/Vs* ratio, inferring the presence of depleted Archean mantle lithosphere beneath most cratons. The Ordos Block of the WNCC also shows high velocities and low *Vp/Vs* ratio, suggesting the presence of the depleted mantle lithosphere beneath it. Conversely, cratonic blocks such as ENCC, TNCO, and the Wyoming Craton show contrasting results. The ENCC with the lowest velocities and high *Vp/Vs* ratio in both full and short-distance datasets infer that the whole Archean mantle lithosphere has been removed and replaced by a younger mantle. The TNCO with results between the ENCC and the Ordos Block of the WNCC infer an intermediate mantle lithosphere between the other two parts. The Wyoming Craton with high *Vp/Vs* ratio as well as high P-wave velocity implies that the Archean mantle lithosphere has been preserved, but has been highly modified by the metasomatism.

References

Artemieva, I.M. (2009). The continental lithosphere: Reconciling thermal, seismic, and petrologic data. Lithos. 109, 23–46.

Carlson, R.W., Pearson, D.G. and James, D.E. (2005). Physical, chemical, and chronological characteristics of continental mantle. Rev. Geophys. 43, 1–24.

Celli, N.L., Lebedev, S., Schaeffer. A.J. and Gaina. C. (2020). African cratonic lithosphere carved by mantle plumes. Nat. Commun. 11, 92.

Dong, X., Yang, D., Niu, F., Liu, S. and Tong, P. (2021). Adjoint traveltime tomography unravels a scenario of horizontal mantle flow beneath the North China craton. Sci Rep 11, 12523.

Gao, S., Rudnick, R.L., Carlson, R.W., McDonough, W.F. and Liu, Y.S. (2002). Re-Os evidence for replacement of ancient mantle lithosphere beneath the North China craton. Earth Planet. Sci. Lett. 198, 307–322.

Hu, J., Liu, L., Faccenda, M., Zhou, Q., Fischer, K.M., Marshak, S. and Lundstrom, C. (2018). Modification of the Western Gondwana craton by plume–lithosphere interaction. Nat. Geosci. 11, 203–210.

Humphreys, E.D., Schmandt, B., Bezada, M.J. and Perry-Houts, J. (2015). Recent craton growth by slab stacking beneath Wyoming. Earth Planet. Sci. Lett. 429, 170–180.

Lee, C.-T.A., 2003. Compositional variation of density and seismic velocities in natural peridotites at STP conditions: Implications for seismic imaging of compositional heterogeneities in the upper mantle. J. Geophys. Res. Solid Earth 108, 2441.

Pei, S., Zhao, J., Sun, Y., Xu, Z., Wang, S., Liu, H., Rowe, C.A., Nafi Toksöz, M. and Gao, X. (2007). Upper mantle seismic velocities and anisotropy in China determined through Pn and Sn tomography. J. Geophys. Res. Solid Earth 112, 1–16.

Shulgin, A. and Artemieva, I.M. (2019). Thermochemical Heterogeneity and Density of Continental and Oceanic Upper Mantle in the European-North Atlantic Region. J. Geophys. Res. Solid Earth 124, 9280–9312.

Wu, F.Y., Xu, Y.G., Zhu, R.X. and Zhang, G.W. (2014). Thinning and destruction of the cratonic lithosphere: A global perspective. Sci. China Earth Sci. 57, 2878–2890.

MHD LINEAR THEORY OF TEARING INSTABILITY FOR FOURTH-ORDER DIFFERENTIAL MAGNETIC DIFFUSION EFFECT

T. Shimizu[1] and K. Fujimoto[2]

ABSTRACT: MHD (Magneto-Hydro-Dynamic) linear theory of magnetic reconnection process is studied for fourth-order differential magnetic diffusion effects which may be called hyper−resistivity. In general, the second-order magnetic diffusion, i.e., resistivity, is employed to drive the reconnection process. In this paper, the fourth-order diffusion is examined and compared with the second-order diffusion. In fact, the importance of such a higher-order diffusion is predicted from plasma kinetic particle simulations of reconnection process. Rather than the second-order diffusion, higher-order diffusion may be important to achieve the fast magnetic reconnection. In this paper, firstly, the equilibrium is numerically derived for the magnetic annihilation process in a 1D current sheet by an initial value problem (shooting) technique. It is shown that the equilibrium established by mixing those two types of the magnetic diffusion is simply dominated by the ratio of two Lundquist numbers defined for each magnetic diffusion. Second, on the basis of the equilibrium, the linear growth rate of the tearing instability is studied as an initial value problem technique. As the remarkable point, it is shown that, the linear growth rate is determined by two dimensionless parameters, i.e., the aspect ratio ε of the magnetic diffusion region and the ratio of two Lundquist numbers, in addition to the wave length k and upstream boundary condition c.

Keywords: MHD Linear Theory, Magnetic Reconnection, Tearing Instability, Magnetic Dissipation.

INTRODUCTION

Magnetic reconnection is believed to be an energy conversion process from magnetic energy to plasma kinetic energy in space plasma explosions, such as solar flares and geomagnetic substorms. Tearing instability is caused by the magnetic reconnection and is believed to trigger such plasma explosions. The linear theory started from Furth, et al. (1963) and then was improved by Loureiro, et al. (2007). On these days, the former and latter theories are respectively called FKR and LSC theories. Recently, numerically solving the initial value problem of the perturbation equations derived in LSC theory, the LSC theory was modified by Shimizu (2018) and extended by Shimizu (2021) for the introduction of viscosity effect. The basic concept proposed by Shimizu is illustrated in Figure 3.

In general, the magnetic reconnection is driven by the second-order magnetic diffusion, i.e., resistivity, but can be also driven by the fourth-order magnetic diffusion, i.e., hyper-resistivity. In fact, such higher-order diffusion is predicted from plasma kinetic particle simulations of reconnection process (Fujimoto & Sydora (2021)). In this paper, the tearing instability driven by the fourth-order magnetic diffusion effect is studied. The induction equation incorporated with the second and fourth-order diffusions is as follows.

$$\frac{\partial \boldsymbol{B}}{\partial t} = \nabla \times (\boldsymbol{V} \times \boldsymbol{B}) + \eta\left(\frac{\partial^2 \boldsymbol{B}}{\partial x^2} + \frac{\partial^2 \boldsymbol{B}}{\partial y^2}\right) - \alpha\left(\frac{\partial^4 \boldsymbol{B}}{\partial x^4} + \frac{\partial^4 \boldsymbol{B}}{\partial y^4}\right) \quad (1)$$

In Shimizu (2021), α was switched to zero to avoid the inversion of magnetic diffusion but, in this paper, α is set to be steadily a constant. For Eq. (1), the equilibrium can be numerically obtained by the initial value problem technique (Shimizu, 2018, 2021, and 2022). Then, on the basis of the equilibrium, the linear theory of the tearing instability can be studied where the initial value problem technique is again employed. Finally, it is shown that the linear growth rate is basically dominated by two dimensionless parameters, i.e., the aspect ratio ε of the magnetic diffusion region and the ratio of two Lundquist numbers defined for those two types of diffusions.

EQUILIBRIUM

The equilibrium for the second-order diffusion has been analytically found by Loureiro, et al.(2007), where incompressible 2D MHD equations including Eq.(1) was solved for α=0 and ∂/∂t=0. However, that for the fourth-order diffusion is not yet found. The equilibrium in which the second-order and fourth-order diffusions simultaneously work satisfies the following equation.

$$\xi f(\xi) + (1/S_i) f'(\xi) - (1/S_{Hi}) f'''(\xi) + c = 0, \quad (2)$$

Excepting the third terms on the left side of Eq.(2), the notation is the same as that of Loureiro, et.al. (2007), where f(ξ) is the magnetic field function of 1D anti-parallel field and ξ is taken as the normal axis to the current sheet. The prime is the derivative for ξ. From the

[1] RCSCE, Ehime University, Matsuyama City Bunkyo Town 2, 790-8577, JAPAN
[2] School of Space and Environment, Beihang University, Beijing 100191, CHINA

 https://doi.org/10.1142/9789811275449_0056

left hand first term of Eq.(2), each term respectively corresponds to the convection, second-order diffusion (i.e., resistive), and fourth-order diffusion electric fields. Si and S_{Hi} are the Lundquist numbers for inflow speed Vi to the diffusion region, respectively for the second and fourth-order diffusions, and hence, defined by translating η and α in Eq.(1), as follows.

$$(1/S_i) = \eta/(\delta_{cs}\epsilon V_A),\ (1/S_{Hi}) = \alpha/(\delta_{cs}^3\epsilon V_A), \quad (3)$$

where δ_{cs} is the thickness of the current sheet and V_A is the Alfven speed measured in the upstream field region at $y=\delta_{cs}$, i.e., $\xi=1.307$. Then, c and ε are defined, as follows.

$$c = E_0/(\epsilon V_A^2),\ \epsilon = 2\delta_{cs}/L_{cs} \quad (4)$$

where δ_{cs} is the length of the magnetic diffusion region, and hence, ε is the aspect ratio of the magnetic diffusion region based on Sweet-Parker model and hence is equal to the Alfven Mach number $M_A=Vi/V_A$. Since $Vi=\varepsilon V_A$ is the plasma inflow speed to the magnetic diffusion region, and generally, $Vi \neq V_A$, Si and S_{Hi} defined by Eq.(3) are not the Lundquist numbers S and S_H defined in the usual MHD studies of magnetic reconnection process. Then, constant Eo is the background uniform electric field, and constant c is a control parameter to find the equilibrium.

Eq.(2) can be numerically solved as an initial value problem, where f(0)=f''(0)=0 is steadily fixed because f(ξ) is an odd function at ξ=0, for the anti-symmetric field. Once either of Si or S_{Hi} is given, the equilibrium f(ξ) which satisfies three conditions of f(1.307)=1, f'(1.307)=0, and f(ξ=+∞)=0 as the physical requirements, is numerically found by adjusting three control parameters of c, f'(0), and the remaining S_{Hi} or Si. Note that, unlike f(ξ) of the original LSC theory (Loureiro,2007), f(ξ)=1 is not kept at ξ>1.307, to rigorously keep the equilibrium.

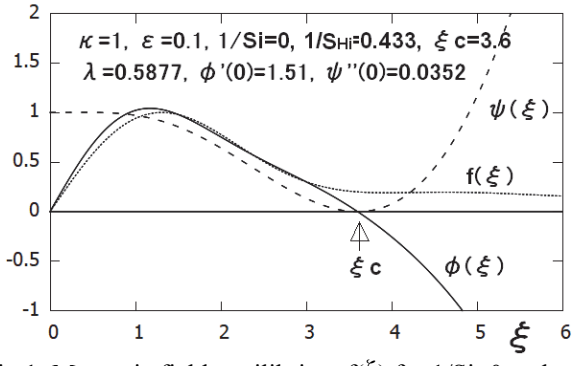

Fig.1: Magnetic field equilibrium f(ξ) for 1/Si=0 and $1/S_{Hi}$=0.433 is obtained from Eq.(2). Perturbed functions ϕ and ψ for k=1, ε=0.1, and ξ_c=3.6 are obtained from Eqs.(5) and (6).

Figure 1 shows f(ξ) for 1/Si=0 which satisfies f(1.307) =1 and f'(1.307)=0. However, it is unclear that f(+∞)=0, because f(+∞) cannot be numerically solved by the initial value problem technique. However, if $1/S_{Hi}$=0.433, c=0.9314, and f'(0)=1.2547 are slightly changed, f(ξ) sensitively diverges to either of + or -∞ at large ξ. Hence, if there is the equilibrium, it should be close to f(ξ) shown in Figure 1. In the same manner, f(ξ) and $1/S_{Hi}$ are obtained for different 1/Si values. Eventually, Figure 2 shows how $1/S_{Hi}$ varies for 1/Si. Figure 1 for 1/Si=0 and $1/S_{Hi}$=0.433 corresponds to the most left side of Figure 2, in which the fourth-order diffusion only works. The case of 1/Si=1.0 and $1/S_{Hi}$=0 corresponds to the most right side of Figure2, in which the second-order diffusion only works.

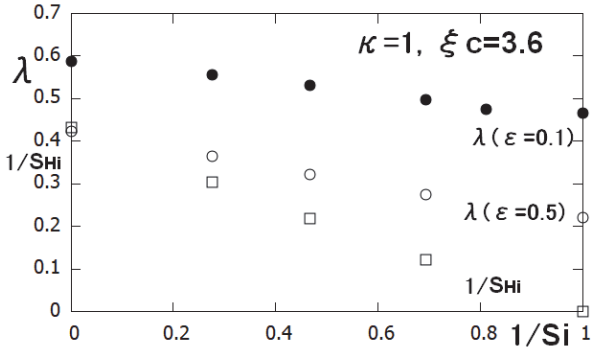

Fig.2: The relation between 1/Si and $1/S_{Hi}$ is shown by square boxes, which is obtained from Eq.(2). The linear growth rate λ is shown by black and white circles, which are obtained from Eqs.(5)-(6) for k=1 and ξc=3.6.

LINEAR THEORY

The perturbation equations based on the equilibrium f(ξ) found in Eq.(2) is written as below.

$$\lambda(\phi'' - \kappa^2\epsilon^2\phi) = -f(\xi)(\psi'' - \kappa^2\epsilon^2\psi) + f''(\xi)\psi, \quad (5)$$

$$\lambda\kappa\psi = \kappa f(\xi)\phi + (1/S_i)(\psi'' - \kappa^2\epsilon^2\psi) - (1/S_{Hi})(\psi'''' + \kappa^4\epsilon^4\psi) \quad (6)$$

These are the same as eqs.(8)-(9) of Loureiro,et.al., (2007), excepting the $1/S_{Hi}$ term for the fourth-order diffusion and the exchange of *x* and *y* coordinates. According to Figure 2, since 1/Si=1 results in $1/S_{Hi}$=0, Eq.(6) exactly coincides with eq.(9) of Loureiro,et.al.(2007). Once k, ε, Si, and S_{Hi} are given, ϕ and ψ which satisfy $\phi(\xi c)=\psi(\xi c)=\psi'(\xi c)=0$ at a given ξ_c are numerically found by adjusting λ, $\phi'(0)$ and $\psi'''(0)$, where $\phi(0)=\psi'(0)=\psi'''(0)=0$ and $\psi(0)=1$ are fixed as the initial values, because the symmetry field condition is assumed at ξ=0.

Figure 2 shows how λ varies for ε and 1/Si for k=1 and ξ_c=3.6. For each case of ε =0.1 and 0.5, λ monotonically increases from 1/Si=1 to 1/Si=0. It means that the fourth-

order diffusion tends to steadily promote the tearing instability rather than the second-order diffusion. Then, λ for ε =0.1 is steadily higher than that for ε =0.5 in all range of 1/Si. At the point, the fourth-order diffusion has similar characteristics to the second-order diffusion.

DISCUSSIONS

Traditionally, FKR and original LSC theories solve ϕ and ψ in 0<ξ<+∞, which converge to zero at ξ=+∞. To do so, in those theories, the inner and outer regions of current sheet are separately solved, where the inner region is solved as resistive MHD and the outer region is assumed to be ideal MHD. It is implicitly assumed that the inner region is strongly localized at ξ=0 and the outer region essentially dominates (drives) whole of the tearing instability. However, since the local maximum points of ϕ and ψ in Figure 1 are evidently separated from ξ=0, the assumption is violated.

In contrast, in this paper, Eqs.(5)-(6) are seamlessly solved between the inner and outer regions, where all regions are exactly solved as resistive MHD. To do so, Eqs.(5)-(6) are numerically solved by an initial value problem technique from ξ=0 to the upstream open boundary ξc (<+∞). Then, it is expected that the behaviors at ξ=+∞ can be deduced by changing ξc. In our recent studies, it has been observed that, as ξc increases, λ tends to increase and be saturated at large ξc.

Figure 3 shows the schematic image of the linear theory proposed in this paper, where some magnetic field lines combined with the equilibrium and perturbed fields. are drawn by thin solid lines. In addition, the thick arrows show the plasma flow field (V_{x0},V_{y0}) of the equilibrium. The upstream open boundary condition is assumed to be $\phi=\psi=\psi'$=0 at ξc=3.6, where is along the horizontal thick solid line. It means that the perturbed magnetic field satisfies $B_{x1}=B_{y1}=0$ and $V_{y1}=0$ at the open boundary ξc=3.6. However, since $V_{y0}\neq0$ at ξc, the boundary is open.

SUMMARY

The fourth-order magnetic diffusion is studied in the MHD linear theory of tearing instability. First, the equilibrium for Eq.(2) was numerically found, which is an extension of the equilibrium analytically found by Loureiro (2007) for the second-order magnetic diffusion. Second, the perturbation equations, i.e., Eqs.(5)-(6), were numerically solved for the equilibrium and the linear growth of the instability was studied. The characteristic of the linear growth by the fourth-order diffusion is similar to that of the second-order diffusion but the growth rate for the fourth-order diffusion tends to be higher than the second-order diffusion. It suggests that the fourth-order diffusion is more important than the second-order diffusion to promote fast reconnection.

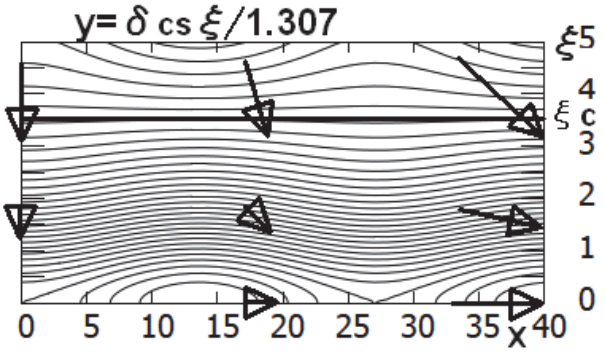

Fig.3: Schematic image of tearing instability proposed in this paper. Magnetic field lines are drawn by mixing the equilibrium field $B_{y0}= V_A f(\xi)$ and perturbed field $(B_{x1},B_{y1})=(\psi', -\partial\psi/\partial x)$. To fit many simulations (e.g., Shimizu, 2021), the *x* and *y* coordinates are exchanged from the definition of original LSC (Loureiro, et al., 2007).

ACKNOWLEDGEMENTS

The research of T. Shimizu is supported by Research Institute for Sustainable Humanosphere (RISH) in Kyoto University of Japan. The research of K. Fujimoto is supported by the NSFC grant (No.41874189).

References

Furth,H.P., Killeen,J., and Rosenbluth,M.N. (1963), Finite-Resistivity Instabilities of a Sheet Pinch, Phys. Fluids 6, pp.459-484.

Loureiro,N.F., Schekochihin,A.A., and Cowley,S.C. (2007), Instability of current sheets and formation of plasmoid chains, Phys. Plasmas, 14, 100703.

Fujimoto, K. and Sydora, D. (2021). Electromagnetic Turbulence in The Electron Current Layer to Drive Magnetic Reconnection, Astrophys. J. Lett., 909:L15.

Shimizu,T. (2018), A new viewpoint for linear theory of tearing instability, 2nd Asia-Pacific Conf. on Plasma Phys., Kanazawa, Japan, SGP-04.

Shimizu,T., (2021), Higher-order Differential Magnetic Diffusion Effect in MHD Simulations of Petschek Reconnection Model, AOGS2021, ST11-A008 (proceedings, pp.209-211).

Shimizu,T., (2022), Linear Theory of Tearing Instability with Some Types of Viscosity Effects, KDK Research Report 2021, Kyoto University Research Information Repository, Kyoto University, Japan, pp.93-96.

EXAMINATION OF DRAG FORCE ON CORONAL MASS EJECTIONS

Chia-Hsien Lin[1], James Chen[2]

ABSTRACT: Coronal mass ejections (CMEs) are large-scale magnetic flux rope that carries large amount of plasma and energy from the Sun to the heliosphere. They can significantly disturb the space weather and disrupt space activities. Therefore, it is important to be able to accurately predict their arrival time. Many prediction studies are based on the commonly believed assumption that the drag force is the dominant force acting on the CMEs and all other forces are negligible. However, there has been no observational evidence to support this assumption. In this study, we apply erupting flux rope (EFR) model, which is a model that includes all force components, to model observed CME trajectories. The results show that the drag force is often not the dominant force and that no force can be assumed negligible.

Keywords: coronal mass ejection; drag force; Lorentz force; solar corona; space weather; coronal magnetic field

INTRODUCTION

Coronal mass ejections are large-scale erupting magnetic structures. The eruption typically consists of a main acceleration phase when the structure rapidly accelerates to a peak velocity, followed by a residual acceleration phase when the outward acceleration decreases to nearly zero, and the CMEs continue to travel outward at a near constant speed. Since CMEs can significantly disturb the space weather and impact our satellites and communication systems (Allen et al. 1989), it has been one of main tasks for space scientists to accurately predict the CME travel time (Brueckner et al. 1998). To predict the travel time, we need to know the equation of motion and all the forces acting on the CME:

$$\mathrm{M_{CME}}\frac{d^2 Z_{CME}}{dt^2} = F_{total} = F_L + F_c + F_p + F_g + F_d \quad (1)$$

where $\mathrm{M_{CME}}$ is the mass of CME, $\mathrm{Z_{CME}}$ is the radial distance from the Sun, $\mathrm{F_L}$ is the self-Lorentz force, composed of hoop force and magnetic tension force, $\mathrm{F_c}$ is the Lorentz force due to the background coronal magnetic fields, $\mathrm{F_p}$ is the pressure gradient force due to the pressure difference between the CME and the background, $\mathrm{F_g}$ is the gravitational force, and $\mathrm{F_d}$ is the drag force. One widely believed assumption is that beyond the main acceleration phase, the drag force becomes the dominant force, and the net force can be approximated by $\mathrm{F_d}$ alone (e.g., Vrsnak, 2001; Vrsnak & Gopalswamy, 2002). Based on this assumption, the equation of motion becomes:

$$M_{CME}\frac{(\mathrm{d^2\,Z_{CME}})}{\mathrm{dt^2}} = F_{total} = F_d = \frac{1}{2}c_d\rho_a A\,\Delta V\,|\Delta V|, \quad (2)$$

where $\mathrm{c_d}$ is the drag coefficient, $\mathrm{\rho_a}$ is the density of ambient solar wind, and $\Delta \mathrm{V} = \mathrm{V_{CME}} - V_{SW}$ is the difference between the CME and solar wind velocities. This is called Drag-Based Model (DBM). Many studies have applied DBM, with some variations, to predict the CME travel time and $\mathrm{c_d}$. However, the validity of this assumption has not been verified by either observational or theoretical studies. The objective of this study is to examine whether the assumption of $\mathrm{F_{total}} = F_d$ is justified in the interplanetary space within 1 AU.

ERUPTIVE FLUX ROPE MODEL

In this study, we use the eruptive flux rope (EFR) model, first developed by Chen (1989), to model observed CME trajectories. EFR is a physics-based model to describe an erupting 3-D coronal flux rope. It is formulated based on the ideal magnetohydrodynamics (MHD). A face-on view of the model structure of the flux rope is shown in Fig. 1. The equation of motion in the model is as follows:

[1] Department of Space Science and Engineering, National Central University, Taoyuan 32001, TAIWAN
[2] Plasma Physics Division, Naval Research Laboratory, Washington DC 20375, USA

 https://doi.org/10.1142/9789811275449_0057

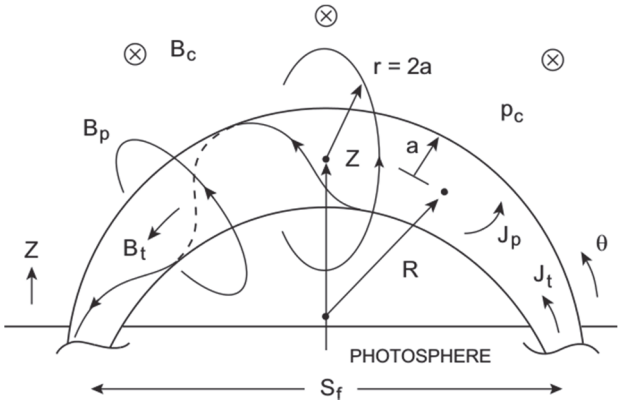

Figure 1 A face-on view of a coronal flux rope (Chen et al. 1996). J_t and J_p are the toroidal and poloidal current; B_t and B_p are B_c and P_c are the magnetic and gas pressure of the ambient corona, respectively; a and R are the minor and major radius, respectively, and S_f is the foot point separation.

$$F_{total} = \left(\frac{\Phi_p^2}{c^4 L^2 R}\right)\left(f_{hoop} + f_{tens} + f_c + f_p\right) + F_g + F_d \quad (3)$$

where $\Phi_p(t)$ is the poloidal flux enclosed by the flux rope and the photosphere, c is the speed of light, L(t) is the self-inductance, and R(t) is the major radius of the flux rope (cf Fig. 1). f_{tens} is the magnetic tension force, $f_{hoop} = J_t B_p$ is the hoop force, and the two comprise the dimensionless self-Lorentz force $f_L = f_{hoop} + f_{tens}$.

We first apply the model to fit observed CME trajectories, then use the best-fit results to derive the forces, and finally examine/compare the temporal change of the magnitudes of different forces to determine whether the DBM assumption can be valid at some stage during a CME process. The consistency between the observed and computed trajectories is evaluated by the average deviation:

$$D \equiv \frac{1}{T}\sum_i \frac{\left|Z_{data}(t_i) - Z_{model(t_i)}\right|}{\sigma_i} \Delta t_i \quad (4)$$

where Z_{data} and Z_{model} are the observed and model trajectories, σ_i is the observational error at measurement i, and T is the duration of the observation.

.

RESULTS

The results of two CMEs are shown in Fig. 2 and Fig. 3. The trajectory data are from Wood et al. (2009) for Fig. 2 and Wood et al. (2010) for Fig. 3.

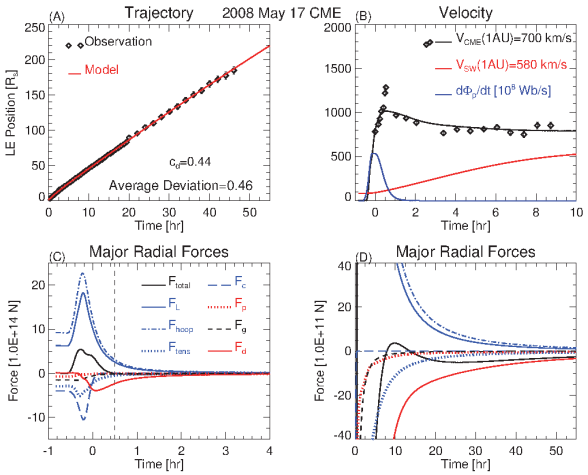

Figure 2 The best-fit result of May 17 2008 CME (Lin & Chen 2022). (A) Observed (symbols) and model (line) trajectories; (B) Observationally derived (symbols) and model (black line) velocities. Model predicted V_{sw} (red line) and flux injection rate (blue line). (C) and (D): the derived major radial forces during the main and residual acceleration phases, respectively.

The May 17, 2008 CME reaches a maximum speed of more than 1000 km/s, and remains faster than the solar wind. Fig.2(A) shows that the model trajectory matches the observed one, with the average deviation equal to 0.46. Panel B shows that the observational and model velocities are also consistent with each other. The derived forces are compared in panels C and D. Panel C shows that during the main acceleration phase, which is within the first hour from the first observed point, the main positive force is F_{hoop}, and the main retarding forces are F_c and F_{tens}. The drag force only becomes the dominant negative force after these two forces have decreased. Panel D shows that F_{total} goes from positive to negative multiple times during the entire eruption process, indicating that the positive and negative forces are comparable and competing with each other over the entire process. F_d is comparable with several other forces, and is very different from F_{total} before about 150 R_s. This means that the assumption of F_d much larger than all other forces is not valid for this event.

The June 1, 2008 CME results are shown in Fig. 3. Panel A and B show that the model trajectory and velocity profiles are consistent with the observed ones, with the average deviation equal to 0.75. Panel B indicates that the main acceleration phase for this event is within the first 30-40 hours from the first observed point. Panel C shows that the dominant outward force is also the hoop force. However, the main inward forces during the main acceleration phase are F_p and F_{tens}, with F_c playing a minor role, for this event. The drag force is very weak at the beginning. Panel D shows that during the residual

acceleration phase, F_d is very different from F_{total}, and is comparable to many other forces during the entire observation period. In short, the drag force is not the dominant force for this case, either. One interesting point is that F_g, which is usually considered as negligible at 1 AU, is a non-negligible retarding force in this case.

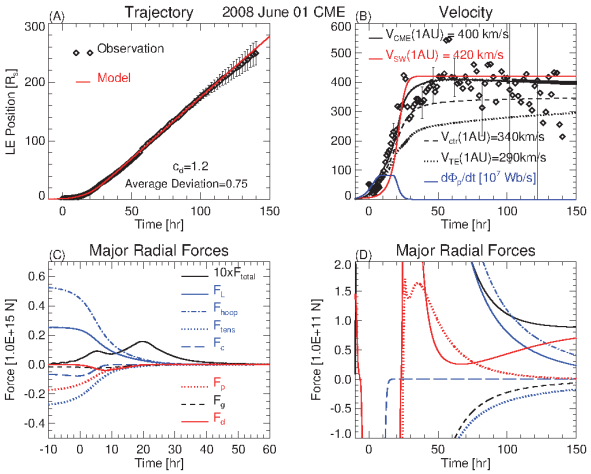

Figure 3 The best-fit result of June 01 2008 event (Lin & Chen 2022). The format is the same as that of Fig, 2. In panel B, model predicted velocities of the centroid (V_{ctr}) and trailing edge (V_{TE}) of the CME are also shown.

CONCLUSION

Our results show that the magnitude of the drag force is usually comparable with other forces after the main acceleration phase. The self Lorentz force is not negligible at any stage during a CME process. Even the gravitational force can be important for some CME events. In short, while the drag force plays an important role in the CME process, the assumption of $F_d = F_{total}$ is usually not valid. No force component should be neglected a priori.

ACKNOWLEDGEMENTS

We thank Dr. Brian Wood for providing the trajectory data. This work is supported by the MOST of Taiwan under the Grant No. MOST 109-2111-M-008-002 and by the U.S. Naval Research Laboratory Base Program before the retirement of JC.

References

Allen, J., Frank, L., Sauer, H., & Reiff, P. (1989). Effects of the March 1989 solar activity. *EOS Transactions*, *70*(46), 1479–1488. https://doi.org/10.1029/89EO00409

Brueckner, G. E., Delaboudiniere, J. P., Howard, R. A., Paswaters, S. E., Cyr, S. O. C., Schwenn, R., et al. (1998). Geomagnetic storms caused by coronal mass ejections (CMEs): March 1996 through June 1997. *Geophysical Research Letters*, *25*(15), 3019–3022. https://doi.org/10.1029/98GL00704.

Chen, J. (1989). Effects of toroidal forces in current loops embedded in a background plasma. *The Astrophysical Journal*, *338*, 453. https://doi.org/10.1086/167211

Chen, J. (1996). Theory of prominence eruption and propagation: Interplanetary consequences. *Journal of Geophysical Research*, *101*(A12), 27499–27520. https://doi.org/10.1029/96JA02644

Vršnak, B. (2001). Deceleration of coronal mass ejections. *Solar Phyiscs*, *202*(1), 173–189. https://doi.org/10.1023/A:1011833114104.

Vršnak, B., & Gopalswamy, N. (2002). Influence of the aerodynamic drag on the motion of interplanetary ejecta. *Journal of Geophysical Research*, *107*(A2), 1019. https://doi.org/10.1029/2001JA000120.

Wood, B. E., & Howard, R. A. (2009). An empirical reconstruction of the 2008 April 26 coronal mass ejection. *The Astrophysical Journal*, *702*(2), 901–910. https://doi.org/10.1088/0004-637X/702/2/901.

Wood, B. E., Howard, R. A., & Socker, D. G. (2010). Reconstructing the morphology of an evolving coronal mass ejection. *The Astrophysical Journal*, *715*(2), 1524–1532. https://doi.org/10.1088/0004-637X/715/2/1524

AUTHOR INDEX